WIDEBAND MONOSTATIC CO-CHANNEL SIMULTANEOUS TRANSMIT AND RECEIVE (C-STAR) ANTENNA AND ARRAY SYSTEMS

by

EHAB ABDALLA ETELLISI

B.S., University of Tripoli, 2005

M.S., University of Colorado Denver, 2011

A thesis submitted to the

Faculty of the Graduate School of the

University of Colorado in partial fulfillment

of the requirement for the degree of

Doctor of Philosophy

Department of Electrical, Computer and Energy Engineering

2018

This thesis entitled:
Wideband Monostatic Co-channel Simultaneous Transmit and Receive (C-STAR) Antenna and Array System
Written by Ehab Abdalla Etellisi
has been approved for the Department of Electrical, Computer, and Energy Engineering

____
Dejan S. Filipović

____
W. Neill Kefauver

Date_______________

The final copy of this thesis has been examined by the signatories, and we find that both the content and the form meet acceptable presentation standards of scholarly work in the above mentioned discipline.

Ehab A. Etellisi (Ph.D., Electrical, Computer and Energy Engineering)

Wideband Monostatic Co-channel Simultaneous Transmit and Receive (C-STAR) Antenna and Array System

Thesis directed by Professor Dejan S. Filipović

Most modern wireless communication systems either operate at different times or frequencies to avoid self-interference. These duplexing techniques require more time or frequency spectrum resources; therefore, alternative solutions are needed. One solution that has attracted more interest lately is referred to as co-channel simultaneous transmit and receive (C-STAR). C-STAR systems enable transmitting and receiving at the same time and over the same frequency channel. Thus, several advantages can be gained, including increased channel capacity, efficient reuse of licensed spectrum, and simplified frequency planning. C-STAR operation is also of a great interest to many applications including radar, electronic warfare, and wireless communications such as Wi-Fi, 5G, and land-mobile radio base-stations. However, a key challenge for C-STAR operation over a wideband and co-polarized diverse coverage is to effectively reduce the significant self-interference. Practically, communication systems desire the overall system transmit/receive (TX/RX) isolation to be >110 dB. To achieve this high TX/RX isolation level, combinations of several advanced passive, analog, and digital self-interference cancellation schemes are often considered. Typically, the antenna layer can maximize the overall system TX/RX self-interference cancellation where >15 dB antenna isolation is sometimes sufficient. However, the higher level of isolation on the antenna layer is; the simpler overall C-STAR systems become which leads eventually to handle much greater transmitted power. Therefore, the main focus in this thesis is on the engineering of C-STAR antenna array layer with high isolation and diverse radiation characteristics using

several novel wideband co-polarized circulator and circulator-less monostatic antenna and array designs.

The monostatic C-STAR antennas are demonstrated first with the multi-arm spiral antennas. As well known, multi-arm spiral antennas have wideband consistent performance and multimode capability. For more than half century to date, spiral antennas have been used for countless applications, but have not been thoroughly investigated yet as a C-STAR monostatic antenna. Research in this thesis shows that multi-arm monostatic spiral antenna (i.e. $N>4$, where N is the number of arms) can achieve theoretically infinite TX/RX isolation without utilizing polarization multiplexing. Due to the use of a multiport TX/RX antenna, where $N/2$ arms are for TX and $N/2$ arms are for RX, its far-field performance is changed compared to a conventional spiral antenna that uses all arms for single function only. Different approaches are considered to mitigate the negative effects on the far-field while maintaining high TX/RX isolation. Theoretical models are also verified by full-wave simulations and measurements of the fabricated prototypes.

Several novel wideband monostatic linearly and circularly co-polarized broadside and omnidirectional C-STAR array configurations are proposed without taking advantage of any antenna-port, polarization, pattern, spatial, time, and frequency multiplexing. These C-STAR arrays have high TX/RX isolation, excellent far-field performance, reduced beamformer network (BFN) complexity, and smaller array size. All developed approaches achieve good C-STAR performance based on the antennas orientation, use of geometrical symmetries, and partially shared BFN cancellation techniques. In the absence of the BFN's imbalances and geometric asymmetries of the array, the proposed concepts can achieve theoretically infinite TX/RX isolation. Although the discussion presented in this thesis focuses on using spiral, monocone, discone, and sinuous antenna elements, the proposed C-STAR concepts can be extended to utilize other types of single/dual polarized antenna elements.

DEDICATION

To my mother and the memory of my father

To my lovely sister Rasha and brothers Gaith and Bisher

ACKNOWLEDGEMENTS

I would like to express my sincere gratitude to my academic advisor, Prof. Filipović, for his continuous support, patience, motivation, and enthusiasm through my Ph.D. study and research. Filip's guidance helped me in all the time of research, and writing of this thesis and journal/conference papers. His knowledge and ideas have greatly enhanced my education especially since I came from a communication and signal processing background. I could not have imagined having a better advisor and mentor for my Ph.D. study. Beside my advisor, I would like to thank my friend Dr. Elmansouri for enlightening me with the first glance of research, for always being deeply involved in my research, and his continues support in the past four years.

I would also like to thank my thesis committee: Prof. Kuester, Prof. Psychogiou, and Dr. Kefauver for their insightful comments, encouragement, time and efforts to evaluate and improve my research. Special acknowledgement is owed to Dr. Kefauver for his thorough and complete review of this thesis. His comments and suggestions have greatly improved this work.

I would like to thank all the graduate students and postdoctoral fellows from Antenna Research Group; Dr. Ignatenko, Dr. Ha, Dr. Lasser, Dr. Jastram, Dr. Altarifi, Elie Tianang, Prathap Prasannakumar, Saurabh Sanghai, Sara Manafi, Riley Pack, Aman Samaiyar, Carlos Mulero Hernández, Selena Leitner, Jake Cazden, Conrad Andrews, Bradley Allen, Ljubodrag Boskovic, Merarys AnnCaquías Olivera, and Mrs. Rodriguez,. Also, I wish to thank all my friends and faculty members: Prof. Popovic, Prof. Gasiewski, Prof. Picket-May, and Prof. Bogathin, and other professors back home for their continuous help and support to reach this point.

I would like to thank the ONR for funding my education, research, fabrication costs, and sponsoring my research conference/journal papers.

Last, I would like to express my gratitude towards my mother and the spirit of my father for their support, love, patience, and guidance to the right path. I would like also to thank my lovely sister, Rasha, and my brothers, Gaith and Bisher, for their unlimited support and encouragement.

CONTENTS

TABLES

Table

FIGURES

Figure

CHAPTER 1

INTRODUCTION

Most modern wireless communication systems transmit and receive RF signals either at different times or frequencies to avoid self-interference. With these duplexing techniques, as shown in Figs. 1.1.a-b, more resources are required due to the increased demand for higher data rate. Therefore, alternative solutions that do not involve more time or frequency spectrum are needed. One of the possible solutions that has lately been gained increasing interest is the co-channel simultaneous transmit and receive (C-STAR), or sometimes referred to as in-band full-duplex system (IBFD), as illustrated in Fig. 1.1.c. Recently, C-STAR has been considered by many as a key to enable technology for the next-generation wireless networks operating in the congested RF spectrum. C-STAR enables transmitting (TX) and receiving (RX) at the same time and over the same frequency channel leading in significant improvement in throughput and spectral efficiency [1]-[5], efficient reuse of frequency spectrum, simplified frequency planning [6]-[9], decreased need to license additional spectrum, reduced communication latency [10], and improved security [11]-[16]. Moreover, C-STAR technology offers several unique applications including; enabling persistent electronic warfare operations with an intention of simultaneously sensing while jamming, and transmitting while operating in direction-finding or null-steering modes. The chief challenge associated with C-STAR systems; however, is the required high TX/RX isolation (110-140 dB) to suppress the self-interference (SI). To obtain the necessary isolation over any bandwidth, a C-STAR transceiver is typically divided into several SI cancellation stages. Specifically, antenna, analog, and digital layers [17]-[19], as shown in Fig. 1.2. Clearly, the antenna layer plays an important role in maximizing the overall system isolation

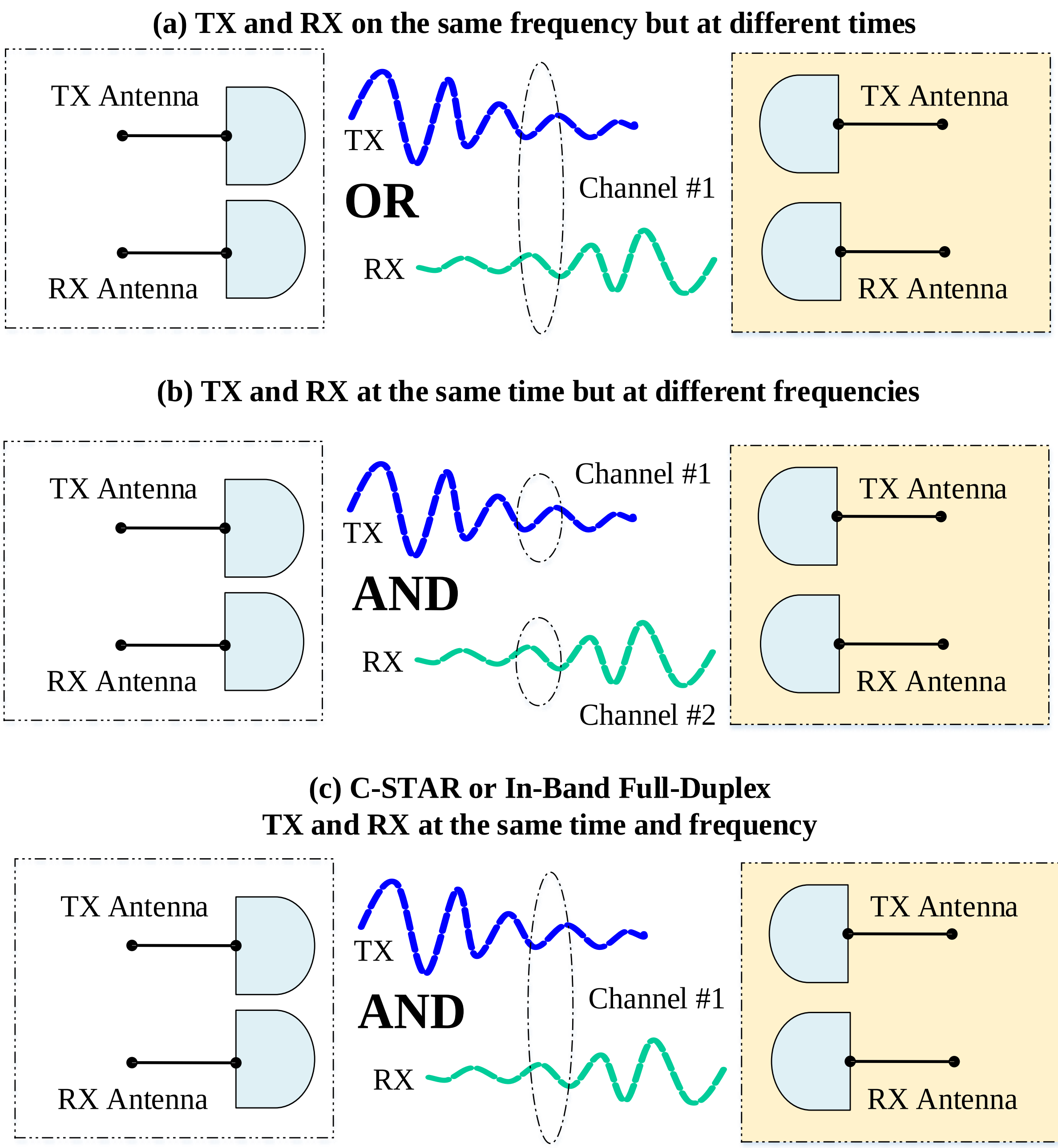

Figure 1.1: An illustration of (a) time-duplexing, (b) frequency-duplexing, and (c) C-STAR operations.

since ~30-40 dB of the required isolation is achieved with a well-designed C-STAR antenna sub-system. The main objective of this thesis is to investigate the challenges associated at the antenna layer to mitigate this SI, as further explained in the following sections.

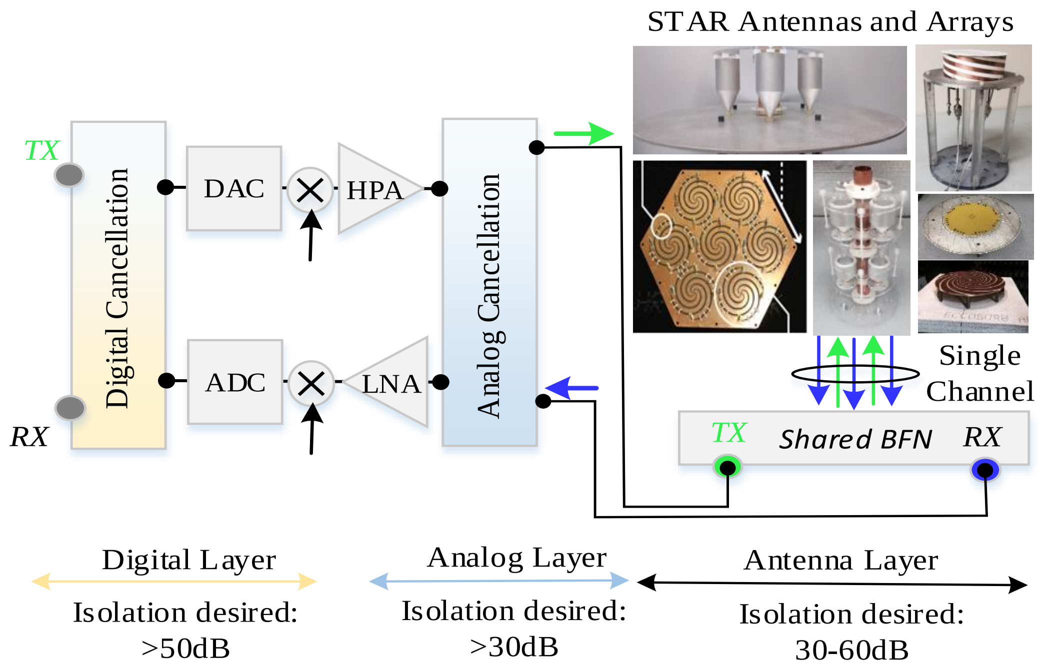

Figure 1.2: Illustration of a typical C-STAR system with the most commonly utilized cancellation layers.

1.1 C-STAR SI Mitigation Techniques

1.1.1 Bistatic C-STAR SI Mitigation Techniques

1.1.1.1 Antenna Separation

Antenna separation is conventionally used to reduce the significant SI by increasing the physical separation between TX and RX antennas. In this case, 2×N physically separated antennas are needed. The SI or isolation can be approximated using the well-known Friis transmission formula [20] assuming the TX and RX antennas are located in each other's far-field [21]-[23]. The main drawback with this approach is the need of larger space to achieve the required isolation.

1.1.1.2 Antenna Polarization Diversity

This approach employs orthogonal polarization in the operation of TX and RX antennas in addition to physical separation, as shown in Fig. 1.3. Several studies in [24]-[32] discuss the use of polarization diversity as a means to improve port-to-port TX/RX isolation using patch antennas [24]. Whereas good isolation can be achieved with less separation between TX and RX antennas, the C-STAR systems based on this approach are suboptimal in terms of used resources.

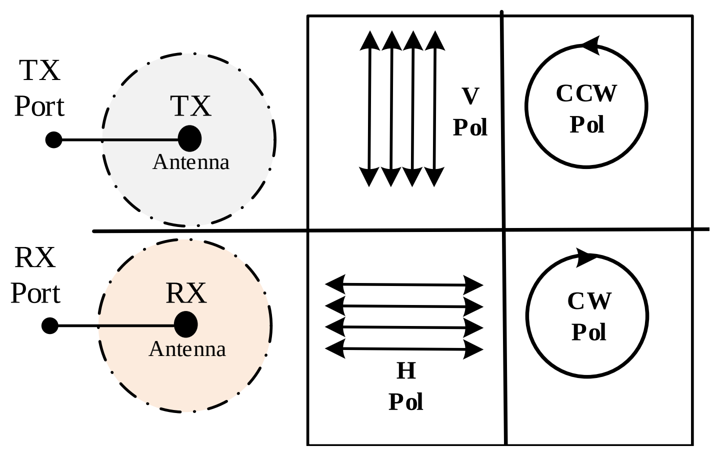

Figure 1.3: C-STAR antennas with different TX and RX polarizations.

1.1.1.3 Decoupling Structure

To further reduce the co-channel SI for the bistatic C-STAR configuration, absorptive reflective panels or decoupling structures [21]-[23], [33]-[43] between TX and RX antennas are sometimes considered. Their role is to absorb/attenuate, redirect, or cancel the undesired SI, as shown in Fig. 1.4. The absorptive shielding uses lossy materials to dissipate electromagnetic energy that would be otherwise coupled to the RX side. The drawbacks of these approaches include sacrificed size, weight, as well as reduced radiation efficiency or altered far-field patterns. Nevertheless, these directional antennas can suppress the co-channel SI by reducing the influence of side-lobes without negatively affecting the coverage and patterns.

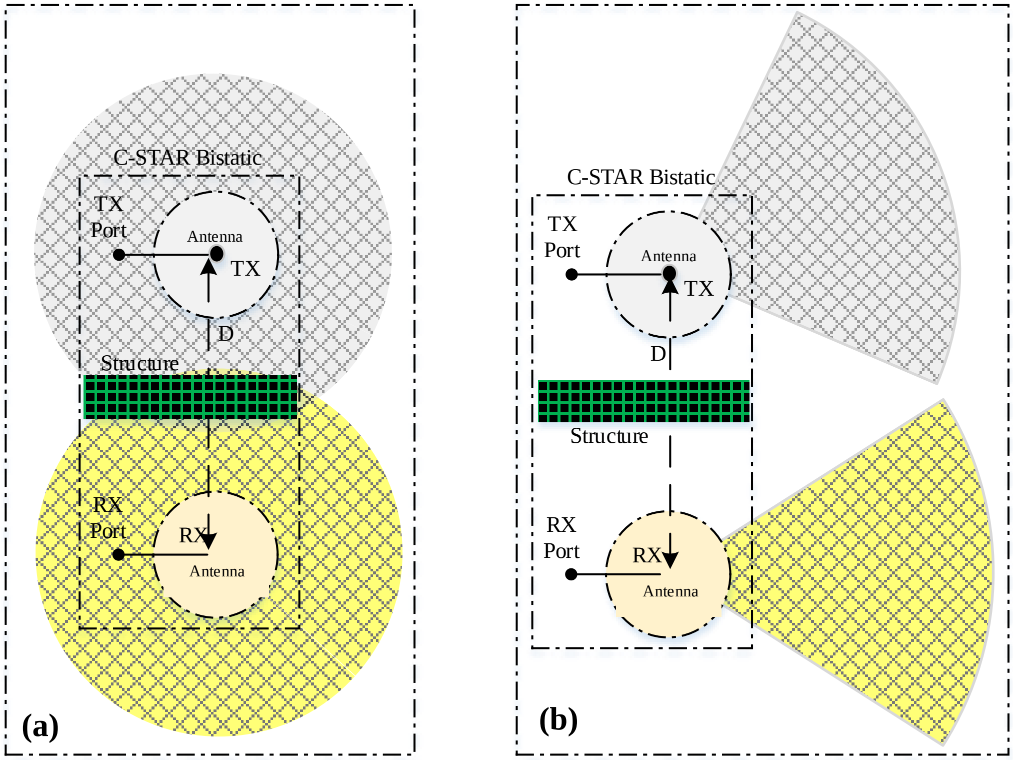

Figure 1.4: Decoupling structure between C-STAR TX and RX antennas for (a) omnidirectional, and (b) directional coverages.

1.1.2 Monostatic C-STAR SI Mitigation Techniques

1.1.2.1 Antenna Polarization Diversity

This approach relies on orthogonal polarizations of a single antenna element to operate in TX and RX modes. Several studies in [25]-[32] discuss the polarization diversity as a means of improving port-to-port TX/RX isolation. For example, in [28]-[31], monostatic dual-polarized microstrip patch or dipole antennas are proposed. Each dual-polarized antenna therein is excited by a differential feed with orthogonal polarizations to enhance TX/RX isolation. These C-STAR antenna sub-systems are suboptimal with respect to the used polarization resources. Furthermore, the SI becomes higher for the patch antennas once TX and RX operate with orthogonal circular polarizations instead of orthogonal linear polarizations.

1.1.2.2 Circulator Approach

Shared TX/RX antenna C-STAR systems typically utilize passive ferrite circulators to isolate TX from RX signals while routing TX and RX signals to/from the antenna, respectively [44]-[45], as shown in Fig. 1.5. Circulators inherently operate over narrowband; yet, the bandwidth thereof can be increased to two octaves [46]-[47] at expense of lower isolation (<15 dB) and higher insertion loss (>1.5 dB). Typical commercial-of-the-shelf (COTS) circulators can achieve high isolation level of >20 dB over an octave bandwidth [47]. However, due to the internal reflections from the antenna impedance mismatch and the circulator leakages, as shown in Fig. 1.5, finite and low TX/RX isolation is obtained in practice. Therefore, the use of these high-isolation circulators for monostatic C-STAR applications requires an antenna with return loss better than the circulator's isolation over the entire operating bandwidth, which is quite challenging. In addition to the passive circulators, other types of circulators are proposed such as active electronic, photonic circulators, and Lange-ferrite circulator [48]-[52].

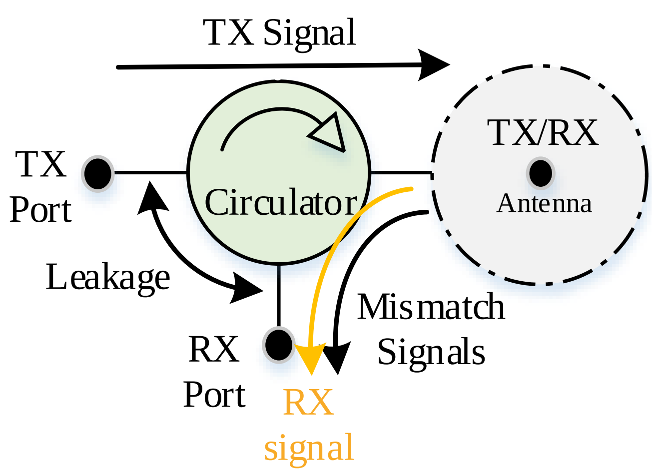

Figure 1.5: Monostatic C-STAR terminal realized based on the shared circulator approach.

1.1.2.3 Beamformer Cancellation

Antenna beamformer cancellation based on phase excitations can significantly reduce SI, [53]-[60]. In [53]-[55], an interesting use of balanced-circulator beamformer cancellation is demonstrated. For example in [54], a circularly-polarized patch antenna with a simple balanced feed network and a second layer of an analog feed-forward cancellation circuitry is used to achieve high isolation over a narrow bandwidth, as shown in Fig. 1.6.a. In [57], a reconfigurable leakage canceller and balanced monostatic antenna structure are presented, as seen in Fig. 1.6.b. The single TX/RX antenna is connected to a circulator, then the TX signal is sampled by a directional coupler then modified by an attenuator and a phase shifter to suppress the co-channel reflected SI. In [60], a loop-circulator structure is proposed. The TX/RX isolation is improved by adding two additional circulators to the antenna port and the RX input port respectively. All these approaches operate over a narrow bandwidth.

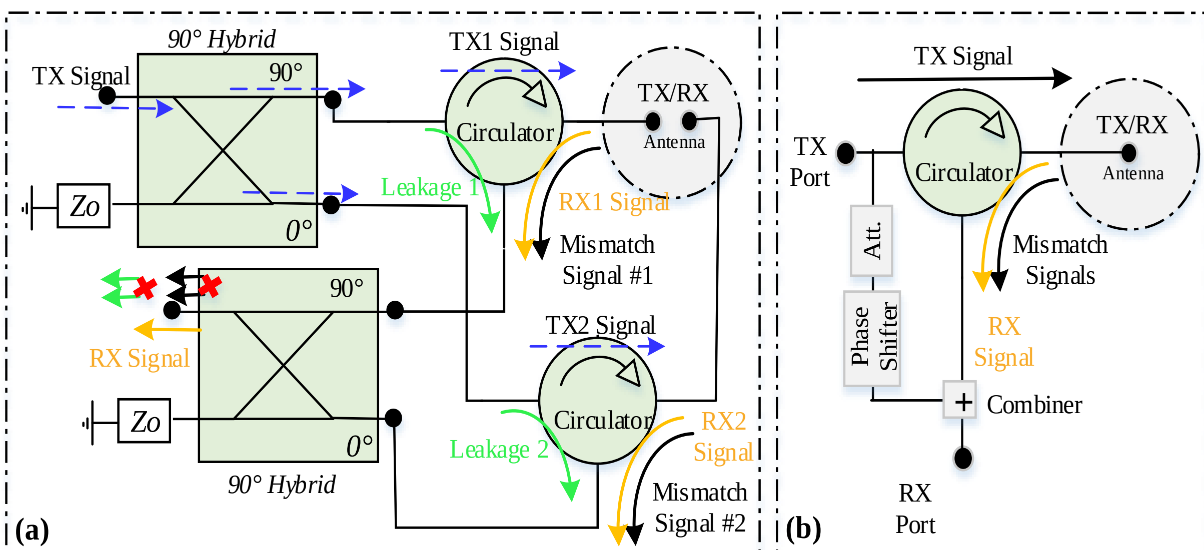

Figure 1.6: Monostatic C-STAR terminal based the balanced-circulator approach. (a) [54], (b) [58].

1.1.3 Array C-STAR SI Mitigation Techniques

1.1.3.1 Nulling Cancellation

Antenna nulling utilizes multiple antennas separated by an additional $\lambda/2$ distance to enforce the near-field signals to add destructively at the RX antenna. Alternatively, an inverse version of the SI signal can be obtained by relying on an internal phase shifter to provide the 180° phase difference for cancellation, as shown in Fig. 1.7. In [41], the C-STAR radio employs three antennas, two of which are are assigned as TX and one as RX. The RX antenna is placed therein so that the distance from the two TX antennas to RX antenna differs by $\lambda/2$ at the center frequency of the carrier. The experimental results in [41]-[42] achieve >30 dB of SI cancellation which drops due to the high dependency on the antenna placement and phase shifter's imbalances.

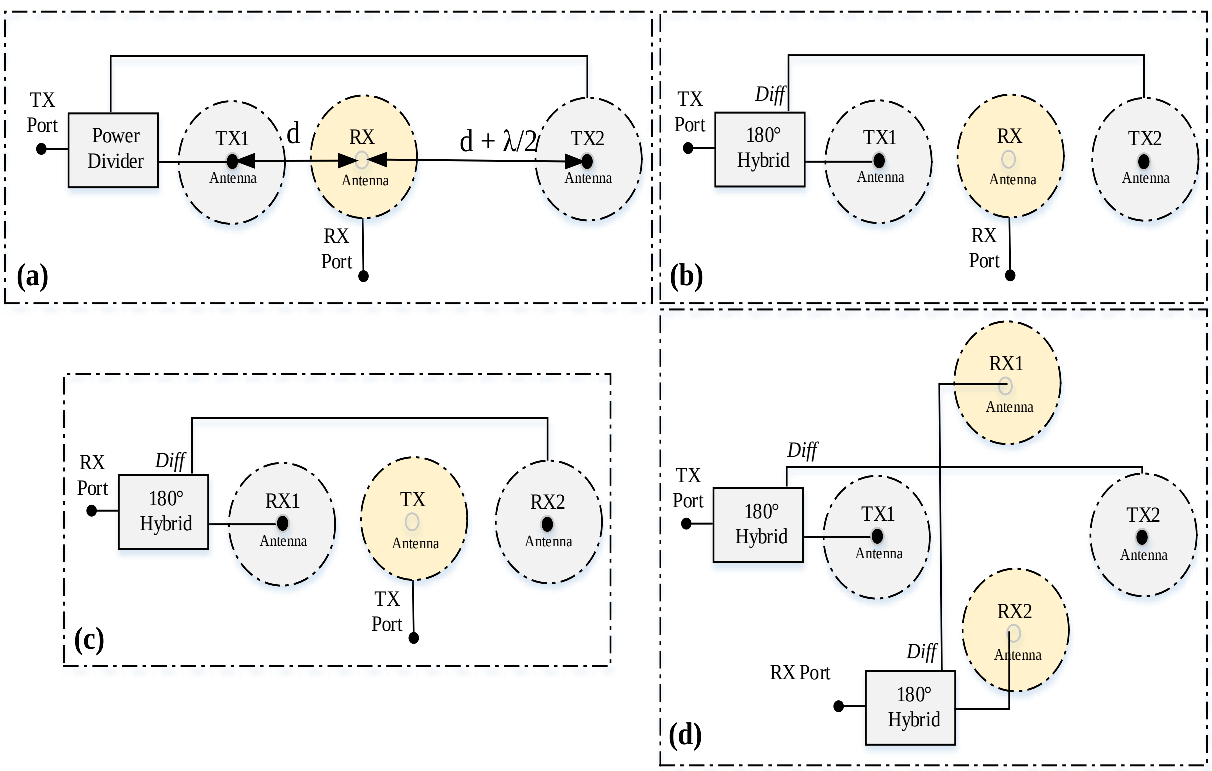

Figure 1.7: C-STAR terminal realized based on different null SI cancellation techniques. (a) [41] and (b)-(d) [42]

Another drawback of these configurations is that the TX and RX have different radiation patterns. More specifically, the TX array has two nulls in the azimuth plane while the RX antenna has an omnidirectional radiation pattern [41] as shown in Fig. 1.8. In [42], the TX and RX radiation patterns are similar, but orthogonal and covering different field of views, also shown in Fig. 1.8.

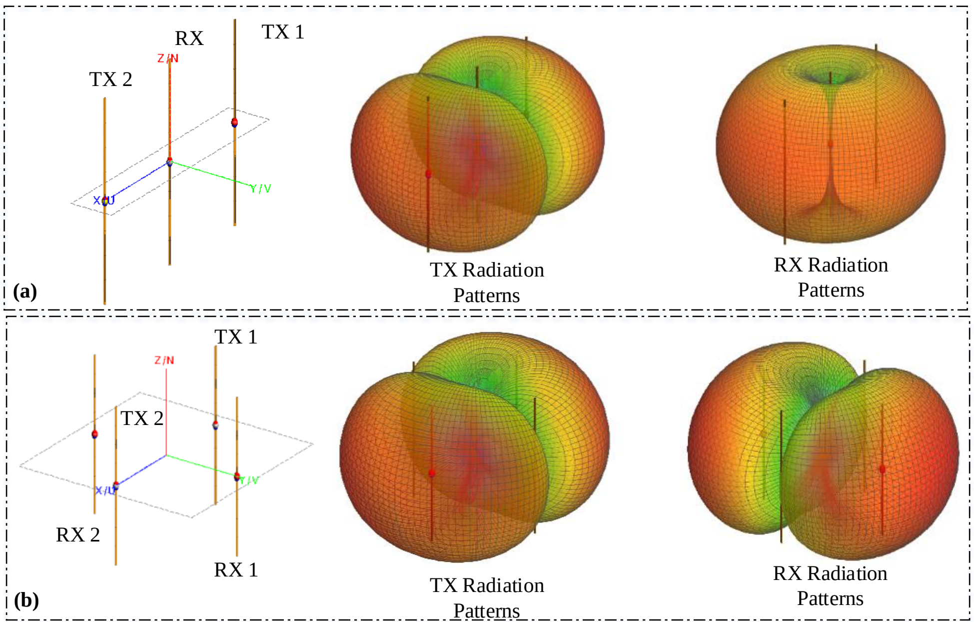

Figure 1.8: C-STAR terminal realized based on different null SI cancellation techniques. Far-field patterns of (a) 2-TX and 1-RX [41] and (b) 2-TX and 2-RX [42].

1.1.3.2 Antenna-Array Multiplexing

In bi-static C-STAR array configurations, multiple antennas can be beamformed for TX and RX functionalities [61]-[67]. Different SI suppression techniques are utilized in parallel to further enhance the TX/RX isolation; TX/RX polarization diversity [65], beamforming [61], [63]-[64], TX/RX pattern diversity [61]-[67], null placement [61]-[64], antenna multiplexing (different TX and RX antenna types) [64], and antenna port multiplexing [61]-[67]. Some C-STAR array configurations are depicted in Figs. 1.9.a-c. For example, in [61], a circular narrow band array is used as TX and a single antenna element as RX. Therein, the TX/RX isolation is obtained based on near-field and beamformer cancellations. High TX/RX isolation can be achieved with this configuration, but the TX and RX sides have different shapes of radiation patterns. To expand the operating bandwidth, a similar principle is applied in [64] using eight TEM horn antennas as TXs and a single monocone antenna as RX. With this configuration, the central element must have an omnidirectional radiation pattern for the C-STAR sub-system to all the full 360° azimuthal coverage. The array on other hand can have antenna elements with either directional or omnidirectional radiation pattern.

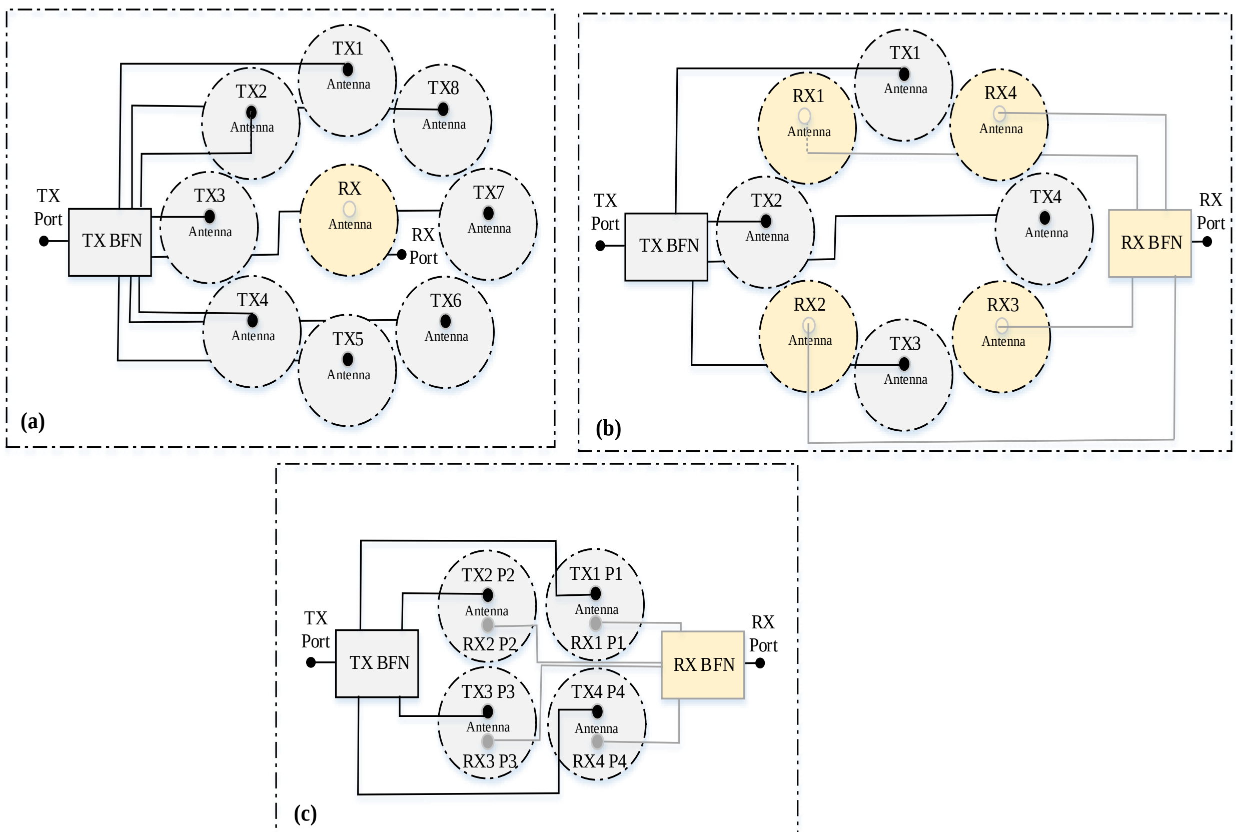

Figure 1.9: C-STAR arrays based on antenna and port multiplexing. (a) Circular array for TX and central element for RX (antenna multiplexing), (b) interleaved TX and RX circular array (antenna multiplexing), (c) monostatic circular array (antenna's port multiplexing).

1.2 Other C-STAR Challenges

Various approaches have been discussed in the previous sections to further mitigate SI between the TX/RX antenna ports in both bistatic and monostatic configurations, thereby aid in realizing C-STAR systems. As the literature survey indicates, there are still many other challenges that have not yet been resolved. Therefore, in this thesis, some of these challenges are researched and overcome, as described in the follwoing sections.

1.2.1 Wideband Monostatic C-STAR Single-Antenna

Monostatic C-STAR antenna sub-systems often utilize circulators [54] or polarization diversity [28]-[31] to achieve high TX/RX isolation. With the balanced circulators approach, the complexity and asymmetry of realistic components can lead to deterioration in isolation. On the other hand, with the polarization diversity, while it is acceptable for some commercial applications, is not acceptable for many military applications including the assessment of electronic warfare. To avoid these limitations, this thesis proposes a novel ultra-wideband, circularly co-polarized, circulator-less monostatic C-STAR antenna sub-system based on an N-arm spiral antenna (N/2-arm for TX and N/2-arm for RX) with corresponding feed cancellation techniques. It is proven; theoretically, that in the absence of asymmetry and BFN imperfections, infinite isolation is possible.

1.2.2 Wideband Monostatic C-STAR Array

Most discussed C-STAR bi-static array sub-systems use polarization diversity [65], null placement [61]-[64], antenna multiplexing (different TX and RX antenna types) [64], or antenna-port multiplexing [61]-[67] to achieve the desired high TX/RX isolation. With these bi-static C-STAR techniques, complexity of BFN, cost, and number of antenna elements are all increased. To avoid this, most of the proposed wideband single- and dual-layer C-STAR arrays in this thesis are designed to be truly monostatic and with simple partially shared BFN to cancel concurrent impedance mismatches, BFN leakages, and mutual coupling between the antenna elements. It is theoretically proven that these C-STAR array configurations can achieve infinite TX/RX isolation regardless of the utilized array's antenna elements and the separation between the antennas. The proposed array approaches can be applied using different types of single/dual linearly/circularly-polarized antenna elements.

1.2.3 TX and RX Patterns Similarity

Some of the discussed C-STAR antenna and array sub-systems utilize pattern [61]-[67] or polarization diversity [28]-[31] between TX/RX sides to further enhance the TX/RX isolation level. In this thesis, most of C-STAR antenna and array configurations operate with similar TX/RX polarizations and radiation patterns. To evaluate the degree of similarity between TX and RX patterns and also compare these C-STAR configurations, a parameter called envelope correlation coefficient is for first time introduced.

1.2.4 Multi-Mode Capability

The reported C-STAR antennas and arrays are typically desired to achieve directional or omnidirectional radiation coverage, [54], [28]-[31], [61]-[65]. Having diverse radiation characteristics with both directional and omnidirectional beams simultaneously while achieving high isolation using a single aperture has rarely been done before. This challenge is addressed in this thesis, where two wideband multimode monostatic C-STAR spiral antenna sub-systems are introduced. Both configurations achieve diverse circularly-polarized mode combinations (broadside and split-beam modes, also known as sum and difference modes) using a single antenna while maintaining theoretically infinite TX/RX isolation over a wide bandwidth. Multi-mode capability can also be utilized in the omnidirectional and broadside array configurations. It is also shown that multi-mode capability can be extremely useful for enabling the proposed antenna and array configurations to operate simultaneously in different applications; for example, communications and direction-finding.

1.2.5 Dual-Polarization Capability

Most of the reported C-STAR antenna and array configurations lack the dual-polarization capability. In this thesis, the path for achieving dual-polarized C-STAR with the majority of the proposed antennas and arrays has been demonstrated and conceptualized. The flexibility to achieve diverse circularly-polarized mode combinations (RHCP and LHCP) while maintaining sufficient TX/RX isolation over a wide bandwidth is demonstrated using a four-arm spiral antenna with circulator-BFN sub-system. This can also be accomplished by replacing the eight-port spiral antenna with an eight-port sinuous C-STAR antenna sub-system. Moreover, all array C-STAR configurations can have dual-polarization capability at the expense of more complex BFNs.

1.3 Thesis Organization

This thesis is organized as follows:

- Chapter 2 proposes a monostatic ultra-wideband C-STAR antenna based on four-arm spiral. The antenna is configured so that one two-arm pair is used for TX and the other for RX. Theoretical and computational studies are conducted and supported by fabrication and measurements to demonstrate the feasibility of each approach under the ideal conditions and in the presence of feed network non-ideality. Far-field issues and feed complexity are investigated and practical approaches are proposed to mitigate them.

- Chapter 3 presents a wideband monostatic C-STAR antenna sub-system supporting multimode operations (i.e. broadside and conical beam radiation) and better far-field performance compared to the antenna configuration presented in Chapter 1. The configuration is composed of a single four-arm spiral and two analog circuit layers integrated to maximize the isolation between the TX and RX channels. The first layer consists of two Butler matrix BFNs one for TX and the other for RX, whereas the second layer integrates four, phase-matched, circulators between the spiral arms and the BFNs. The proposed configuration supports the excitation of diverse radiation patterns, modes 1, 2, and -1, while maintaining high isolation. A simple approach to achieve a dual-polarized C-STAR operation with the proposed sub-system is also discussed.
- Chapter 4 proposes a multimode lens-loaded eight-arm spiral aperture that eliminates the need for circulators in the configuration presented in Chapter 3 while maintaining multimode capability and high isolation. Specifically, the single eight-arm spiral antenna is composed of a four-arm spiral for TX and a 45° spatially rotated four-arm spiral for RX. The eight-arm spiral is connected to two 4×4 Butler matrix BFNs to differentiate between the TX and RX arms/ports and distinguish their functionalities. This approach also enables diverse co-polarized TX and RX radiation modes 1, 2, and 3, while maintaining theoretically infinite isolation.
- Chapter 5 introduces omnidirectional co-polarized monostatic circular antenna arrays based on shared BFN cancellation, antenna symmetry, and mode orthogonality principles. To mitigate the undesired leakages, two possible configurations are demonstrated: (1) a single layer circular array excited

simultaneously with mode 1 at TX and mixed-modes at RX, and (2) a dual layer circular array excited with mode 1 at TX and mode 0 at RX.

- Chapter 6 proposes single and dual polarized C-STAR wideband monostatic broadside co-polarized array configurations. These C-STAR approaches have the capability of utilizing narrow/wide band antennas with single/dual circular sense of polarization. Furthermore, theoretically infinite TX/RX isolation can be achieved by relying on the partially shared BFN and the antennas' orientation to cancel the reflected mismatches, actual BFN's leakages, and near-field couplings.
- Chapter 7 reviews the thesis conclusions, contributions, and outlines potential topics for future work.

CHAPTER 2

WIDEBAND MONOSTATIC CO-POLARIZED FOUR-ARM C-STAR SPIRAL ANTENNA

2.1 Overview

A monostatic co-polarized antenna is rarely used in C-STAR operation due to the resulting significant SI. To mitigate the impact of SI, polarization or beam diversity is often utilized. In this chapter, a novel monostatic ultra-wideband C-STAR antenna front-end is proposed. The inherent geometrical symmetry of a four-arm spiral antenna and feeding rearrangement are exploited to achieve the simultaneous TX and RX functionalities without any time, polarization, beam or frequency multiplexing. The antenna is configured such that one arm-pair is used for TX and the other for RX. Thus, even though the two antennas are spatially separated by 90° rotationally, they still share the same aperture and the system is therefore considered monostatic. Theoretical and computational studies are conducted to demonstrate the feasibility of the proposed approach under ideal conditions as well as in the presence of feed network non-ideality. The experimental data indicate that isolation levels greater than 50 dB over multiple octaves are achievable with realistic components. To improve the TX and RX far-field patterns, the planar four-arm spiral aperture is grounded via resistor-loaded quadrifilar helix with the two-arm TX / two-arm RX feed arrangement preserved. Furthermore, to simplify the feed network and reduce the impact of hybrid imbalances either impedance-transforming microstrip feed or printed coaxial feed are integrated with each arm pair. High isolation and similar high quality measured and simulated TX/RX radiation patterns are obtained over the operating bandwidth. Several relevant parameters are defined before starting a thorough discussion on envelope correlation of spiral antennas. This chapter is organized as follows:

- Section 2.2 discusses the C-STAR spiral antenna and the principle of operation of the proposed C-STAR antenna sub-system.
- Section 2.3 shows the simulated and measured isolation performance of the four-arm Archimedean spiral C-STAR sub-system and discusses effects of the feed network imbalances.
- Section 2.4 demonstrates the analysis of the far-field performance associated issues and introduces a parameter called an envelope correlation coefficient to quantify the cross-correlation between the TX and RX radiation patterns.
- Section 2.5 discusses the improvement in the far-field and BFN using helical-antenna termination techniques.
- Section 2.6 discusses the further simplification in the feed and BFN once the printed coaxial feed is utilized.
- Section 2.7 is a chapter summary.

2.2 C-STAR Spiral Antennas and Principle of Operation

In 1954, Edwin Turner wound the arms of a long dipole into the shape of an Archimedean spiral to demonstrate circular-polarization with nearly constant input impedance over wide bandwidth [86]. Spiral antennas can have any number of arms (N). As the number of arms increases, the BFN gets more complex. The number of arms with corresponding phase and amplitude excitations determine the antenna mode of operation and its performance [83]. Radiating ring or band theory is often used to describe the principle of operation of spiral antennas [81]. According to this theory, the main radiation occurs from the circular ring which has a circumference equal to the guided wavelength of the excited mode of operation. For almost 60 years to date, spiral antennas have been used for different applications including RF communications, electronic warfare, direction finding, surveillance, and ground penetrating radars, to name a few, but not yet thoroughly investigated as a C-STAR monostatic antenna. Using circularly-polarized antennas and particularly spirals in C-STAR systems can offer many advantages including:

- Wide bandwidth operation with good impedance match and radiation patterns characteristics,
- Inherent geometrical symmetry,
- Separable feed excitation of each N/2-arms makes it good candidate for C-STAR,
- The circular polarization propriety provides greater immunity to the impact of scatterers due to the reflection with an opposite sense of circular polarization,
- Multi-mode capability to produce simultaneously different beam shapes (split and conical),
- Dual polarization capability.

Note that the performance characteristics of these conventional spiral antennas are expected to change once they are configured for C-STAR functionality, as discussed in details later. The schematic of a proposed C-STAR antenna configuration is shown in Fig. 2.1. The sub-system is composed of two two-arm spirals; one is used for TX and the other for RX. Each spiral is excited in broadside mode using a single 180° hybrid that effectively serving as a balun [94]-[98]. While the proposed approach works with either a planar or a conical spiral, the former configuration with Archimedean growth is selected for further discussion and demonstration.

Assuming two ideal 180° hybrids and preserved geometrical symmetry of the spiral, the isolation can be simply computed by accounting for all coupling paths as follows (see Fig. 2.2). Starting from the TX hybrid, the transmitted signal voltage (V) passes through the hybrid. The output voltages from the TX hybrid enter the TX spiral arms (i.e. arms 1 and 3) with equal amplitude and opposite phase ($\pm V/\sqrt{2}$).

Due to the impedance mismatch, the accepted voltages (V_1 and V_3) at the TX spiral arms are,

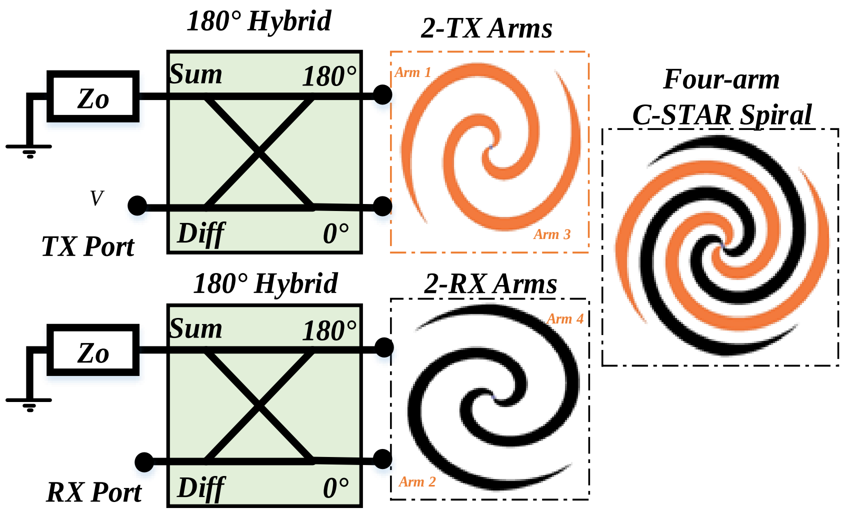

Figure 2.1: Spiral antenna C-STAR sub-system configuration: two arms for transmit (light color) and the other two arms for receive (dark color).

$$V_1 = (1 - \Gamma_1)\,(+V/\sqrt{2}) \tag{2.1.a}$$

$$V_3 = (1 - \Gamma_3)\,(-V/\sqrt{2}) \tag{2.1.b}$$

where Γ_1 and Γ_3 are the arm 1 and 3 input reflection coefficients. Because of the antenna geometrical symmetry $\Gamma_1 = \Gamma_3 = \Gamma$. Thus, V_1 and V_3 are related as,

$$V_3 = -V_1 \tag{2.2}$$

The coupled voltages from the transmitting arms to their receiving counterparts (i.e. arms 2 and 4) can be computed using the transmission S-parameters as,

$$V_{21} = +|S_{21}|e^{j\varphi_{21}} \tag{2.3.a}$$

$$V_{23} = -|S_{23}|e^{j\varphi_{23}} \quad (2.3.b)$$

and,

$$V_{41} = +|S_{41}|e^{j\varphi_{41}} \quad (2.3.c)$$

$$V_{43} = -\ |S_{43}|e^{j\varphi_{43}} \quad (2.3.d)$$

Since the spiral is symmetric,

$$S_{21} = S_{23} = S_{41} = S_{43} \quad (2.4)$$

By substituting (2.2) and (2.4) in (2.3), the total coupled TX voltage to the first receiving arm can be found as,

$$V_{21} +\ V_{23} = |S_{21}|e^{j\varphi_{21}} - |S_{23}|e^{j\varphi_{23}} = 0 \quad (2.5.a)$$

Similarly for the second receiving arm,

$$V_{41} +\ V_{43} = |S_{41}|e^{j\varphi_{41}} - |S_{43}|e^{j\varphi_{43}} = 0 \quad (2.5b)$$

The above analysis shows that the coupled TX voltages are cancelled at the receiving arms' ports leading to theoretically infinite isolation between the transmitting and receiving spirals. The impact on other C-STAR front-end parameters (far-field) will be discussed later. In order to validate that the isolation is theoretically infinite, the method of moments (MoM) solver FEKO [99], is used to model a two-turn 15.24 cm diameter Archimedean spiral configured in the proposed C-STAR sub-system arrangement. The simulated S-parameters are linked to the

AWR circuit simulator where the ideal 180° hybrids are implemented and the system isolation is computed. The simulated system as well as the TX to each RX arm isolations are shown in Fig. 2.3

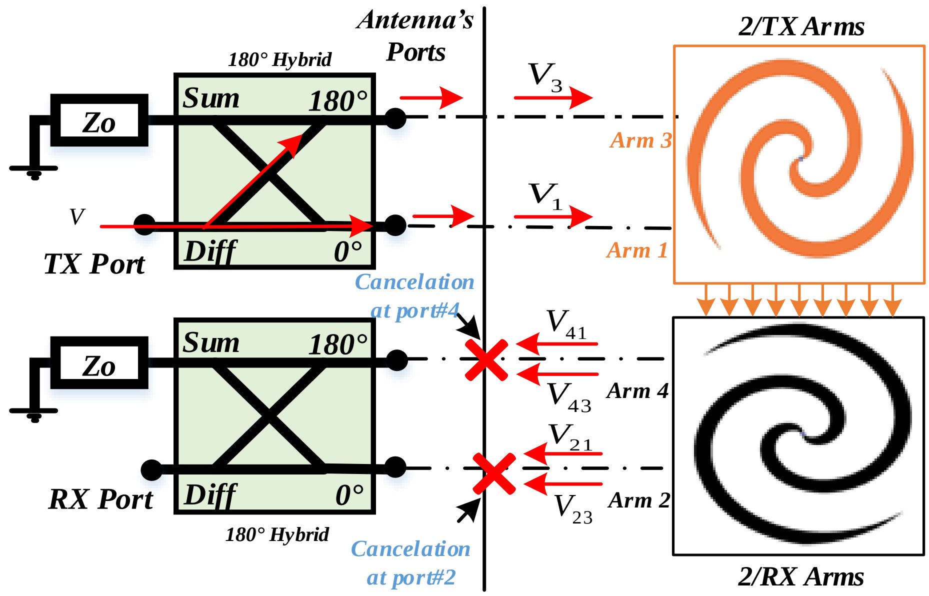

Figure 2.2: Signal flow diagram of the spiral C-STAR sub-system.

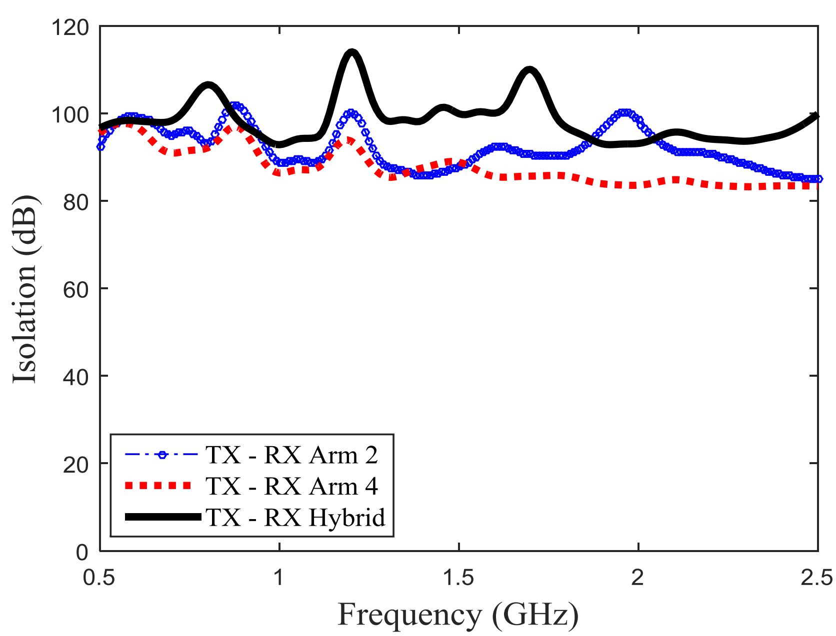

Figure 2.3: Simulated isolation of an ideal Archimedean spiral C-STAR sub-system.

As seen, high system isolation of >95 dB is obtained over the operating bandwidth. The isolation between the TX port and both RX arms is also high, further validating the cancellation process (2.1)-(2.5). The discrepancies between the ports' isolation levels are due to mesh quality, specifically the mesh differences between arms. In absence of any imbalances and asymmetries the computed isolation is limited by the simulation noise level. Notice that this cancellation approach works with any four-arm spiral topology regardless of its geometrical parameters as long as the symmetry is maintained. Theoretical analysis discussed above also shows that this cancellation approach is particularly sensitive to any factor that may affect (2.2) and (2.4) including the antenna's geometrical symmetry, beamformer errors (i.e. imbalances), and antenna surroundings. The implementation and the performance of a practical spiral C-STAR sub-system and sensitivity thereof are discussed in the following section.

2.3 Antenna Design and Performance

To experimentally demonstrate the proposed (but not optimized) C-STAR sub-system, a two-turn four-arm Archimedean spiral was fabricated (see inset of Fig. 2.4). The antenna has outer and inner radii of 7.62 cm and 0.25 cm, respectively, and it was fabricated on a 0.15 cm-thick Rogers RO3003 substrate ($\varepsilon_r = 3, tan\,\delta = 0.0013$). A 50 Ω coaxial bundle composed of four 0.36 cm semi-rigid cables is used to feed the antenna. To reduce the input impedance and achieve good impedance match with the utilized bundle, a two-step approach is used: firstly, the spiral's metal-to-slot ratio (MSR) is increased to 2.3:1, and secondly, the antenna is fabricated in a dual-layer configuration [100] where the bottom and the top layers are connected using vias located at the center and the arms ends. Two Werlatone 180° hybrids (Model H7492) operating over 0.5-2.5 GHz and four phase-matched cables configured as in Fig. 2.1 are used to complete the feed. The antenna aperture is backed by a hand-cut metal-backed Emerson and Cuming Eccosorb AN-77 multilayered microwave absorber. Isolation tests were conducted in anechoic chamber. Measured and simulated active VSWRs of the TX and RX spirals are shown in Fig. 2.4. The unused port of each hybrid is terminated by a 50 Ω load. As seen, the VSWR<2.2 is measured from 620MHz for both TX and RX spirals. Overall good agreement is observed between measurements and FEKO simulations and slight differences are due to the beamformer and fabrication imperfections.

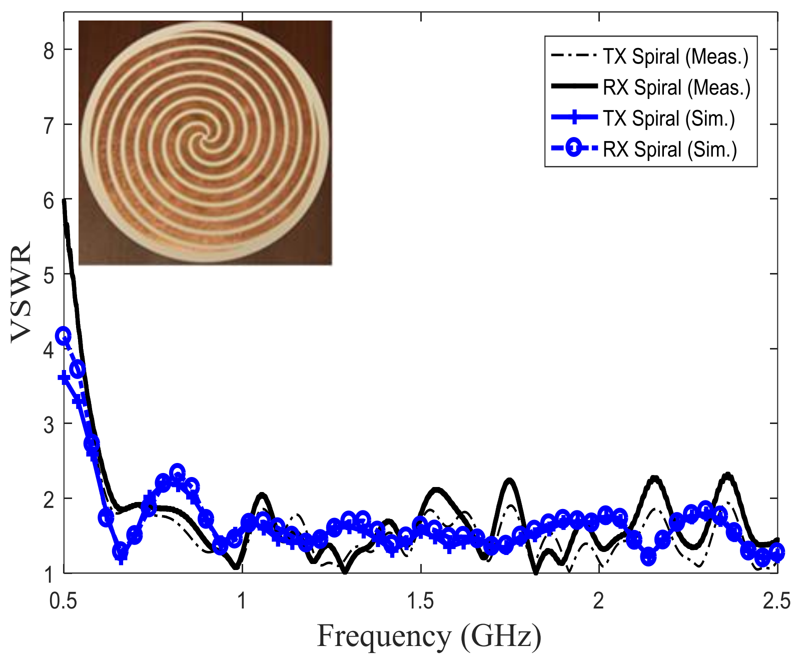

Figure 2.4: Measured and simulated VSWRs of the Archimedean spiral C-STAR TX and RX antenna ports.

The measured isolation levels for the realized sub-system are shown as dash-dot line in Fig. 2.5 while the simulation with ideal beamformer is re-plotted as solid-line. As seen, the TX/RX isolation >39.6 dB is measured over the operating bandwidth with average value of 48 dB. The hybrids' imbalances, bundle imperfections, spiral fabrication and integration with hand-cut absorber backing, and measurements non-idealities lead to significantly lower isolation levels compared to those of an ideal C-

STAR sub-system. To show the impact of the beamformers' imbalances-only, the ideal hybrids are replaced with actual Werlatone hybrid measurements in AWR model (plotted as cross-symbols). The used hybrids have amplitude and phase imbalances ranges as 0.6-1.4dB and ±8°, respectively. As seen from Fig. 2.5, the simulated isolation of the ideal system degrades up to 30 dB due to the hybrid imbalances. This indicates the significant impact phase and amplitude imbalances have on signal cancellation. In addition to beamformer imbalances, other sources of asymmetries also contribute to isolation degradation as can be seen from the measured results which account for all these sources.

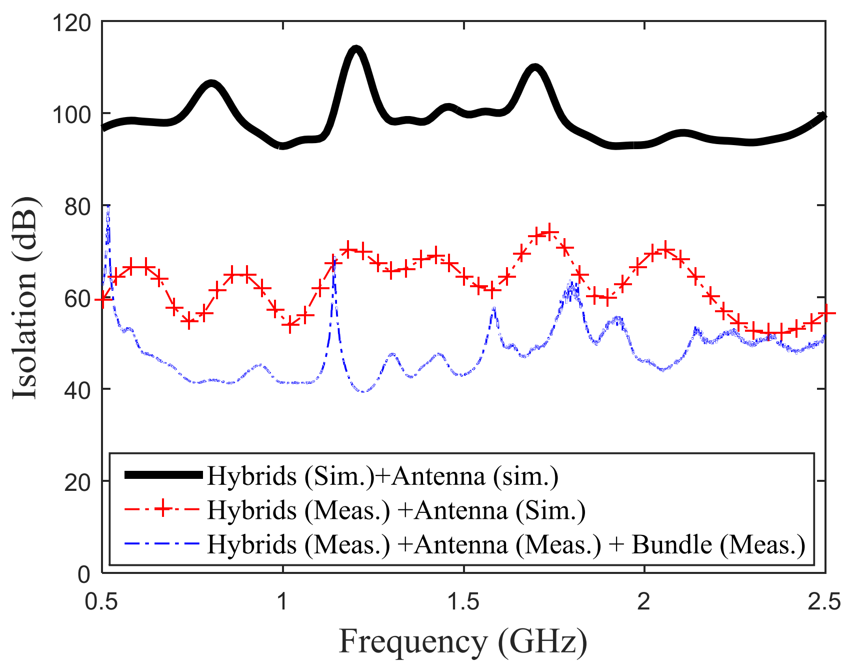

Figure 2.5: Measured and simulated isolation between the TX and RX ports of the Archimedean spiral C-STAR sub-system shown in Fig. 2.4.

The geometrical symmetry and electrical (signal-routing) balance are critically important for achieving high isolation levels over multi-octave bandwidths with the proposed multi-arm spiral C-STAR sub-system. In the proposed configuration, two hybrids are required to excite the four-arm spiral C-STAR antenna. One hybrid feeds TX-arms while the other feeds RX-arms. In Section II, we derived that the coupled TX signals are cancelled at the receiving ports of the RX spiral antenna before even reaching the RX hybrid. This means the imbalances of the RX hybrid are irrelevant if the TX hybrid and spiral are perfect. Nevertheless, if the TX hybrid and spiral are not perfect, the RX hybrid may improve or degrade the overall sub-system isolation. To determine the isolation variations imposed by the imbalances of the TX and RX hybrids, a computation-based sensitivity study is considered. To simplify the model, the amplitude and phase imbalances are assumed to be frequency-independent. While the frequency independence of imbalances is not true in practice, it is still a good model that will enhance the understanding of the causes and impacts of imbalances on isolation.

Table 2.1: Setup for Determining the Impact of Beamformer Imbalances on C-STAR Sub-system Isolation.

Feed Imbalance	Start	Step	End	Freq. Step (0.5-2.5Ghz)	Number of Cases/Freq.
Amplitude	0 dB	0.1dB	0.6dB	0.01	625
Phase	0°	2°	8°	0.01	6,561

Furthermore, since the main objective is to examine the effects of the hybrids imbalances, the bundle and the spiral are assumed to be perfect (up to the numerical noise). The four-arm dual-layer 15.25 cm Archimedean spiral is considered and the simulations are conducted in FEKO. Table 2.1 shows the range of the considered amplitude and phase imbalances.

Fig. 2.6 shows the impact of amplitude and phase imbalances on the isolation performance. The black solid-line represents the simulated isolation for the ideal case (perfect hybrids). Due to mesh asymmetry, the ideal isolation higher than 95 dB is achieved over 5:1 bandwidth. Once the defined amplitude imbalance of the hybrids is introduced, the isolation is negatively impacted and drops down by 10-30 dB as seen in Fig. 2.6.a. A noticeable difference in isolation can be observed with the effect of the phase imbalance as shown in Fig. 2.6.b where the isolation decreases from 95 dB to 41 dB and remains almost flat within the same level with the measured results (blue dashed-line).

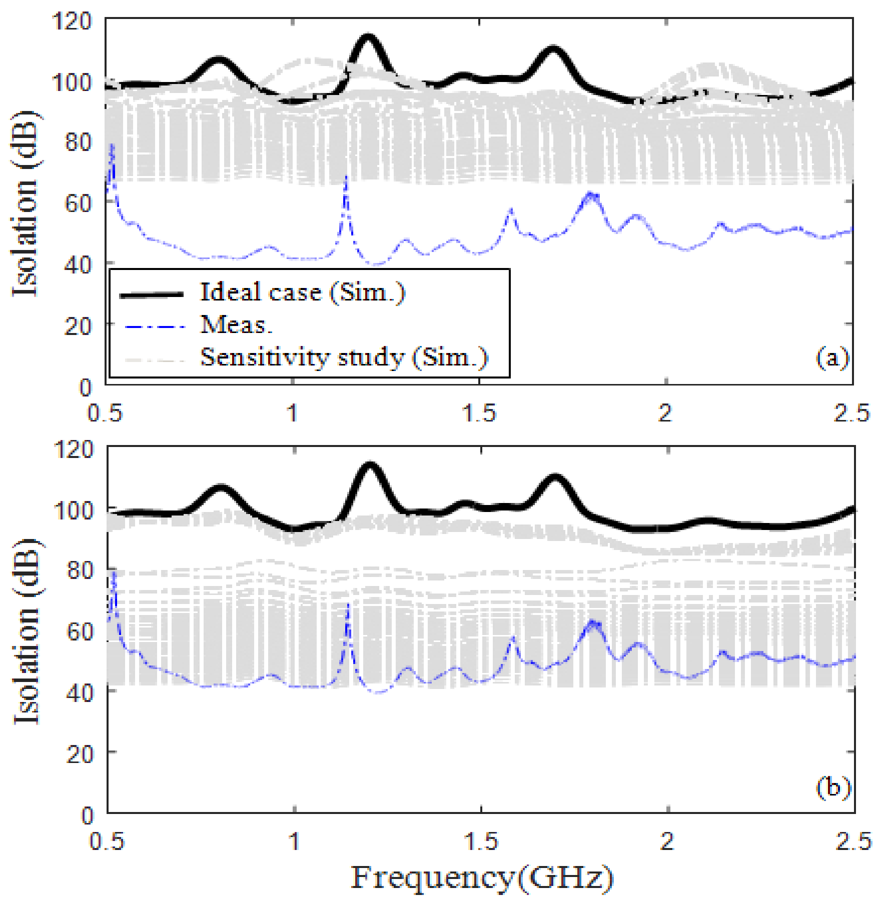

Figure 2.6: Isolation variation with: (a) $\pm 0.6dB$ amplitude imbalance; (b) $\pm 8°$ phase imbalance. The imbalances are varied as in Table 2.1.

It is clear from these results that the phase imbalance has noticeably stronger impact on isolation than the amplitude imbalance. It can also be observed that the worst expected isolation is around 41dB when the hybrids have amplitude imbalance ≤0.6 dB combined with ≤±8° phase imbalance and Fig. 2.5 conforms this conclusion. Note that the results of combined amplitude/phase imbalance studies produce almost the same isolation levels as the phase-only. To further enhance the isolation performance, a better assembly of the 4-arm spiral is needed to decreases the impact of the antenna assembly on the overall TX/RX isolation [99]. The full geometry of the four-arm C-STAR spiral is shown in Fig. 2.7. As seen, measured TX/RX isolation higher than 50 dB is achieved over 10:1 bandwidth.

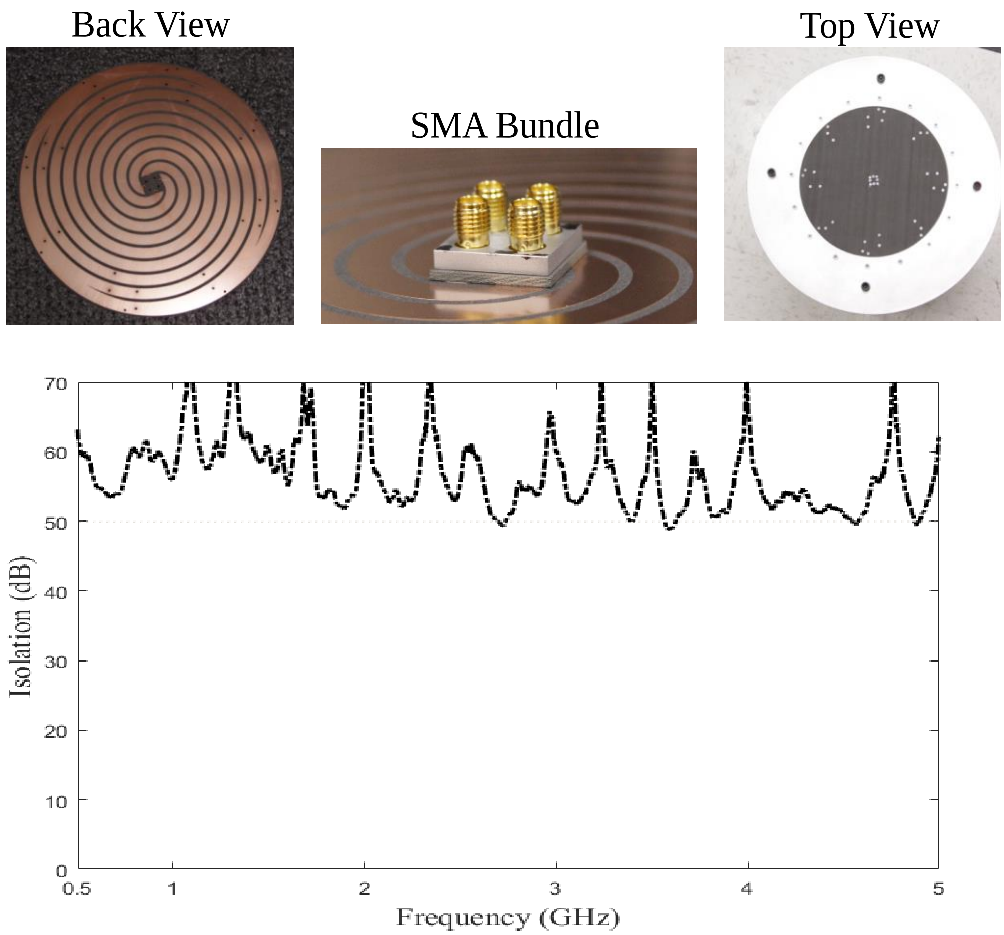

Figure 2.7: Measured isolation between the TX and RX ports of the Archimedean spiral C-STAR sub-system over 10:1 bandwidth.

2.4 Far-Field Performance

2.4.1 Pattern Similarity

The radiation pattern shapes of the TX and RX monostatic C-STAR sub-systems are dictated by application; yet, the TX and RX pattern similarity may be considered a baseline feature of a true monostatic C-STAR system. Achieving identical TX and RX patterns while maintaining very high isolation over wide bandwidth is very challenging. To improve isolation, antenna diversity techniques are often considered, but they may have negative impact on the overall performance of a C-STAR system. This is especially true if the TX and RX patterns are completely dissimilar. To quantify the degree of similarity between TX and RX radiation patterns over the C-STAR system bandwidth, a parameter referred to as the envelope correlation coefficient (ECC) is adopted from MIMO [101]-[103] and for first time proposed in this thesis to be utilized for C-STAR applications [96]. Traditionally, ECC is utilized to quantify signal correlation between MIMO antennas. A small signal correlation between the MIMO's antennas can lead to high diversity gain, 10 $\sqrt{1-ECC^2}$, and enhanced channel capacity [103]. The ideal ECC value from the MIMO system perspective is 0; however, in a C-STAR system, if ECC is 0, then the TX and RX patterns are entirely uncorrelated. If ECC=1, the two patterns are identical. Thus it is important to differentiate between the two applications, MIMO and C-STAR, and avoid confusion in using this parameter. Note that the minimal value of acceptable ECC depends on the specific C-STAR application. ECC is calculated using far-field 3D radiation patterns of the TX and RX antennas as

$$ECC = \frac{\left| \oint\!\!\oint \begin{bmatrix} E_{co-TX}(\theta,\Phi).\,E^*_{co-RX}(\theta,\Phi).\,P_{co}(\theta,\Phi) \\ +E_{x-TX}(\theta,\Phi).\,E^*_{x-RX}(\theta,\Phi).\,P_{x}(\theta,\Phi) \end{bmatrix} sin\theta.\,d\theta d\Phi \right|^2}{{\sigma_{RX}}^2.\,{\sigma_{TX}}^2} \tag{2.6}$$

with

$$\sigma_{RX} = \left[\oiint \left[G_{co-RX}(\theta,\Phi).P_{co}(\theta,\Phi) + G_{x-RX}(\theta,\Phi).P_x(\theta,\Phi)\right] sin\theta.\,d\theta d\Phi\right]^{0.5}$$

(2.7.a)

$$\sigma_{TX} = \left[\oiint \left[\, G_{co-TX}(\theta,\Phi).P_{co-}(\theta,\Phi) + G_{x-TX}(\theta,\Phi).P_x(\theta,\Phi)\right] sin\theta.\,d\theta d\Phi\right]^{0.5}$$

(2.7.b)

Where E_{co-TX} and E_{x-TX} are the $co-$ and $x(cross)-$ polarized electric field patterns of the TX antenna. E_{co-RX} and $E_{x-pol_{RX}}$ are the $co-$ and $x-$ polarized electric field patterns of the RX antenna. G_{co-TX} and G_{x-TX} are the $co-$ and $x-$ polarized realized gain patterns of the TX antenna. G_{co-RX} and G_{x-RX} are the $co-$ and $x-$ polarized realized gain patterns of the RX antenna. P_{co} and P_x are the $co-$ and $x-$ angular density functions (for $\theta = 0 - \pi\ and\ \Phi = 0 - 2\pi\ , P_{co}\ and\ \ P_x = 1/4\pi$).

In the proposed approach, two arms of the spiral are co-located and rotated by 90° with respect to the other two arms. Therefore, due to the geometrical rotation of the arms, inherent azimuthal pattern rotation with frequency, and undesired higher-order modes, some dissimilarity between the TX and RX radiation patterns is expected. To compute the ECC as a measure of pattern (dis)similarity, two sets of simulations or measurements are needed to obtain two radiation patterns. In each case, two arms are excited while the other two are terminated with matched loads. ECC is then calculated using (2.6). Fig. 2.8 shows the results of the computed ECC for the simulated 2TX/2RX C-STAR Archimedean spiral antenna that is shown in the inset of Fig. 2.4. Different beam elevation angles are chosen to compute ECC. From the obtained plot, two main conclusions can be drawn: ECC deteriorates with frequency; ECC deteriorates with the wider elevation angle.

To understand the physics associated with the noticeable decrease in ECC at higher frequencies and wider elevation angles, the spiral's far-field patterns are decomposed into their constituted spiral modes by applying the Fourier series decomposition [81] and [83]. As a baseline, Fig. 2.9.a illustrates the performed pattern modal decompositions of a two-arm spiral-only obtained by removing the two arms from a four-arm configuration (θ = 30°). The antenna is not self-complementary and thus the undesired modes reach -15 dB within the considered bandwidth.

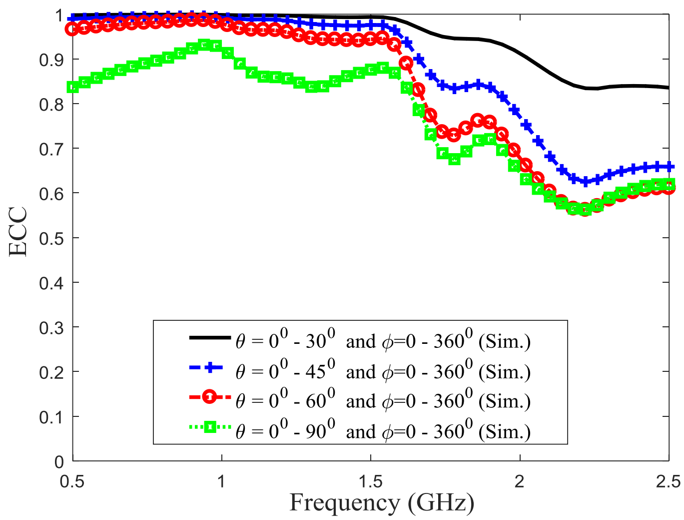

Figure 2.8: Simulated C-STAR-ECC for 2TX /2RX C-STAR Archimedean spiral antenna. Note that for many applications elevation angles through 30° are sufficient.

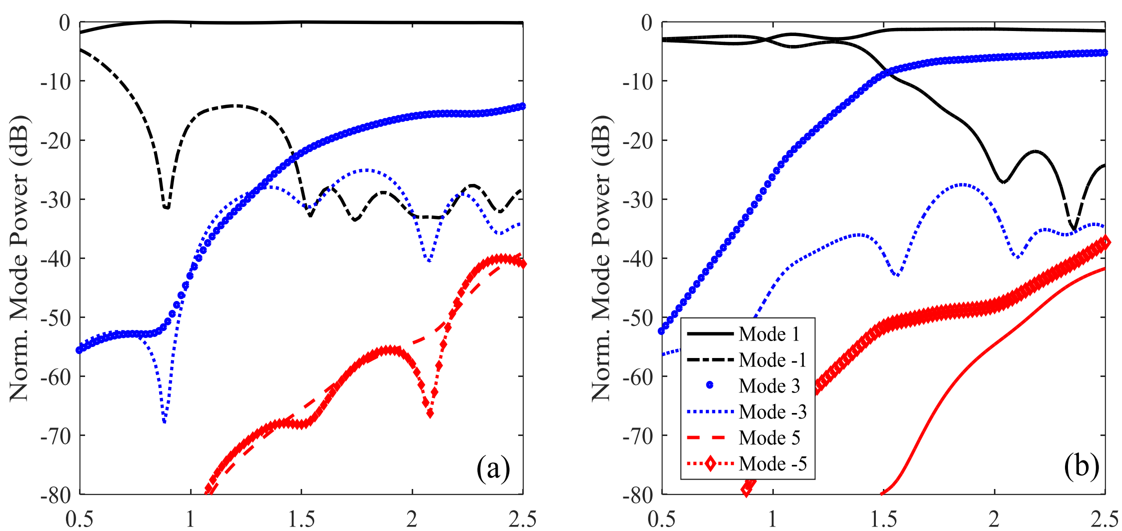

Figure 2.9: Simulated pattern modal decomposition of (a) a two-arm spiral without parasitic arms, (b) a two-arm spiral with two parasitic arms.

Fig. 2.9.b plots the modal spectrum of a TX two-arm spiral embedded in a four-arm spiral C-STAR sub-system. Each of the normalized mode power curves represents a specific mode of operation. The polarization sense of the spiral depends on the sign of m and the direction of the arm wrap. Mode 1 has the maximum gain at the boresight while the higher order modes do not radiate at boresight and have peak gains squinted further out as their corresponding mode number increased [81]. In our case, mode -1 shows up at lower frequencies when the residual currents undergo reflection from the arms' ends and reradiate after passing through the mode -1 radiating region. As a consequence, the AR deteriorates; however, ECC remains >0.8 until 1.55 GHz (<3:1 bandwidth). When the frequency increases, the spiral becomes electrically large and may support the higher order modes 3 and -3, which are excited around 1.55GHz (when radiation patterns starts to deteriorate). Notice the ECC starts to deteriorate in the same frequency range when the undesired higher order modes start to appear as shown in Fig. 2.8 and 2.9. The following two important differences with respect to the baseline case are noticed; 1) the higher order co-polarized modes are much stronger; 2) mode -1 is very high. While the former is used to explain the ECC behavior from Fig. 2.8, the latter indicates increased axial ratio (discussed next).

Fig. 2.10 shows the simulated broadside axial ratio of the TX Archimedean spiral when the RX spiral arms are terminated with matched loads (plot labeled as "C-STAR: 4-arm"). The axial ratio of a conventional two-arm Archimedean spiral described above is also shown (plot labeled as "2-Arm"). As seen, compared to the conventional two-arm topology, the axial ratio of the two-arm spiral in the proposed C-STAR configuration is significantly deteriorated over the low and the mid bands. This is due to the presence of a very strong mode -1 in the far-field (see Fig. 2.9.b) radiated by the induced currents on the RX spiral arms.

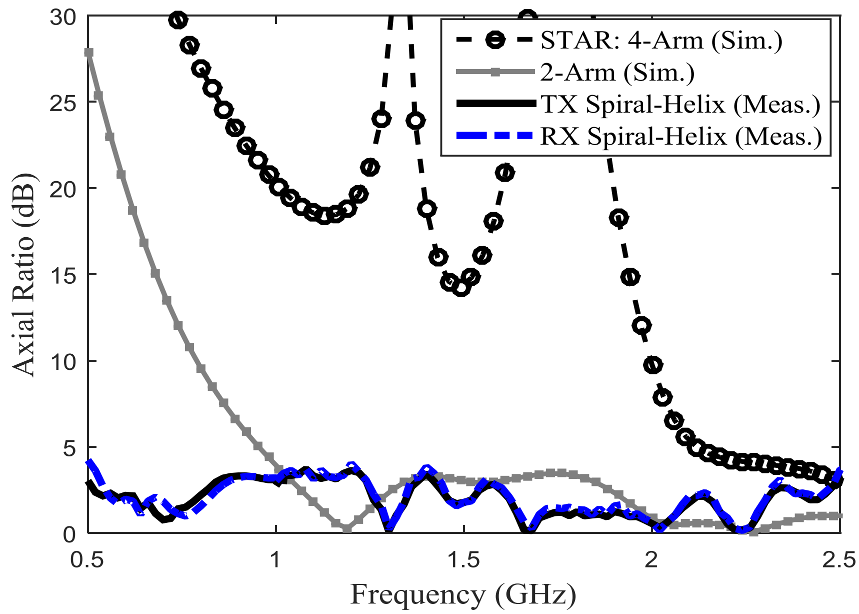

Figure 2.10: Broadside axial ratios of the simulated two arm Archimedean spirals with and without two-parasitic arms compared to the measured broadside axial ratio of the TX/RX spiral-helix antennas.

Due to the near-field coupling between the co-located TX/RX spirals, currents are induced on the RX spirals arms; hence, the RX arms can be viewed as parasitic elements for the TX spiral. Fig. 2.11 shows the surface currents on the active TX arms and their RX counterpart at different frequencies. The parasitic currents will radiate and contaminate the radiation patterns of the TX spiral leading to the axial ratio degradation. Notice that any residual currents cancel at the feed maintaining high isolation levels between the TX and RX ports as derived in previous section. The modal decomposition shown in Fig. 2.9 clearly demonstrates the negative impact of the parasitic arms' radiation. At low frequencies, the currents on parasitic arms radiate significant mode -1 (i.e. LHCP-polarized fields) which combines with mode 1 radiation (i.e. RHCP-polarized fields) from the active TX arms in far-field forming highly elliptically-polarized patterns. Certainly, the reflections from the TX spiral arms also contribute to the deterioration of the axial ratio (i.e. mode -1 radiation); however, the deterioration is more significant and present over wider bandwidth in the presence of parasitic arms as seen from Fig. 2.10. At high frequencies, the parasitic arms enhance the spectrum of higher-order modes thus deteriorating the azimuthal symmetry and TX/RX pattern similarity (ECC) as previously discussed.

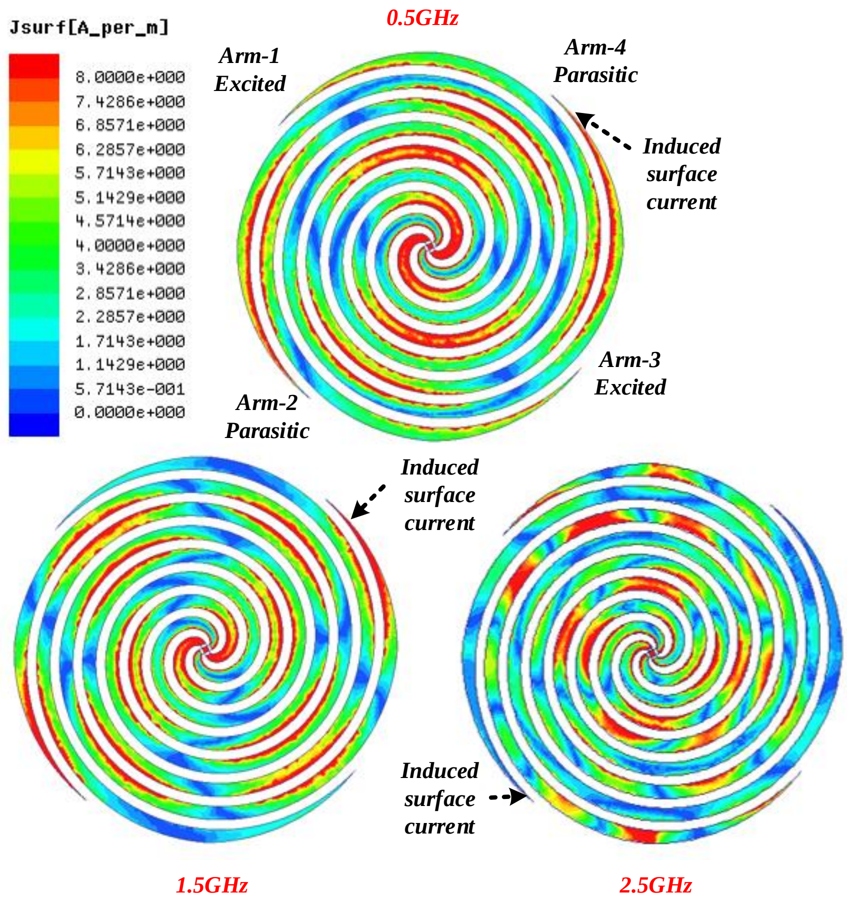

Figure 2.11: Surface currents on a four-arm 2TX/2RX C-STAR spiral antenna when two-arms are excited and the other two are not.

To improve the overall quality of the radiation patterns in the proposed four-arm spiral C-STAR sub-system, the impact of radiation from parasitic arms (TX for RX mode and RX for TX mode) must be reduced. Different arm termination techniques have been used with conventional spirals including resistive [104], absorber ring [105], and helix terminations [106]. In this thesis, a simple approach based on a combined quadrifilar helix / resistive termination is used not only to improve the axial ratio but also to enhance gain and efficiency of the proposed C-STAR sub-system.

2.5 C-STAR Spiral Realization: Spiral-Helix

This section demonstrates a design of a practical C-STAR spiral sub-system that maintains high isolation, good match, patterns and ECC over more than a two-octave bandwidth. As shown before, high isolation can be achieved with an absorber-backed four-arm spiral C-STAR sub-system. However, the system gain is reduced more than 3dB due to the loss in the absorber and the axial ratio is deteriorated due to the induced currents on the RX spiral arms as discussed in the previous section. To improve system gain, efficiency, axial ratio, and allow the use of metallic backing instead of absorber, a spiral-helix configuration [106] is considered.

In its mode 1 excited configuration, the quadrifilar helix having attached lumped resistors at its bottom end reduces interaction between the aperture and the ground, thus improving the impedance match and axial ratio of the four-arm spiral over a ground plane. Also, due to its own radiation the helix improves the four-arm spiral's gain at the low-end. The fabricated antenna with its geometrical parameters is shown in the inset of Fig. 2.12. The aperture is a single-turn Archimedean spiral with 5:1 MSR, outer radius of 7.6 cm, inner radius of 0.2 cm, and is fabricated on a 0.05 cm thick Rogers RO3003 substrate ($\varepsilon_r = 3, tan\,\delta = 0.0013$). The self-complementary quadrifilar helix termination has 0.75-turns and height of 5.08 cm and it is electroplated on a hollow Teflon cylinder. The helix top ends are carefully soldered to the spiral arms to maintain good electrical connection. A 75 Ω lumped resistive loading is implemented between the bottom arm ends of the helix and the ground plane to terminate the residual currents that reach the ends of the helix arms. Two microstrip feeds printed on the opposite side of the spiral arms maintain spiral shape with impedance following a Klopfenstein taper. They are employed to provide

180° phase offset between the sets of opposite arms as well as match 50 Ω coaxial feed to 140 Ω at the center of the spiral. The metallic spiral arms act as a ground plane for the two microstrip lines. The outer conductors of 0.141” semi-rigid coaxial feed cables are soldered to the spiral arms while the inner conductors are soldered to the microstrip lines at the taper’s outside. Ferrite beads are placed around the coaxial feeds to choke currents on the outer conductor that can possibly short the helix to the ground. To mitigate the destructive pattern interference that occurs at 3 GHz for a 5.08 cm (~λ/2) cavity, a 1.27 cm tall, 14.23 cm diameter metal cylinder is inserted inside the cavity. This inset pushes the frequency of the destructive pattern interference beyond 3 GHz. The design and the performance of the antenna as a single four-arm spiral aperture are discussed in [106]. Note that a full-wave optimization of this configuration may predict significant improvement to its C-STAR performance. The spiral-helix is used in this chapter to demonstrate that the practical C-STAR sub-system with reasonable far-field and high isolation over multi-octave bandwidth is attainable, due to demanding computational resources the full-wave optimization is not undertaken at this time.

The spiral-helix C-STAR sub-system is composed of two two-arm spirals terminated by corresponding helices and fed by a microstrip line. One is for TX and the other two-arm spiral-helix is used for RX. Fig. 2.13 shows the measured and simulated VSWRs of the TX and RX antennas at the input of the microstrip feed. VSWR <2 is measured over 7:1 bandwidth with good agreement between the measurements and HFSS simulations. The measured and simulated TX to RX isolation is shown in Fig. 2.13. As seen, the measured isolation >37 dB (spiral-helix case) is obtained over the antenna’s operating bandwidth with average value of about 43 dB. It is important to note that the isolation can be further improved by enhancing the symmetry of the feed region shown in the inset of Fig. 2.13. Manufacturing tolerances and antenna construction asymmetries also contribute to the isolation degradation and lead to the observed discrepancies between the measured and simulated results.

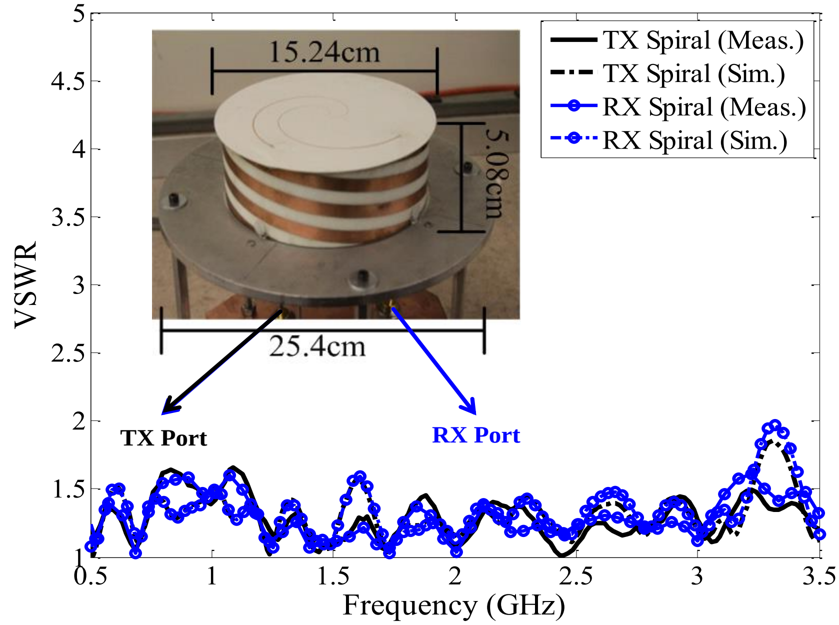

Figure 2.12: Measured and simulated VSWRs of the TX and RX antennas.

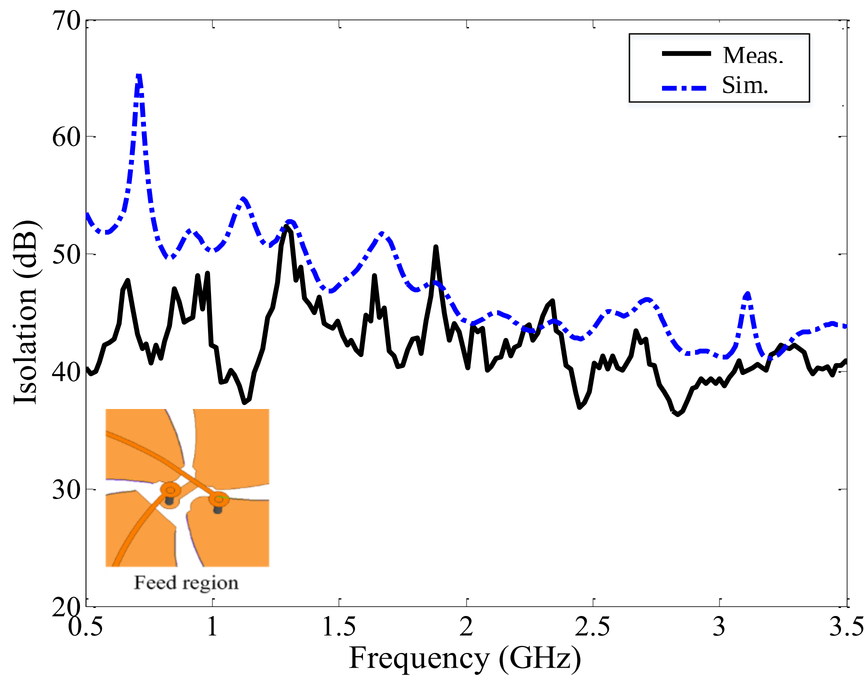

Figure 2.13: Measured and simulated isolation between the TX and RX antennas.

To demonstrate the improvements in the quality of elliptical polarization with this configuration, the measured broadside axial ratios of the TX and RX antenna are shown in Fig. 2.10 (labeled as “RX Spiral-Helix” and “TX Spiral Helix”). As seen, axial ratio below 4 dB is measured over the plotted bandwidth, and its low value is maintained through 2.5 GHz (AR remains consistent even between 2.5-3.5 GHz). While a somewhat larger than typically desired axial ratio value of 3 dB (AR >3 dB over ~14% bandwidth within 0.5-2.5 GHz range) is seen, this axial ratio can be further reduced by optimizing the spiral and helix growth rates, feed design and integration, backing, and loading. The combined helix-resistive loading reduces the impact of parasitic and residual currents and radiation of mode -1 which contaminates the quality of the antenna’s circular polarization. Compared to the axial ratio of the absorber-backed Archimedean spiral shown in the same figure, a significant improvement is achieved at the lower portion of the operating bandwidth. Shown in Fig. 2.14 are the measured and simulated broadside co-polarized TX/RX (RHCP) gains. The helix noticeably improves the radiation of the spiral at the low end while the ferrite beads’ losses contribute to the gain reduction at higher frequencies. The gain starts to drop around 3.5 GHz due to the destructive interference between the antenna and metallic backing. Overall good agreement between measured and simulated results is obtained. Fig. 2.15 shows the measured RHCP radiation patterns of the TX/RX spiral-helix antennas. At low frequencies similar patterns are obtained for the TX and RX antennas. However, above 1.5 GHz the patterns in the same plane start to differentiate since they rotate with frequency. Also shown are the simulated patterns for the TX case (RX is very similar and is not plotted for clarity). Shown in Fig. 2.16 are simulated and measured ECCs. As seen ECCs> 0.7 are obtained over $\theta = 0 - 30°$ and $\Phi = 0 - 360°$, indicating similar transmitting and receiving radiation and polarization characteristics over the operating bandwidth.

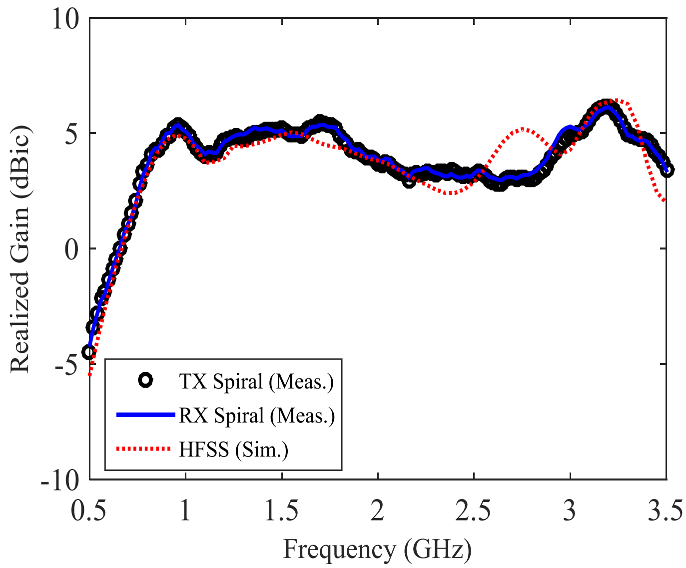

Figure 2.14. Measured and simulated co-polarized (RHCP) realized gains of the TX/RX spiral-helix.

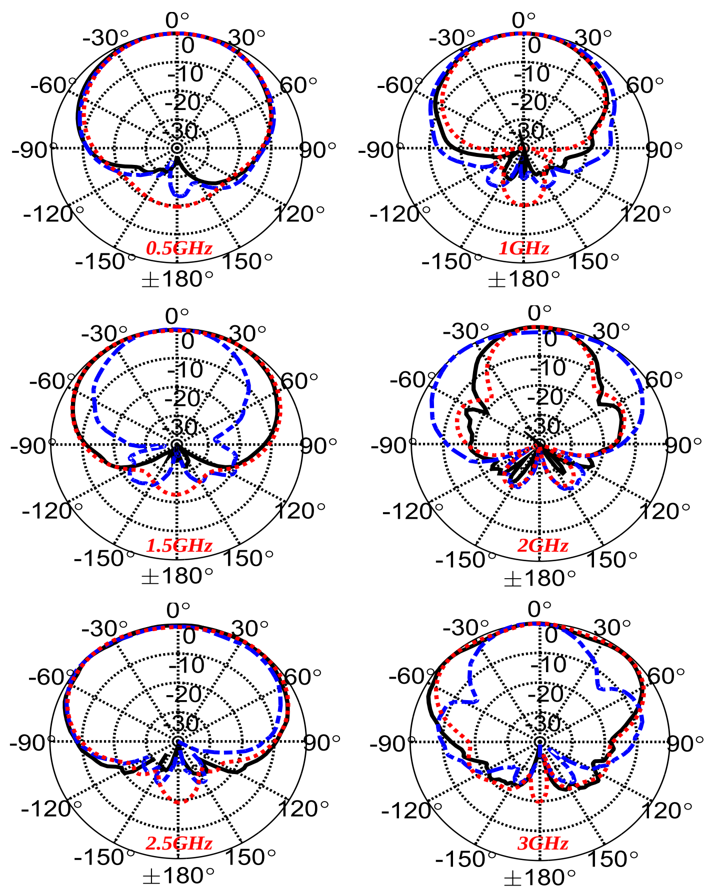

Figure 2.15: Measured RHCP radiation patterns of the TX (solid lines) and RX (dashed-dotted lines) spiral-helix. Simulated patterns of the TX spiral-helix (dotted lines) are also shown.

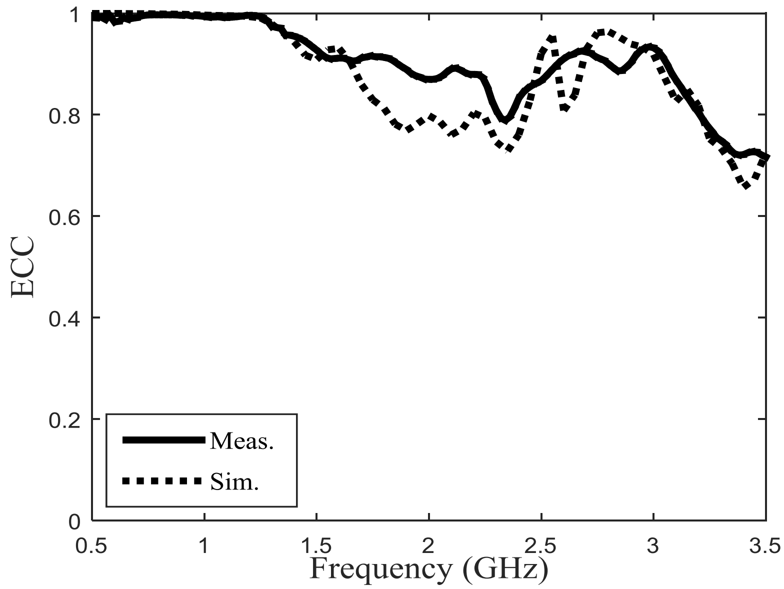

Figure 2.16: Measured and simulated ECC of spiral-helix C-STAR sub-system computed between elevation angles 0° *to* 30°.

2.6 C-STAR Spiral with Coaxial-Feed

To decrease the complexity of the C-STAR four-arm spiral and eliminate the two 180° hybrids, the symmetric printed coaxial feed is utilized. The schematic of the coaxial feed C-SATR four-arm antenna configuration is shown in Fig. 2.17. Similar to before, the sub-system is composed of two two-arm spirals; one is used for the transmission and the other for the reception. Each spiral is excited in a broadside mode. The TX arms are excited with an exponentially tapered strip line that is closer to the bottom spiral than the top spiral antenna layer. The RX arms on the other hand are fed with a second exponentially tapered strip line that is closer to the top spiral antenna layer. The top and bottom layers are shorted to decrease the coupling from the TX antenna arms to the RX strip taper. Thus, these excitations resemble more a coaxial feed rather than the strip line feed. Isolation performance > 50 dB over more than 5:1 bandwidth is achieved as shown Fig. 2.18. The far-field has similar performance to the C-STAR spiral discussed above.

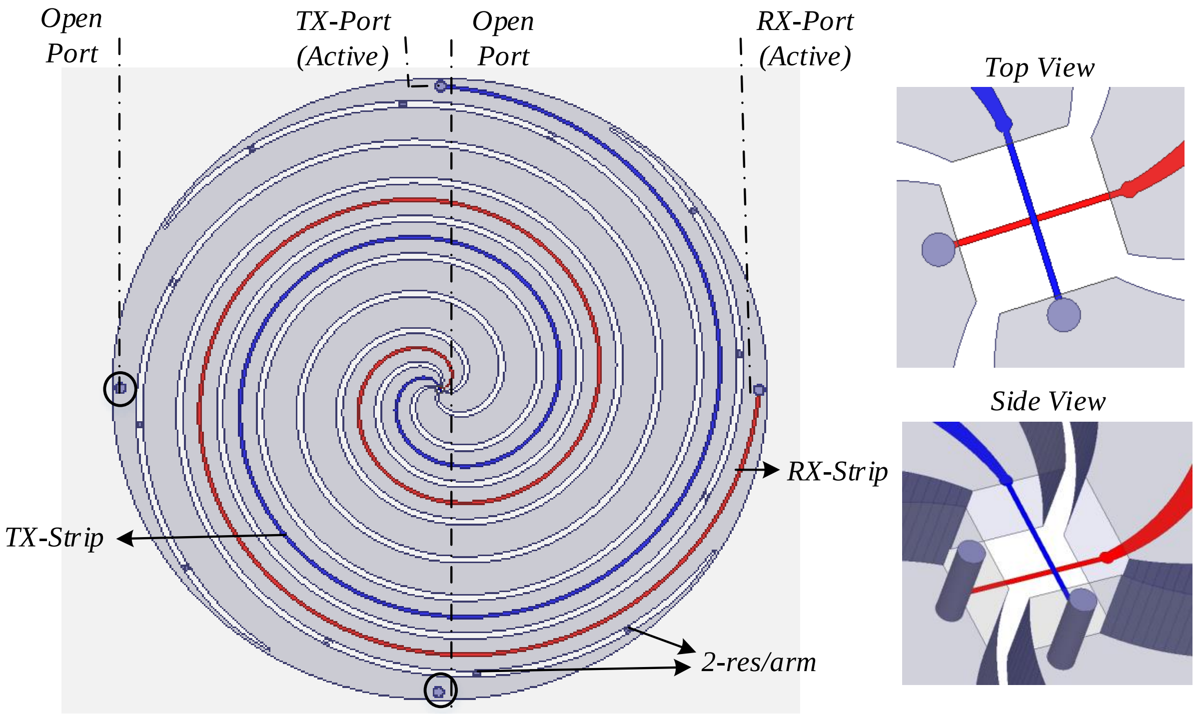

Figure 2.17: C-STAR Archimedean spiral with printed coaxial feed Archimedean.

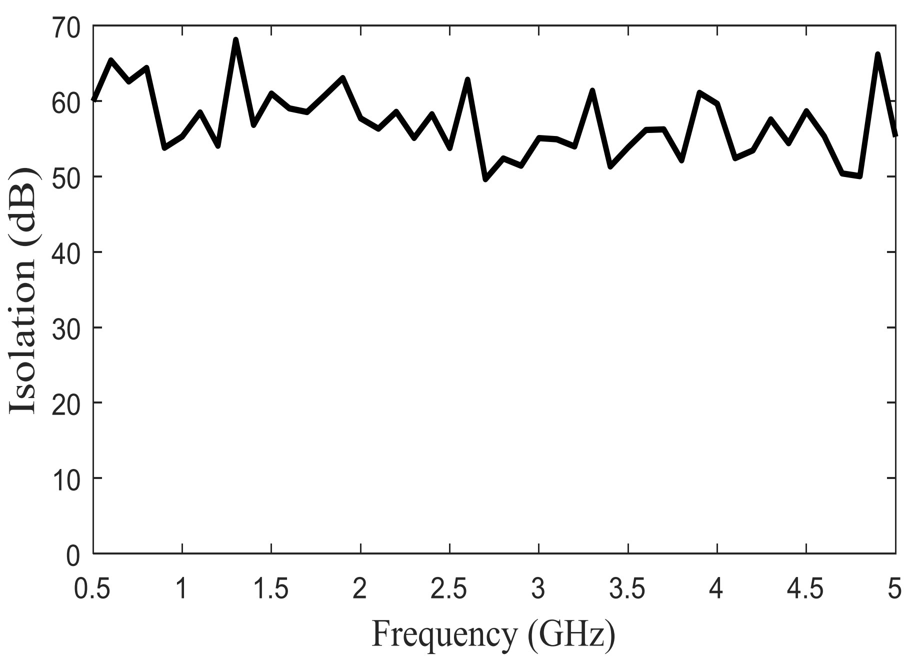

Figure 2.18: Isolation of the C-STAR Archimedean spiral with printed coaxial feed shown in Fig. 2.17.

2.6 Summary

In this chapter, an ultra-wideband, circularly-polarized, cost effective, circulator-less, monostatic C-STAR antenna sub-system based on a multi-arm frequency-independent antenna geometry and feed cancellation technique is demonstrated. It is shown that theoretically, in the absence of imperfections, infinite TX/RX isolation is obtained. Full-wave simulations (>95 dB) and measurements (>50 dB) are used to demonstrate that the very high isolation is indeed achieved with the proposed configuration. A sensitivity study on the influences of the feed imbalances is conducted to address some practical issues regarding the achievable isolation levels. Envelope correlation coefficient is introduced to quantify the degree of similarity between the TX and RX patterns. To enhance the far-field performance and mitigate radiation contamination effects of the parasitic arms, the spiral-helix is considered and its fabrication is used to experimentally demonstrate the proposed concept. Good match, isolation, patterns, gain, and ECC with moderate axial ratio (over some parts of the bandwidth) are obtained with this proposed (but non-optimized) C-STAR aperture sub-system.

CHAPTER 3

WIDEBAND MULTIMODE MONOSTATIC CO-POLARIZED FOUR-ARM C-STAR ANTENNA SUB-SYSTEM

3.1. Overview

Conventional RF front-ends usually utilize passive ferrite circulators to isolate the TX and RX paths. These circulators are inherently narrowband; however, the bandwidth thereof can be improved to two octaves [107] at expense of lower isolation (<15 dB) and higher insertion loss (>1.5 dB). State of the art commercial-of-the-shelf (COTS) circulators can achieve high isolation level of >20 dB over an octave bandwidth [30]. Yet, the return loss of the antenna limits their use due to the leaked reflected signal. Thus, the use of these high-isolation circulators for monostatic STAR applications requires an antenna with return loss better than the circulator's isolation over the entire operating bandwidth, which is quite challenging. In addition to passive circulators [108]-[110], active electronic and photonic circulators are demonstrated in [32]-[36]. These devices outperform the passive counterparts in terms of isolation and bandwidth with a decade bandwidth of isolation >40 dB is achieved as shown in [32]. The recognized drawbacks of the photonic as well as active circulators include complexity, limited power handling capability, linearity, size and higher cost.

The geometric characteristics of the four-arm C-STAR spiral antenna presented in the previous chapter are exploited to cancel the coupled TX signal at the RX port. These circulator-less techniques have shown isolation >50 dB over 10:1 bandwidth. However, the STAR spiral's far-field performance (i.e. axial ratio and gain) is degraded at lower frequencies compared to the performance of a conventional spiral due to the existence of the parasitic arms. In [38], isolation >40 dB is demonstrated over the designated bandwidth from 900-930 MHz. The system bandwidth is limited by the operation bandwidth of the components and performance quality.

This chapter proposes a monostatic approach that fully exploits the characteristics of a four-arm spiral, its BFN and circulators to achieve high isolation. This configuration is composed of a single four-arm spiral and two analog circuit layers designed to maximize isolation between the TX/RX channels. The first layer consists of two Butler matrix beamformer networks (BFNs); one for each TX, and RX. The second layer integrates four, ideally phase-matched, circulators between the spiral arms and the BFNs. Theoretically, this configuration achieves infinite isolation irrespective of the circulator's quality. Nevertheless, the BFN imbalances and the dissimilarities between the four circulators degrade the overall isolation. The operational principles are discussed under the ideal conditions and in the presence of circuit imperfections. For a four-arm spiral, the utilized BFN provides orthogonal modes 1, -1, 2, and 3 allowing C-STAR capability with multimode and diverse radiation patterns. The sub-system isolation and far-field performances are characterized experimentally and computationally for different modes of operation. A simple approach to achieve a dual-polarized C-STAR operation over narrower bandwidth with the proposed sub-system is also discussed. The multimode sub-system is demonstrated over 4:1 bandwidth with high isolation, VSWR <2, consistent patterns, axial ratio <3 dB over a wide field of view for the broadside modes (1, -1) and <4.2 dB for other conical modes (2, 3).

The sub-system architecture and principle of operation are fully discussed in this chapter. The impact of circuit component imperfections on the overall TX/RX isolation is also analyzed. Furthermore, the demonstration STAR spiral sub-system is prototyped and measured with actual components to showcase the practical feasibility of the proposed antenna sub-system. This chapter is organized as follows:

- Section 3.2 discusses the operational principle of the proposed multimode STAR antenna sub-system.
- Section 3.3 shows the impact of the circuitry's imbalances and asymmetry on the TX/RX isolation.
- Section 3.4 describes the realized antenna sub-system and characterizes the performance thereof for mode 1 operation.
- Section 3.5 discusses the feasibility of multimode C-STAR operation
- Section 3.6 is the chapter's summary.

3.2 C-STAR Antenna Sub-system Description and Operational Principles

The proposed monostatic C-STAR antenna sub-system is shown in Fig. 3.1. The sub-system consists of a single four-arm spiral aperture and two Butler matrix BFNs (i.e. one for TX channel and the other for RX channel). Phase-matched circulators are integrated on each arm between the antenna and BFNs. The main components of the sub-system are:

(1) Antenna: Four-arm spiral is employed to achieve wideband operation with good and consistent impedance match, and stable radiation patterns. This antenna can also support three different frequency independent modes. Each mode has its own input impedance and far-field characteristics. Mainly, mode 1 (broadside mode) and modes 2 and 3 (conical beam modes) can be excited by applying equal amplitude and proper phase vector splits between spiral arms. Particularly, to excite mode m of operation the relative phase between spiral arms has to be $m\pi/2$ [81]. Notice that the turn-on frequencies of modes 2 and 3 are two and three times the turn-on frequency of mode 1; respectively. The multimode capability is crucial for the antenna sub-system performance, as it will be demonstrated. Another interesting feature of this aperture is the ability to radiate both senses of circular polarization (i.e. RHCP and LHCP) over ~3:1 bandwidth if it is appropriately designed and excited

[81]. The dual-polarized spiral principle of operation is based on the support of mode 3 which will not radiate efficiently until three times mode 1 turn-on frequency due to the size of the used spiral aperture. Thus, the non-radiating currents reach the open end of the spiral arms and reflect back as mode -1 which then radiates with the opposite polarization sense of mode 1. This feature will be utilized to demonstrate a dual-polarized monostatic STAR antenna sub-system. The proposed approach works with any four-arm spiral topology, planar or conical. The right-handed wrapped Archimedean spiral is selected herein for further discussion and demonstration.

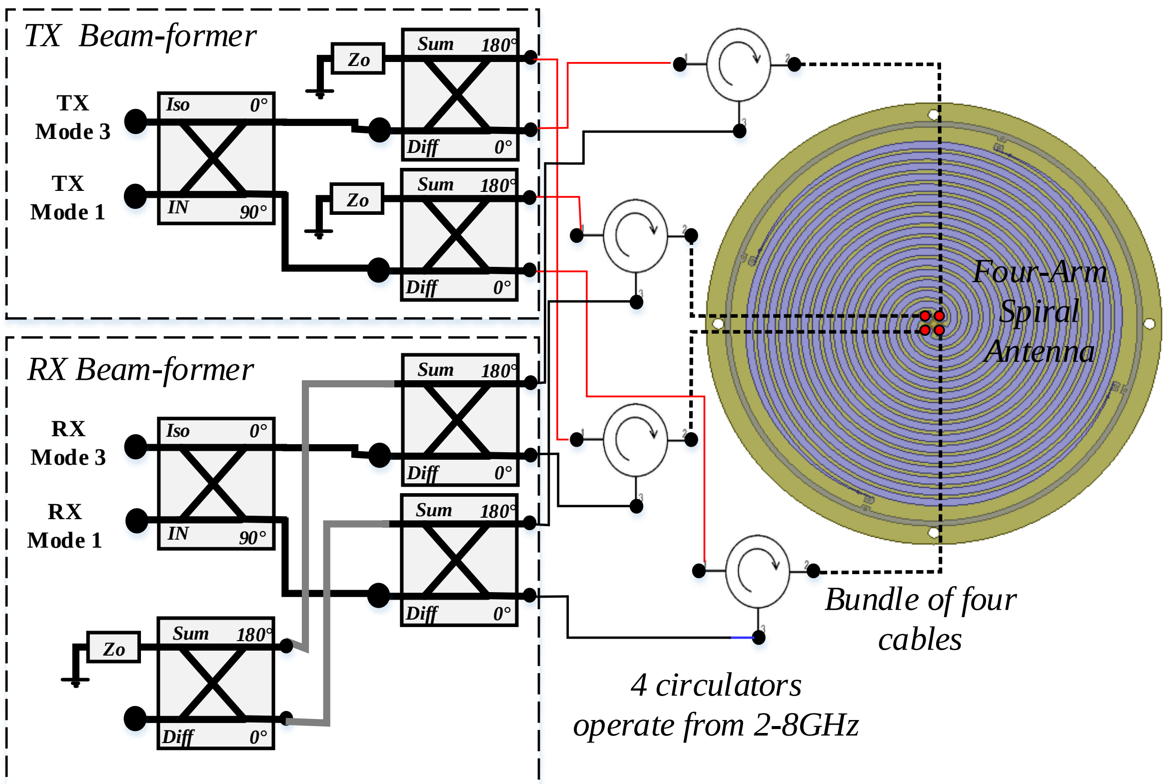

Figure 3.1: Schematic of the proposed STAR antenna sub-system.

(2) Circulators: Four ferrite circulators are connected to the four-arm spiral through a bundle of four coaxial cables. The other two circulators' ports are connected to the TX and RX BFNs as shown in Fig. 3.1. Circulators are employed to realize a monostatic STAR operation; however, they can be replaced with power dividers, directional couplers, or other three port routing device [38]. The circulators are chosen here since they provide the lowest insertion loss for both TX and RX paths. Theoretically, as will be shown later, the proposed STAR antenna sub-system can achieve infinite isolation, irrespective of the circulator's quality. However, it is important that the four circulators are phase-matched to avoid any extra imbalances that could degrade the isolation. Also, it should be noted that the circulator bandwidth limits the proposed system's operational bandwidth.

(3) Beamforming Network (BFN): 2(inputs)×4(outputs) Butler matrix BFN consisting of two 180º hybrids and one 90º hybrid is used at the TX side as shown in Fig. 3.1. TX BFN supports the excitation of modes 1 and 3. The RX BFN is 4× 4 Butler matrix BFN. It consists of three 180º hybrids and one 90º hybrid as shown in Fig. 3.1. The RX BFN supports the excitation of modes 1, 2, 3, and 4. Mode 4 is unused in this configuration and its port is terminated with a matched load. The proposed STAR antenna sub-system can operate in broadside beam mode 1 or conical beam mode 3 with similar RHCP TX and RX radiation patterns. Different TX and RX patterns can also be obtained by operating the TX and RX BFNs in modes 1 and 2; respectively. Moreover, LHCP broadside patterns can be radiated by exciting mode -1 (i.e. mode 3 below its turn-on frequency) at TX and RX BFNs. For all these arrangements, high isolation is preserved between the TX and RX channels. If the antenna is fully symmetric and TX/RX BFNs are ideal (i.e. imbalances-free), the proposed sub-system should eliminate completely the self-interference at RX port and re-route the coupled TX signal to the unused input ports.

To demonstrate the STAR antenna sub-system operational principles, the signal flow from the TX port to the RX port is analyzed as shown in Fig. 3.2. To simplify the analysis, lossless ideal hybrids and phase-matched circulators are assumed. The principle of operation for each TX/RX mode is explained as follows:

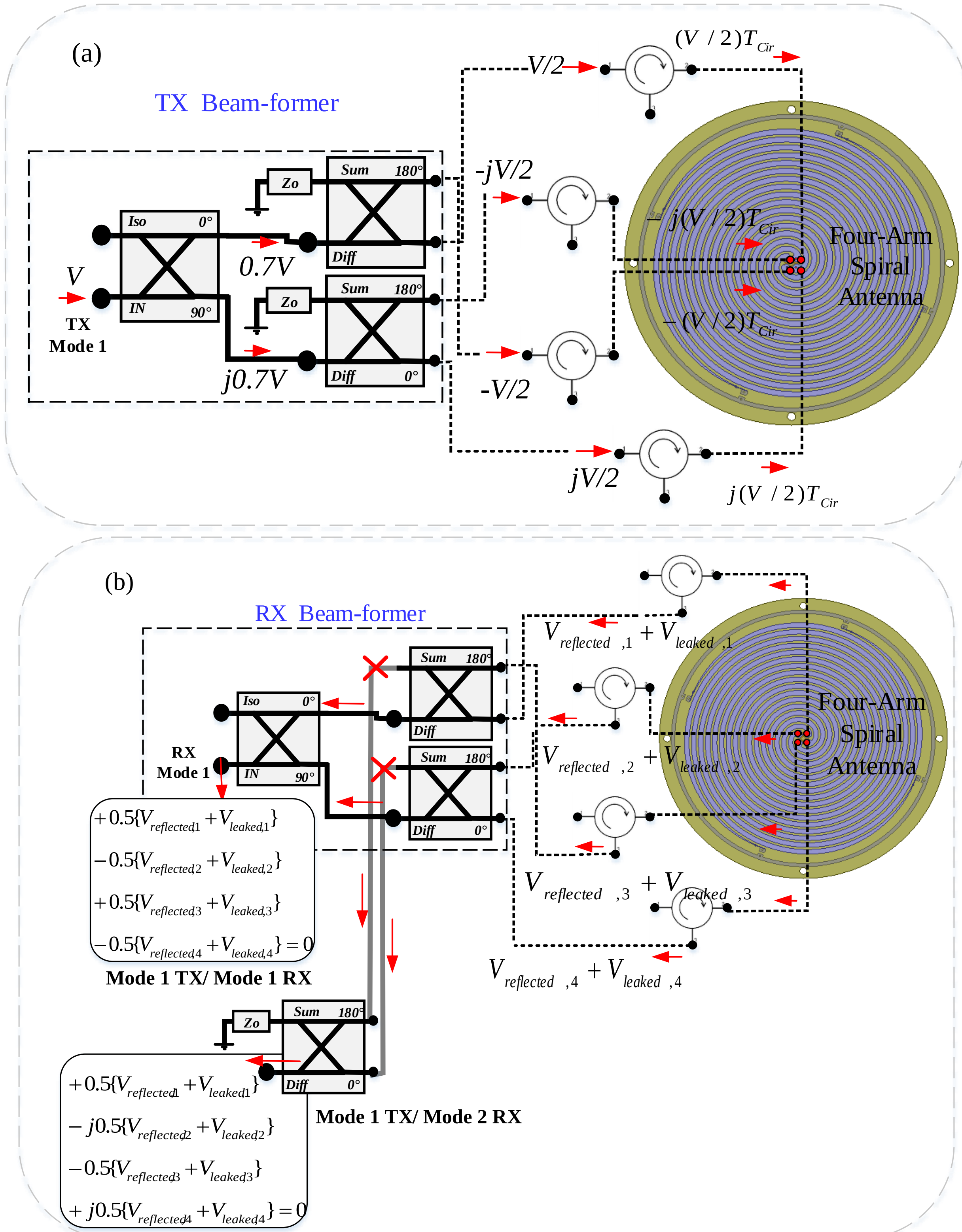

Figure 3.2: Signal flow diagram of the proposed STAR sub-system for (a) TX, and (b) RX sides. TX BFN supports the excitation of modes 1 and (3,-1) and the RX BFN supports the excitation of modes 1, 2, and (3,-1). Only (Mode 1) TX and (Mode 1 and Mode 2) RX coupling signal cancellation mechanism is shown.

A. Mode 1 TX / Mode 1 RX: For mode 1 operation at the TX and RX sides, the antenna sub-system isolation can be computed by accounting for all coupling paths as follows:

1) Starting from TX BFN, mode 1 port is excited with a voltage signal of magnitude V. The output voltages can be simply written as:

$$V_{TX,n} = (\, V/\, 2)\; e^{-j\phi_{TX,n}} \tag{3.1.a}$$

and

$$\phi_{TX,n} = \{0°, \pi/2, \pi, 3\pi/2\}\,;\; n = 1,2,3, and\; 4 \tag{3.1.b}$$

The four output signals have equal magnitude of (V/2) and phase vector of ϕ_{TX}.

2) The output signals are routed by the circulators to the antenna ports which excite mode 1 radiation. A portion of the signal ($V_{leaked,n}$) is leaked to the RX paths due to the insufficient isolation of the circulator. The input signal to each spiral arm is defined as,

$$V_{input,n} = V_{TX,n}\, T_{Cir.,n} \tag{3.2}$$

and the leaked signal,

$$V_{leaked,n} = V_{TX,n}\, L_{Cir.,n} \tag{3.3}$$

where $T_{Cir.,n}$ and $L_{Cir.,n}$ are the circulator transmission coefficient and leakage factor, respectively. Then, the reflected TX signal from the antenna arms ($V_{reflected,n}$) couples through the circulators to the RX paths as shown in Fig. 3.2.b,

$$V_{reflected,n} = V_{input,n}\ \Gamma_{arm,n}\, T_{Cir.,n} \tag{3.4}$$

where $\Gamma_{arm,n}$ is the active reflection coefficient of each antenna's arm.

3) The TX coupled signals from the spiral reflection ($V_{reflected,n}$) and circulators leakage ($V_{leaked,n}$) are then routed through the RX BFN. The coupled TX signals at RX port can be written as:

$$C_{1\_(TX\ to\ RX)} = \left(\frac{1}{2}\right)\left(V_{leaked,1} + V_{reflected,1}\right) e^{-j\{0\}} \qquad (3.5.a)$$

$$C_{2\_(TX\ to\ RX)} = \left(\frac{1}{2}\right)\left(V_{leaked,2} + V_{reflected,2}\right) e^{-j\{\pi/2\}} \qquad (3.5.b)$$

$$C_{3\_(TX\ to\ RX)} = \left(\frac{1}{2}\right)\left(V_{leaked,3} + V_{reflected,3}\right) e^{-j\{\pi\}} \qquad (3.5.c)$$

$$C_{4\_(TX\ to\ RX)} = \left(\frac{1}{2}\right)\left(V_{leaked,4} + V_{reflected,4}\right) e^{j\{\pi/2\}} \qquad (3.5.d)$$

By plugging (3.3) and (3.4) in (3.5), the previous equation can be simplified further and re-written as:

$$C_{1\_(TX\ to\ RX)} = \left(\frac{V}{4}\right)\left(L_{Cir.,1} + T_{Cir.,1}\ \Gamma_{arm,1}\, T_{Cir.,1}\right) \qquad (3.6.a)$$

$$C_{2\_(TX\ to\ RX)} = \left(\frac{-V}{4}\right)\left(L_{Cir.,2} + T_{Cir.,2}\ \Gamma_{arm,2}\, T_{Cir.,2}\right) \qquad (3.6.b)$$

$$C_{3\_(TX\ to\ RX)} = \left(\frac{V}{4}\right)\left(L_{Cir.,3} + T_{Cir.,3}\ \Gamma_{arm,3}\, T_{Cir.,3}\right) \qquad (3.6.c)$$

$$C_{4\_(TX\ to\ RX)} = \left(\frac{-V}{4}\right)\left(L_{Cir.,4} + T_{Cir.,4}\ \Gamma_{arm,4}\, T_{Cir.,4}\right) \qquad (3.6.d)$$

4) If the symmetry is maintained along all circulators; the TX and RX BFNs, and active reflection coefficients of the four spiral antenna's arms, are assumed to be similar, meaning:

$$L_{Cir.,1} = L_{Cir.,2} = L_{Cir.,3} = L_{Cir.,4} \tag{3.7.a}$$

$$T_{Cir.,1} = T_{Cir.,2} = T_{Cir.,3} = T_{Cir.,4} \tag{3.7.b}$$

$$\Gamma_{arm,1} = \Gamma_{arm,2} = \Gamma_{arm,3} = \Gamma_{arm,4} \tag{3.7.c}$$

these routed coupled signals in (3.6) should cancel one another since each two coupling paths are out of phase compared to the other two. Then, the total routed coupled signals from the TX ports to the RX port can be expressed as (8.a).

$$C_{(TX\ to\ RX)} = C_{1\_(TX\ to\ RX)} + C_{2\_(TX\ to\ RX)} + C_{3\_(TX\ to\ RX)} + C_{4\_(TX\ to\ RX)} = 0 \tag{3.8.a}$$

Or, in more general form as

$$C_{(TX\ to\ RX)} = \left(\frac{1}{2}\right) \sum_{n=1}^{4} \left(V_{leaked,n} + V_{reflected,n}\right)\, e^{-j\phi_{RX(n)}} = 0 \tag{3.8.b}$$

Where

$$\phi_{RX(n)} = \{0°, \pi/2, \pi, 3\pi/2\}\ ;\ n = 1,2,3,4 \tag{3.8.c}$$

Hence, the BFNs effectively cancel part of the coupled TX signals that travel to the RX port; while redirecting the rest of the non-radiated coupled signals from the transmitter to the unused mode 3 port of the RX 90° hybrid which is appropriately terminated.

B. Mode 3 TX / Mode 3 RX & Mode -1 TX / Mode -1 RX: for this arrangement, the other port of the 90° hybrids in both TX and RX BFNs is used to excite mode 3 (higher band) and mode -1 (lower band), as illustrated in Fig. 3.1. It can be proven that the TX coupled signals are also cancelled for TX/RX mode 3 and mode -1 operation and the residual signals are redirected to the RX BFN mode 1 port. Even though the signal flow is not included in Fig. 3.2, a similar analysis to Mode 1 can be easily repeated. Only, the TX and RX phase progressions of (3.1.b) and (3.8.c) need to be replaced by:

$$\phi_{TX(n)} = \{0°, 3\pi/2, \pi, \pi/2\}\,;\ n = 1,2,3,4 \tag{3.9.a}$$

$$\phi_{RX(n)} = \{0°, 3\pi/2, \pi, \pi/2\}\,;\ n = 1,2,3,4 \tag{3.9.b}$$

C. Mode 1 TX / Mode 2 RX: Once mode 1 is excited as TX, mode 1 RX and mode 2 RX can be received simultaneously. For mode 1 TX / mode 2 RX configuration, the coupled mode 1 TX signals are cancelled at the sum ports of first two 180º RX hybrids before entering the last RX 180° hybrid. Hence, for the ideal case no coupled signal should be directed through the last mode 2 180º hybrid as shown in Fig. 3.2.b. To compute the coupling, (3.1)-(3.8) can be re-applied and only the RX phase progression in (3.8.c) is needed to be replaced to produce mode 2 as:

$$\phi_{RX(n)} = \{0°, \pi, 0, \pi\}\,;\ n = 1,2,3,4 \tag{3.10}$$

The above analysis for the various modes shows that the coupled TX signals are cancelled at the receiving BFN ports leading to theoretically infinite isolation between TX and RX channels. To validate the proposed assumption computationally, the method of moments (MoM) solver FEKO, [99], is used to model a dual-layer 7 cm diameter four-arm Archimedean spiral. The simulated s-parameters are then imported to AWR circuit simulator [112] where the ideal hybrids and 10 dB isolation circulators are implemented in order to compute the antenna sub-system TX/RX isolation. The simulated isolation is plotted in Fig. 3.3 and as expected, a high sub-system isolation of >75 dB is obtained for the three configurations over a 4:1 bandwidth.

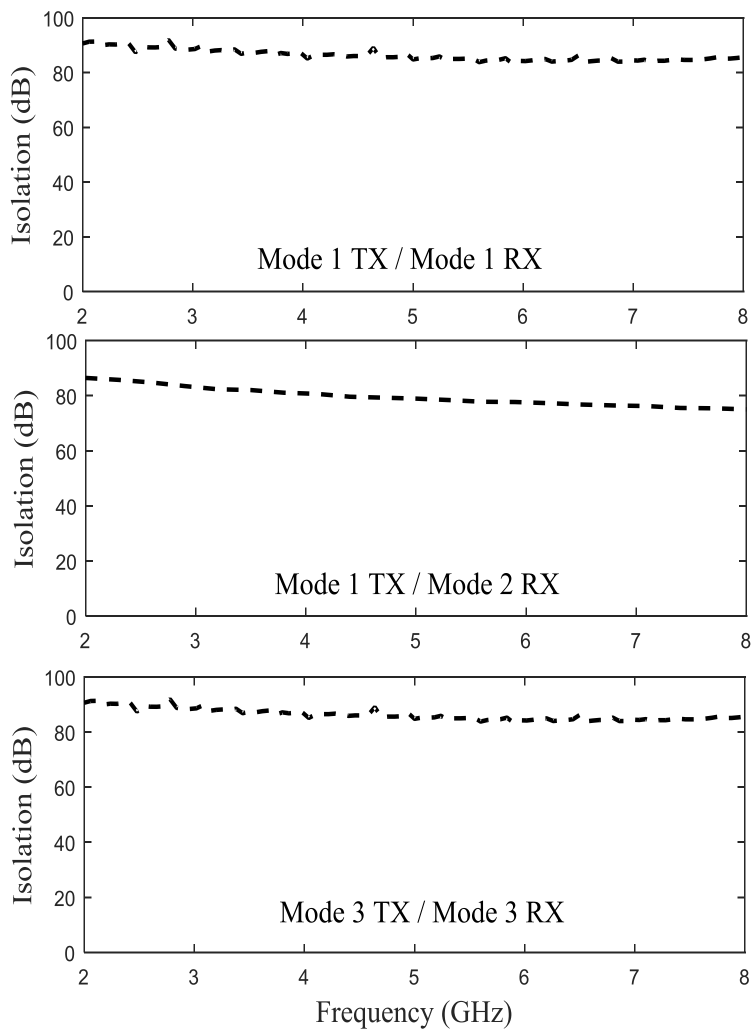

Figure 3.3: Mode 1 TX / Mode 1 RX, Mode (3,-1) TX / Mode (3,-1) RX, and Mode 1 TX / Mode 2 RX simulated isolation of an ideal spiral STAR system.

3.3 Non-Ideal Effects

In previous section, the circuit components were assumed to be ideal. However, in practice, these components have responses that vary differently over the frequency band of operation. This imperfect response introduces some asymmetry to each of the TX coupled signal paths causing deterioration in the isolation performance. In other words, the general expression stated in (3.8.b) is no longer accurate and should be substituted by (3.11) to account for these imperfections.

$$C_{(TX\ to\ RX)} = \left(\frac{1}{2}\right) \sum_{n=1}^{4} \left\{ V_{leaked,n} + V_{reflected,n} + V_{inc} \right\} e^{-j\left\{\phi_{RX(n)} + \phi_{RX_{inc}}\right\}} \neq 0 \qquad (3.11)$$

where $\phi_{RX_{inc}}$ and V_{inc}, are the errors introduced by the circuit components imperfections. To investigate these effects, numerical studies are conducted by varying the isolation levels of (a) the four circulators and (b) the amplitude and phase of the hybrids. For space restrictions, only mode 1 TX / mode 1 RX configuration is considered; however, similar conclusions apply to other antenna sub-system configurations.

A. Circulators: the differences among the circulators' characteristics lead to changing the complex weights of each of the TX coupled signal paths. As a consequence, the overall isolation decreases significantly since no full-cancellation is achieved at the RX port/s. Assessment of the isolation behavior can be examined by changing each of the four matched circulators' isolation. The chosen isolation for the four circulators are 10 dB, 20 dB, and 30 dB. Notice, the employed ideal circulators in this study are assumed to be frequency-independent just to demonstrate the overall impact. The results are shown in Fig. 3.4.a, and as seen when all circulators have identical behavior, the overall TX/RX isolation remains the same even though the isolation levels of each circulator changes from 10 dB to 30 dB. This result confirms our observation in (3.8.b). Nevertheless, once the circulators are different, the total TX/RX isolation drops from the range of 80 dB-90 dB into 30 dB-40 dB, as seen in Fig. 3.4.b. The more the performance of the four circulators deviates from one another, the more the antenna sub-system isolation changes according to the levels of the four circulators' isolation, as shown in Fig. 3.4.b. For instance, comparing the two cases of (C1=10 dB, C2=11 dB, C3=12 dB, C4=13 dB) with (C1=20 dB, C2=21 dB, C3=22 dB, C4=23 dB), around ~5-7 dB improvement is observed.

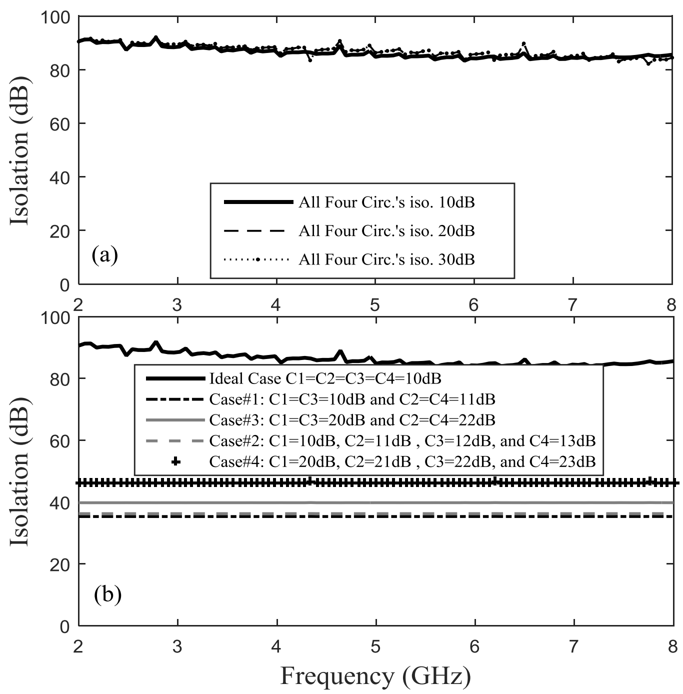

Figure 3.4: The effect of the four circulators on Mode 1 TX / Mode 1 RX isolation. "C" denotes isolation of each circulator.

B. Hybrids: The impacts of the amplitude and phase imbalances of the two Butler-matrices are considered next. The chosen frequency-independent amplitude and phase imbalances of the hybrids are varied within 0 dB-0.6 dB and 0°-8°, respectively. The amplitude and phase errors can be introduced in circuit simulator or using (3.11). The TX/RX isolation study shown in Fig. 3.5 depicts the spread of isolation values for considered hybrids' amplitude and phase imbalances. Notice that even in the worst case isolation of 20 dB, the antenna sub-system still achieves >10 dB extra isolation compared to the 10 dB circulators' isolation over 4:1 bandwidth. Overall, these results emphasize the importance of the circuit components on controlling the sub-system level of isolation.

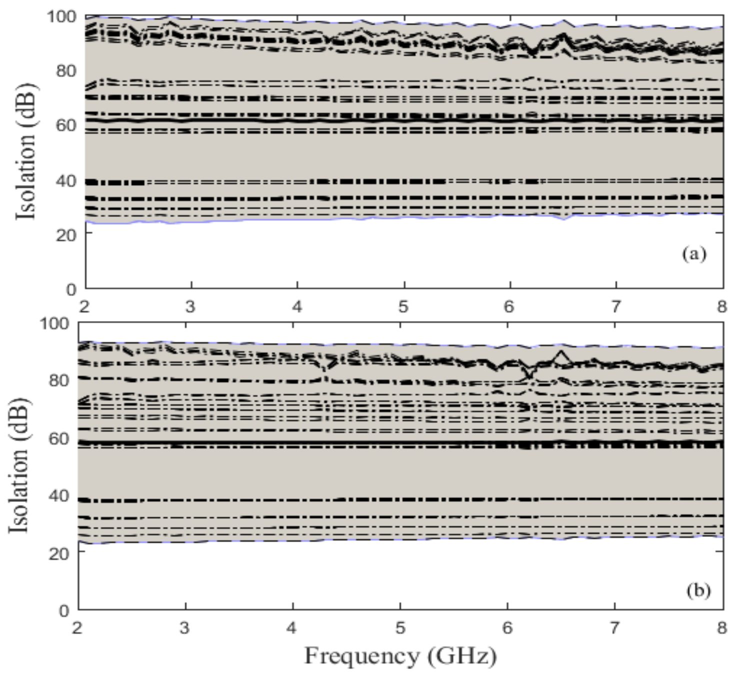

Figure 3.5: Study demonstrates the effects of the hybrids' imbalances on Mode 1 TX/ Mode 1 RX isolation; (a) Amplitude, and (b) phase imbalances. The ideal circulators' isolation is fixed at 10 dB.

3.4 Implementation and Mode 1 Performance

To experimentally demonstrate the proposed STAR sub-system, a dual-layer right-handed four-arm Archimedean spiral with four turns is fabricated (see inset of Fig. 3.6). The antenna has outer and inner radii of 70 mm and 2.5 mm, respectively, and it was fabricated on a 0.76 mm-thick Rogers 5870 Teflon based substrate ($\varepsilon_r = 2.33, tan\,\delta = 0.0012$). A 50 Ω coaxial bundle composed of four semi-rigid cables is used to feed the antenna. To reduce the input impedance and achieve good impedance match with the utilized bundle, the metal to slot ratio (MSR) of the spiral is increased to 3:1. To further improve the match, the dual-layer configuration is used; where the bottom and the top layers are connected with vias located at the center and the arms ends [100]. The antenna aperture is backed by ECCOSORB AN-75 absorber. The mode 1 of this spiral full turn-on at ~1.5 GHz. The BFN is composed of five 180°, two 90° hybrids, and four circulators all operating over 2-8 GHz and integrated as depicted in Fig. 3.1. All isolation measurements were conducted in the University of Colorado anechoic chamber.

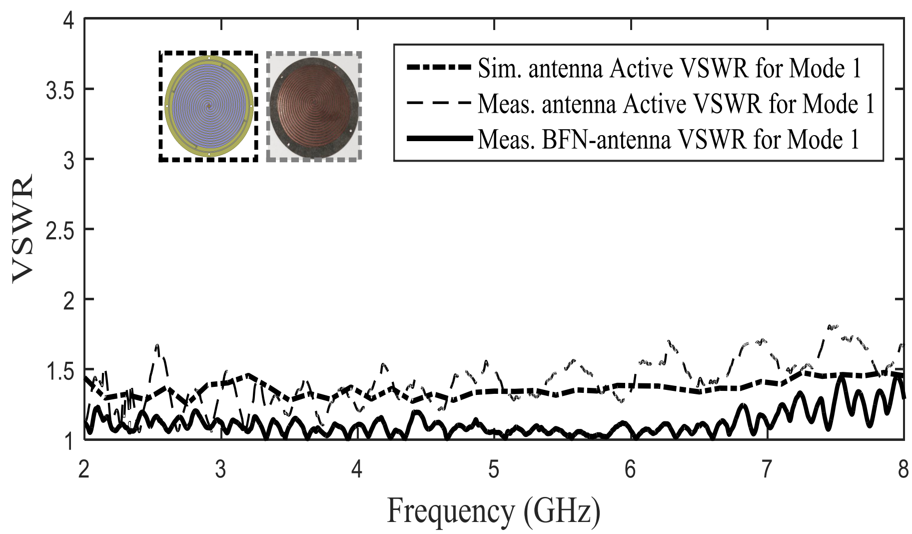

Figure 3.6: Measured and simulated active VSWRs for one port of the four-arm spiral antenna. Also shown is the measured VSWR for the TX/RX circulator-BFN's ports once connected to the fabricated antenna. Shown in the inset are the computational model and the photo of the fabricated spiral aperture.

Measured and simulated active VSWRs of the fabricated spiral antenna are shown in Fig. 3.6. Overall active VSWR <1.7 is obtained from 2-8 GHz and further improvement is obtained in VSWR performance once the antenna is connected to the TX or RX circulators and BFNs. This is due to the re-routing of reflections to the terminated ports of TX and RX 90° hybrids. The complete layout of the mode 1 STAR antenna sub-system including the Butler matrix TX/RX BFNs, circulators, and the fabricated four-arm spiral is shown in Fig. 3.7. Two sets of isolation measurements are conducted; one for a single circulator, and other for the entirely integrated STAR antenna sub-system (BFNs, circulators, and fabricated four-arm spiral antenna). The measured isolation for one of the four COTS circulators is around 10 dB; while for (mode 1 TX / mode 1 RX) the isolation is >27 dB (maximum of 38 dB) with nominal of 32 dB over the band.

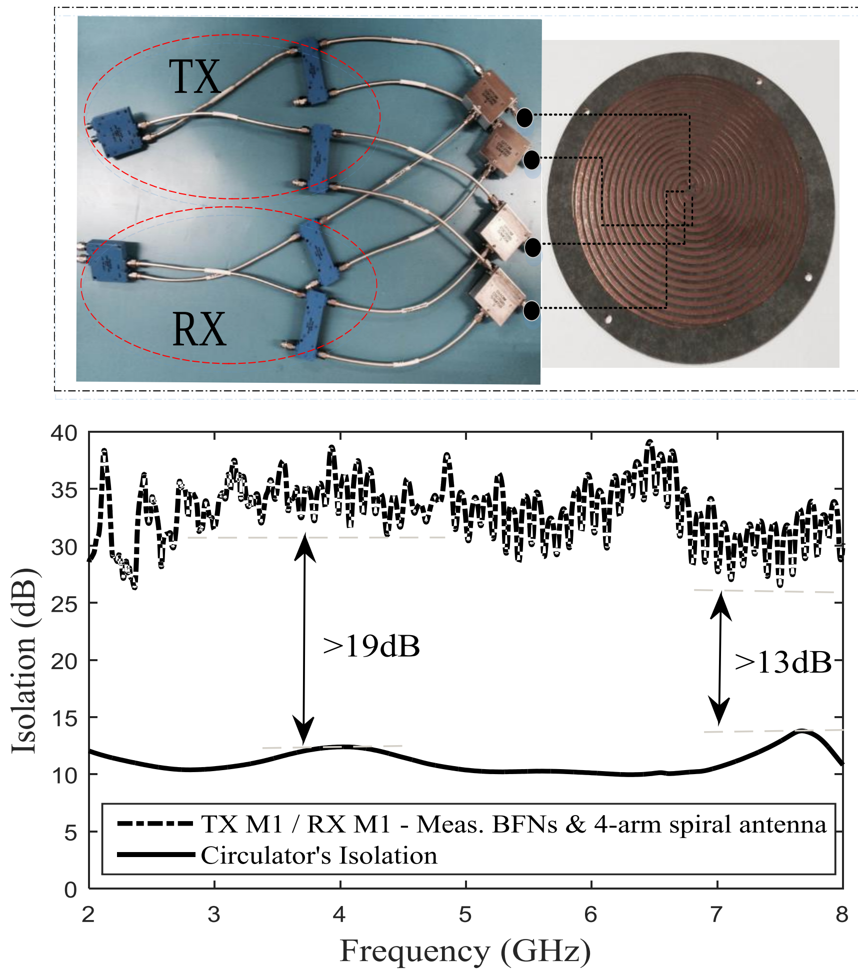

Figure 3.7: Mode 1 TX / mode 1 RX measured isolation between the TX/RX BFN's ports compared to one of the four used circulators. The inset shows the STAR sub-system of mode 1 TX / mode 1 RX configuration.

As discussed in the previous section, both the imbalances of the hybrids, and asymmetry of the four circulators contribute negatively on the performance of the total TX/RX isolation. Even though there is a drop in isolation with respect to the ideal case where >13 dB improvement is still achieved over 4:1 bandwidth compared to the measured COTS circulators. If the hybrids, phase matched circulators, and interconnects are monolithically integrated, the isolation will be further enhanced. Since the same antenna is used as transceiver, the far-field performances of modes 1 TX and mode 1 RX are quite similar.

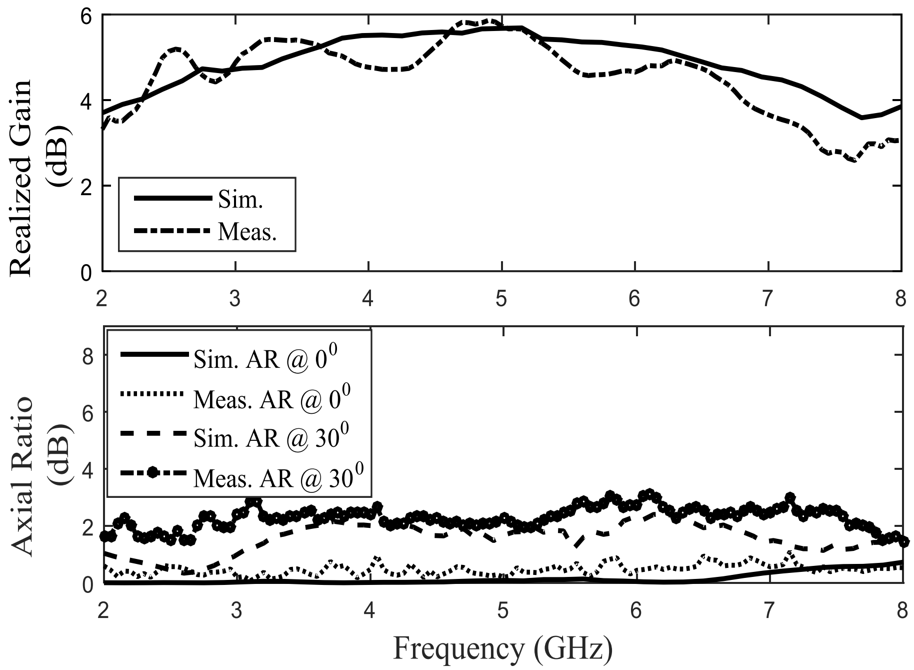

Figure 3.8: Simulated and measured (a) realized gain of the four-arm spiral antenna in mode 1 and (b) axial ratio at $\theta = 0°$ and 30°.

To quantitatively characterize the similarity between the TX's and RX's radiation patterns over the operational bandwidth, the ECC parameter defined in chapter 2 is used. Overall ECC >95% is obtained over the entire band. Therefore, only the TX side's performance is presented herein. The measured and simulated realized gain and axial ratio are shown in Fig. 3.8. As seen, the realized gain at broadside is >3.8 dB over most of the band. Excellent axial ratio of <3 dB up to elevation angles 30° off broadside are obtained throughout 4:1 bandwidth. The measured and simulated co-polarized (RHCP) shows high quality mode 1 radiation patterns over the entire bandwidth (Fig. 3.9).

3.5 Multimode STAR Antenna Sub-system Performance

The measured and simulated active matches of mode 2, mode 3, and mode -1 are shown in Fig. 3.10. As seen, the VSWR is <2 for mode 2 after ~3 GHz-3.5 GHz (almost 2 times the turn-on frequency of mode 1), whereas Mode 3 full turn-on at ~4.5 GHz, while mode -1 operates from ~2-4.3 GHz (below the turn-on of mode 3). Further improvement in VSWR <1.7 for mode -1 and mode 3 is obtained once the antenna is connected to the complete circulator-BFN. The measured isolation for different cases is shown in Fig. 3.11. The measured isolation is >27 dB (maximum of 38 dB) over the band with a nominal value of 32 dB over the band for mode 1 TX/mode 2 RX. For mode 3 TX/mode 3 RX and mode -1 TX/mode -1 RX configurations, the isolation is >24 dB (maximum of 35 dB) with nominal value of 30 dB over the band. Improvement in isolation of >12 dB and >15 dB are achieved for mode 3 and mode (2,-1); respectively, compared to the stand-alone circulator's isolation.

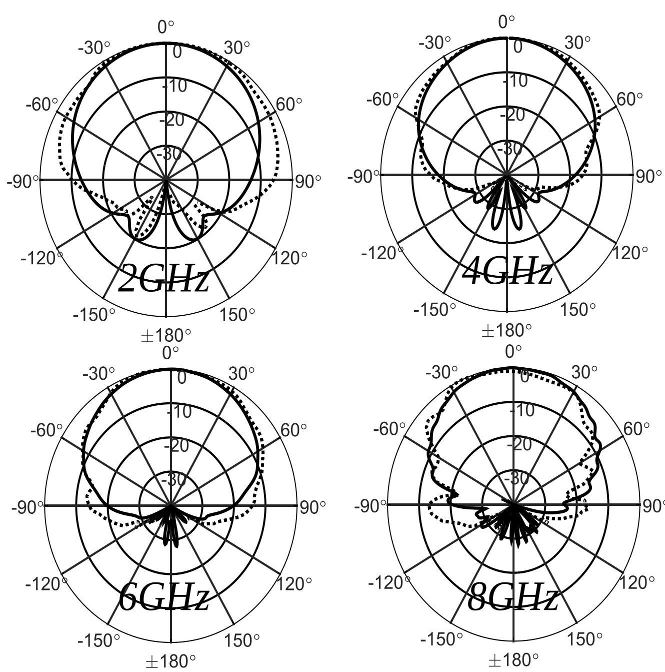

Figure 3.9: Simulated (solid) and measured (dotted) normalized RHCP far-field radiation patterns of the TX/RX STAR four-arm spiral antenna.

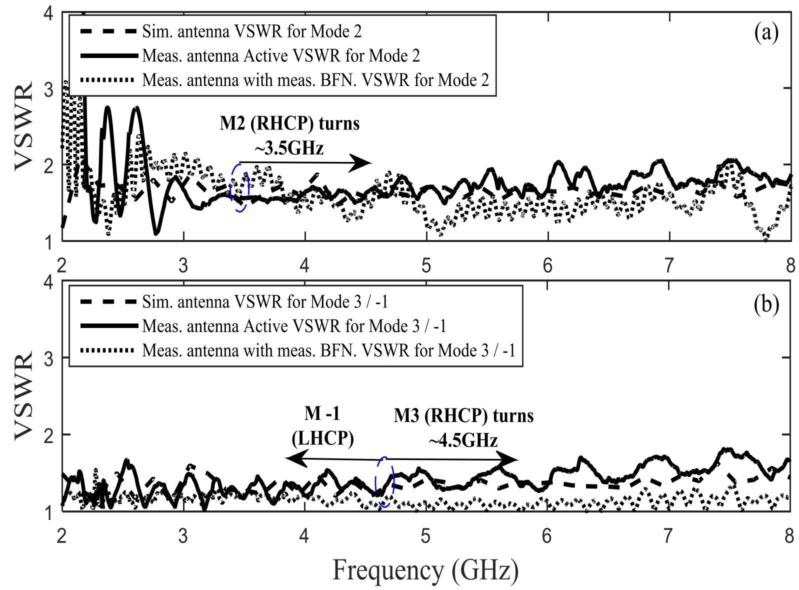

Figure 3.10: Simulated and measured active VSWRs for the antenna and the TX/RX circulator-BFN's ports including the antenna: (a) Mode 2 and (b) mode 3 and mode -1.

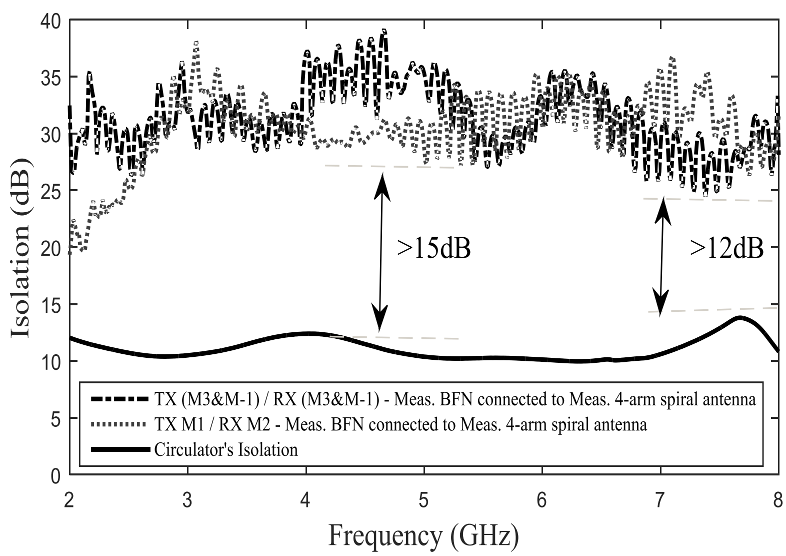

Figure 3.11: Measured isolation between the TX/RX BFN's ports for RHCP Mode 3 TX / Mode 3 RX in ~4 GHz -8GHz, and LHCP Mode -1 TX / Mode -1 RX in 2GHz - ~3.9GHz range. Also shown is Mode 1 TX / Mode 2 RX measured isolation between the TX/RX BFN's ports (3.5GHz-8GHz).

The measured and simulated far-field performances are obtained for mode 2 (RHCP), mode -1 (LHCP), and mode 3 (RHCP). The axial ratio for mode 2 is measured at the peak gain elevation angle of 36°. As shown in Fig. 3.12, the achieved axial ratio is less than 4.2 dB over 4.7-5.2 GHz and 6-6.2 GHz and less than 3 dB over most (84%) of the designated bandwidth of operation 3.5 GHz-8 GHz. Mode 3 on the other hand, has an axial ratio at the peak gain of 48° less than 4 dB over the frequency band of 4.5 GHz - 8 GHz; while mode -1 (LHCP) has an axial ratio less than 3 dB over 2 GHz - 4.2 GHz at 0°. Overall, good circularly-polarized performance is achieved with this fabricated four-arm multimode spiral. The realized gain over the specified operational band for mode 2, mode 3, and mode -1 is >2 dBic, >1.2 dBic, >1.5 dBic, respectively.

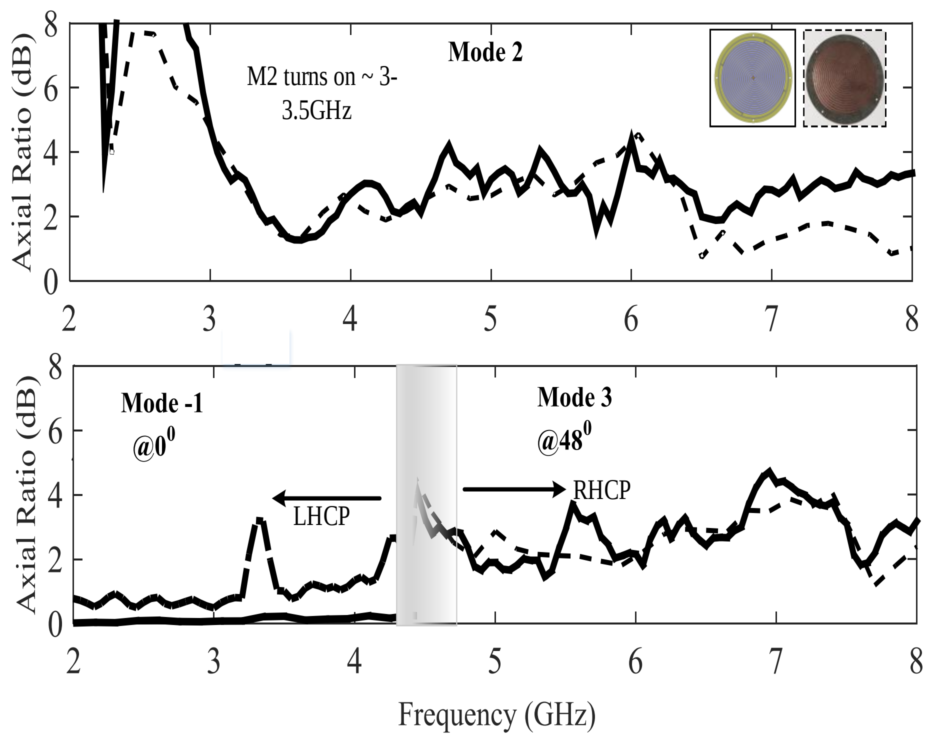

Figure 3.12: Simulated and measured axial ratio of the four-arm spiral antenna at θ equals 36° for Mode 2 (RHCP), 0° for Mode -1 (LHCP), and 48° for Mode 3 (RHCP). (Simulated antenna is backed with ideal absorber).

Figs. 3.13 and 3.14 show the plotted far-field patterns for the mode 2, mode -1, and mode 3 at different frequencies. The power loss of the complete beamformer is dependent on the match of the four-arm spiral and the leakage from the circulators.

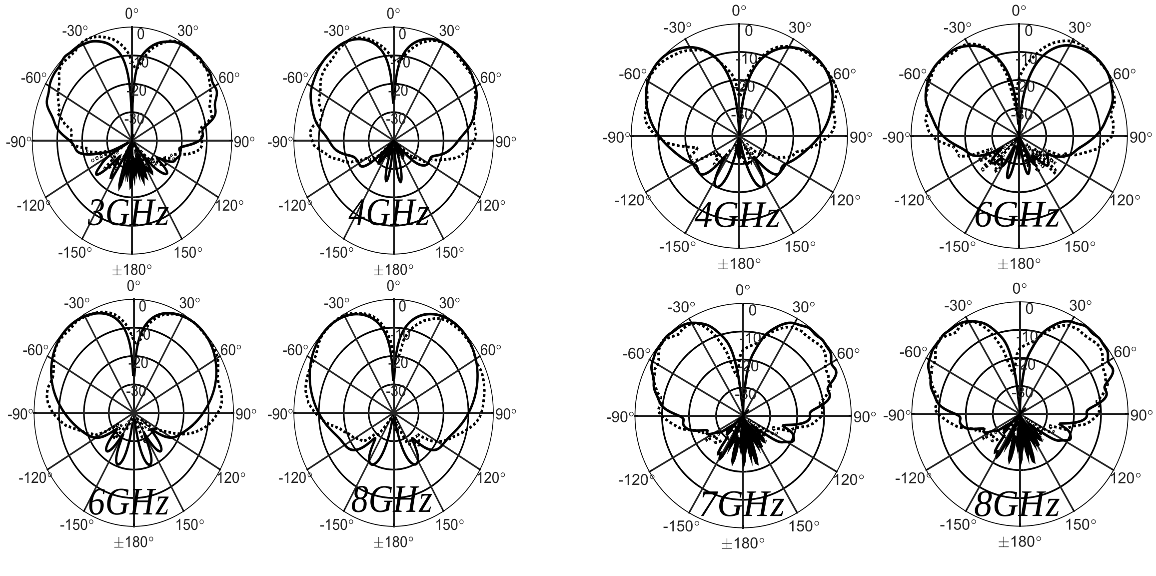

(a) (b)

Figure 3.13: (a) Mode 2 simulated (solid) and measured (dotted) RHCP far-field radiation patterns of the STAR four arm spiral antenna. (b) Mode 3 simulated (solid) and measured (dotted) RHCP far-field radiation patterns of the STAR four arm spiral antenna. Only at higher frequency band (higher than 4GHz).

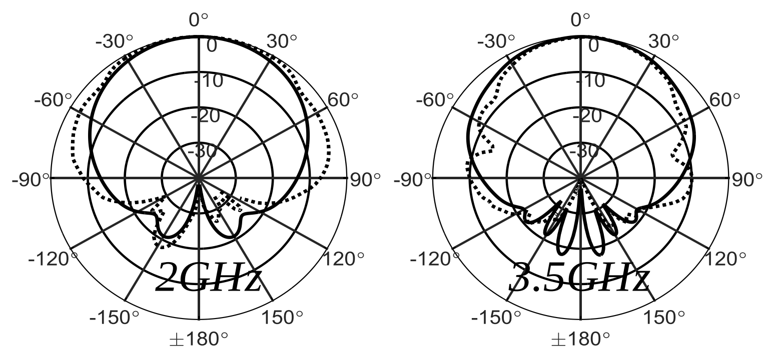

Figure 3.14: Mode -1 simulated (solid) and measured (dotted) LHCP far-field radiation patterns of the STAR four arm spiral antenna. Only at lower frequency band (below 4GHz).

The measured power loss of the Butler-BFNs once connected to the measured antenna is shown in Fig. 3.15. The inherent loss of this feeding network is within 10%-20% for all different mode configurations. This loss can be further reduced and overall system performance improved with custom made, tight tolerance components or integrated networks.

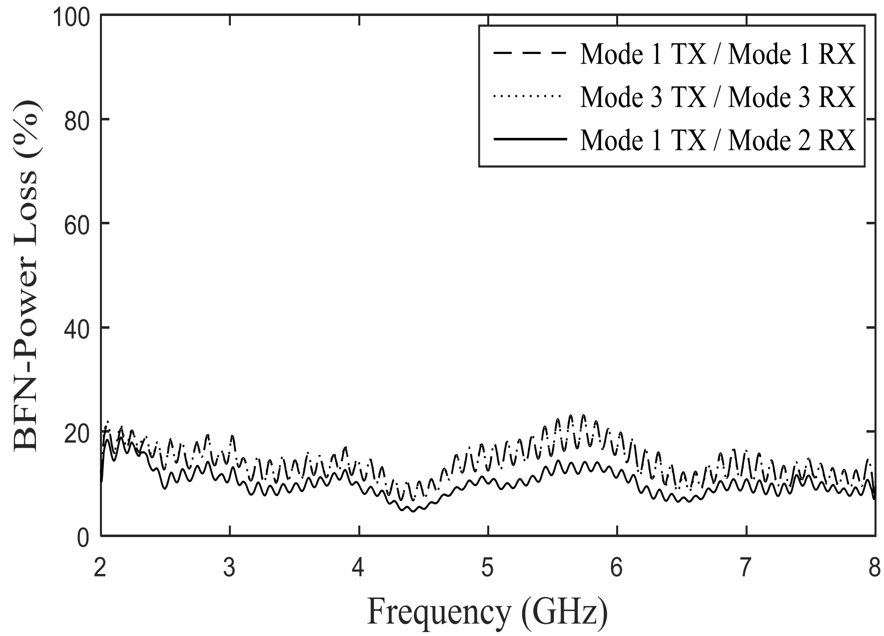

Figure 3.15: The measured power loss of the STAR BFN once it is connected to the measured circulators and spiral antenna.

3.6 Summary

A wideband multimode monostatic STAR antenna sub-system is introduced [113]-[114]. The configuration is composed of a single four-arm spiral with four circulators, and two Butler matrix BFNs. It is theoretically demonstrated that infinite isolation between the TX and RX ports without any need for duplexing in time, frequency, polarization, or spatial domains is possible with ideal conditions. Moreover, the flexibility of achieving diverse circularly-polarized mode combination (broadside and split-beam modes or RHCP and LHCP) using a single aperture while maintaining reasonable isolation over a wide bandwidth is demonstrated. High-simulated isolation is achieved for all mode arrangements (1, 2, 3, and -1). The proposed theoretical baseline used to explain the isolation phenomenology is fully confirmed with these results. The measurements on a prototype are carried out to experimentally prove the proposed concept. Results show isolation between 23 and 38 dB for different mode arrangements. The obtained data emphasize the significance of imbalances and even though the theoretical isolation is compromised in the presence of said imbalances; more than 12 dB improvement is still seen compared to the inherent COTS circulator isolation. All modes have shown to have good quality radiation patterns. Specifically, modes 1 and -1 have axial ratio < 3 dB over a large field-of-view. Modes 2 and 3 measured AR levels are <4 dB at the peak gain angle of 36° and < 4.2 dB at the peak gain angle of 48°, respectively.

CHAPTER 4

WIDEBAND MULTIMODE LENS-LOADED CO-POLARIZED EIGHT-ARM C-STAR SPIRAL ANTENNA SUB-SYSTEM

4.1 Overview

Enabling simultaneous transmit and receive within the same frequency band in modern wireless communication systems while having diverse radiation characteristics can be very attractive for next-generation wireless networks operating in congested spectrum environments. Several advantages may thus be gained including increased channel capacity, efficiently reusing licensed spectrum, and avoiding time-frequency duplexing. Moreover, having diverse radiation characteristics with broadside and conical beams can provide full spatial coverage over the upper hemisphere. So far, several isolation improvement methods at the antenna layer have been presented in the open literature [27], [32], [38], [45], [46], and [48], with either omnidirectional or directional coverages. Most of these techniques rely on using multiple antennas or antenna arrays where the isolation is achieved in particular by null-placement, symmetry and phase manipulation, beamforming and near-field cancellation, mode orthogonality principles, or incorporating the antenna elements' orientation and beamforming techniques. A shared C-STAR aperture system can also be employed to realize C-STAR operation which traditionally utilizes passive ferrite circulators to isolate the TX and RX paths/ports. However, even with state-of-the-art broadband circulators with isolation >20 dB, the TX/RX isolation is limited by the return loss of the antenna. Most discussed C-STAR approaches are capable of mitigating the SI issue; yet, the problem of achieving high isolation while having simultaneous, co-polarized, and diverse TX and RX broadside and conical radiation patterns is seldom addressed, especially using a single aperture instead of an array.

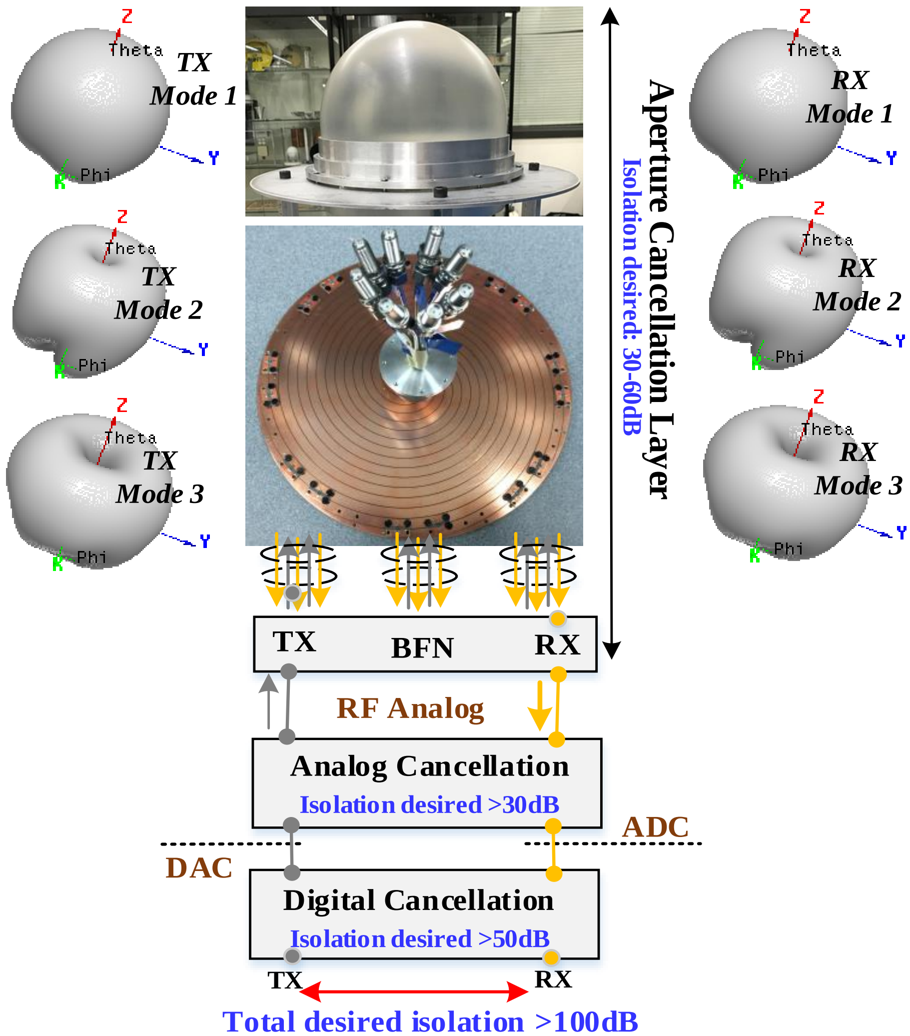

Figure 4.1: Achieving a C-STAR operation with an eight-arm single aperture spiral and multiple cancellations layers. The diverse co-polarized TX and RX radiation patterns (modes 1, 2, and 3) are also shown.

In chapter 2, the four-arm C-STAR spiral antenna (two-arm-TX and two-arm-RX) is utilized to achieve ideally infinite isolation by relying on antenna geometrical characteristics, symmetry, and applied excitation. This approach has shown measured isolation >52 dB over a 10:1 bandwidth. However, the far-field performance degrades at the lower frequency end due to the existence of the parasitic arms. In chapter 3, a C-STAR antenna sub-system that mitigates the two main limitations of circulators, specifically, leakage and return loss, was proposed. High

TX/RX isolation is achieved by utilizing the characteristics of a four-arm spiral and Butler matrix BFN to re-route coupled and leaked TX signals through the circulators away from the receiving port. Four circulators are therefore required to realize the C-STAR antenna sub-system. In this chapter, a single eight-arm spiral antenna C-STAR sub-system without expensive, bulky, bandwidth, power, and isolation-limited circulators is proposed, as shown in Fig. 4.1. Moreover, the proposed antenna sub-system enables operation of TX/RX mode 2, thus allowing the RX side to have another concurrent functionality (for example amplitude/phase direction finding). A multimode lens-loaded eight-arm spiral aperture is proposed for C-STAR applications and investigated in this chapter. Specifically, the single eight-arm spiral antenna is composed of a four-arm spiral for TX and a 45° spatially rotated four-arm spiral for RX. The eight-arm spiral antenna is connected into two 4×4 Butler matrix beamforming-networks (BFN) to differentiate between the TX and RX arms/ports and distinguish their functionalities. In the absence of BFN imbalances and antenna geometry asymmetries, the isolation is theoretically infinite due to full cancellation at the RX-antenna's and RX-beamformer's ports. This approach also enables diverse co-polarized TX and RX radiation modes while maintaining theoretically infinite isolation. The considered spiral antenna supports mode 1, with a broadside pattern, and modes 2 and 3, with conical patterns. The aperture is loaded with a hyper-hemispherical dielectric lens to improve the far-field performance. The operational principles are discussed first under ideal conditions, followed by computational and experimental results. Average measured isolation >38 dB is achieved over 3:1, 1.5:1, and 1.3:1 bandwidths for the radiating TX and RX modes 1, 2, and 3, respectively. Once the TX and RX are driven with identical modes, similar radiation patterns with high envelope correlation coefficient are obtained. To theoretically achieve infinite TX/RX isolation with diverse radiating modes, the multimode C-STAR concept of operation are shown in Figs. 4.1-4.3 for the following configurations:

A. Mode 1 at TX/ modes 1 and 2 at RX or vice versa

B. Mode 2 at TX/ modes 1, 2, and 3 at RX or vice versa

C. Mode 3 at TX/ modes 2 and 3 at RX or vice versa.

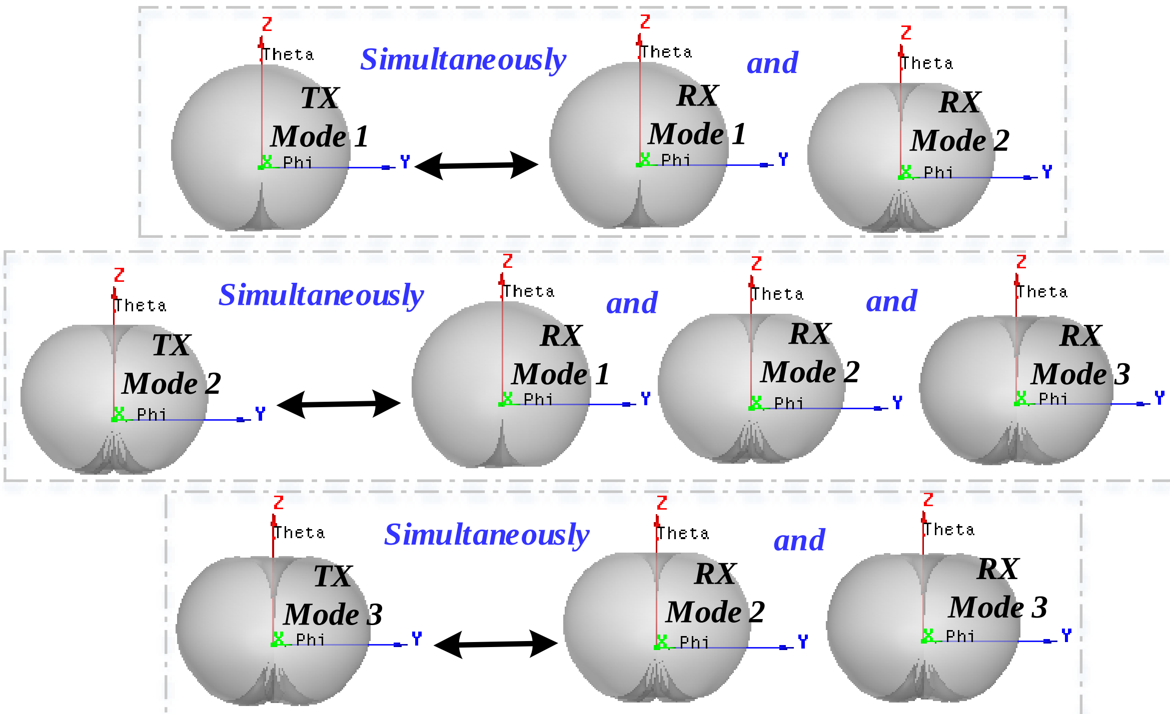

Figure 4.2: Possible simultaneous TX and RX radiating modes with high isolation inherent to the proposed C-STAR monostatic eight-arm spiral.

For more details, this chapter is organized as follows:

- Section 4.2 discusses the C-STAR spiral multimode configuration and the theory behind the SI suppression.
- Section 4.3 shows the simulated isolation performance of an eight-arm spiral C-STAR and the impact of the BFN imbalances.
- Section 4.4 presents the measured performance of the lens-loaded eight-arm spiral.
- Section 4.5 discusses the similarity between TX and RX patterns.
- Section 4.6 summarizes this chapter.

4.2 Single Aperture C-STAR Multimode Configuration

The proposed multimode C-STAR single aperture eight-arm spiral antenna (four-arm for TX/ four-arm for RX) is connected to the TX and RX Butler-matrix BFNs as illustrated in Fig. 4.3. The TX and RX four-arm spirals have a wide operational bandwidth, good impedance match, and can support three different wideband modes. Mode 1 is directional toward broadside whereas modes 2 and 3 have conical beams. These modes can be excited by applying equal amplitude and proper phase progression [81]. Notice that the turn-on frequencies for modes 2 and 3 are two and three times the turn-on frequency for mode 1, respectively. Therefore, if the C-STAR operation is desired to function with mode (pattern) multiplexing, the operational bandwidth is restricted by the higher order excited modes. In order to provide the desired phase and excite multiple modes, two 4×4 Butler matrix BFNs consisting of three 180° hybrids and one quadrature hybrid are used at the TX and RX sides, as shown in Fig. 4.3. Different TX and RX modes are considered, as demonstrated by the signal flow from TX/RX ports in Fig. 4.3. Based on the chosen excited TX mode, four signals exit the TX-BFN side at points 2-a to 2-d in Fig. 4.3 to excite the four-arm-TX spiral at points 3-a to 3-d. At points 4-a to 4-d, the RX-BFN receives the RX signal of interest in addition to the TX SI signals. If the antenna is fully symmetric and TX/RX BFNs are ideal, the proposed sub-system completely eliminates the SI at the RX port and re-routes the remaining coupled TX/RX signals to the RX-BFN's unused ports. To demonstrate the concept and discuss the operational principles, the right-handed wrapped Archimedean planar spiral is chosen. To understand the SI cancellation mechanisms, the following theoretical analysis accounts for all SI paths using multiport network formalism. Ideal TX and RX Butler-matrix BFNs and symmetric eight-arm spiral are assumed to simplify analysis. The general isolation expression is derived first for all possible excited modes; then, specific driven mode cases are considered. To start, one of the TX ports in Fig. 4.3 is excited, then four signals denoted by complex coefficients determined based on the desired mode of operation exit the TX BFN, as listed in Tables 4.1-4.3. These excitations cause the TX spiral to radiate and couple to the RX spiral. Equation (4.1) represent the RF TX/RX SI at the RX antenna ports (arm number 2, 4, 6, and 8) where the transmission coefficients (S_{ij}) represent the SI from the j-TX arms/ports to i-RX arms/ports.

$$b_{RX,TX,i} = 0.5\{S_{i1}a_1 + S_{i3}a_3 + S_{i5}a_5 + S_{i7}a_7\} \tag{4.1}$$

Where $b_{RX,TX,i}$ is the total TX/RX SI at each port of the RX arms, i is the number of RX arm (2, 4, 6, and 8), and (a_j) are the excitation coefficients of the operated TX or RX mode as specified in Tables 4.1-4.3. Due to the inherent symmetry along the spiral arms, the transmission coefficients between the adjacent and non-adjacent arms are related as in (4.2.a) and (4.2.b).

$$S_{21} = S_{23} = S_{43} = S_{45} = S_{65} = S_{67} = S_{87} = S_{81} \tag{4.2.a}$$

$$S_{25} = S_{27} = S_{41} = S_{47} = S_{61} = S_{63} = S_{85} = S_{83} \tag{4.2.b}$$

All the coupled signals that are induced on the RX's four arms/ports (4.1) are re-routed toward the RX-BFN's port. By substituting (4.2) in (4.1), the total TX/RX SI is then can be computed as

$$\begin{aligned} SI_{RX,TX} = {} & 0.25\{S_{21}a_1 + S_{21}a_3 + S_{25}a_5 + S_{25}a_7\}a_2 + \\ & 0.25\{S_{25}a_1 + S_{21}a_3 + S_{21}a_5 + S_{25}a_7\}a_4 + \\ & 0.25\{S_{25}a_1 + S_{25}a_3 + S_{21}a_5 + S_{21}a_7\}a_6 + \\ & 0.25\{S_{21}a_1 + S_{25}a_3 + S_{25}a_5 + S_{21}a_7\}a_8 \end{aligned} \tag{4.3}$$

(4.1) - (4.3) can now be used to determine the TX/RX SI cancellation for different combinations of TX and RX modes as follows:

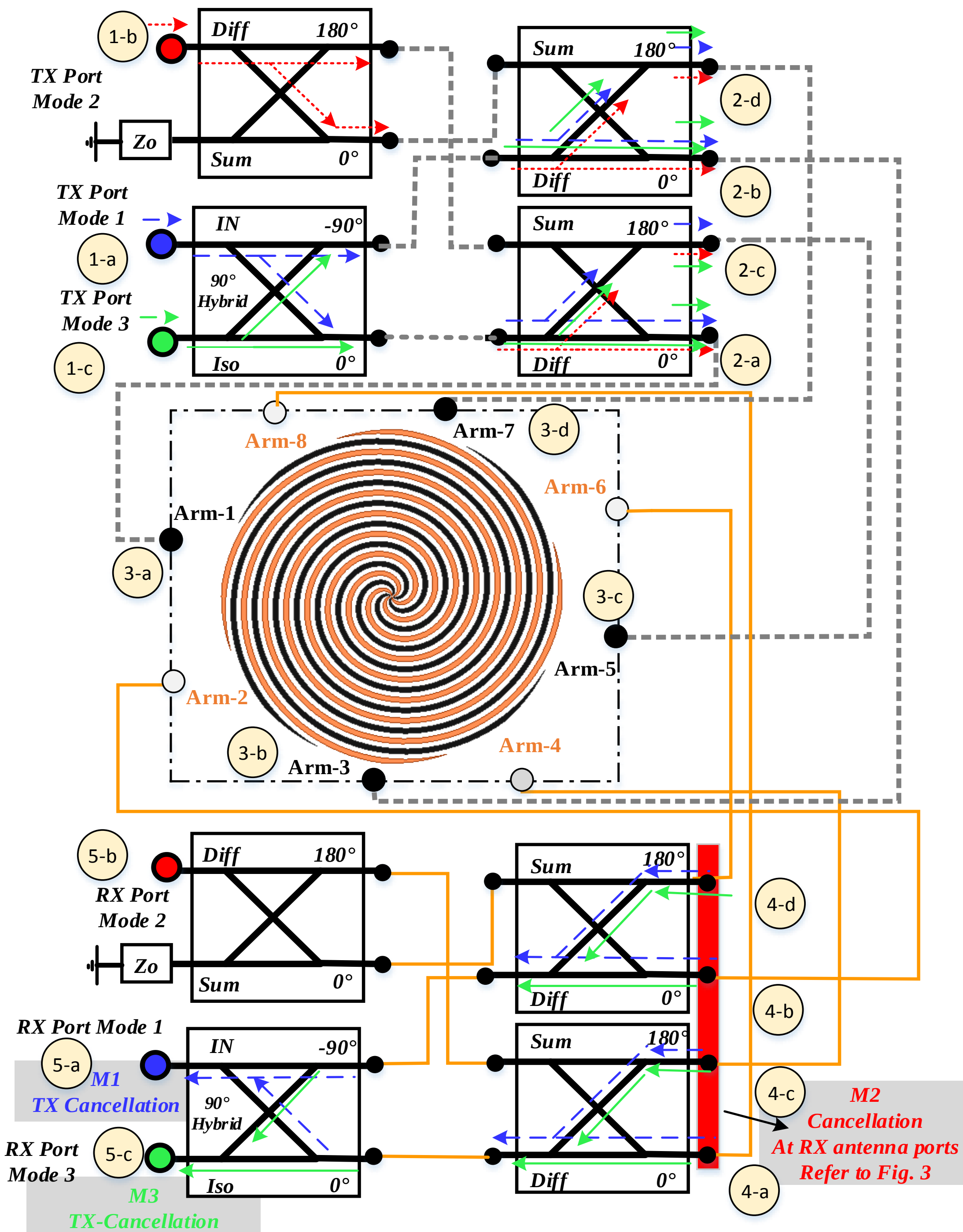

Figure 4.3: Realization of multimode C-STAR aperture with high isolation. The eight-arm spiral is connected to the TX and RX BFNs. The dark-colored arms represent TX spiral and light-colored arms represent RX spiral.

A. Mode 1 at TX/ modes 1 and 2 at RX: In this C-STAR configuration, mode 1 is transmitted and modes 1 and 2 are simultaneously received. The case of mode 1 at TX and RX is only considered to demonstrate the TX/RX SI cancellation mechanisms. To operate in TX mode 1, the TX BFN's port labeled as point 1-a in Fig. 4.3 is excited to produce four signals with the same magnitudes and $-90°$ phase progression (Fig. 4.3, points 2-a to 2-d and Table 4.1). The SI from TX to RX antenna ports can be computed using (4.1)-(4.3) to obtain (4.4). Hence, the TX antenna mismatched signals are phased as undesired modes (-1 or 3) and re-routed toward the TX quadrature hybrid's terminated port (Fig. 4.3, point 1-c). The SI TX signals are not fully canceled at the RX antenna ports, the reason being is that each of the two similar TX/RX adjacent or non-adjacent mutual coupling paths have phase difference of ($\pm j$) which prevents the full cancellation at the RX antenna ports, as shown in Fig. 4.4. Thus, the SI signals expressed in (4.a)-(4.d) are re-routed toward the RX-BFN at points 4-a to 4-d in Fig. 4.3. The RX-BFN then changes the phases of the TX SI signals, leading to full cancellation at the RX-BFN-port, as shown in (4.5). In theory, the sum of all TX/RX RF SI signals equals to "zero" assuming the TX/RX BFNs are ideal and the geometrical symmetry is maintained. Similar steps can be repeated for mode 1 at TX/ mode 2 at RX excitations.

Table 4.1: Excitation Coefficients of C-STAR 8-arm Spiral Excited with mode 1 at TX / modes 1 and 2 at RX.

Mode 1 TX	Mode 1 RX	Mode 2 RX
$a_1 = V_{TX}e^{-j0}$	$a_2 = V_{RX}e^{-j0}$	$a_2 = V_{RX}e^{-j0}$
$a_3 = V_{TX}e^{-j\pi/2}$	$a_4 = V_{RX}e^{-j\pi/2}$	$a_4 = V_{RX}e^{-j\pi}$
$a_5 = V_{TX}e^{-j\pi}$	$a_6 = V_{RX}e^{-j\pi}$	$a_6 = V_{RX}e^{-j0}$
$a_7 = V_{TX}e^{j\pi/2}$	$a_8 = V_{RX}e^{j\pi/2}$	$a_8 = V_{RX}e^{-j\pi}$

$$b_{RX,TX,2} = 0.5\{S_{21} - jS_{21} - S_{25} + jS_{25}\} \quad (4.4.a)$$

$$b_{RX,TX,4} = 0.5\{S_{25} - jS_{21} - S_{21} + jS_{25}\} \quad (4.4.b)$$

$$b_{RX,TX,6} = 0.5\{S_{25} - jS_{25} - S_{21} + jS_{21}\} \quad (4.4.c)$$

$$b_{RX,TX,8} = 0.5\{S_{21} - jS_{25} - S_{25} + jS_{21}\} \quad (4.4.d)$$

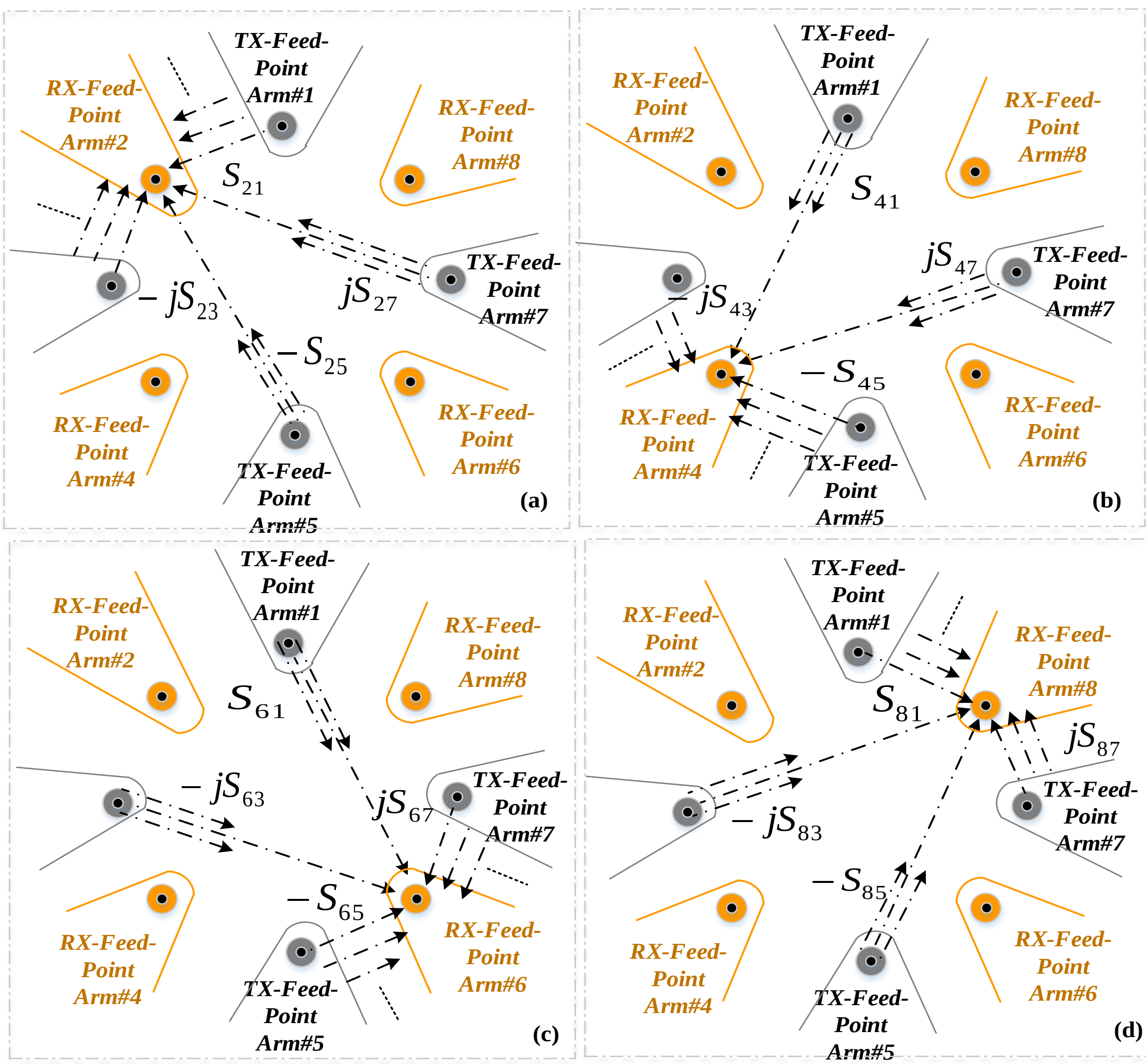

Figure 4.4: The SI from TX mode 1 to RX mode 1, as represented by the transmission coefficientsS_{ij}. Due to the provided phase difference of ±90°, the SI cancellation does not occur at the RX antenna ports.

The only difference is that the excitation coefficients listed in the third column in Table 4.1 are used to excite mode 2 at RX instead of the second column that excites mode 1 at RX.

$$SI_{RX,TX} = 0.25\{b_{RX,TX,2} - jb_{RX,TX,4} - b_{RX,TX,6} + jb_{RX,TX,8}\} = 0 \tag{4.5}$$

B. Mode 2 at TX/ modes 1, 2, and 3 at RX: In this C-STAR configuration, mode 2 is driven for the TX operation and modes 1, 2, and 3 are simultaneously used for RX. The complex excitation coefficients for the different TX and RX modes are shown in Table 4.2. To illustrate this mode of operation, only mode 2 at TX and RX case is considered. If the TX BFN's port labeled as point 1-b in Fig. 4.3 is excited, four signals with similar magnitudes and 180° phase progression are produced. Once all signals reach the 4-TX arms, mode 2 radiation is formed. The SIs from TX to RX arms can be computed as in (4.6.a)-(4.6.d) using (4.1)-(4.2). Due to the similar magnitude of the S-parameters between each adjacent and non-adjacent pair of TX arms and the 180° phase difference, all the coupled signals from the TX arms are canceled at the RX antenna's ports before entering the RX-BFN, as expressed in (4.6-a)-(4.6-d) and shown in Fig. 4.5. With this configuration, there are no TX/RX SI signals being routed to the RX-BFN since all are cancelled at the RX-antenna ports, assuming everything is ideal. Notice that the excited TX/RX mode 2 is unique among the excited TX/RX modes in its cancellation mechanism.

Table 4.2: Excitation Coefficients of C-STAR eight-arm Spiral Excited with mode 2 at TX / modes 1, 2 and 3 at RX.

Mode 2 TX	Mode 1 RX	Mode 2 RX	Mode 3 RX
$a_1 = V_{TX}e^{-j0}$	$a_2 = V_{RX}e^{-j0}$	$a_2 = V_{RX}e^{-j0}$	$a_2 = V_{RX}e^{-j0}$
$a_3 = V_{TX}e^{-j\pi}$	$a_4 = V_{RX}e^{-j\pi/2}$	$a_4 = V_{RX}e^{-j\pi}$	$a_4 = V_{RX}e^{j\pi/2}$
$a_5 = V_{TX}e^{-j0}$	$a_6 = V_{RX}e^{-j\pi}$	$a_6 = V_{RX}e^{-j0}$	$a_6 = V_{RX}e^{-j\pi}$
$a_7 = V_{TX}e^{-j\pi}$	$a_8 = V_{RX}e^{j\pi/2}$	$a_8 = V_{RX}e^{-j\pi}$	$a_8 = V_{RX}e^{-j\pi/2}$

$$b_{RX,TX,2} = 0.5\{S_{21} - S_{21} + S_{25} - S_{25}\} = 0 \quad (4.6.a)$$

$$b_{RX,TX,4} = 0.5\{S_{25} - S_{21} + S_{21} - S_{25}\} = 0 \quad (4.6.b)$$

$$b_{RX,TX,6} = 0.5\{S_{25} - S_{25} + S_{21} - S_{21}\} = 0 \quad (4.6.c)$$

$$b_{RX,TX,8} = 0.5\{S_{21} - S_{25} + S_{25} - S_{21}\} = 0 \quad (4.6.d)$$

In reality, there is an impedance mismatch between the realistic TX BFN components and the TX four arms, and therefore some reflected TX antenna mismatched signals are phased as undesired modes (-2) and re-routed toward the TX 180° hybrid's excited port (Fig. 4.3, point 1-b). Similar steps can be repeated for other excitations from Fig. 4.3. The only difference is that the excitation coefficients listed in the second and fourth columns in Table 4.2 are used to excite modes 1 or 3 instead of 2 at RX.

C. Mode 3 at TX/ modes 2 and 3 at RX: In this C-STAR configuration, mode 3 is excited for TX operation and modes 2 and 3 are simultaneously received. Similar analysis to mode 1 at TX/ modes 1 and 2 at RX can be repeated, but using the excitation coefficients that are shown in Table 4.3 instead of Table 4.1.

Table 4.3: Excitation Coefficients of C-STAR eight-arm Spiral Excited with mode 3 at TX / modes 2 and 3 at RX.

Mode 3 TX	Mode 2 RX	Mode 3 RX
$a_1 = V_{TX}e^{-j0}$	$a_2 = V_{RX}e^{-j0}$	$a_2 = V_{RX}e^{-j0}$
$a_3 = V_{TX}e^{j\pi/2}$	$a_4 = V_{RX}e^{-j\pi}$	$a_4 = V_{RX}e^{j\pi/2}$
$a_5 = V_{TX}e^{-j\pi}$	$a_6 = V_{RX}e^{-j0}$	$a_6 = V_{RX}e^{-j\pi}$
$a_7 = V_{TX}e^{-j\pi/2}$	$a_8 = V_{RX}e^{-j\pi}$	$a_8 = V_{RX}e^{-j\pi/2}$

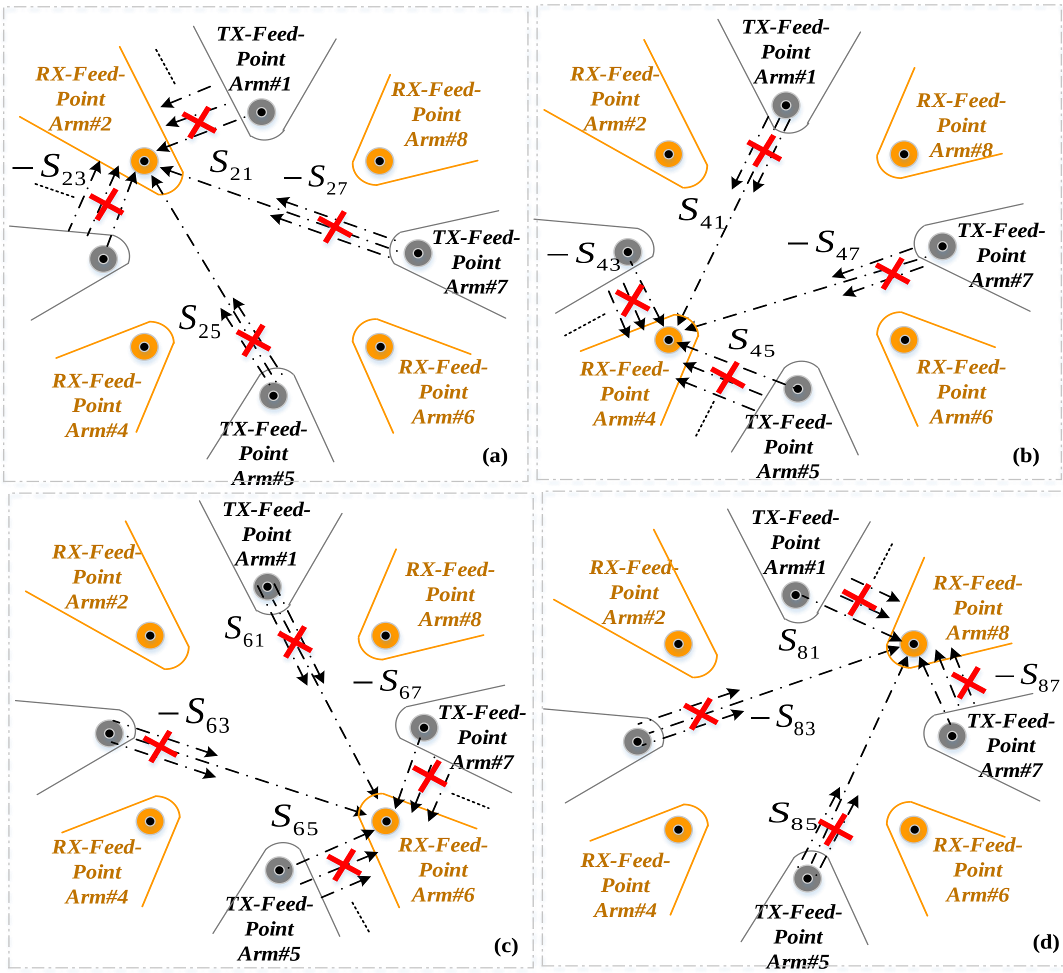

Figure 4.5: The SI from TX to RX mode 2, as represented by the transmission coefficients S_{ij}. The cancellation occurs at the RX antenna ports.

4.3 Computational Analysis

To validate the discussed SI cancellation concept, the eight-arm spiral is modeled in the finite element method (FEM) solver ANSYS HFSS [115]. The two-turn Archimedean spiral antenna has 20.3 cm diameter and metal to slot ratio (MSR) of 3.3:1. Ideal TX and RX BFN are used in the AWR circuit simulator schematic, as shown in Fig. 4.3. To find the total TX/RX isolation between the different mode combinations using the proposed configuration, the obtained S-parameters from HFSS are imported in the circuit simulator. As seen in Fig. 4.6, the isolation between the different excited modes is found to be >60 dB, which confirms the proposed concept. Notice that about >40 dB improvement is achieved with the multimode C-STAR configuration compared to the isolation between the TX and RX arms/ports which is between 10-20 dB. In absence of the BFNs' imbalances, the isolation is limited by the computational resources and mesh quality/symmetry of the modeled spiral. Practically, under the influence of the realistic circuit components' imbalances, the isolation degrades because the SI weights become asymmetric and the total SI accounting for all TX and RX BFN's imbalances is then finite. To estimate the isolation variations, the amplitude and phase imbalances for the BFN are varied for the amplitude and phase imbalances in the circuit simulator within 0-0.6 dB and 0-8°, respectively, which is chosen based on the specifications of commercial off-the-shelf (COTS) BFN components. The last trace in Fig. 4.6 shows the worst-case effect of these imbalances over frequency. As seen, the isolation drops from >60 dB to 28-32 dB, indicating the importance of the BFN to achieve high isolation.

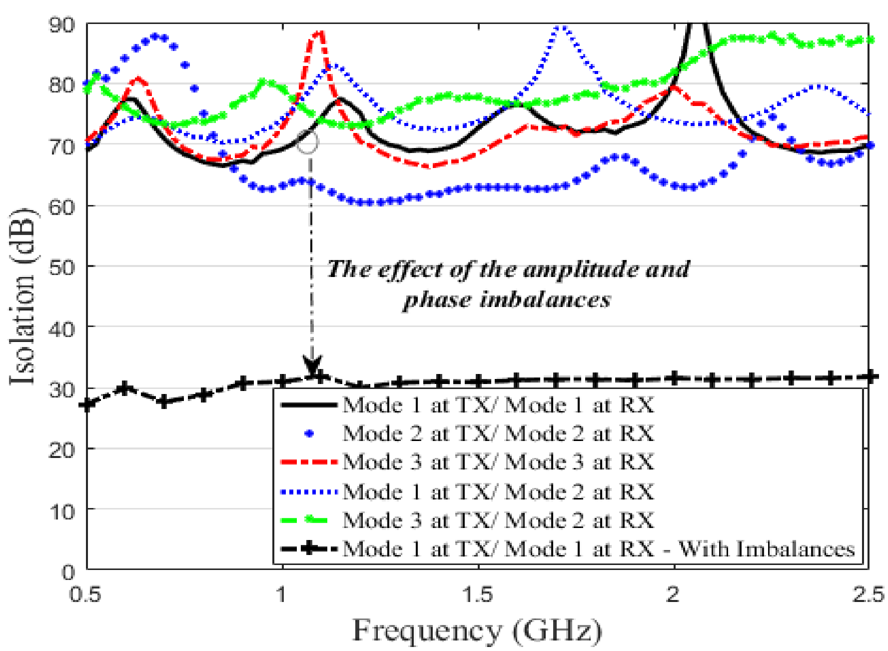

Figure 4.6: Simulated TX/RX isolation of an eight-arm spiral connected to the ideal TX/RX BFN and excited with different modes. The worst case impact of the BFN imbalances on the mode 1 TX/RX isolation is also shown.

4.4 Design, Fabrication, and Performance

To experimentally validate the theory, simulation results, and practical limitations of the proposed C-STAR concept, a non-self-complementary two-turn eight-arm Archimedean slot spiral antenna is fabricated as shown in Fig. 4.7. The spiral has outer and inner diameter of 20.3 cm and 0.6 cm; respectively, and it is fabricated on a 0.15 cm-thick Rogers TLY-5 substrate with ε_r and $tan\,\delta$ of 2.2 and 0.0009, respectively. A 50 Ω coaxial bundle composed of eight 0.2 cm diameter semi-rigid cables is assembled such that the inner conductors are soldered directly to the TX and RX arms. A spacer ring with radius 2 cm made of a 0.15 cm thick Rogers TLY-5 substrate is placed between the coaxial bundle feed-end and spiral to prevent any shorting. To achieve good impedance match over the operational bandwidth, the spiral's MSR is increased to 3.3:1 and each arm is terminated with two lumped resistors with values of 100 Ω and 300 Ω. The spiral antenna is cavity backed to allow flush mounting and is loaded with a dielectric lens. The lens has a hyper-hemispherical shape which is determined based on the previous numerical studies in [116] where better performance was obtained by using lens with higher permittivity and matched layers. However, the true optimization of the dielectric lens is part of the future work, and the desired effects can be demonstrated with a Rexolite lens with parameters $\varepsilon_r = 2.53$ and $tan\,\delta = 0.0005$. The diameter of the lens is 20.3 cm. Notice that the lens-loading is used to reduce the negative impact on the far-field due to the radiation from parasitic arms and cavity backing. Dielectric lens also has a positive impact on radiation efficiency since more radiation is directed upwards.

The simulated and measured active match of the eight-arm spiral excited with different phase modes is shown in Fig. 4.8. Active VSWR<2 over most of the designated operational bandwidth for each mode is obtained. Overall, good agreement is obtained between the simulated and measured results. Once the antenna is connected to the realistic BFNs, further improvement is observed for modes 1 and 3, but not mode 2. The improvement in VSWR performance for mode 1 and 3 is due to re-routing some of the antenna mismatched signals as undesired phase modes toward the quadrature hybrid's terminated port.

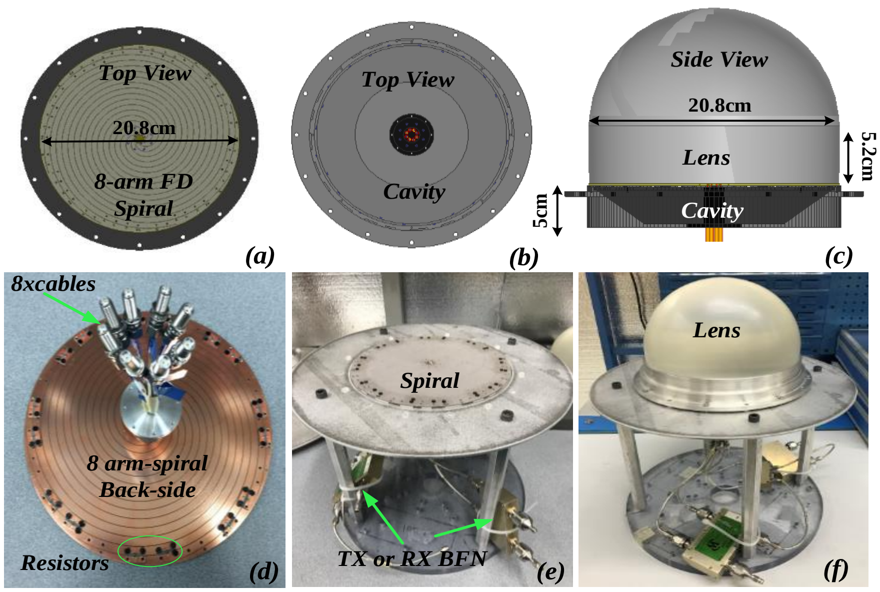

Figure 4.7: Geometrical details of the (a)-(c) simulated and (d)-(f) fabricated cavity-backed lens-loaded slot spiral antenna with resistive termination and bundle.

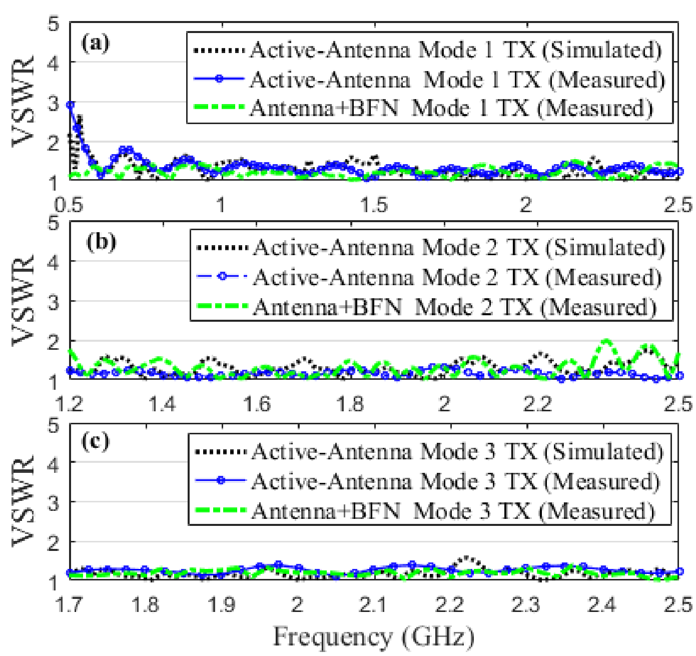

Figure 4.8: Simulated and measured VSWR at the input of the TX antenna without lens and BFN for different modes: (a) mode 1, (b) mode 2, and (c) mode 3.

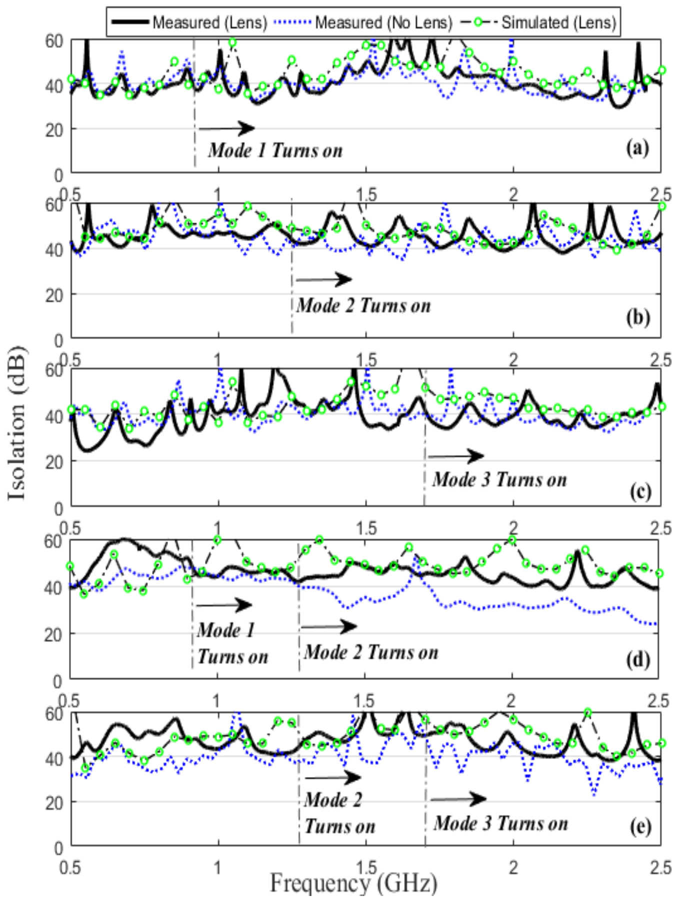

Figure 4.9: Data include simulated antenna with realistic BFN and lens; measured antenna-realistic BFN with and without lens. TX/RX isolation for (a) mode 1, (b) mode 2, and (c) mode 3. (d) TX mode 1/RX mode 2, and (e) TX mode 3/RX mode 2.

The isolation results of eight-arm C-STAR spiral excited with various TX and RX modes are shown in Fig. 4.9. The simulated antenna with the realistic BFN and lens loading, and measured antenna with and without lens-loading connected to realistic BFN are all plotted. The figure shows that the average measured isolation is approximately 38 dB for all different excited modes once they turn on. The lens loading slightly improves the measured isolation at certain frequency bands due to improved radiation of the induced surface current on the RX arms before getting re-routed toward to the RX-BFN. To highlight the impact of the realistic BFN imbalances, the ideal hybrids are replaced with measured COTS hybrids in the AWR circuit model and connected to the simulated eight-arm C-STAR spiral. As seen from

Fig. 4.9, the obtained isolation of the ideal system degrades to the range of the measured isolation of the fabricated antenna once connected to the realistic BFN and that is mainly due to the realistic hybrids' imbalances. Also, any bundle or spiral antenna fabrication imperfections would further degrade the system isolation as shown in Fig. 4.9.

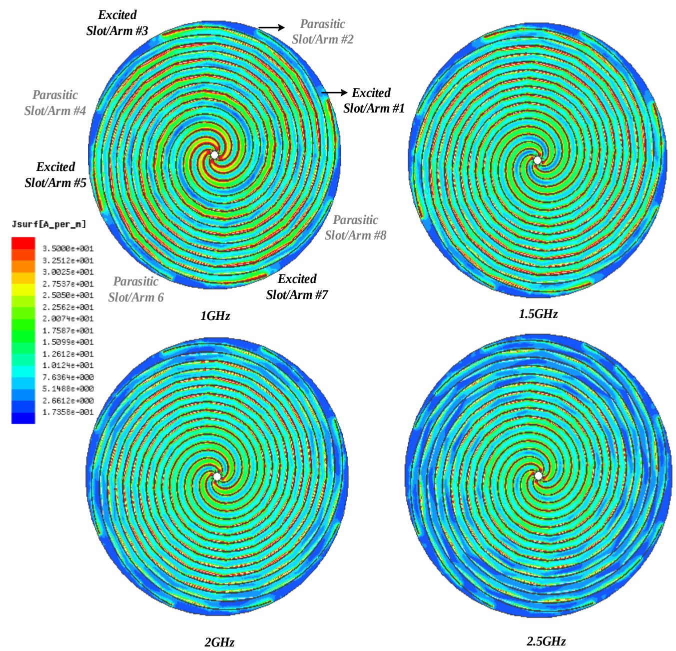

Figure 4.10: Simulated surface currents of the resistively-terminated eight-arm C-STAR spiral antenna with TX arms excited with mode 1 (active) and the other four arms not excited (parasitic).

Due to the near-field coupling between the co-located TX/RX spirals, currents are induced on the RX spiral arms when the TX arms are excited, as shown in Fig. 4.10. Therefore, the RX arms can be viewed as parasitic elements for the TX spiral. These induced surface currents excite the undesired higher order modes of the eight-arm spiral antenna, leading to degraded far-field performance [81]. To determine these induced higher order modes and their impact, the far-field of multi-arm spiral is decomposed into its constituent phase modes by applying Fourier series decomposition [81],[117]-[118]. The following analysis is performed for a mode 1 excitation, but other modes can be similarly analyzed. First, the far-field is exported from the simulated conventional four-arm spiral and the C-STAR eight-arm spiral antenna where four arms are excited (e.g. TX-arms) and the other four arms are terminated (RX-arms). Then, each far-field pattern is decomposed into its constituent phase modes at $\theta = 30°$, as shown in Fig. 4.11.

For an eight-arm C-STAR spiral, the cross-polarized mode -3 radiates more strongly than in conventional four-arm spiral once the spiral is electrically large enough. Note that mode -3 exists due to the radiation of mode 1's residual and reflected surface currents. The radiation of mode -3 can have a negative impact on the far-field performance, such as reduced boresight radiation (drop in gain for mode 1 above 1.5 GHz), deteriorated axial ratio at higher elevation angles above 1.5 GHz, and reduced efficiency at lower frequencies when resistive terminations are introduced. Increasing the size of the spiral or resistively terminating it may help improve the performance, with drawbacks of increased size and reduced efficiency, respectively.

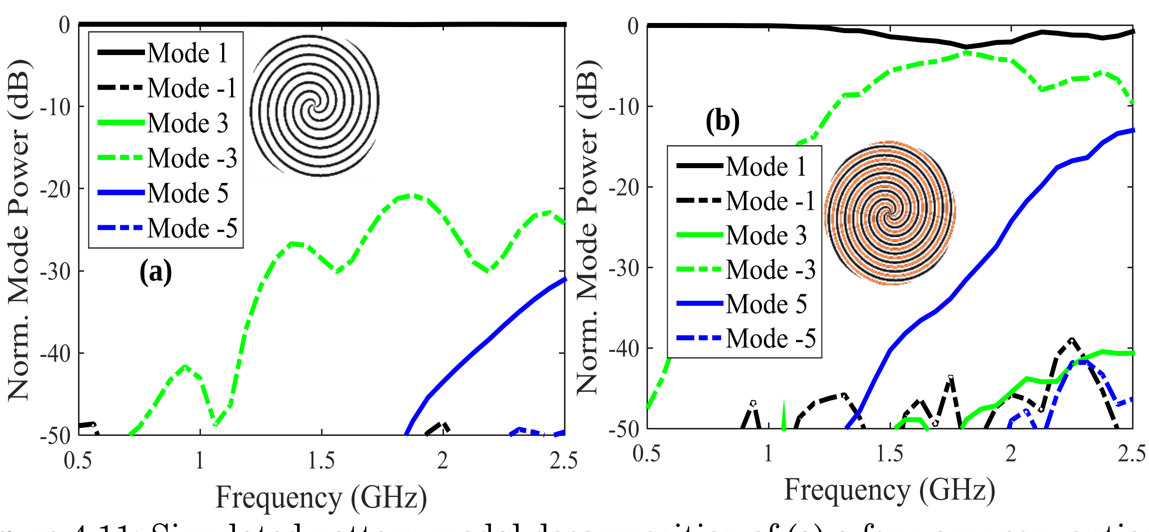

Figure 4.11: Simulated pattern modal decomposition of (a) a four-arm conventional 8" spiral antenna without parasitic arms at $\theta = 30°$ and (b) an eight-arm C-STAR spiral with four arms active (excited) and four arms parasitic (terminated).

The measured co-polarized broadside mode 1 realized gain of the four-arm TX spiral antenna without lens is shown in Fig. 4.12. As mentioned previously, the parasitic arms (RX arms) can effectively radiate higher order modes, leading to a drop in gain at boresight. Therefore, to improve the realized gain for mode 1, the spiral antenna is loaded by a hyper-hemispherical lens as shown in Fig. 4.7(f). It can be seen from Fig. 4.12 that the realized gain of mode 1 improves at higher frequencies once the lens loading is introduced. However, there is no much gain improvement below 1 GHz due to the size of the lens and the resistive termination. The simulated and measured realized gain of modes 2 and 3 at $\theta = 35°$ and 43°, respectively, are also shown in Fig. 4.10. From the far-field performance, the operational bandwidth for mode 1 is from ~0.8-2.5 GHz, mode 2 is from 1.2-2.5 GHz, and mode 3 is from ~1.7-2.4 GHz. Note that the high frequency of operation is limited by the COTS BFN and can be extended if a wider bandwidth BFN is used. The average simulated (and measured as gain/directivity) radiation efficiency of the TX and RX antennas is 40% (40%) from 0.8-1.8 GHz and 65% (62%) from 1.8-2.5 GHz.

The measured axial ratio of the eight-arm spiral with and without the lens dielectric loading is shown in Fig. 4.13. As seen, mode 1 has an axial ratio <1.5 dB at boresight while modes 2 and 3 have an average axial ratios of around 5 dB at $\theta = 35°$ and 43°, respectively. To improve the circular polarization purity of modes 2 and 3, a third resistor to each arm-end is required to reduce the negative impact of the undesired higher order modes (-2 and -1) induced due to cavity and parasitic arms. However, this additional resistor reduces the radiation efficiency of mode 1. The simulated and measured four-arm TX mode 1 co- (RHCP) and cross-polarized (LHCP) radiation patterns are shown in Fig. 4.14. Samples of modes 2 and 3 co- (RHCP) and cross-polarized (LHCP) patterns are also shown in Fig. 4.14 at different azimuthal cuts ($\phi = 0°, 45°$, and 90°).

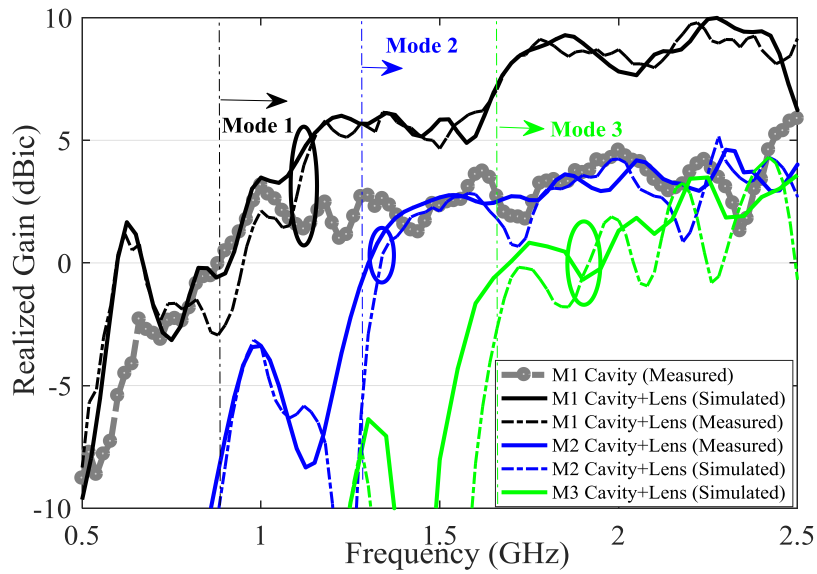

Figure 4.12: Simulated and measured co-polarized realized gain of the eight-arm (four-TX) C-STAR spiral antennas with and without the lens loading for mode 1, as well as with lens for modes 2 and 3.

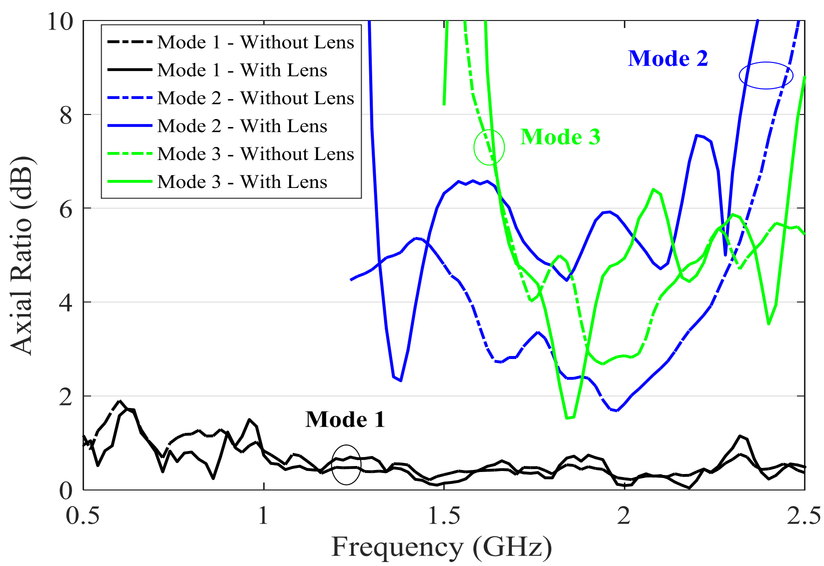

Figure 4.13: Measured axial ratio of the eight-arm (4-TX) C-STAR spiral antenna (with and without lens) that is excited with modes 1, 2, and 3.

4.5 Envelope Correlation Coefficient (ECC)

A true C-STAR single aperture ideally has identical TX and RX radiation patterns. In the proposed configuration, the RX spiral arms are rotated by 45° with respect to the TX spiral arms where the two sets of patterns in ideal conditions, are replica of each other with the same azimuthal shift. At higher frequencies, the higher order modes are more noteworthy and pattern changes at higher angles may become significant. Thus, the similarity between the TX and RX radiation patterns will degrade. To quantify the degree of similarity between the TX and RX patterns, ECC is used. To calculate ECC, two sets of independent TX and RX far-field simulations or measurements are needed. In each simulations or measurements set, the four-arm (TX for example) are excited while the four-arm (RX) are terminated with matched loads, and an opposite set-up for the other set. ECC is then calculated.

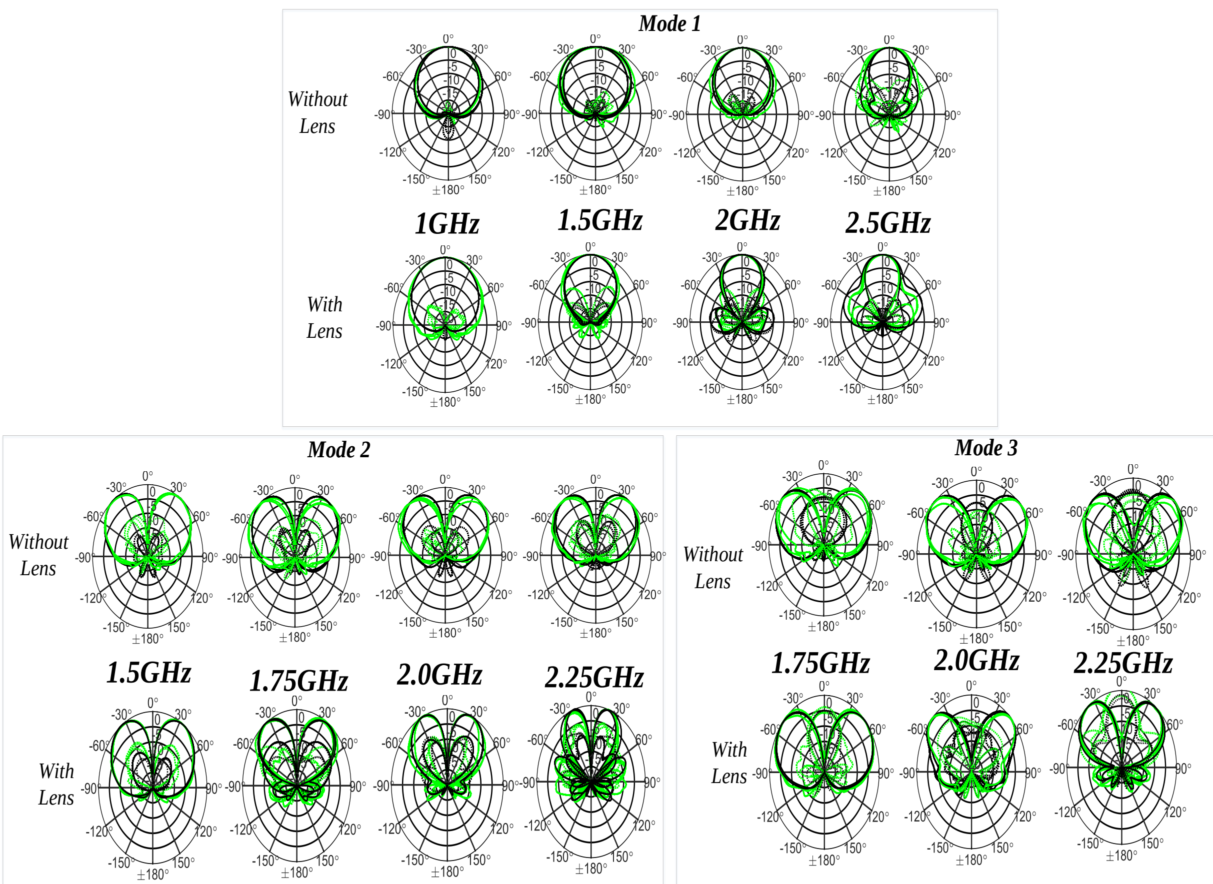

Figure 4.14: Simulated (black) and measured (green) normalized co- (solid) and cross-polarized (dotted) modes 1, 2, and 3 TX radiation patterns over ($\phi = 0°, 45°$, and $90°$).

The results for the ECC of mode 1 at TX and RX are shown in the Fig. 4.15. As seen, as the frequency and elevation angle increase, the measured ECC starts to deteriorate due to the radiation of the undesired higher order modes and the 45° RX arms rotation. In particular, modes -3 and 5 start to radiate, which causes an expected deviation between the TX and RX radiation patterns specifically at higher elevation angles. The ECCs for the excited TX/RX (same mode) modes 2 and 3 are also shown in Fig. 4.16.a and 4.16.b. Good pattern agreement is obtained when the TX and RX sides are excited with similar TX/RX modes 2 and 3. Once mode-multiplexing between the TX and RX sides is considered, ECC decreases below the full turn-on frequency of each mode due to internal reflections while ECC remains > 0.68 at the higher frequencies, Fig. 4.16.c. All measured ECCs of the TX and RX radiation patterns are taken between azimuthal cuts of ($\phi = 0 - 180°$) and within different ranges of elevation angles.

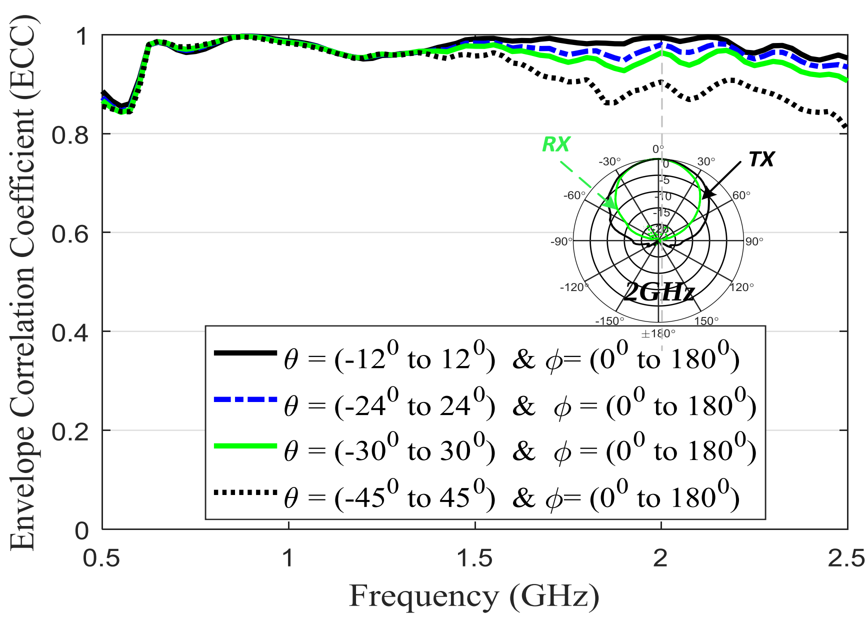

Figure 4.15: Measured ECC of an eight-arm C-STAR spiral antenna excited with mode 1 at both TX and RX at different elevation angles. The inset shows the radiation patterns of the excited mode 1 at TX (black color) and RX (green color).

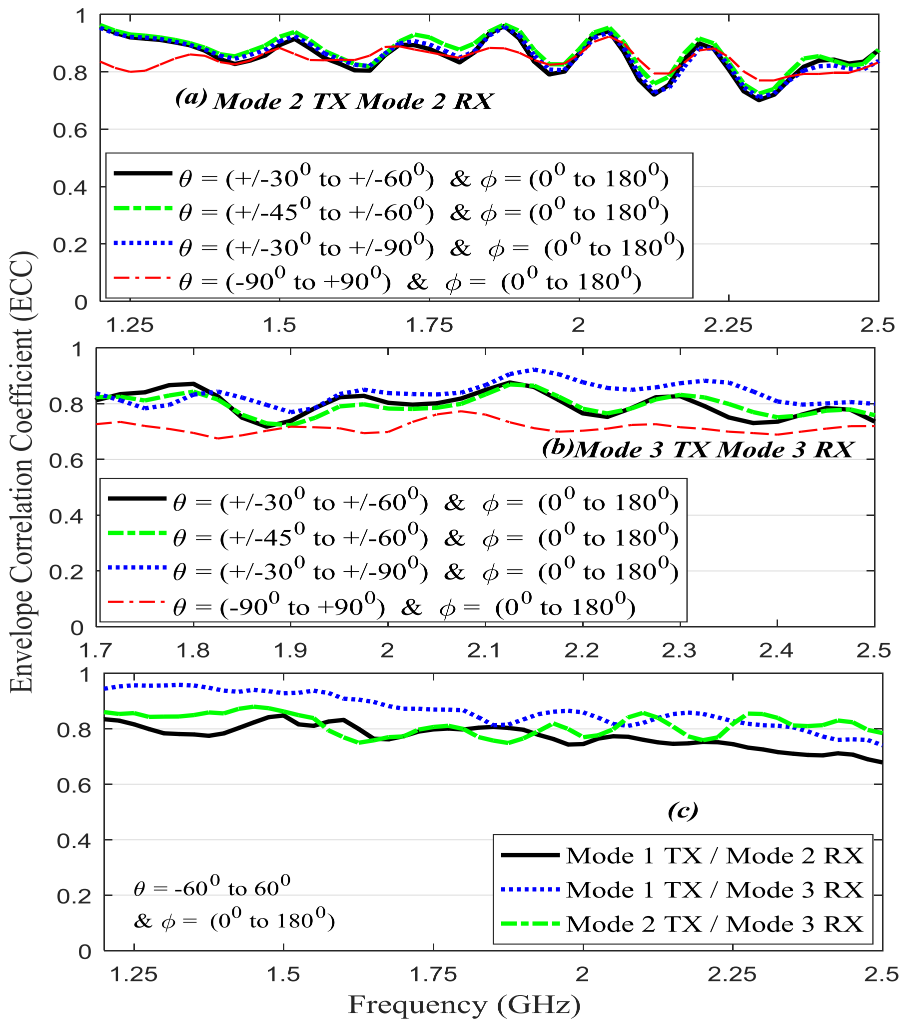

Figure 4.16: Measured ECC of an eight-arm C-STAR spiral antenna at different elevation angles. (a-b) show ECC for similarly excited TX and RX modes 2 and 3; respectively, while (c) shows ECC for different excited TX and RX modes over their operational frequencies.

4.6 Summary

A lens-loaded eight-arm spiral antenna with diverse co-polarized mode patterns is introduced for C-STAR applications [117]-[118]. The proposed C-STAR shared antenna has two interleaved sets of 4-TX and 4-RX arms that are connected to two 4×4 Butler matrix BFNs. In the absence of any BFN imbalances and antenna geometry asymmetries, the proposed concept can achieve theoretically infinite TX/RX isolation between various TX/RX modes. Computational and experimental studies are presented to address the coupling from TX to RX arms which is not really suppressed, but rather re-radiated and re-routed to the BFN or canceled. Therefore, reduction in efficiency and far-field deterioration are the cost of achieving a, multimode, C-STAR antenna sub-system. As has been shown, the average measured TX/RX isolation over the operating modes' bandwidths is >38 dB. A comparison between the proposed multi-arm spiral sub-systems in Chapters 2-4 with respect to isolation, size, complexity, and far-field performance is presented in Table 4.4. In summary, this chapter has outlined some interesting features and capabilities of multimode spiral antennas of interest for the "true" C-STAR systems with maximum resource (frequency, time, space, polarization, beam, etc.) utilization. Modal diversity with inherently high and wideband antenna element isolation may pave the way for new uses in various commercial and defense applications.

Table 4.4: Comparison between the Proposed Three Multi-Arm Spiral Sub-systems in Chapters 2-4

C-STAR Approach	*Size / Compl-exity*	*Isolation (Simulated / Average Measured)*	*BW*	*Far-Field (Eff.)*	*Far-Field (Axial Ratio)*	*Far-Field (ECC)*	*Dual-Polarization and Multi-Mode Capability*
4-Arm Spiral (Ch.2)	*Dimeter =203 mm / Low*	*Infinite / >50 dB*	*>5:1*	*- Low (30-50% <2:1 BW) - High (50-90% >2:1 BW)*	*- Low (30-50% <2:1 BW) - High (50-90% >2:1 BW)*	*- High (>90% <3:1 BW) - Moderate (70-90% >3:1 BW)*	*NO*
4-Arm Spiral 4-Ciruator BFN (Ch.3)	*Dimeter =140 mm / High*	*Infinite / >28 dB*	*>4:1*	*High (90-100%)*	*Excellent <3 dB for mode 1*	*Excellent ~100%*	*Yes*
8-Arm Spiral BFN (Ch.4)	*Dimeter =203 mm*	*Infinite / >30 dB*	*>4:1*	*- Low (30-50% <2:1 BW)*	*Excellent <3 dB for mode 1*	*Good 80-100% For mode 1*	*Yes*

	/ Moder ate			*- High (50-80% >2:1 BW)*			

CHAPTER 5

WIDEBAND MULTIMODE CO-POLARIZED MONOSTATIC OMNIDIRECTIONAL C-STAR ANTENNA ARRAYS

5.1 Overview

Circular antenna arrays are attractive for the azimuthal, omnidirectional radiation pattern coverage, which is desired for many applications including base stations, repeaters, ship-borne communications, radars, direction finding, and jamming [119]-[122]. Typically, circular antenna arrays operate in half-duplex or out-of-band full-duplex modes to isolate the TX and RX paths; therefore consuming at least twice the time or frequency resources. By incorporating C-STAR capability to the circular antenna array systems, it is possible to theoretically double the channel throughput, simplify spectrum management, efficiently re/use the existing commercial radio spectrum, simultaneously perform electronic attack and support, and, most importantly, avoid time or frequency duplexing [123]-[126]. Yet, C-STAR systems have not been widely implemented in circular arrays due to strong SI. To overcome SI issues, the C-STAR systems are typically sub-divided into several stages of cancellation; antenna, analog, and digital layers as shown in Fig. 5.1.

Several C-STAR circular antenna arrays have been proposed for suppression of SI, as mentioned in Chapter 1. The most common approaches assign some antenna elements from the circular array as TX and the remaining as RX, in addition to physical separation, near-field cancellation, polarization-multiplexing, nulling placement, beam-multiplexing, or beamforming techniques. Measured isolation varying from 30 dB to 55 dB is demonstrated with one or more drawbacks between narrow bandwidth, large number of TX or RX antenna elements, radiation patterns and polarization dissimilarity between TX and RX, and system efficiency.

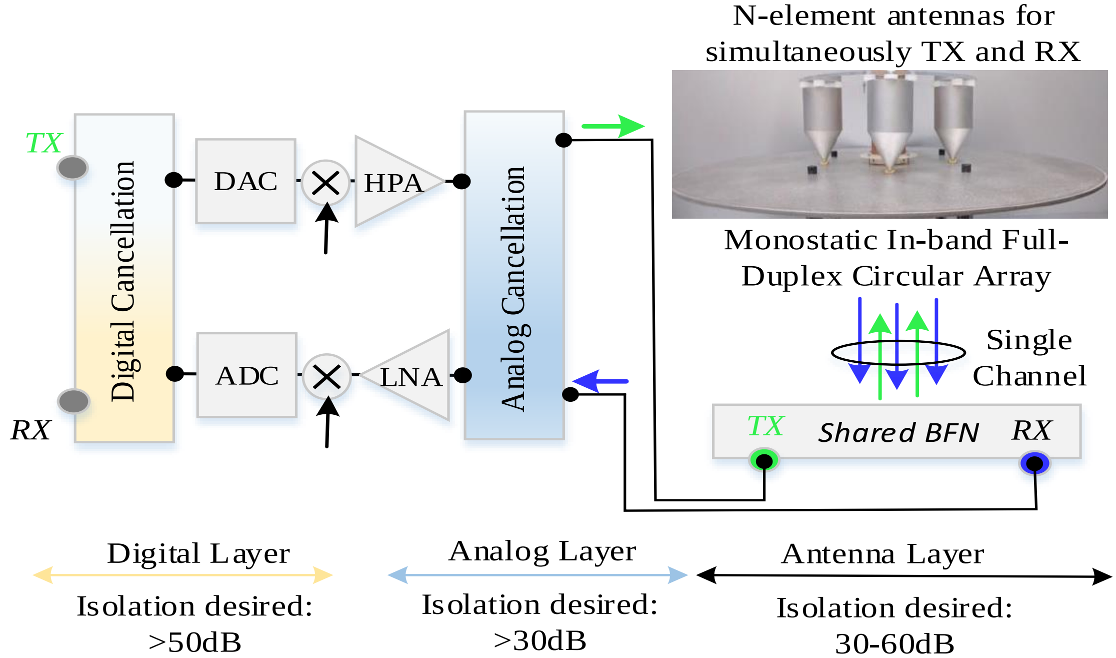

Figure 5.1: Way of achieving C-STAR operation with a monostatic circular array and multiple cancellations layers.

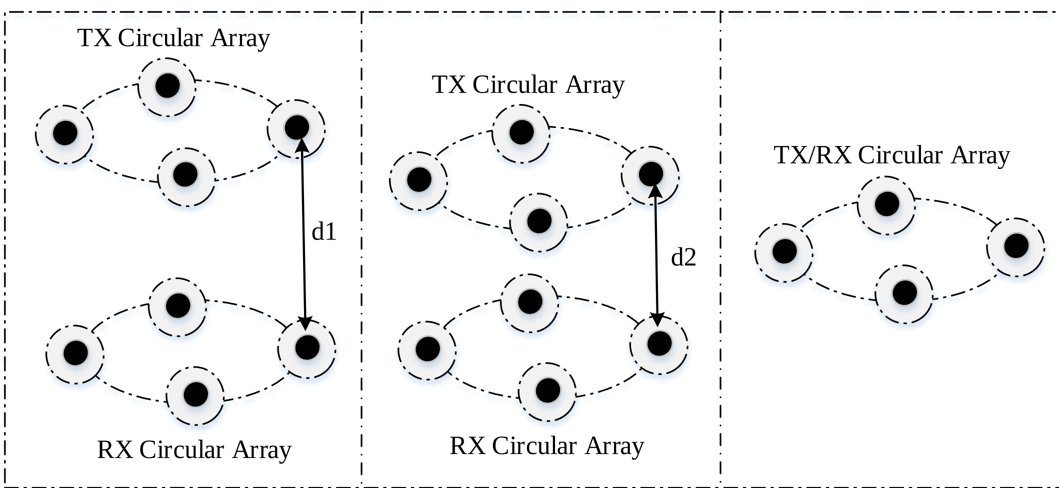

Figure 5.2: C-STAR omnidirectional circular arrays; (left) separation-dependent C-STAR array, (middle) separation-independent C-STAR array d2<<d1, and (right) separation-dependent C-STAR array.

In this chapter, several wideband C-STAR circular array configurations are considered to handle the space limitation and efficient use of wireless spectrum. Starting with the separation-dependent bi-static configuration, separation-independent bi-static configuration, and finally the monostatic single and dual-layer C-STAR configuration, as seen in Fig. 5.2. The organization of this chapter is as follows:

- Section 5.2 discusses a separation independent dual-layer circular discone antenna C-STAR array.
- Section 5.3 discusses monostatic C-STAR arrays.
- Section 5.4 summaries this chapter.

5.2 Dual-layer Separation-Independent C-STAR Array

5.2.1 Overview

In this configuration, a wideband C-STAR dual-layer circular array is considered to handle the space limitation and efficient use of wireless spectrum. The proposed STAR aperture configuration is composed of upper and lower-layer circular arrays, where one works as TX and the other as RX antenna. Each array consists of four wideband antennas that are equally spaced on the circumference of a circle. As the C-STAR approach is antenna independent, different antenna types can utilize it. The proposed STAR array utilizes both mode diversity and BFN SI cancellation techniques to achieve theoretically infinite isolation over a wide operational bandwidth without any time, frequency, or polarization duplexing. A theoretical study is discussed under both ideal conditions and the presence of circuit components' non-idealities; the feasibility thereof to significantly mitigate the SI is shown computationally and experimentally. Simulated isolation higher than 74 dB and measured between 28 and 50dB is obtained over more than 2:1 bandwidth while still maintaining nearly identical TX/RX radiation patterns.

5.2.2 Operational Principles

The proposed C-STAR configuration utilizes two circular arrays each composed of four discone antennas as shown in Fig. 5.3. One layer is used for TX and other for RX. The system exploits the multi-mode characteristic of a four-element circular array along with the utilized BFN operational principles to achieve high SI cancellation.

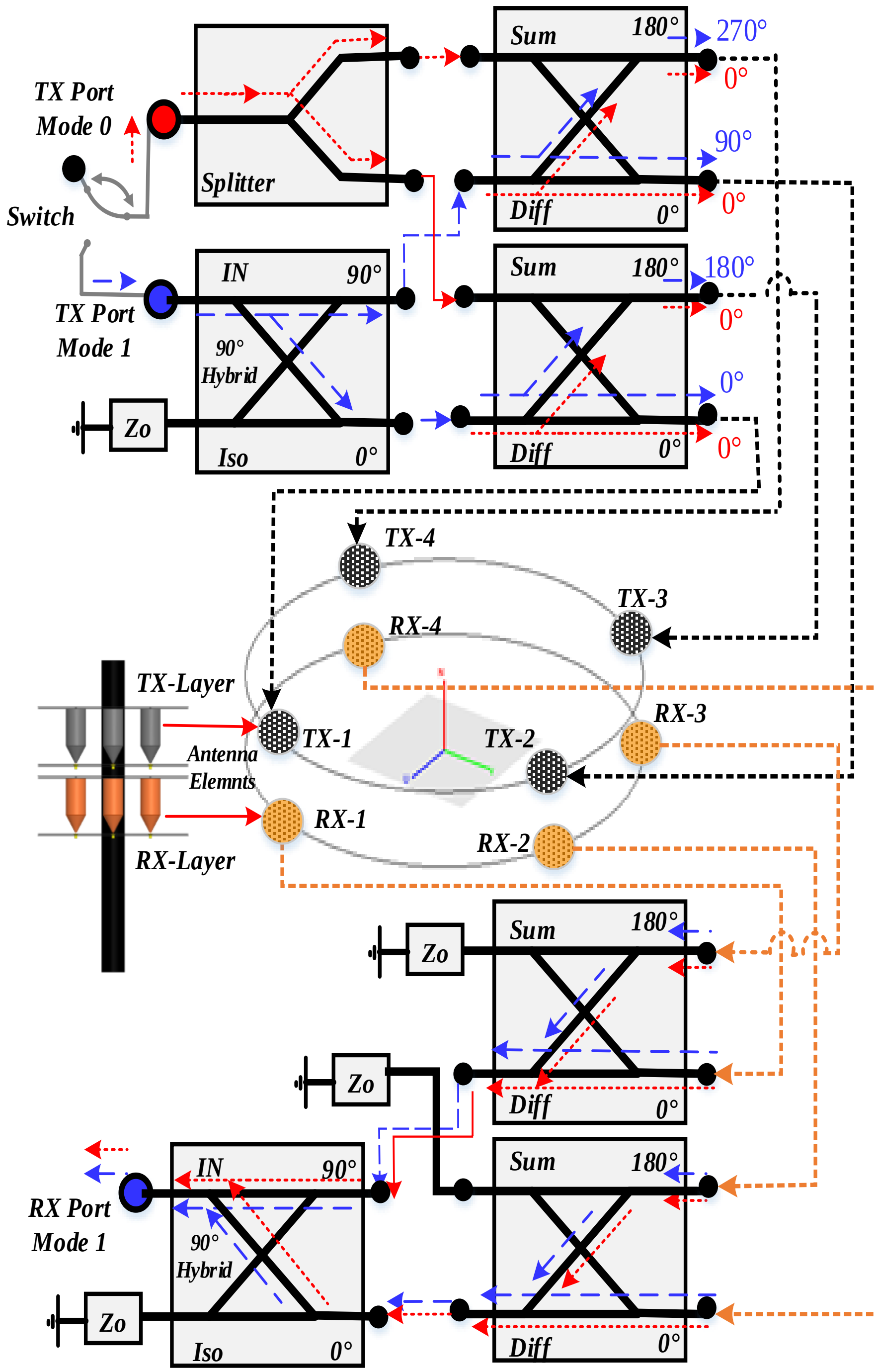

Figure 5.3: Illustration of the proposed dual-mode C-STAR phased-array system, including a signal-flow diagram.

Two excitation arrangements are considered in the first configuration; both the TX/RX arrays are excited in a circular mode 1. In the second topology, the TX array is excited in mode 0 while the RX array is excited in mode 1. The mode 1/mode 1 excitation arrangement provides ideally identical TX/RX radiation characteristics (similar to that of a monostatic system), better match, and improved isolation sensitivity; whereas the mode 1/mode 0 excitation arrangement (which also works vice versa) has a simpler RX's BFN and excellent omnidirectional characteristics over wider bandwidth. Having a 90° phase difference between the TX/RX layers, could slightly improve the sensitivity of the isolation with respect to the system's imbalances. Both proposed configurations with depicted SI cancellation flow diagrams are shown in Fig. 5.3. For better understanding and demonstration, the operational principles for each configuration will be considered separately:

A. TX-Mode 1/RX-Mode 1 Excitation Arrangement: High isolation is obtained in this arrangement by exploiting the signal flow in the BFNs as shown in Fig. 5.3. When the TX upper layer is excited in mode 1, each of the incident signals reach the TX elements, enabling mode 1 omnidirectional radiation; whereas the mismatched signals are re-routed to the input at the TX/RX BFN's 90° hybrids' terminated ports. Also, coupling from the TX upper layer (odd numbered elements: 1, 3, 5, and 7) to the RX bottom (even numbered elements: 2, 4, 6, and 8) layer starts to occurs as,

$$b_{RX,TX,i} = 0.5\{S_{i1}a_1 + S_{i3}a_3 + S_{i5}a_5 + S_{i7}a_7\} \tag{5.1}$$

Where $b_{RX,TX,i}$ is the total TX/RX SI at each port of the RX antennas, i is the coupling number (i =1 to 4) from the TX elements to each individual RX element, and (a_j) are the excitation coefficients of the operated TX elements in mode 1. Due to the inherent symmetry of the single layer array elements, the ideal transmission coefficients between the adjacent and non-adjacent arms are related as in (5.2.a)-(5.2.c).

$$S_{41} = S_{81} = S_{23} = S_{63} = S_{45} = S_{85} = S_{67} = S_{27} \tag{5.2.a}$$

$$S_{21} = S_{43} = S_{65} = S_{87} \quad (5.2.b)$$

$$S_{61} = S_{83} = S_{25} = S_{47} \quad (5.2.c)$$

All the coupled signals that are induced on the RX's four arms/ports (5.1) are re-routed toward the RX-BFN's port. By substituting (5.2) in (5.1), the total TX/RX SI can be then easily computed

$$b_{RX,TX,1} = 0.5\{S_{21}a_1 + S_{41}a_3 + S_{61}a_5 + S_{41}a_7\} \quad (5.3.a)$$

$$b_{RX,TX,2} = 0.5\{S_{41}a_1 + S_{21}a_3 + S_{41}a_5 + S_{61}a_7\} \quad (5.3.b)$$

$$b_{RX,TX,3} = 0.5\{S_{61}a_1 + S_{41}a_3 + S_{21}a_5 + S_{41}a_7\} \quad (5.3.c)$$

$$b_{RX,TX,4} = 0.5\{S_{41}a_1 + S_{61}a_3 + S_{41}a_5 + S_{21}a_7\} \quad (5.3.d)$$

For mode 1 excitations, (5.3) becomes

$$b_{RX,TX,1} = 0.5\{S_{21} - jS_{41} - S_{61} + jS_{41}\} \quad (5.4.a)$$

$$b_{RX,TX,2} = 0.5\{S_{41} - jS_{21} - S_{41} + jS_{61}\} \quad (5.4.b)$$

$$b_{RX,TX,3} = 0.5\{S_{61} - jS_{41} - S_{21} + jS_{41}\} \quad (5.4.c)$$

$$b_{RX,TX,4} = 0.5\{S_{41} - jS_{61} - S_{41} + jS_{21}\} \quad (5.4.d)$$

Due to the symmetry and the partial cancellation at the RX antenna ports, as shown in Fig. 5.4, Then (5.4) can be further simplified as (5.5).

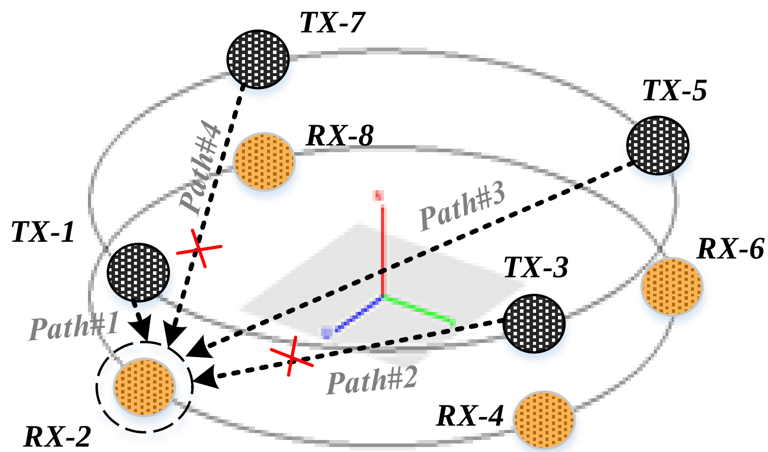

Figure 5.4: Signal flow diagram of the TX-Mode 1/ RX-Mode 1 STAR dual-layer array configuration.

As written in (5.5), portion of the coupled TX signals is cancelled at each RX antenna ports that are located at the lower layer (also excited in mode 1). For more clarifications, let's consider the special case shown in Fig. 5.4. Let's assume the TX layer is excited with mode 1 where all TX elements have similar magnitude and 90° phase progression. Once the TX coupled signals reach, for instance, RX-2, some partial cancellation happens because the coupled signals from TX-3 and TX-7 have similar magnitude but are 180° out of phase; therefore, both TX coupled signals are cancelled. However, since the TX-1 element is located above RX-2, TX-1 has more pronounced coupling than TX-5, so the coupled signals from TX-1 and TX-5 are only partially cancelled because TX-1 will have a higher magnitude, regardless of being out of phase by 180 degrees. Similar principles can be repeated for the rest of the RX elements.

$$b_{RX,TX,1} = 0.5\{S_{21} - S_{61}\} \tag{5.5.a}$$

$$b_{RX,TX,3} = 0.5\{-jS_{21} + jS_{61}\} \qquad (5.5.b)$$

$$b_{RX,TX,5} = 0.5\{S_{61} - S_{21}\} \qquad (5.5.c)$$

$$b_{RX,TX,7} = 0.5\{-jS_{61} + jS_{21}\} \qquad (5.5.d)$$

The residual of TX coupled signals that have not been cancelled at each RX element travels back to the RX's BFN, where all have similar magnitude and 90° phase progression. Once these residual TX coupled signals reach the RX-BFN port, two of them will be 180° out of phase with respect to the other two (5.6). As a consequence, all TX coupling paths that are circulated back to the RX-BFN port are cancelled. This assumes the ideal case where the BFN is ideal, the antenna elements are identical, and there are no nearby scatterers.

$$SI_{RX,TX} = 0.25\{\{S_{21} - S_{61}\}a_2 + \{-jS_{21} + jS_{61}\}a_4 + \{-jS_{21} + jS_{61}\}a_6 + \{-jS_{61} + jS_{21}\}a_8 \qquad (5.6)$$

By applying the excitations of mode 1 at the RX side, as in (5.7), the SI equals zero.

$$SI_{RX,TX} = 0.25\{\{S_{21} - S_{61}\} - j\{-jS_{21} + jS_{61}\} - \{-jS_{21} + jS_{61}\} + j\{-jS_{61} + jS_{21}\} = 0 \qquad (5.7)$$

This mode 1 TX/ mode 1 RX configuration thus has a two-level cancellation; one at the array level and one at the BFN level.

B. TX-Mode 0/RX-Mode 1 Excitation Arrangement: For mode 0 at TX /mode 1 at RX excitation arrangement; no partial cancellation of the TX coupled signals is achieved at the antenna ports since the upper layer is excited with mode 0. In this case, all the TX coupled signals have similar magnitude and phase. However, all SI cancellation is achieved at the RX-BFN's port, and as a result infinite isolation is achieved (5.8). Notice that reciprocal excitations also can be considered, i.e. mode 1 at TX /mode 0 at RX, with two level of cancellations as before.

$$SI_{RX,TX} = 0.25\{\{S_{21} + S_{61}\} - j\{S_{21} + jS_{61}\} - \{S_{21} + S_{61}\} + j\{S_{61} + S_{21}\}\} = 0 \qquad (5.8)$$

Two important observations; specifically, the high isolation of both configurations depends only on the symmetry between the TX and RX paths and not on the physical separation between the layers which makes the proposed approach separation-independent, unless the symmetry is not preserved. The second observation is that the mutual coupling between the upper- and lower-layers is around -18 dB to -10 dB; however, by implementing the proposed approach, the overall isolation is greatly enhanced since these TX coupling signals are hypothetically fully cancelled at RX-BFN's port.

5.2.2 Computational Analysis

The aforementioned analysis for the coupled TX signals led to theoretically infinite isolation between the TX and RX ports for either (mode 1 / mode 1) or (mode 0 / mode 1). To validate this observation, the finite element method (FEM) solver, HFSS, is used to model the TX/RX bi-layer array. The simulated S-parameters are then linked to the circuit simulator where the ideal hybrids are implemented. The isolation results for both cases are plotted in Fig. 5.5. As expected, high system isolation of >80 dB and >74 dB are obtained over the operating bandwidth for both configurations. The level of achieved isolation and discrepancies between the two curves are due to the numerical noise and the sensitivity of each approach to recover from breaking the symmetry.

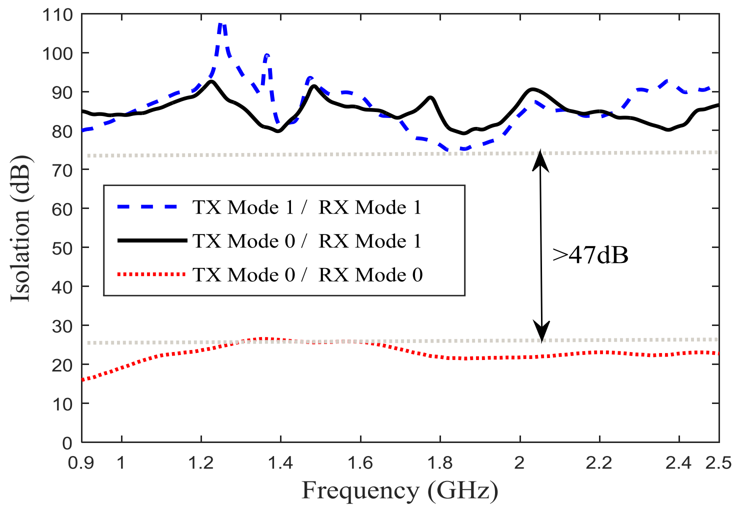

Figure 5.5: The simulated isolation of the proposed STAR circular array using ideal components and comparison to a conventional Mode 0/Mode 0 case.

To show the improvement in isolation, a comparison of the isolation of both C-STAR topologies with the conventional system Mode 0/Mode 0 excitation will be shown. As seen in Fig. 5.5, more than 47 dB isolation improvement is obtained without any increase in spatial separation between TX and RX. The analysis presented so far assumed ideal BFN and antenna elements. However, in practice, it is extremely difficult, if not impossible, to maintain the perfect mechanical and electrical symmetry between all elements. Therefore, to evaluate the influence of symmetry imperfections, the effect of imbalances of the BFN on the overall isolation is considered. The imbalances are chosen to be within the range of the commercial off-the-shelf hybrids, where the amplitude and phase variations are 0.1 dB - 2 dB and 0°- 8°, respectively. Furthermore, the imbalances in this study are assumed to be frequency-independent, even though that is not true in practice, but can still provide good insight into the imperfections' impact on STAR isolation. Obtained results are illustrated in Fig. 5.6; and it is determined that the worst case scenario for both configurations is when the isolation drops to 35dB while the mean value is within 40 dB to 60 dB. It is clear from this study that the imbalances are a critical factor in deterioration of the isolation between the TX and RX layers.

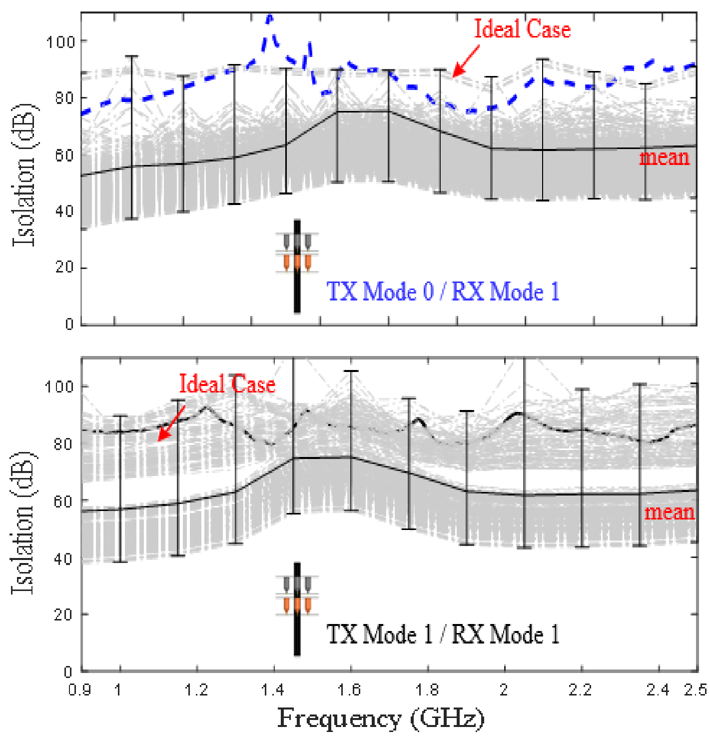

Figure 5.6: The sensitivity of the STAR isolation to the BFN's amplitude and phase imbalances.

5.2.3 Design and Fabrication

After the self-cancellation approach is validated theoretically and computationally, the STAR bi-layer array is designed with intent of experimental validation. As stated previously, each array is composed of four wideband discone antennas whose dimensions are illustrated in Fig. 5.7. The cone part of the antenna is connected to the inner-pin of the SMA while the disc is in-direct contact with the SMA's shield. The separation between the disc and upper cone is 0.14 cm and the inner-pin of the SMA penetrates 0.2 cm inside the cone. The wideband antennas are distributed uniformly in two circular layers with chosen center-to-center spacing of the circular array's elements to be 6.5 cm. The feed-to-feed spacing between the top and the bottom layer is 9 cm (i.e. ~λ/3.7 computed at 0.9 GHz). The separation between the TX and RX layers is chosen based on the spacing availability for mounting and fitting the phase matched cables. As shown in Fig. 5.7, both TX and RX arrays are mounted on a metallic cylinder with radius and length of 2.15 cm and 45 cm, respectively. Plexiglas is used to provide necessary mechanical support for the elements. The measured and simulated VSWRs of each element in the TX/RX array are shown in Fig. 5.8.

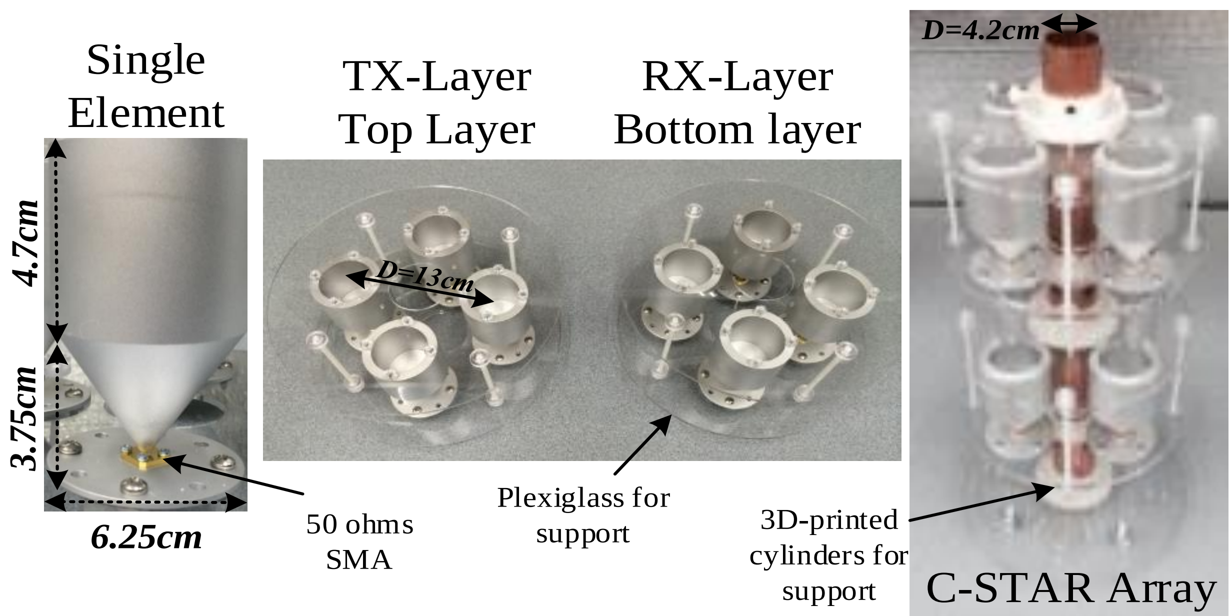

Figure 5.7: Geometry of the discone antenna and the full configuration of the TX/RX STAR bi-layer array.

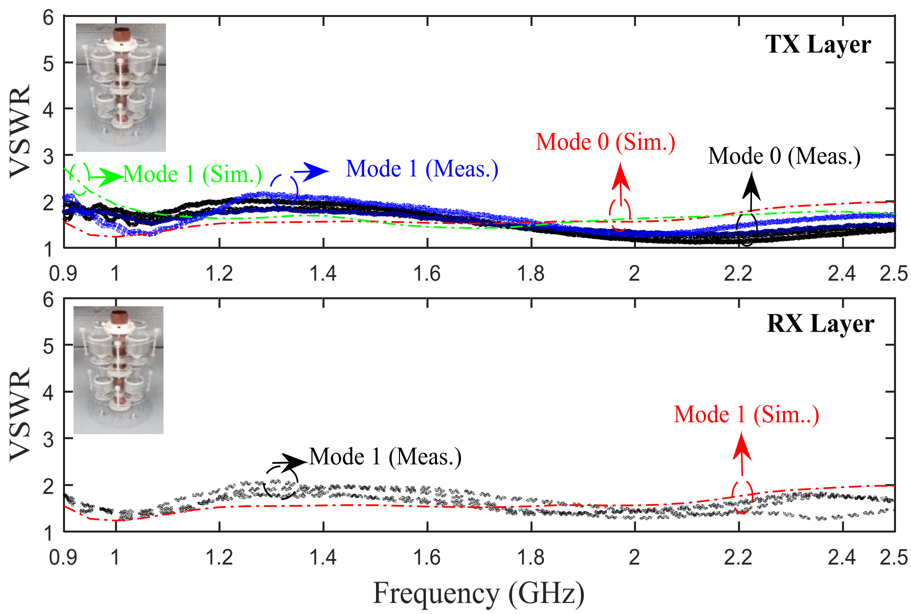

Figure 5.8: The active VSWRs of individual elements in each array when excited with either mode 0 or mode 1 for TX layer and only mode 1 for the RX layer.

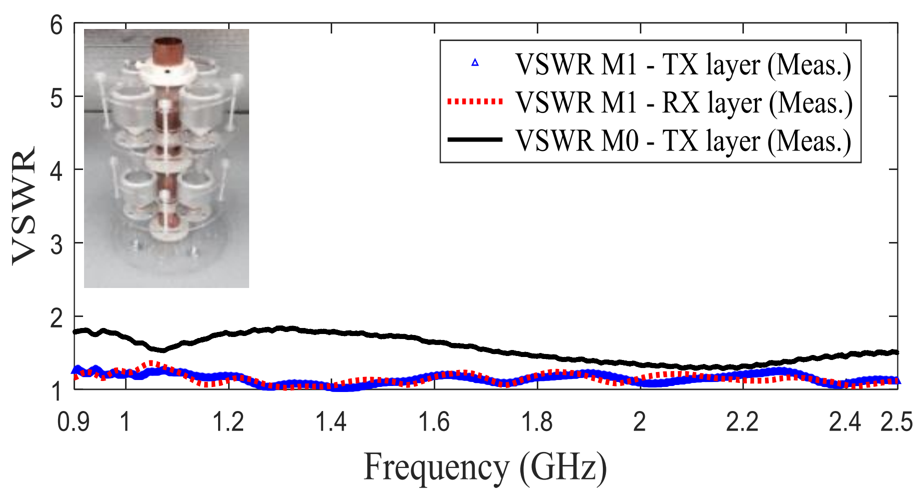

Figure 5.9: The VSWR of the single layer at the TX or RX BFN when excited with either mode 0 or mode 1 for TX and only mode 1 for the RX layer.

As seen in Fig. 5.8, the average VSWR is below 2 over the designated bandwidth of operation for elements in both layers. It is clear that the TX and RX have different VSWRs since each layer sees a different environment, but each element in each layer should have similar performance to achieve good cancellation. Some variation between the curves is noticed, which indeed will have some impact on the measured isolation. The VSWRs of each layer when excited with different modes at the TX or RX ports of BFN are shown in Fig. 5.9. The measured isolation for all configurations is shown in Fig. 5.10. As seen, excellent, wide bandwidth performance is seen for both considered configurations. For completeness, the mode 0/ mode 0 configuration is also shown.

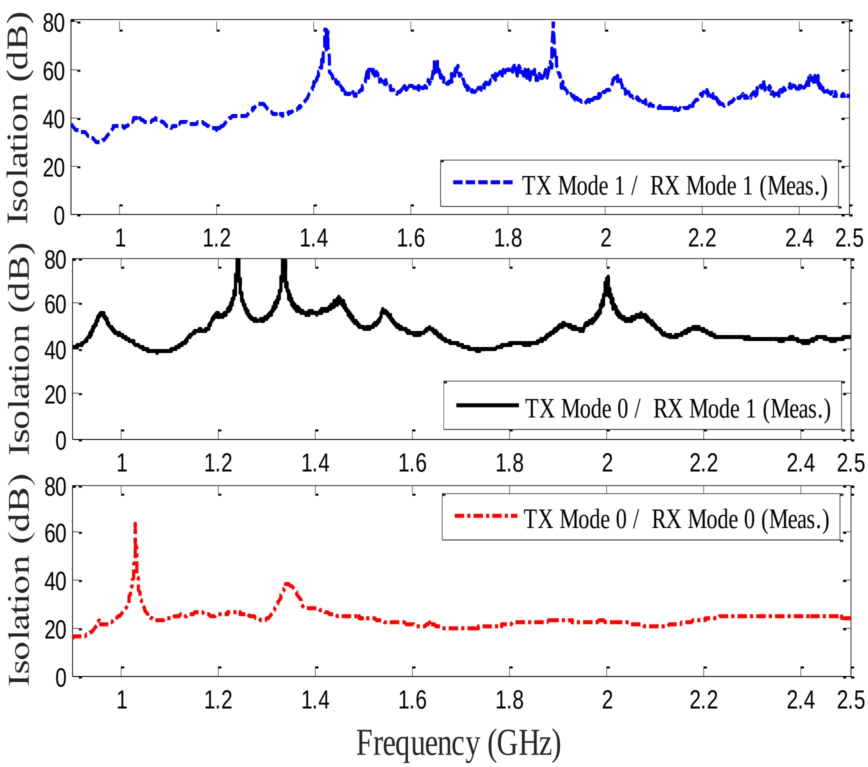

Figure 5.10: Measured isolation between the TX and RX arrays. (Top) mode 1 / mode 1, (middle) mode 0/ mode 1, and (bottom) mode 0/ mode 0.

5.2.5 Measured Far-Field Performance

The far-field performance and match of the circular array depends mainly on the radiation characteristics of the chosen array's elements, number of elements, array's radius, and the mutual coupling between the elements. For the proposed system, an omnidirectional element is chosen. However, due to the other parasitic sources located in the both layers and the supporting cylinder, the radiation patterns of the single element discone antennas once in the array became a directional pattern with a wide beam. For instance, Fig. 5.11 shows samples of the measured radiation pattern at 1.5 GHz for a single element located at the RX layer. As expected, the omnidirectional pattern of the single element becomes more directional due to the existence of the seven remaining parasitic elements and the supportive cylinder in the middle.

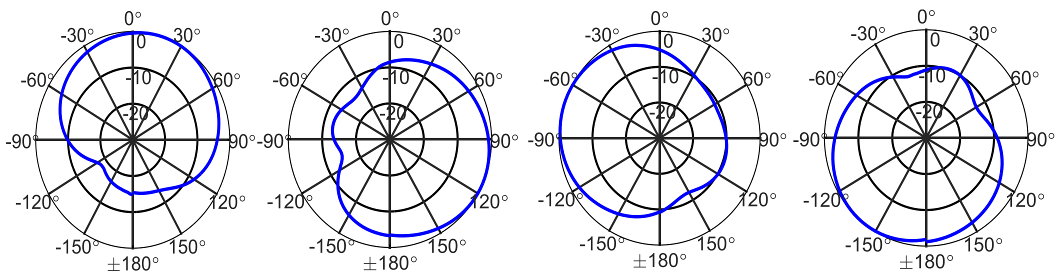

Figure 5.11: Sample of normalized measured radiation patterns of the individual discone antenna RX with the existence of the other seven parasitic elements and the cylinder at frequency 1.5GHz.

The eight elements of the complete array are measured individually and their far-field patterns are combined to produce the desired mode. Recall, the TX layer is excited with mode 0 and mode 1 while the RX layer is excited only with mode 1. Measured normalized radiation patterns are illustrated in Fig. 5.12 and 5.13 at different frequencies and elevation angles (45° and 90°). Good TX and RX omnidirectional radiation patterns are obtained for all the mode permutations; notice, Mode 0 performs slightly better than Mode 1, especially at higher frequencies due to the array factor. By increasing the number of elements to 8 or 16, the appearance of nulls at higher frequencies can be mitigated to increases the bandwidth of the C-STAR array. Unfortunately, the BFN in this case becomes more complex and sensitive to the imbalances, which could negatively impact the overall TX/RX isolation.

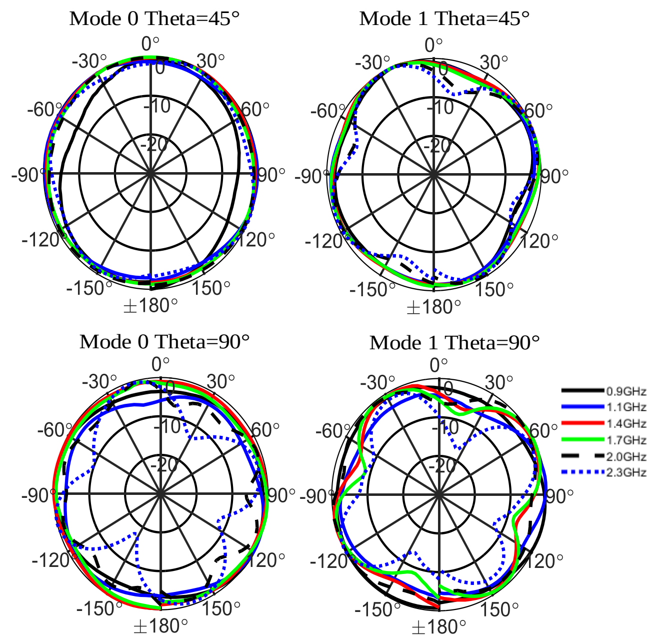

Figure 5.12: Radiation patterns of the TX layer with the existence of the parasitic RX layer and the cylinder. (Left) mode 0 excitation (right) mode 1 excitation.

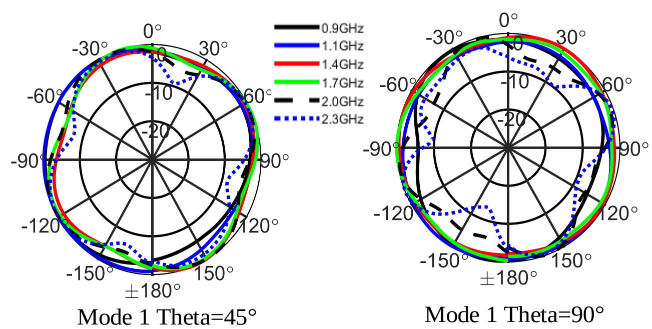

Figure 5.13: Radiation patterns of the bottom RX layer with the existence of the parasitic TX layer and the cylinder, mode 1 only.

5.2.6 Envelope Correlation Coefficient

In addition to the system isolation, the high-quality azimuthal TX/RX omnidirectional patterns are also important for many practical systems and, herein, are treated as an additional design requirement. Usually achieving identical TX and RX patterns while maintaining very high isolation over wide patterns' shapes of the

TX and RX arrays are dictated by application; however, the TX and RX patterns similarity may be considered a baseline feature of a true C-STAR antenna system. To quantify the degree of similarity between TX and RX radiation patterns over the STAR system bandwidth, ECC is calculated. Two independent sets of simulations or measurements are required to calculate ECC; the first is exciting the TX layer while the RX layer is terminated with matched loads, and vice versa. Then both the TX and RX far-fields results are used to compute ECC. Obtained results are shown in Fig. 5.14. As seen, near perfect symmetry (ECC >0.95) is obtained by comparing the TX and RX radiation patterns of the mode 1 TX / mode 1 RX case. By changing to the second configuration (mode 0 / mode 1), the TX and RX patterns remain reasonably similar (ECC >0.81), even though the modes are different.

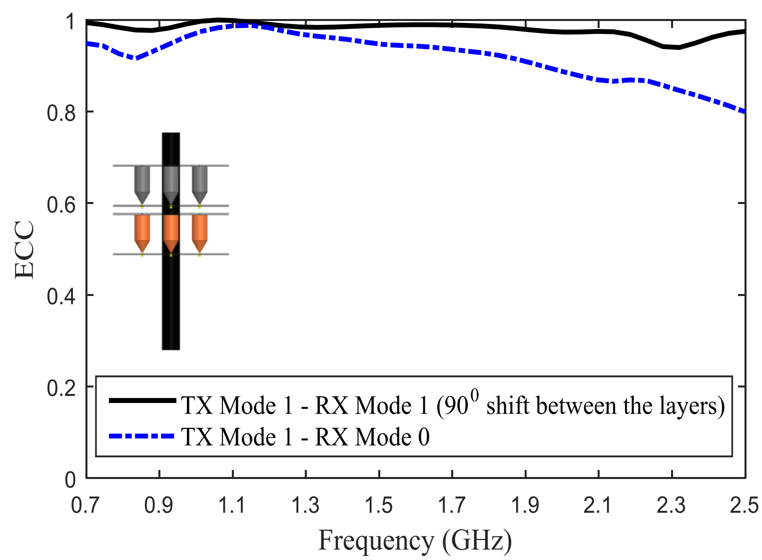

Figure 5.14: ECC for the STAR circular array that are excited with TX/RX mode 1, or TX mode 0 and RX mode 1.

As discussed previously, a wideband dual-mode STAR antenna system is presented [121], [127]-[129]. Theory is validated by simulating the array in HFSS and TX/RX isolation >74 dB is obtained. More than 45 dB improvement in the TX/RX isolation is achieved over the conventional approach (Mode 0 / Mode 0). Several advantages are observed by applying this approach; including: (1) wideband TX/RX isolation is achieved without relying on the spatial separation between the TX and RX layers, (2) in conjunction with analog and digital cancellation schemes, the efficient use of the wireless spectrum is feasible, (3) similar TX and RX radiation patterns are demonstrated, (4) mode diversity to control the radiations patterns and improve the operational bandwidth is achieved. The sensitivity of the proposed system to the amplitude and phase imbalances of the BFN is investigated to show the impact of the asymmetry on the overall performance. Measured isolation in the 30 to 50 dB range is achieved by either applying Mode 1/Mode 1 or mode 0/mode 1. To quantify the similarity between the TX/RX radiation patterns, the ECC is used and values greater than 80% are achieved.

5.3 Monostatic C-STAR Omnidirectional Arrays

5.3.1 Overview

Broadband co-polarized monostatic single layer circular antenna arrays based on mode orthogonality principles are presented for C-STAR applications. The simultaneous excitation of circular phase modes in a circular array with four elements provides ideally infinite isolation. However, once the realistic BFN is used, the isolation between TX and RX is reduced and becomes bound by the internal leakages. To mitigate the undesired leakages, two possible configurations are demonstrated: (1) a single layer circular array excited simultaneously with mode 1 at TX and mixed-modes (i.e. combination of modes 0 and 2) at RX, and (2) a dual layer circular array excited with mode 1 at TX and mode 0 at RX. The arrays are prototyped, where each single layer array is made of four broadband monocone antennas. Measured VSWR <2 and average isolation of 45 dB for a single layer array over at least an octave bandwidth, and 35 dB from 0.8 GHz to 1.3 GHz and 45 dB above 1.3 GHz for the dual layer array. A simple isolation enhancement layer is integrated with the shared BFN to recover from the imbalances and asymmetric leakages with isolation improvement up to 50 dB over 2.8 MHz tunable bandwidth. The ECC is used to quantify the similarity between circular TX/RX array modes.

5.3.2 Operational Principles

A C-STAR shared circular antenna array can theoretically achieve infinite TX/RX isolation or full SI cancellation by relying on mode orthogonality between mode 0 (M0) and mode 1 (M1). However, the isolation level is practically restricted by the shared COTS BFN's leakages. In this section, the theory of using a four element circular array operating with M0 at TX / M1 at RX is explained [121]. Then, two different circular arrays are demonstrated to achieve full SI or leakage cancellation. The chosen antenna element for this chapter is a broadband monocone. The array is excited with different circular phase modes as,

Phase M0: excited by applying equal amplitudes and equal phase between the four antennas, placed in a single array layer.

Phase M1: excited by applying equal amplitudes and -90° phase progression between the four antenna elements, {0, -90°, 180°, -270°}, in a single layer.

Phase M2: excited by applying equal amplitudes and 180° phase progression between the four antenna elements, {0, 180°, 0°, 180°}, in a single layer.

Phase mixed-modes: excited as a combination of M0 and M2 by assigning the same amplitudes and phases of {0, -90°, 0°, -90°} to the elements in a single layer.

A. Mode 0 TX / Mode 1 RX Four-Element Single Layer Circular Array: The first topology utilizes the orthogonality of modes 0 and 1 [121], [127]-[129]. The considered circular array and excitation arrangement are shown in Fig. 5.15. As seen, two 180° hybrids, one quadrature hybrid, and one power divider are used. Once the TX port is excited with a voltage signal, V, the power divider splits the TX signal into two, which enter the sum port of each 180° hybrid. Due to the imperfect isolation of

180° hybrids, a portion of TX signals leak from the two 180° hybrids to the quadrature hybrid's RX ports, as shown in Fig. 5.15. This can be expressed as,

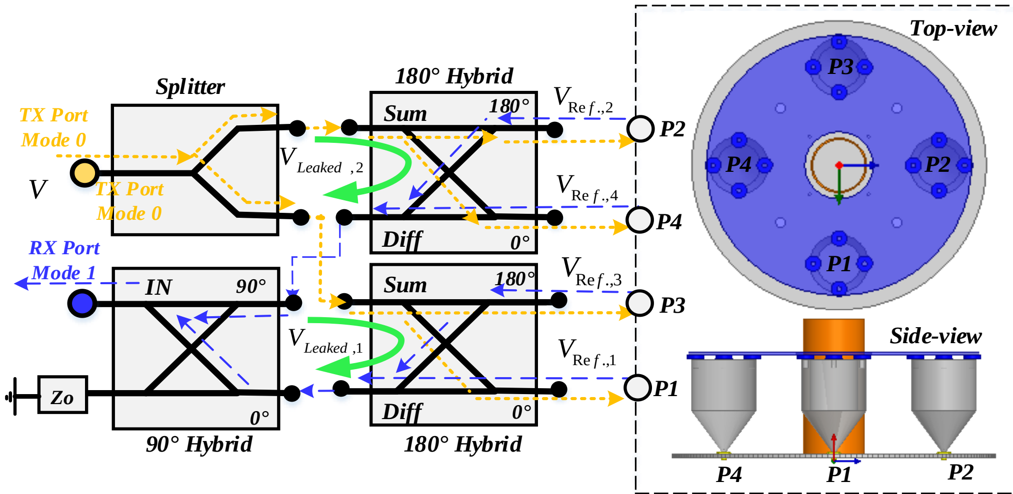

Figure 5.15. Signal flow diagram of M0 at TX / M1 at RX monostatic circular array C-STAR sub-system.

$$V_{leaked\_1,2} = (V/\sqrt{2})(Iso_{180°\,Hyb.,1,2}) \tag{5.9.a}$$

$$V_{leaked\_to\_RX} = (1/2)(V_{leaked\_1} + jV_{leaked\_2}) \tag{5.9.b}$$

where $Iso_{180°\,Hyb.,1}$ and $Iso_{180°\,Hyb.,2}$ are the (limited) isolations of the two 180° hybrids. Most of the TX signals combine constructively once reaching the four TX/RX antenna elements to enable Mode 0 (M0) omnidirectional radiation patterns. Due to the antenna impedance mismatch, reflections at the four antenna ports are generated. These TX reflected signals ($V_{ref.,n}$) are combined with the leaked signals and are then re-routed back to the RX-90°-hybrid's ports. The total TX to RX SI is,

$$SI_{(TX\ to\ RX)} = (1/2)\left\{V_{ref.,1} - j\,V_{ref.,2} - V_{ref.,3} + j\,V_{ref.,4}\right\} + V_{leaked\_to\_RX} \tag{5.10}$$

If the symmetry is maintained along all the array's elements ($V_{ref.,1} = V_{ref.,2} = V_{ref.,3} = V_{ref.,4}$) and both 180° hybrids are identical ($Iso_{180°\,Hyb.,1} = Iso_{180°\,Hyb.,2}$), the BFN effectively cancels the reflected signals, while redirecting the 180° hybrid's leaked signals to the RX port at the quadrature hybrid. Therefore, the total TX to RX SI becomes a function only of the undesired leakages as,

$$SI_{(TX\ to\ RX)} = (1/\sqrt{2})\, V_{leaked}(1 + j) \tag{5.11}$$

From (5.11), it is clear that the leakage from the 180° hybrids due to their finite isolation remains a limiting factor for the overall array isolation.

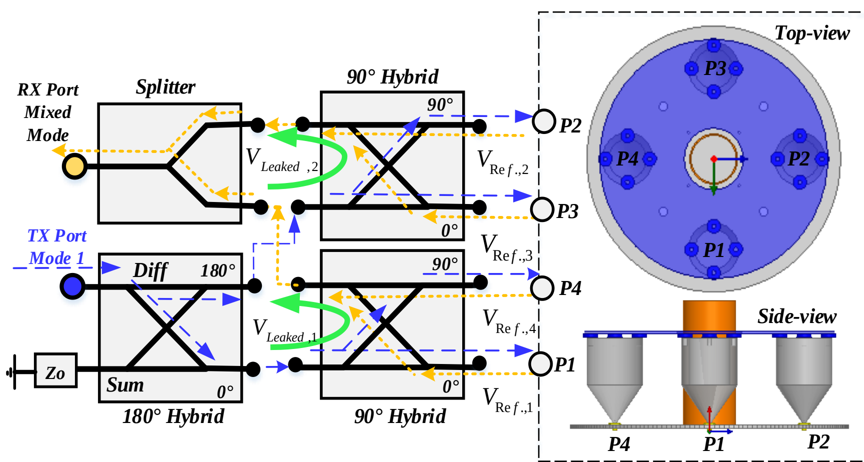

Figure 5.16. Signal flow diagram of M1 at TX / mixed-modes at RX monostatic circular array C-STAR sub-system.

B. Mode 1 TX / Mixed-Mode RX Single Layer Circular Array: For this configuration, mixed-modes principles are used to achieve full SI cancellation. The considered mixed-modes combination utilizes the orthogonal modes (M0+M2) and eliminates the remaining leakages in (5.11), at the expense of deteriorated quality of the RX radiation patterns. The excitation arrangement is M1 at TX / mixed-modes at RX (or vice versa), as shown in Fig. 5.16. Two quadrature hybrids, one 180° hybrid, and one power divider are used, which is different than the BFN presented in Fig. 5.15. Once the TX port is excited with V, two out-of-phase TX signals enter the two quadrature hybrids, as in (5.12). Some of the TX signal leaks in from the two quadrature hybrids and then is re-routed back to the RX port at the power divider, as (5.13),

$$V_{TX} = V_{TX1} = -V_{TX_2} = -\left(V/\sqrt{2}\right) \tag{5.12}$$

$$V_{leaked\_to\_RX} = (\,1/\sqrt{2})V_{TX}\left(Iso_{90°\,Hyb.,1} - Iso_{90°\,Hyb.,2}\right) \tag{5.13}$$

where $Iso_{90°\,Hyb.,1}$ and $Iso_{90°\,Hyb.,2}$ are the (limited) leakages from the two quadrature hybrids. Then most of the TX signals, with 90° phase progression, excite the four TX/RX antenna elements, enabling M1 omnidirectional patterns. The TX coupled reflected signals and leakages are re-routed back to the RX port, as shown in Fig. 5.16. If the symmetry is maintained, then

$$SI_{(TX\ to\ RX)} = (1/2)\left\{-j\left(V_{ref}\right) + \left(j\,V_{ref}\right) - \left(V_{ref}\right) - j\left(j\,V_{ref}\right)\right\} + V_{leaked\_to\_RX} \tag{5.14.a}$$

Where,

$$V_{leaked\_to\_RX} = (\,1/\sqrt{2})V_{TX}\left(Iso_{90°\,Hyb.,1} - Iso_{90°\,Hyb.,2}\right) = 0 \tag{5.14.b}$$

The TX reflected coupling signals then cancel at the RX port since each of the two coupling paths are out of phase with respect to the other two. Similar analysis holds for the out of phase TX leaked signals. Thus, the SI from TX to RX port is fully cancelled as,

$$SI_{(TX\ to\ RX)} = \left(\frac{1}{2}\right)\left\{-j\,V_{ref} + j\,V_{ref} - V_{ref} + V_{ref}\right\} = 0 \tag{5.15}$$

As evidenced here, this configuration cancels both the reflected and leaked TX coupled signals, leading to theoretically infinite isolation between the TX and RX ports.

C. Mode 1 TX / Mode 0 RX Dual Layer Circular Array: To preserve good omnidirectional TX and RX radiation patterns and maintain full leakage cancellation, an additional circular antenna array layer is introduced. Effectively, this layer is a leakage canceller. The introduced leakage has an opposite phase compared to the existing one in (5.11) and as a result, the sum of the two opposite-sign leakages leads to full cancellation. The additional upper layer is a mirror of the referenced single layer and is excited with 180° phase difference to have omnidirectional radiation patterns, as shown in Fig. 5.16. The TX and RX excitation arrangements are; Phase M0 assigned to RX excitation: all elements of the dual layer circular array are excited with a phase set of {0°, 0°, 0°, 0°} for the lower layer and a cancellation set of {180°, 180°, 180°, 180°} for the upper layer; Phase M1 assigned to TX excitation: the lower layer is excited with equal magnitudes and phases of {0°, -90°, 180°, -270°} while the upper layer is excited with {180°, -270°, 0°, -90°}. Regarding the SI and leakage cancellation, once the TX port of the BFN is driven, the eight TX signals excite the antenna ports (Mark-1 in Fig. 5.17) to generate M1 omnidirectional radiation patterns. In the meantime, eight TX reflections and four leaked signals are induced within the shared four far-end 180° hybrids BFN. Each two out-of-phase TX mismatch reflections at each of the four far-end 180° hybrids are cancelled at the sum ports (Mark-2 in Fig. 5.17). Similarly, four leaked signals are induced due to the (limited) isolation of the four far-end 180° hybrids. The introduced and inverted circular antenna array layer has also two new leakages that are out of phase with respect to the two other corresponding leakages of the lower circular array. Once all four leakages reach the RX port, they cancel each other assuming the ideal case where all the leakages are symmetric (Mark-3 on Fig. 5.17) as in (5.17).

$$SI_{(TX\ to\ RX)} = (1/\sqrt{2})V_{leaked}\{(1+j)-(1+j)\} = 0 \tag{5.16}$$

The proposed dual layer array is capable of canceling the inherent leakages of COTS BFN while preserving nearly identical TX and RX omnidirectional patterns.

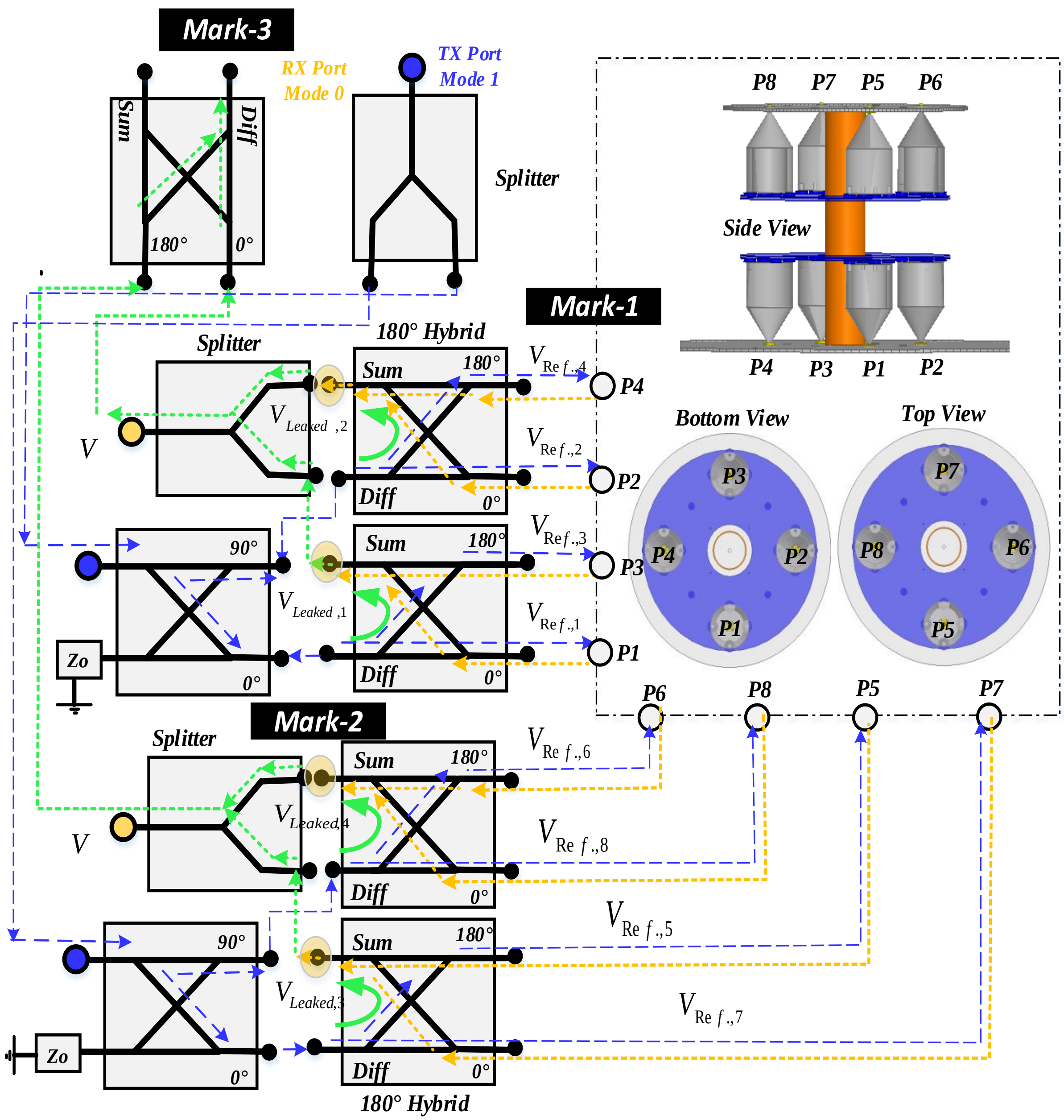

Figure 5.17: Signal flow diagram of M1 at TX / M0 at RX monostatic circular array C-STAR sub-system.

5.3.3 Computational Analysis

To validate the theory, a computational analysis is conducted with the Ansys-HFSS solver. The single element is a wideband monocone antenna with height 8.45 cm ($\lambda/4.4$ at 0.8 GHz) and top diameter of 6.25 cm, as shown in Fig. 5.18.a. The ground plane's radius of the single layer array is $R1 = 20.4$ cm ($\lambda/1.8$ at 0.8 GHz), Fig. 5.18.b; while the dual layer's lower and upper ground plane radii are $R1 = 30$ cm and $R2 =$ 15.7 cm ($\lambda/1.25$ and $\lambda/2.38$ at 0.8 GHz), respectively, as seen Fig. 5.18.c. The separation between the layers in the dual layer is 12 cm ($\lambda/2.8$ at 0.8 GHz). Each cone antenna in the array is connected to the inner-pin of the SMA while the ground plane is in direct contact with the SMA's shield. The elements are supported by Plexiglass and a copper cylinder with radius and length of 2.8 cm and 30 cm, respectively.

The isolation results of the two cases using ideal circuit components are plotted in Fig. 5.19. Simulated average isolation of 68 dB is obtained over the operating bandwidth for both configurations using ideal circuit components. Hence, the isolation level is limited by the mesh quality driven by the available commercial resources and computation time. The numerical analysis presented in Fig. 5.19 assumes the BFN is imbalances-free. However, under the influence of the realistic circuit's components' imbalances, the isolation degrades. To demonstrate this, the imbalances are chosen within the range of the available COTS hybrids; with amplitude and phase variations of 0.1 dB - 0.8 dB and 0° - 8°, respectively. To avoid repetition, only the isolation response for a single layer with mixed-modes configuration is presented. The isolation response for the other cases is very similar, so they are not included herein. Two regions are shown in Fig. 5.20, where region 1 represents the isolation when the imbalances affect each of the two opposite elements symmetrically. Once the imbalances are different at all four antenna elements, the isolation drops to different levels as shown in region 2 in Fig. 5.20. The worst isolation level in region 2 is 30 dB, while the mean value is around 40 dB.

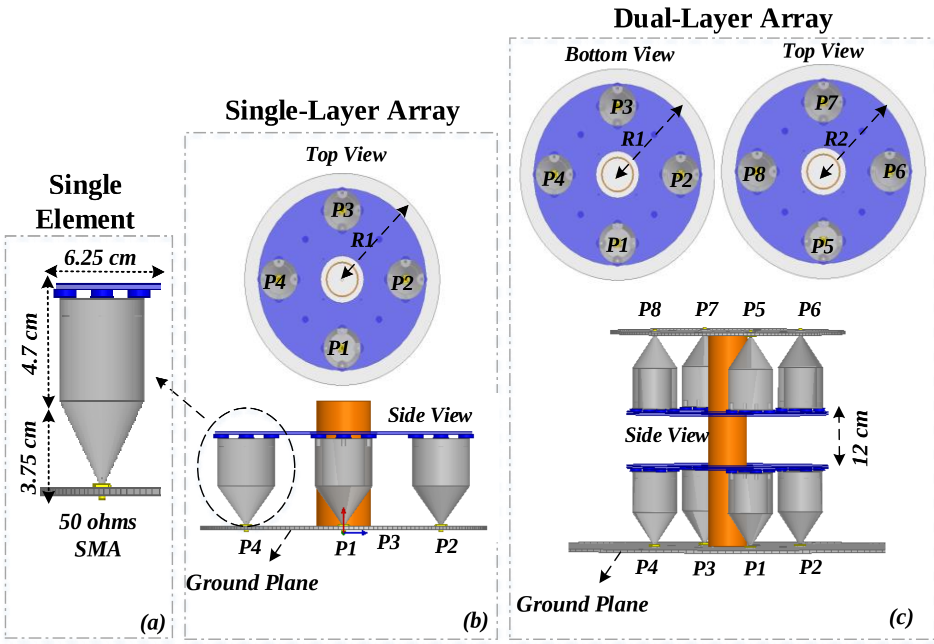

Figure 5.18: Geometry of the modeled C-STAR circular arrays, (a) single monocone antenna, (b) single layer four-element array, (c) dual layer eight-element array.

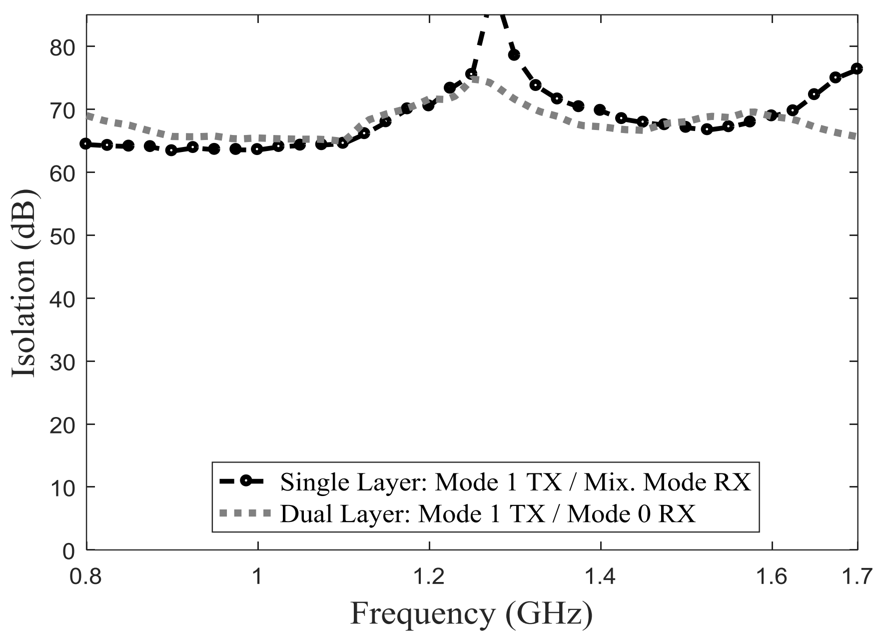

Figure 5.19: Computed isolation for M1 at TX / mixed-modes at RX single layer configuration and M1 at TX / M0 at RX dual layer configuration. Antenna array simulated in HFSS and linked to ideal BFN.

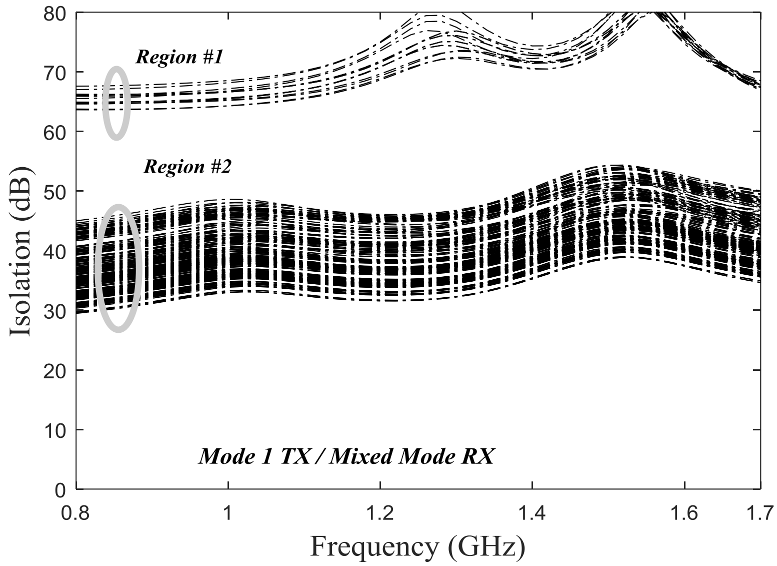

Figure 5.20: The effects of BFN imbalances on the simulated array sub-system isolation using ideal circuit components of M1 at TX / mixed-modes at RX.

5.3.4 Fabrication and Measurements

The fabricated C-STAR single and dual layer circular antenna array configurations are shown in Fig. 5.21. Details of both array geometries were discussed in Section 5.3.3 and shown in Fig. 5.18. The isolation measurements of the monostatic circular arrays were conducted in an anechoic chamber.

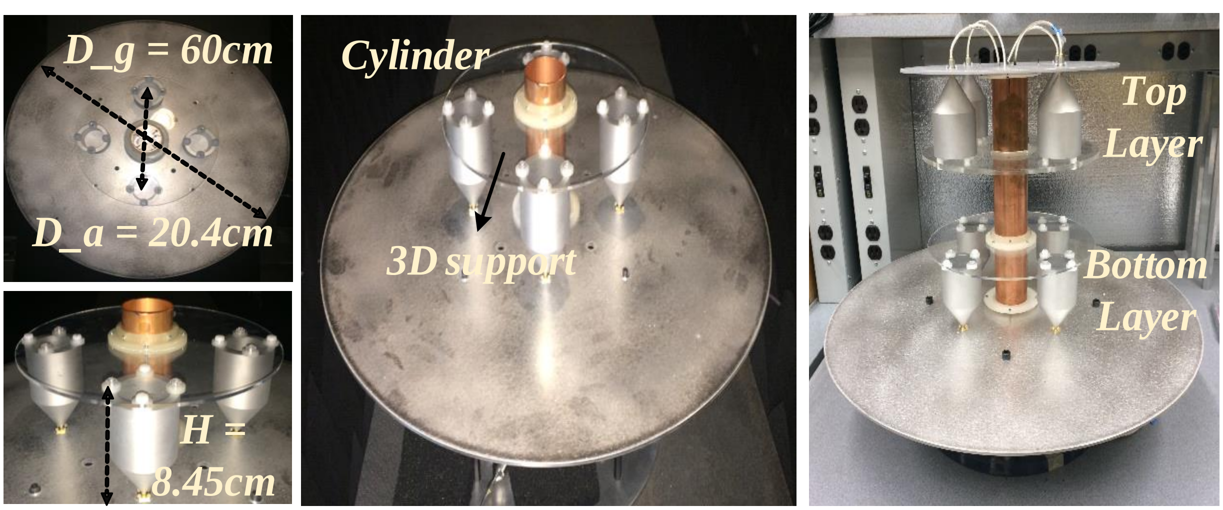

Figure 5.21: Photographs of the fabricated C-STAR circular arrays, (left and middle) single layer four-element array, (right) dual layer eight-element array.

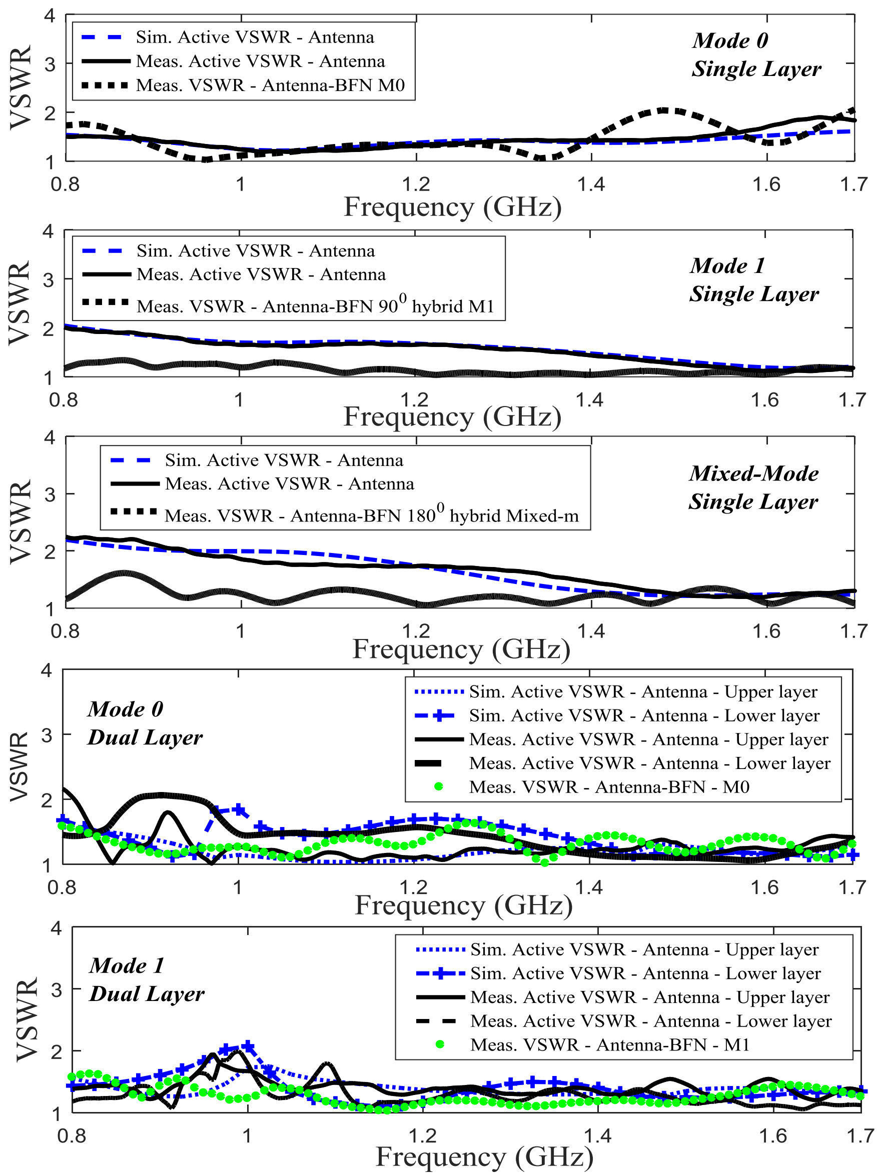

Figure 5.22: Simulated and measured active VSWRs of an individual element in the array once excited with M0, M1, and mixed-modes (other elements have similar performance). Also shown are the measured VSWRs for single and dual layer arrays once connected to the BFN for all excited modes.

The measured and simulated active VSWR of one antenna element in the TX or RX modes are shown in Fig. 5.22. The active VSWR is <2 over most of the frequency band for M0, M1, and mixed-modes. Good agreement is obtained between the simulated and measured results. For the dual-layer array, the active VSWRs for the upper and lower arrays do not behave similarly due to the different ground plane sizes. The differences between the active antennas VSWRs of the various modes are due to the provided excitation phases. Once the array is connected to the BFN, M1 and mixed-modes indicate improvement in VSWR because the reflections either cancel at the RX port or dissipate at the BFN's terminated ports at the input hybrid as shown in Figs 5.15 - 5.17. Once the BFN's TX port is excited for the single or dual layer configurations, some of the TX signals dissipate within the BFN and reflect back to the terminated loads, which is considered as a power loss and measured here for the different TX modes. The power loss for each excited TX mode is below 12% over 86% of the operational frequency band and below 20% over 2:1 bandwidth.

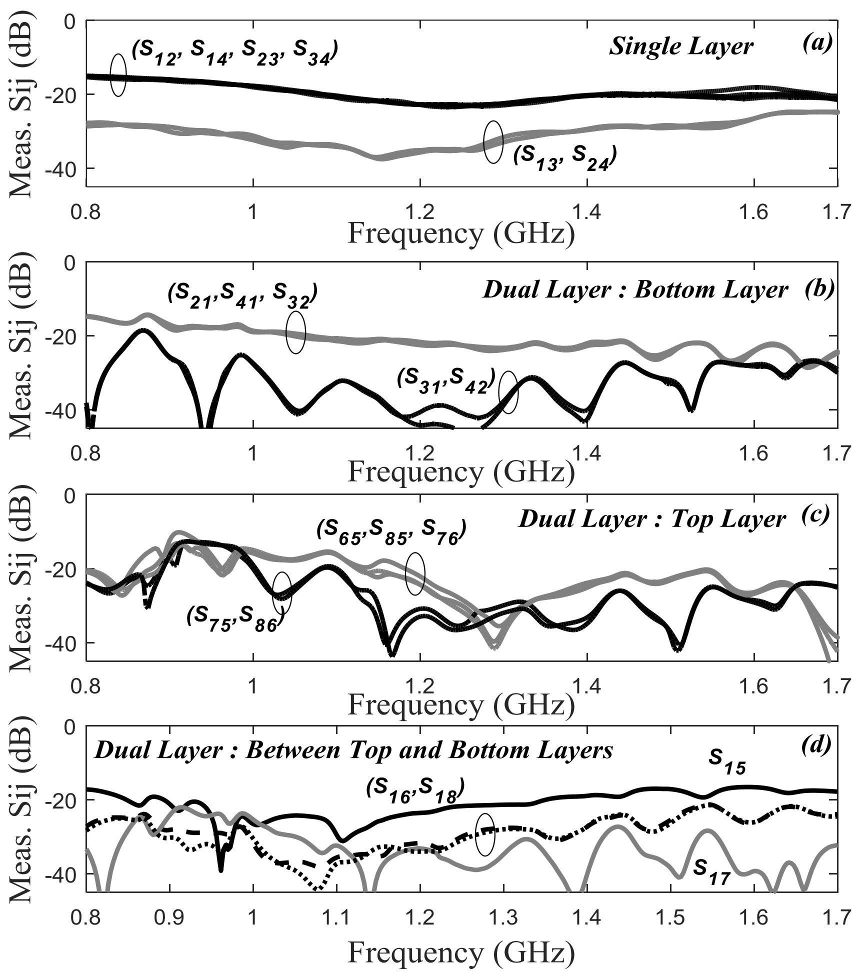

Figure 5.23: Comparison of the measured mutual coupling between the monocone elements located within the single or dual layer arrays.

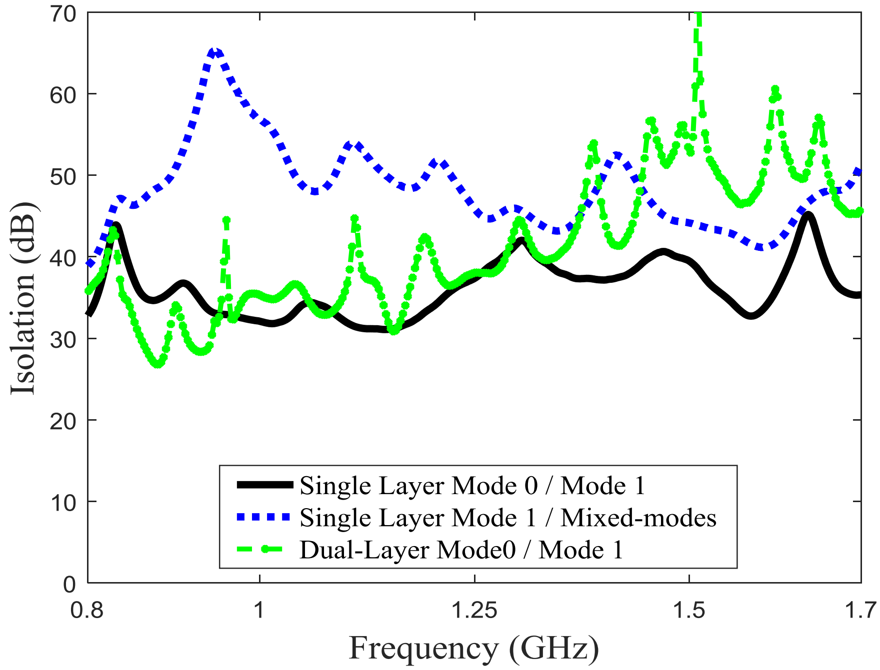

Figure 5.24: Comparison of the measured isolation between the herein C-STAR circular arrays.

The mutual coupling between the monopole elements located within the single and dual-layer arrays are shown in Fig. 5.23. With the proposed configurations, isolation improvement from 5 dB - 30 dB can be achieved. More specifically, the measured isolation of the three discussed monostatic C-STAR circular array configurations are shown in Fig. 5.24. For the single layer M1 at TX / mixed-modes at RX, the measured isolation is >40 dB and improvement up to 23 dB is achieved compared to the single layer M0 at TX / M1 at RX. The dual layer M1 at TX / M0 at RX configuration also achieves good isolation with greater improvement at higher frequencies. The aforementioned configurations are compared to some of the measured state-of-art C-STAR circular arrays in Table 5.1 that rely on assigning a certain number of antenna elements from the circular array as TXs and the remaining elements as RXs; along with physical separation and polarization-multiplexing, near-field cancellation techniques and mode orthogonality. The level of measured isolation of the monostatic array is comparable to the others, if not higher at certain bands. This proves mode orthogonality has great potential to improve the isolation in monostatic circular arrays over a wide operational bandwidth.

Table 5.1: Measured Isolation Comparison between the C-STAR Circular Arrays and other State-of-the-Art Circular Array C-STAR Approaches.

Ref. #	TX/RX Polarization	TX/RX Antenna Similarity/ Number		BW	Measured Isolation [dB]		
					Min	Avg	Max
[61]	Similar Polarization	Different TX and RX antennas (not mono-static)	5	4.8%	31	35	55
[43]			5	2:1	48	62	70
[63]			9	4.1%	47	60	78
[64]			5	15%	30	40	62
[65]	Different Polarization		5	2:1	38	40	49
[121]	Similar Polarization	Similar TX and RX antennas (mono-static)	16	2:1	45	52	63
SL Modes 0/1			4	2:1	28	35	45
SL M1 / Mix-modes			4		40	44	85
DL Modes 0/1			8		28	40	81

5.3.5 Integrating the Isolation Enhancement Layer

In this section, an additional isolation enhancement layer is introduced to partially recover from the BFN's imbalances, asymmetric leakages, and geometrical misalignment due to fabrication and assembly imperfections. Only the dual layer circular array configuration (Figs. 5.17) is considered in this section; however, a similar approach can be applied for the single layer topology. As shown in Fig. 5.25, this extra isolation circuitry layer is connected to the unused sum port of the RX-180°-hybrid which has the combined signals of sustained leakages and reflections from the shared COTS BFN. The used isolation enhancement layer is composed of a tunable attenuator, tunable phase shifter, and power divider. This layer improves the isolation performance by adjusting the amplitude and phase weights of the signals at the unused sum port of the RX-180°-hybrid to favorably superpose with the referenced signal at the difference port, leading to enhanced cancellation. This cancellation does not greatly affect the TX or RX radiation patterns and is done by linking the measured S-parameters of the dual layer array and COTS BFN in AWR to the ideal tunable isolation enhancement layer. The tuned attenuator and phase shifter used each varies up to 70 dB with 1 dB step and 90° with 1° step, respectively. Six frequencies with 0.92-1.64 GHz range are considered, and the isolation is improved up to 50 dB (see Fig. 5.25). Employed attenuation and phase shift of these marked points are listed in Table 5.2.

Table 5.2: Employed Attenuation and Phase Shift at the Marked Points

Frequency Points	Attenuation Level	Phase Shift
P1: 0.92 GHz	8 dB	97°
P2: 1.06 GHz	0 dB	68°
P3: 1.13 GHz	24 dB	43°
P4: 1.40 GHz	12 dB	80°
P5: 1.55 GHz	4 dB	39°
P6: 1.64 GHz	6 dB	80°

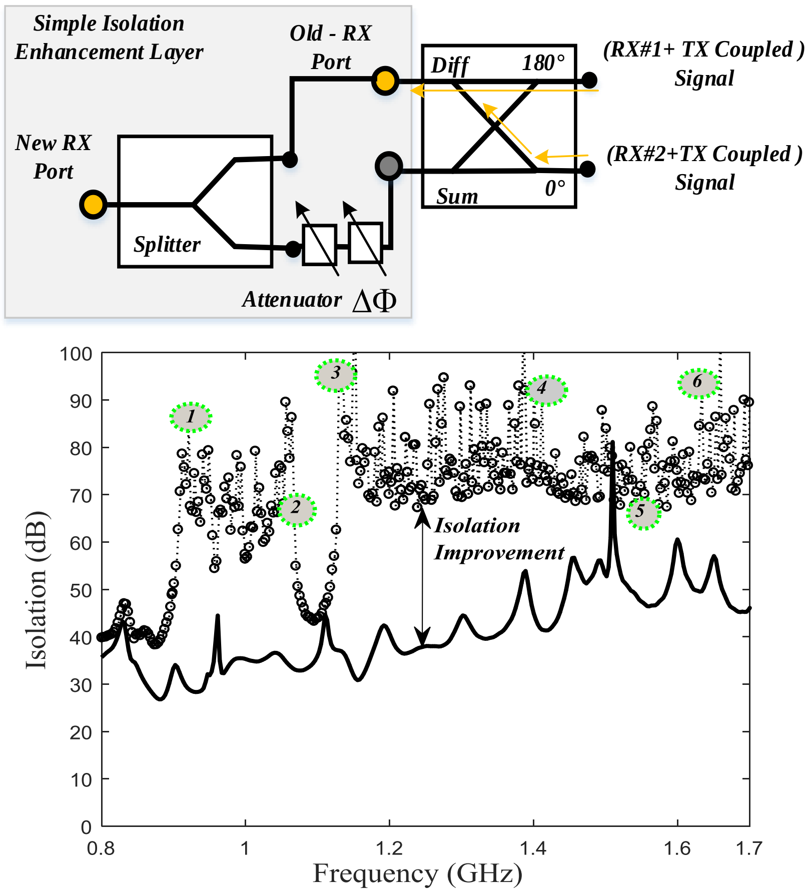

Figure 5.25: The isolation enhancement layer (top) and measured isolation for dual layer M0 at TX / M1 at RX before (solid-line) and after (circle-marker) introducing the isolation enhancement layer (bottom).

5.3.6 Far-Field Performance

The measured radiation patterns of each individual element in the single layer array are shown in Fig. 5.26. Clearly, the other surrounding elements, including the cylinder, act as parasitic reflectors, causing slight changes in the embedded radiation patterns of the TX/RX single elements. Fig. 5.26 shows the simulated and measured co- and cross-polarized radiation patterns at 0.8 GHz and $\theta = 90°$ xy-plane for the single layer array. Good agreement between the simulated and measured results is obtained for the four elements, i.e., similar patterns are obtained with a rotation of a 90° due to the spatial location of each antenna element. The measured radiation patterns of the single and dual layer array configurations are shown in Figs.

5.27 - 5.30 at different frequencies, azimuthal angles in yz-plane, and elevation angles in xy-plane. Overall, good TX and RX omnidirectional radiation patterns are obtained, especially for M0 and M1, while the patterns for the mixed-mode are not purely omnidirectional due the phase excitation and the nulls of M2. The cross-polarization is low for M0 while it becomes stronger for M1 and mixed-modes at off-axis elevation angles due to the shared ground plane and undesired higher order modes. The variations in radiation patterns over different frequencies is due to the spacing between the antenna elements. At higher frequencies, the spacing becomes electrically large, leading to deeper nulls and change in overall shape. For the four element array, the nulls is are seen once the operational bandwidth is higher than ~1.5:1 bandwidth. The measured and simulated peak gain of the single and dual layer circular C-STAR arrays with different excited modes are shown in Fig. 5.30. The peak gains for all modes are >3 dB over the 2:1 bandwidth. The agreement between the measurements and simulations fully verify the cancellation theory and implementations. Hence, the mixed mode has the highest peak gain due to the provided excitation phases, which lead to the patterns to be more directive at certain azimuthal angles, 90° and 270°, as shown in Fig. 5.28.

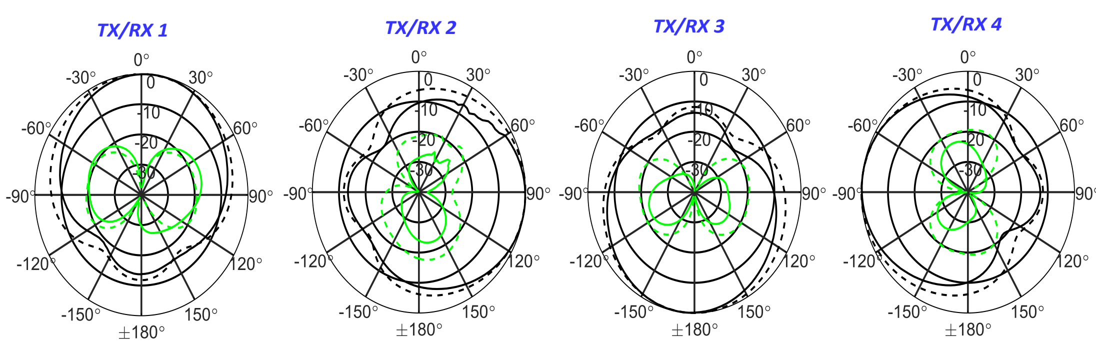

Figure 5.26: Simulated (dashed) and measured (solid) co- (balck) and cros-(green) normalized radiation patterns of the four monocone antennas at 0.8 GHz and $\theta = 90°$ plane.

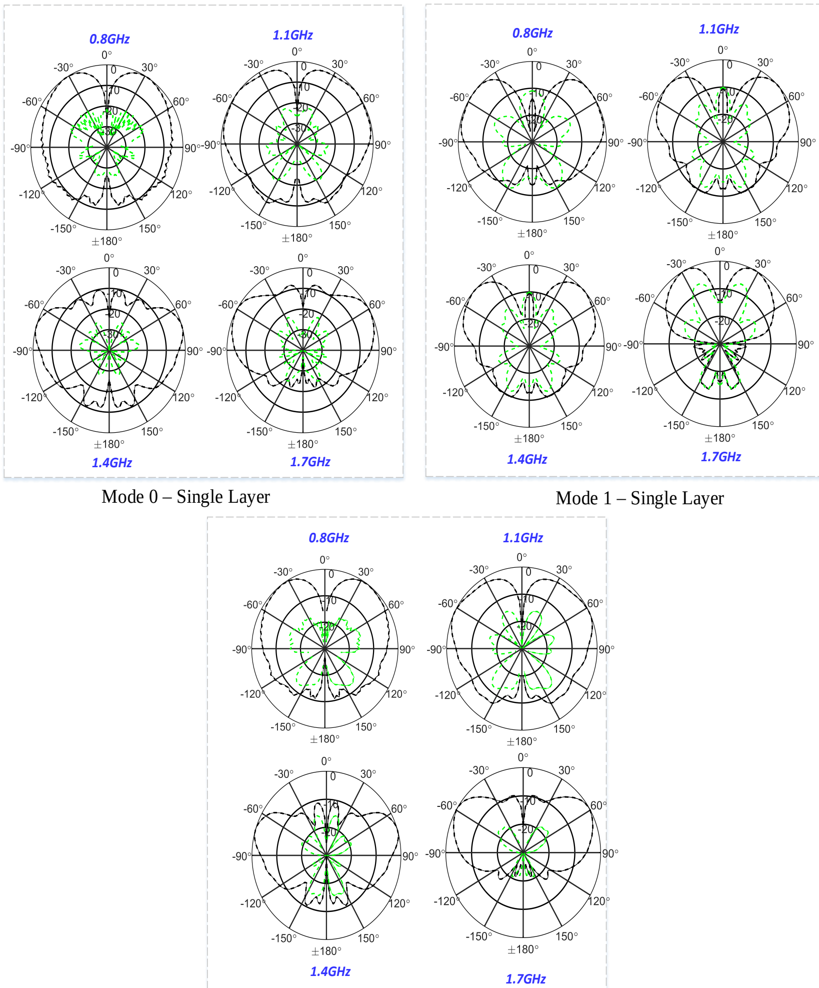

Mixed-modes – Single Layer

Figure 5.27: Measured yz-plane patterns of the monostatic C-STAR single layer circular array once excited with different modes.

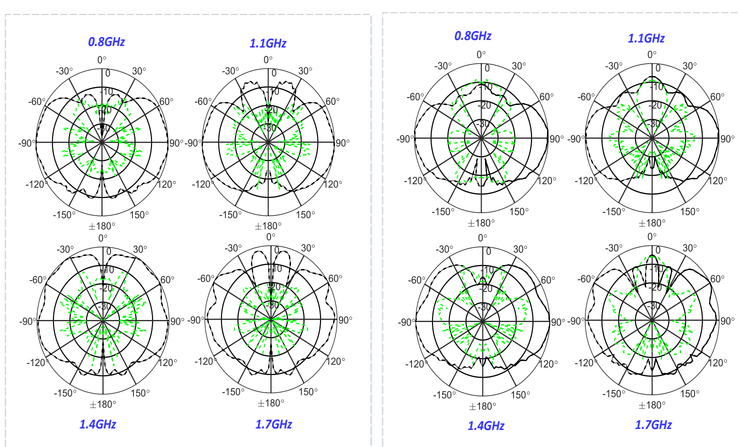

Mode 0 – Dual Layer   Mode 1 – Dual Layer

Figure 5.28: Measured xy-plane patterns of the monostatic C-STAR dual layer circular array excited with different modes.

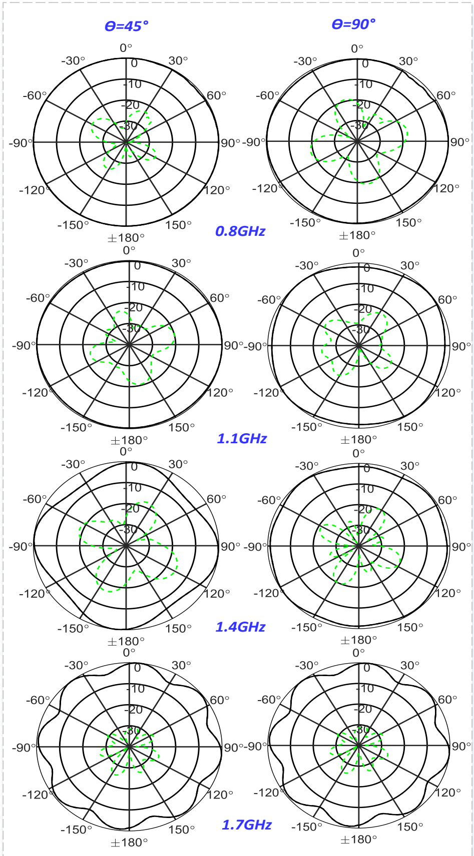

Mode 0 – Single Layer

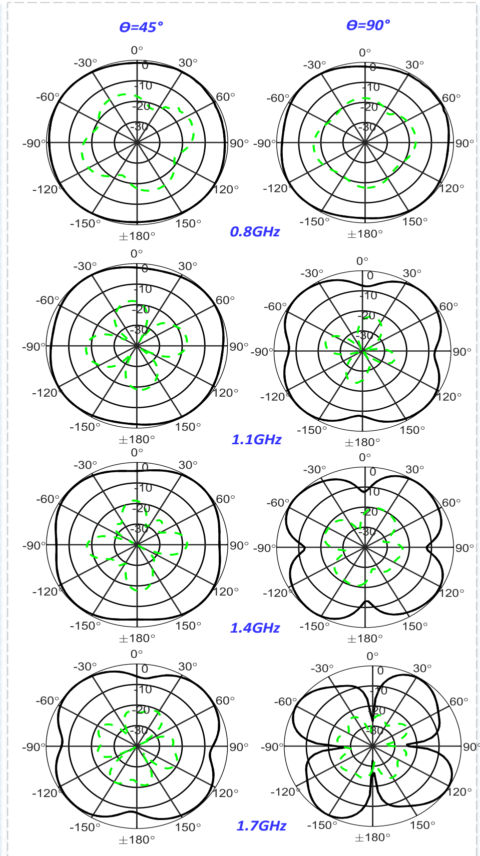

Mode 1 – Single Layer

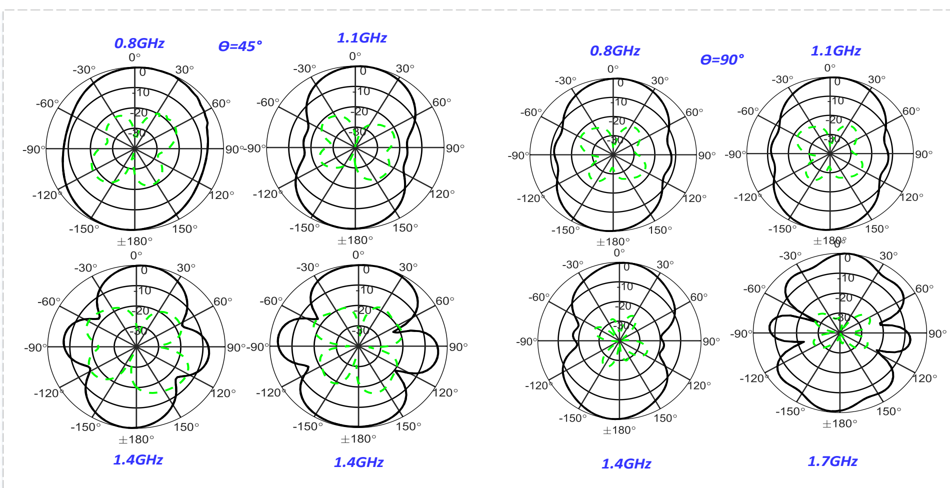

Mixed-modes – Single Layer

Figure 5.29: Measured xy-plane patterns of the monostatic C-STAR single circular array excited with different modes at elevation angles of (45° *and* 90°).

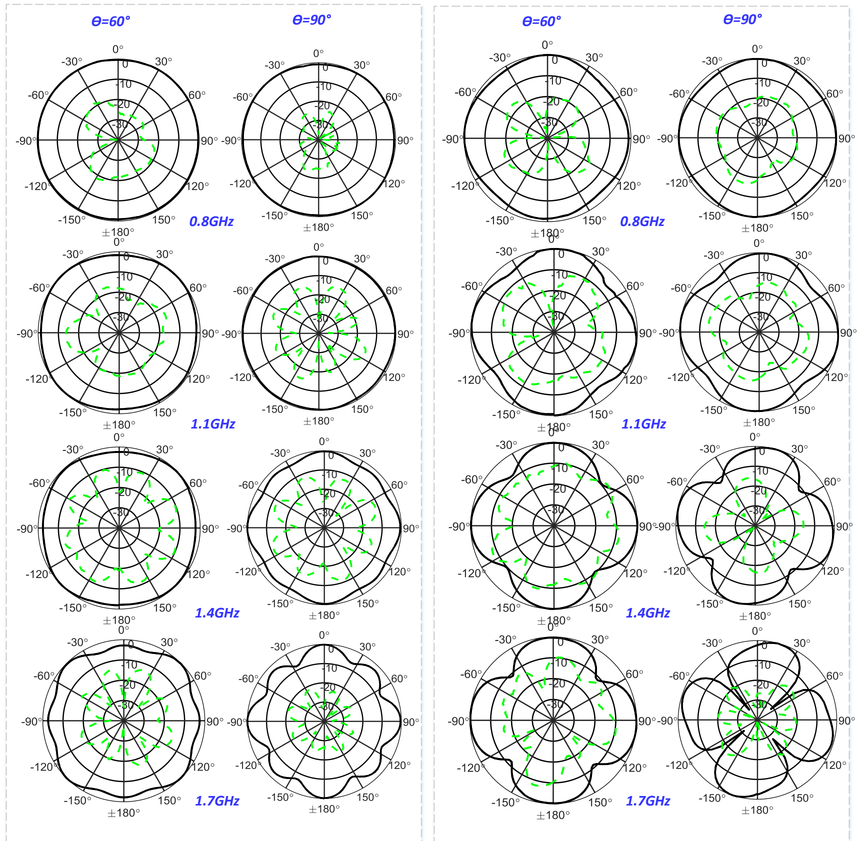

Mode 0 – Dual Layer

Mode 1 – Dual Layer

Figure 5.30: Measured xy-plane patterns of the monostatic C-STAR dual layer circular array excited with different modes at elevation angles of 60° *and* 90°.

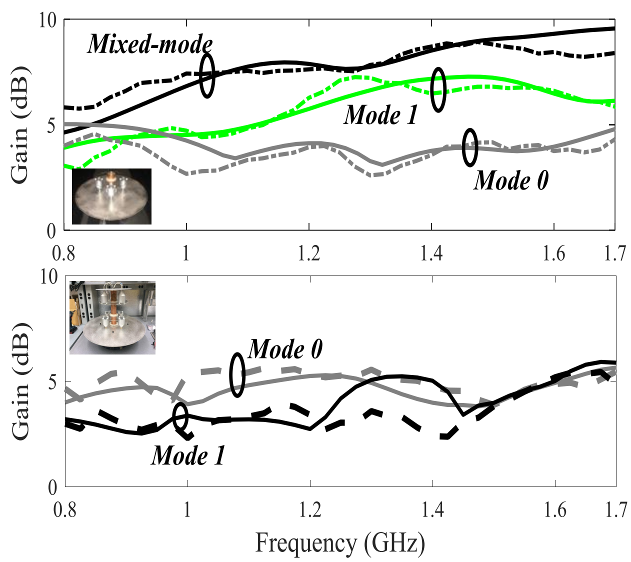

Figure 5.31: Peak gains of the simulated and measured monostatic C-STAR circular single and dual layer arrays once excited with M0, M1, and mixed mode. Single layer (top) and dual layer (bottom) circular arrays.

5.3.7 Envelope Correlation Coefficient

A true C-STAR monostatic antenna system should have ideally identical TX and RX radiation patterns. In this chapter, mode multiplexing is utilized to achieve high isolation in the circular monostatic arrays at the expense of breaking the similarity between the TX and RX radiation patterns. To quantify precisely the degree of similarity, ECC is used. The ECC can be calculated by obtaining either the simulated or measured far-field within $\theta = 45° - 90°$ for every configuration. As seen in Fig. 5.32, good symmetry is obtained with M0 at TX / M1 at RX single layer and M1 at TX / M0 at RX dual layer. Noticeably, as the frequency increases, ECC starts to deteriorate due to the excitation of higher order phase modes. By switching to M1 at TX / mixed-modes at RX single layer configuration, ECC >0.6 and is less than before, as expected. ECC >0.75 is obtained by comparing the radiation patterns of M0 at TX / M1 at RX single layer and M1 at TX / M0 at RX dual layer. Overall, good agreement between the simulated and measured ECC is observed.

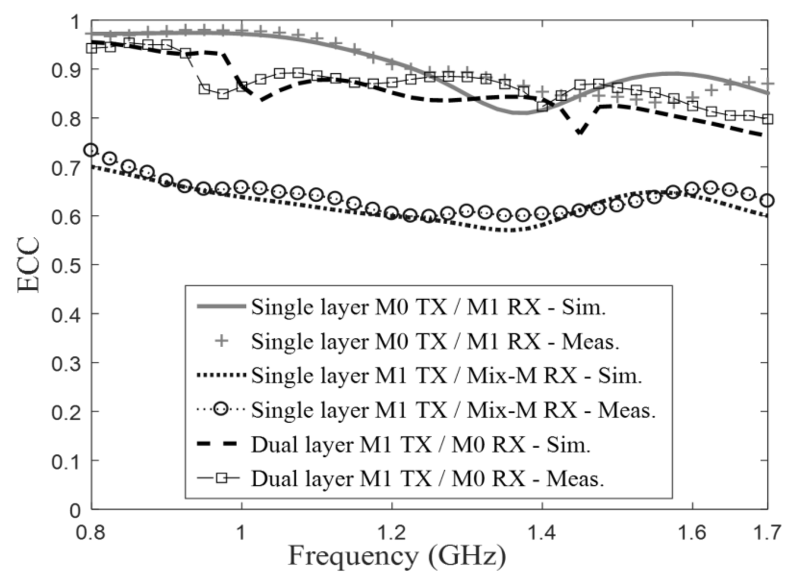

Figure 5.32: Simulated and measured ECC between $\theta = 45° - 90°$ and $\phi = 0° - 360°$ for the C-STAR circular array for (1) single layer excited with M0 at TX / M1 at RX, (2) single layer excited with M1 at TX / mixed-modes at RX, and (3) dual layer excited with M1 at TX / M0 at RX.

Table 5.3: Comparison between the Proposed Omnidirectional C-STAR Circular Array Sub-systems

C-STAR Approach	*Comp-lexity*	*Isolation (Simulated/ Average Measured)*	*BW*	*Far-Field (Eff.)*	*Far-Field (ECC)*	*Extend to Multi-Mode and Dual-Polarization Capability*
Dual-Layer Separation-Independent	*High*	*Infinite / >40 dB*	*~2.5:1*	*Excellent (100%)*	*Good (>80%) for mode 1*	*Yes*
Single-layer Monostatic (Mode 0 TX and Mode 1 RX)	*Low*	*Limited by leakages / >30 dB*	*~2:1*	*Excellent (100%)*	*Good (>80%) for mode 1*	*Yes*
Single-layer Monostatic (Mode 1 TX and Mixed-modes 1 RX)	*Low*	*Infinite / >40 dB*	*~2:1*	*Excellent (100%)*	*Moderate (>60%) for mode 1*	*Yes*
Dual-layer Monostatic	*High*	*Infinite / >30 dB*	*~2:1*	*Excellent (100%)*	*Good (>80%) for mode 1*	*Yes*

5.3.8 Summary

Broadband co-polarized monostatic circulator-less circular antenna arrays based on mode orthogonality principles are proposed for in-band C-STAR applications. Analytical, computational, and experimental steps are demonstrated in detail to show the limitations of each configuration and showcase the isolation improvement. The first C-STAR circular array configuration utilizes the mixed-modes excitation to overcome the shared realistic BFN's leakage at the expense of sacrificing the omnidirectionality of the RX radiation patterns. The second configuration is the dual-layer circular array where the second layer is introduced to cancel the leakage of the existing single layer while maintaining good omnidirectionality of TX M1 and RX M0 radiation patterns. Average isolation of 45 dB for a single layer array over at least an octave bandwidth, and average isolation of 30 dB from 0.8 GHz to 1.3 GHz and 45 dB above 1.3 GHz for the dual layer array, are obtained. For the dual layer, the isolation can be enhanced up to 50 dB once the narrowband tunable isolation enhancement layer is introduced. ECC >0.6 for M1 at TX / mixed-modes at RX single layer and >0.75 for M1 at TX / M0 at RX dual layer are measured. A comparison between the proposed omnidirectional C-STAR arrays sub-systems in this chapter with respect to isolation, size, complexity, and far-field performance is presented in Table 5.3. All arrays can theoretically achieve infinite TX/RX isolation and good far performance except the RX side of the single layer once is excited with mixed modes in order to cancel the leakages and further improve the overall TX/RX isolation. In summary, the mode orthogonality of the monostatic circular array shows great potential for improving the isolation between TX and RX without relying on any separation, time-, frequency-, polarization-, or antenna-multiplexing.

CHAPTER 6

WIDEBAND MULTIMODE CO-POLARIZED MONOSTATIC BROADSIDE C-STAR ANTENNA ARRAYS

6.1. Overview

Several co-channel self-interference mitigation techniques on the array layer have been considered in the past. In [45]-[49], an antenna-multiplexing technique is used to mitigate the self-interferences by assigning some array elements as TX and the others as RX with two BFNs, as shown in Fig. 6.1(a). In [130]-[134], antenna-ports-multiplexing is utilized where each antenna has its own TX and RX ports and two separate TX/RX BFNs, as seen in Fig. 6.1(b). Clearly, most of these C-STAR approaches can suppress the self-interferences, but with one or more drawbacks. Among these are: twice the number of antennas and BFNs; reduction in efficiency; narrow bandwidth; high cost; insufficient isolation; dissimilar TX and RX radiation patterns; different TX and RX polarizations; and larger size. Realizing a monostatic C-STAR broadside circular array configuration with a shared TX/RX BFN, as shown in Fig. 6.1(c), can reduce the antenna elements by half and further simplify the BFN. To the best of our knowledge, this C-STAR topology has not been widely used since the achieved TX/RX isolation of ~15 dB is low. The SI is high mainly due to the BFN's leakages and antenna's mismatch which are re-routed to the RX port of the C-STAR antenna sub-system.

In this chapter, a novel wideband monostatic C-STAR circular array with a shared BFN is proposed to overcome some of these aforementioned limitations while achieving higher TX/RX isolation, maintaining similar co-polarized TX and RX radiation characteristics, as shown in Fig. 6.2. Both TX and RX sides have similar single or dual circular polarization capability which is desirable to mitigate polar-

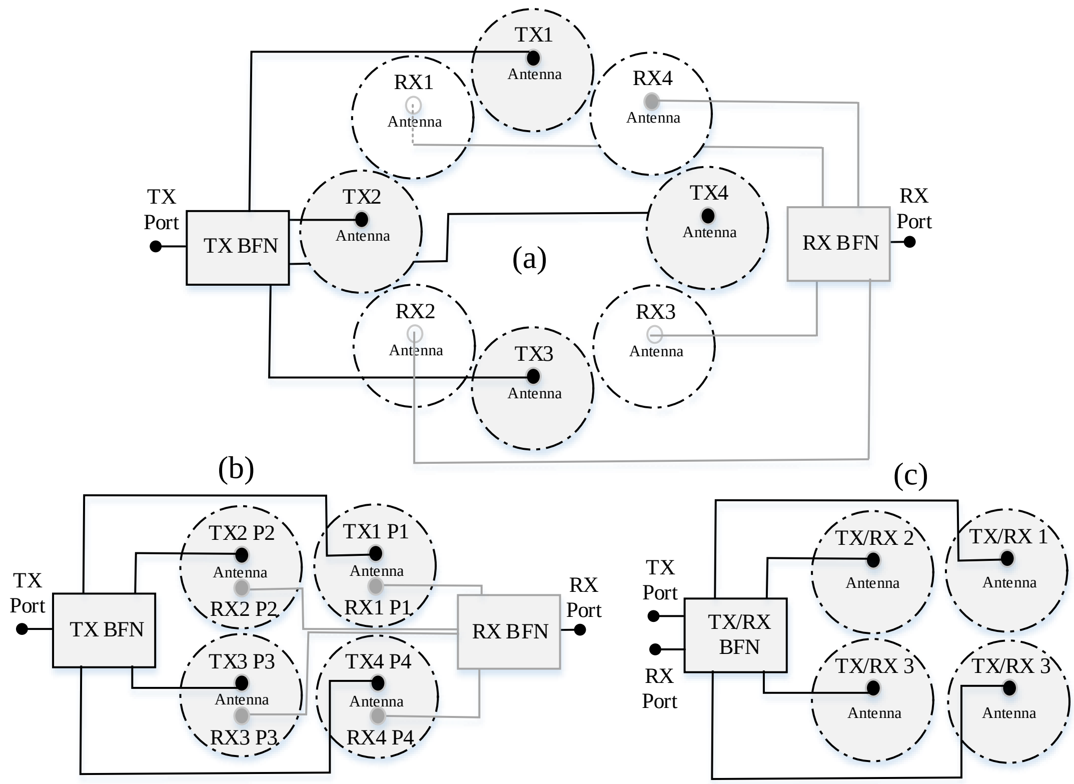

Figure 6.1: A circular C-STAR array, (a) with antenna-multiplexing and two BFNs, (b) with antenna's ports-multiplexing and two BFNs, and (c) with a shared TX/RX BFN and without any antenna-multiplexing.

ization mismatch and multi-path effects. With the proposed C-STAR configuration, the complexity of the BFN is reduced and the number of antenna elements in the array are either reduced by half or decreased compared to the existing C-STAR techniques [45]-[49], [130]-[134]. The proposed array configuration incorporates antenna elements orientation and partially shared BFN [135] to eliminate the self-interference from the TX to the RX without any time, frequency, spatial, pattern, antenna port, or polarization multiplexing. In the absence of geometrical asymmetry and feed imperfections, this approach achieves ideally full self-interference cancellation. To experimentally verify the proposed concept, a C-STAR circular array of four planar spiral antennas is designed, fabricated, and measured. Several studies are being carried out, including the effects of BFN amplitude and phase imbalances.

To mitigate the impact of imbalances and imperfect assembly on TX/RX isolation, a simple tunable isolation enhancement circuit layer is integrated. Extending the proposed C-STAR configuration to allow dual-polarization capability is briefly discussed using a conical sinuous antenna. Note that the discussion in this chapter places special emphasis on the spiral and sinuous antennas, although the C-STAR technique can be adapted to use different types of circularly-polarized antenna elements.

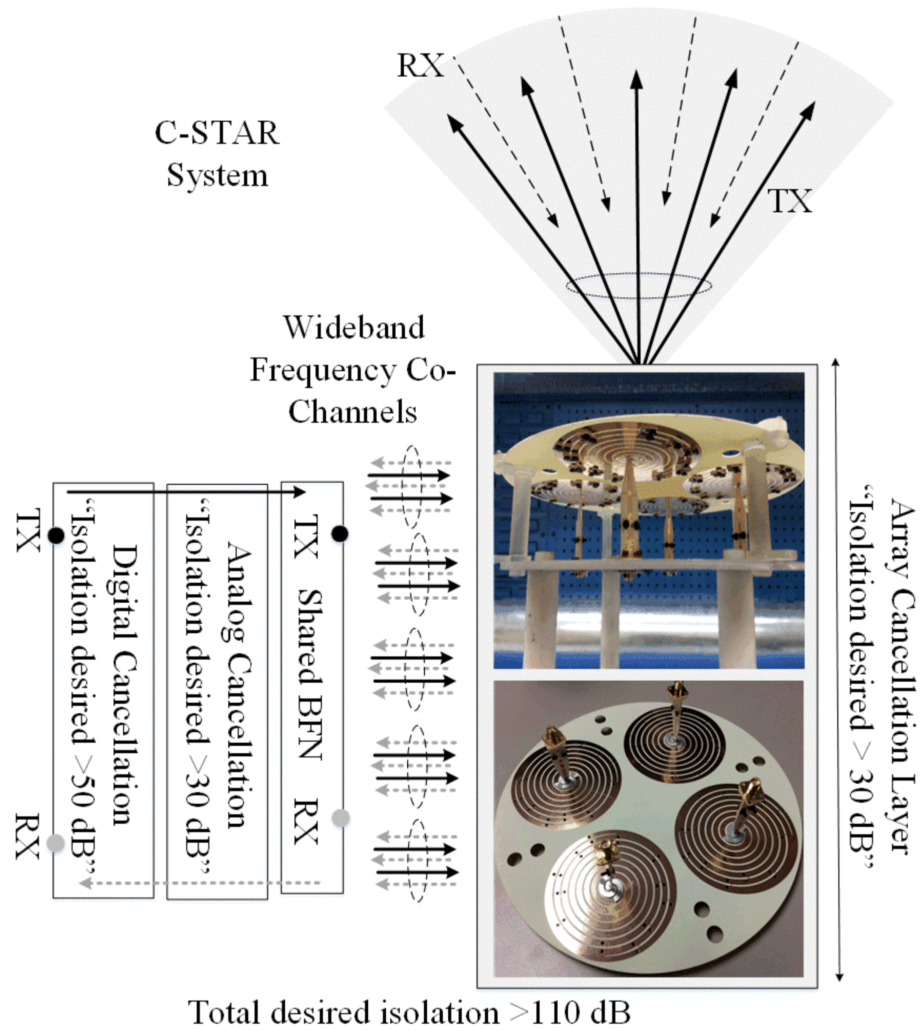

Figure 6.2: Illustration of C-STAR operation using multiple self-interference cancellations layers system.

In this chapter, a wideband C-STAR broadside circular array configuration is thoroughly discussed with a narrative organized as follows:

- Section 6.2 discusses the theory behind the SI cancellation as applied to the proposed sub-system.
- Section 6.3 presents the full-wave analysis of the considered spiral and sinuous arrays to validate the theory.
- Section 6.4 discusses the prototyped C-STAR spiral arrays and far-field performance to experimentally validate the proposed antenna array sub-system.
- Section 6.5 provides a comparison between different measured C-STAR circular arrays.
- Section 6.6 summarizes this chapter.

6.2 Theory of Self-Interference Cancellation

6.2.1 Single Circularly-Polarized C-STAR Array Configuration

Broadside circular arrays with four antenna elements are often driven with uniform magnitudes and $\{0°, \pm 90°, 180°, \pm 270°\}$ phase progression to generate a pure circular polarization (CP) [136]. In this chapter, the broadside circular array is excited differently to allow the simultaneous TX and RX operation on the same frequency; high TX/RX isolation; similar TX and RX broadside beams with good CP quality; less complex TX/RX BFN without 90° hybrids; less number of TX/RX antenna elements; and lower power loss. The schematic of the proposed C-STAR monostatic circular array configuration is shown in Fig. 6.3. As seen, the array consists of four CP antenna elements that are rotated by 90° around the origin. Each monostatic antenna element has a single port that is used simultaneously for TX and RX operation. The array is then integrated with a partially shared BFN which consists of three 180° hybrids and one power divider. The power divider is assigned to the TX side and two 180° hybrids are shared by both TX and RX sides whereas the third 180° hybrid is dedicated to the RX port. As seen in Fig. 6.3, the full BFN has three input ports denoted as 1-TX, 1-RX, and 1-unused ports. The other four output ports are connected to the four antennas which could be spirals, patches, helices, and any other antenna elements operating with CP capability. The array's TX and RX excitations are assigned as follows:

TX mode: the four antennas have similar magnitudes whereas their phases are assigned as {0°, 180°, 180°, 0°}.

RX mode: the four antennas have similar magnitudes whereas their phases are assigned as {0°, 0°, 180°, 180°}.

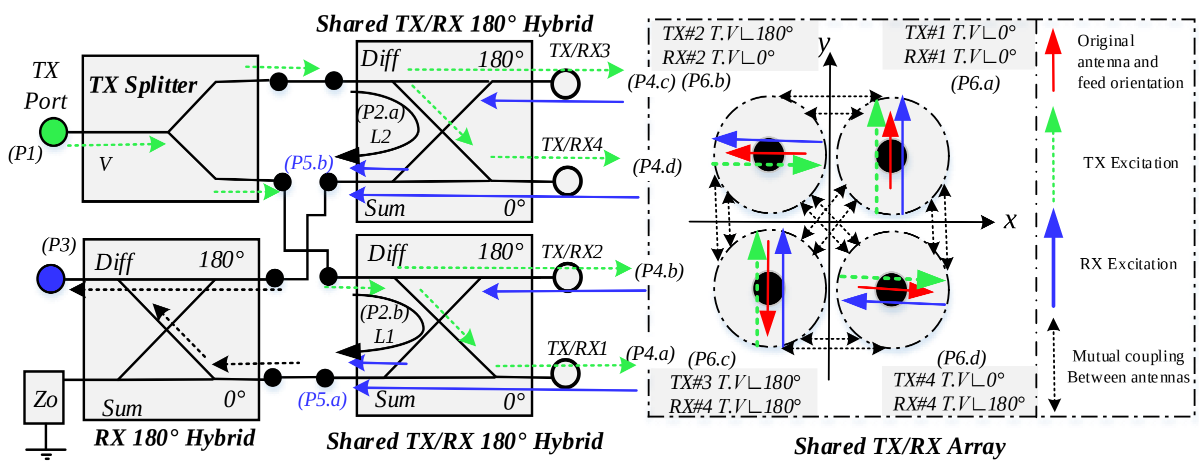

Figure 6.3: Signal flow diagram of the TX/RX excitation and TX signal cancelation of the broadside monostatic circular C-STAR array configuration.

Notice that the considered BFN typically excites circular array mode 2 {0°, 180°, 0°, 180°}; but, with the proposed configuration, the BFN ports are connected to different antenna ports and switched to {0°, 180°, 180°, 0°} and {0°, 0°, 180°, 180°}. By changing the arrangement of the excited phases, the simultaneous TX/RX with two broadside TX/RX beams is realized. Moreover, the induced self-interferences by the BFN's leakages, element-to-element mutual coupling, and mismatch reflections are all cancelled. In this C-STAR configuration, the applied excitations to the shared array are essential for the cancellation process along with the antennas' orientation. To demonstrate the operation of the C-STAR circular array, the signal flow diagram from the TX port to RX port is analyzed as illustrated in Fig. 6.3. In order to simplify the analysis, it is assumed that the shared TX/RX BFN is imbalances-free and its components have limited isolation. Symmetry along the antenna elements is also assumed; the four active reflection coefficients are ideally identical. Three cancellation mechanism are then utilized in this C-STAR circular array and explained as follows:

(1) Leakage Cancellation: First, the TX port is excited with a voltage signal V, as shown in Fig. 6.3 (P1). Then, the power divider splits the input TX signal into two signals (light-green color), where each enters the difference port of the two shared TX/RX 180° hybrids. Due to their limited isolation, the two in-phase TX leaked signals are re-routed back (blue color) to the third 180° RX hybrid (P2. a-b). The latter provides the needed phase difference of 180° between these two leakages, therefore enabling the full cancellation at (P3).

(2) Antenna Cancellation: Once the through signals reach the four antenna elements, the array becomes excited in TX mode, as shown in Fig. 6.3 (P.6 a-d). Note that the excitations of the second and third antenna elements are reversed by 180° to ensure broadside TX radiation patterns. Once the four antenna elements are excited, some coupling occurs, as shown in Fig. 6.4. As seen in Fig. 6.4.a, the coupling from the adjacent elements (antennas 2 and 4) are cancelled at antenna 1 due to the provided 180° phase difference, 180° rotation, and the Balun's differential phase. However, the coupling from the diagonal element is remained and redirected to the shared BFN. The same principle applies to the excited antenna elements, as shown in Fig. 6.4.b-d. The coupling of these diagonal elements slightly affects the active reflection coefficient of each antenna element.

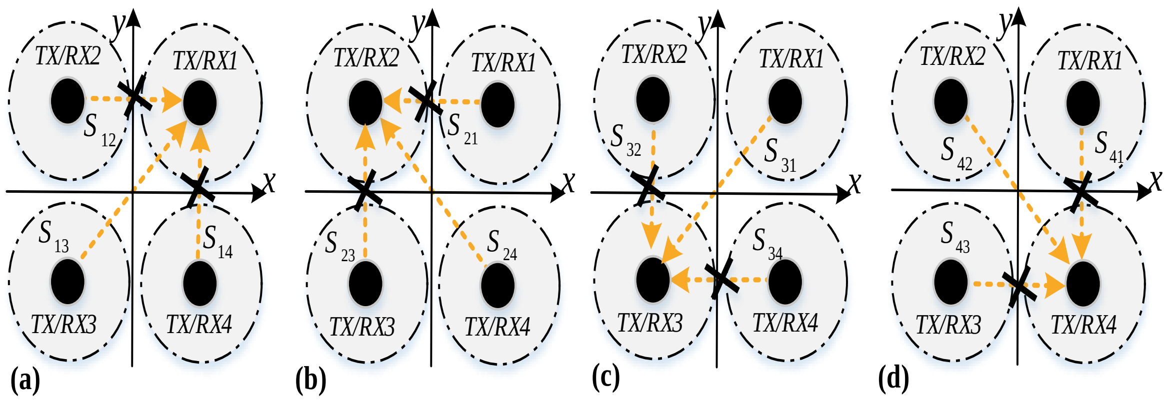

Figure 6.4: Illustration of coupling between the C-STAR circular array's antennas. (a) Coupling mechanisms for antenna element 1 (b) Coupling mechanisms for antenna element 2 (c) Coupling mechanisms for antenna element 3, and (d) Coupling mechanisms for antenna element 4.

(3) <u>Mismatch Reflections Cancellation:</u> The four generated signals pass through the shared two TX/RX 180° hybrids (P4. a-d in Fig. 6.3), where all have equal amplitudes and {0°, 180°, 180°, 0°} phases. Once they reach the antennas' ports, four reflected signals are induced due to the limited return loss of each antenna port. Note that these four reflections contain also the coupling that comes from the diagonal elements which have not been cancelled at the antennas' ports. These mismatches are then re-routed back through the shared TX/RX 180° hybrids (P4. a-d). Each two reflections ideally has similar magnitudes and 180° out of phase, thus they are cancelled out at the sum ports of the two shared TX/RX hybrids before reaching the third 180° RX hybrid (P5. a-b). If the symmetry is maintained along all the array elements and both 180° hybrids, the shared TX/RX BFN effectively cancels all four reflections. Ideally, in this C-STAR configuration, only the RX signal of interest is routed to the 180° RX hybrid port. Hence, the array is excited to operate simultaneously in TX and RX modes. Where the RX side is excited as well with equal magnitudes, but different {0°, 0°, 180°, 180°} phases compared to the TX excitation in the shared TX/RX array. With this RX excitation, the phase excitations of the third and fourth elements are reversed to ensure that the shared array produces a broadside RX beam similar to the TX.

6.2.2 Dual Circularly-Polarized C-STAR Array Configuration

Another interesting feature of the proposed configuration is that it can be readily extended to have dual circularly-polarized capability over a wide operating bandwidth. The schematic of the proposed dual CP monostatic C-STAR circular array configuration is shown in Fig. 6.5. As seen, the array consists of four dual CP antenna elements rotated 90° around the origin. Every individually shared TX/RX antenna element is used simultaneously for TX and RX operation and each two diagonal elements are excited with a differential mode. The dual-polarized array is then integrated with two BFNs, one is assigned to excite the right hand circular polarization (RHCP) mode whereas the other excites the left hand circular polarization (LHCP) mode. Each BFN consists of three 180° hybrids and one power divider, similar to the single CP configuration. In this case; however, there are two TX ports, one assigned for each CP handiness; the same applies to the RX ports. This array is able to operate in TX and RX modes simultaneously with a single polarization at each time.

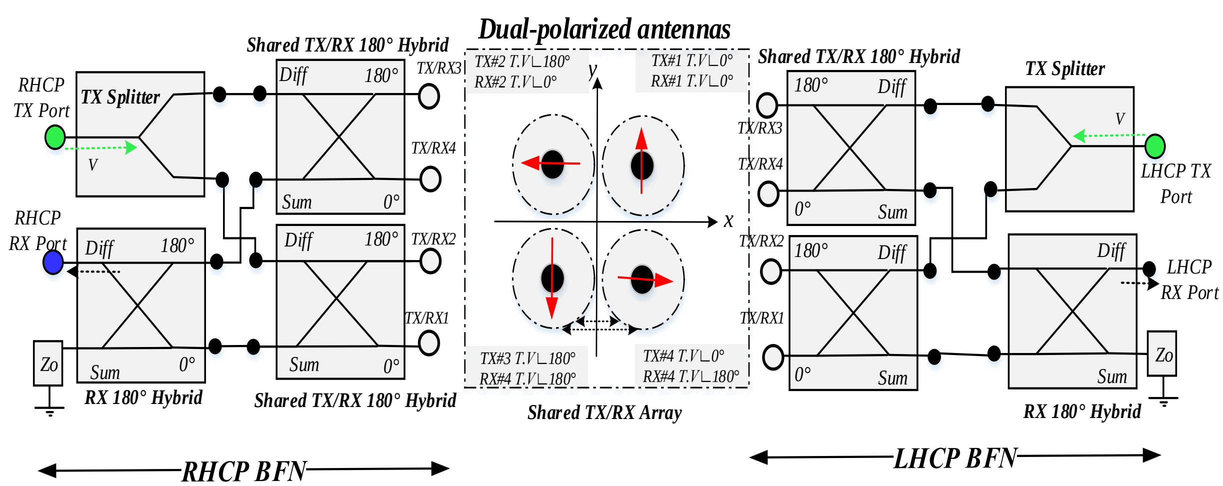

Figure 6.5: Signal flow diagram of the TX/RX excitation and TX signals cancelation of the broadside monostatic dual CP circular C-STAR array.

The self-interference cancellation mechanism herein is similar to the single polarization system in Fig. 6.3. Note that the coupling of RHCP to LHCP depends on the selected dual CP antenna elements. For example, when a dual CP patch antenna is used, the coupling between the RHCP to LHCP ports is typically high (~3-5 dB), resulting in increased power loss. However, when a dual CP sinuous antenna is used as a single element, the coupling between the cross polarizations is limited by the isolation of the realized 90° hybrid; specifically between the two orthogonal feeding ports.

6.3 Computational Analysis

To validate the self-interference cancellation concept, two C-STAR arrays of single and dual CP capabilities are modeled in ANSYS HFSS [115]. The first array consists of four planar RHCP Archimedean spiral antennas. The spiral element in this configuration helps achieve wideband operation with good and consistent impedance match and stable radiation patterns. Each spiral antenna has a two-arm with four-turn and a 3:1 metal-to-slot ratio. Their outer and inner radii are set to 4 cm and 0.15 cm, respectively, resulting in an array with a diameter of 22 cm. The second array consists of four 18 cm tall conical dual-polarized sinuous antennas with outer and inner radii of 5.7 cm and 0.4 cm, respectively. The center-to-center spacing is 6 cm, while the outer radius of the array is 27 cm. Both arrays are illustrated in the inset of Fig. 6.6. The planar and conical configurations are chosen only to prove the proposed concept for the single and dual CP C-STAR configurations shown in Figs. 6.3 and 6.5. The conical dual-polarized sinuous array, as discussed in the previous section, needs two TX/RX BFNs to excite each polarization. Also, there are four shared TX/RX 90° hybrids behind the four sinuous antennas to enable excitation of both RHCP and LHCP. To determine the port-to-port TX/RX isolation of the proposed configurations, the obtained S-parameters from ANSYS HFSS are imported into the AWR circuit simulator, where ideal TX/RX C-STAR BFNs shown in Figs. 6.3 and 6.5 are used. The results for the obtained TX/RX isolation (i.e. negative sign compared to the mutual coupling) are plotted in Fig. 6.6. As seen, the isolation is >60 dB for both arrays, which computationally validates the principle of cancellation. With the ideal BFN, the isolation is limited by mesh quality/symmetry of the modeled antennas. Furthermore, the antenna elements' geometric parameters (e.g. number of turns, height, growth rate, and center-to-center spacing) are irrelevant to the isolation level as long as the geometric symmetry is maintained.

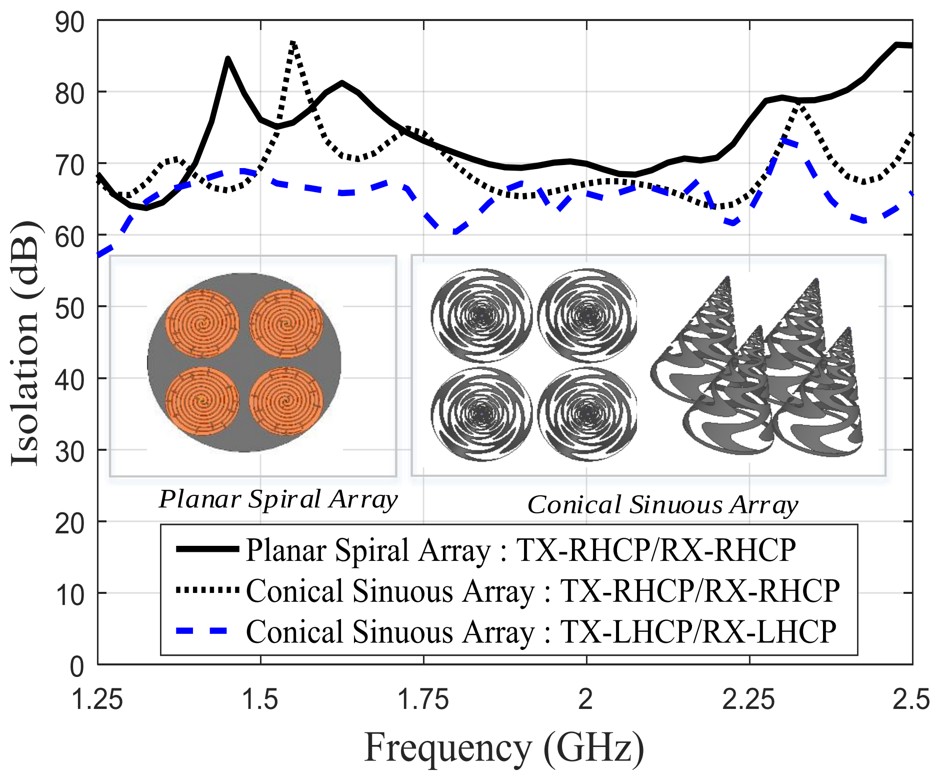

Figure 6.6: Simulated TX/RX isolation of a C-STAR spiral and sinuous arrays that are connected with an ideal TX/RX BFN. Spiral and sinuous circular arrays are depicted in the inset.

Until this point, the BFN's components are considered ideal to simplify the analysis and verify the proposed concept. In practice, however, these components have different responses over the operating bandwidth. This results in an asymmetry between the four mismatches and two internal leakages which causes degradation of TX/RX isolation. To examine more the effects, a study with only the single CP spiral antenna C-STAR array is conducted, where similar conclusions apply to the dual CP C-STAR array configuration. To show the variation in TX/RX isolation due to the BFN imperfections, random amplitude and phase imbalances are introduced to the BFN's components in the AWR circuit simulator. Specifically, these are chosen to be between 0–0.6 dB and 0–8°, respectively. Note that the chosen imbalances in this study are assumed to be frequency-independent to give an insight into the impact of imbalances. In practice; however, they depend on the BFN realization and varies randomly with frequency over the wide bandwidth. As seen in Fig. 6.7, the isolation falls from the 70 dB range to 35 dB. The shaded areas represent the variation margin between the minimum/maximum isolation for a selected random distribution of imbalances. As seen, even in the case of high imbalances, computational results indicate a wideband self-interference cancellation of over 30 dB.

In order to partially recover from BFN imbalances, asymmetric leakages, and geometric misalignment due to fabrication and assembly tolerances, an additional isolation enhancement layer can be introduced as shown in Fig. 6.8. This layer is connected to the unused sum port of the RX 180° hybrid, which carries the combined signals of sustained leakages and reflections. The simple isolation enhancement layer consists of a tunable attenuator, a tunable phase shifter, and a power divider. This layer operates by adjusting the amplitude and phase weights of the residual self-interference at the unused sum port of RX 180° hybrid to favorably superimpose them with the referenced signal at the RX port, thereby enhancing the cancellation. This cancellation should not affect the RX radiation pattern and is accomplished by linking the simulated S-parameters of the C-STAR array and TX/RX BFN with the ideal tunable isolation enhancement layer in the AWR circuit simulator. A tunable attenuator and a phase shifter are used, where each being varied up to 80 dB in 2.5 dB steps and 360° in 0.4° steps, respectively. As seen in Fig. 6.9, the resulting TX/RX isolation is improved up to 50 dB compared to the worst case.

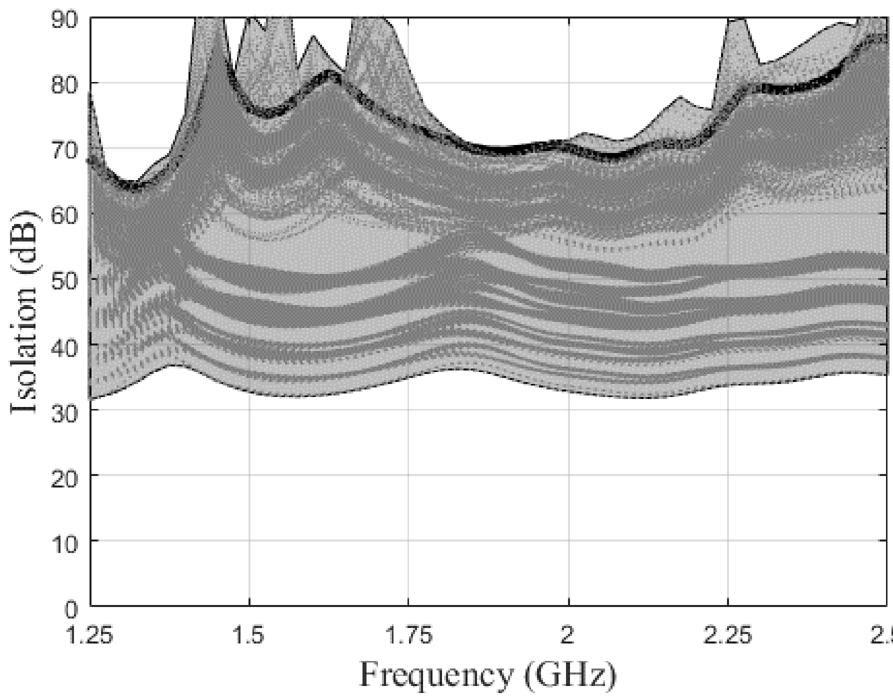

Figure 6.7: The effects of the BFN's amplitude and phase imbalances on the overall C-STAR sub-system isolation.

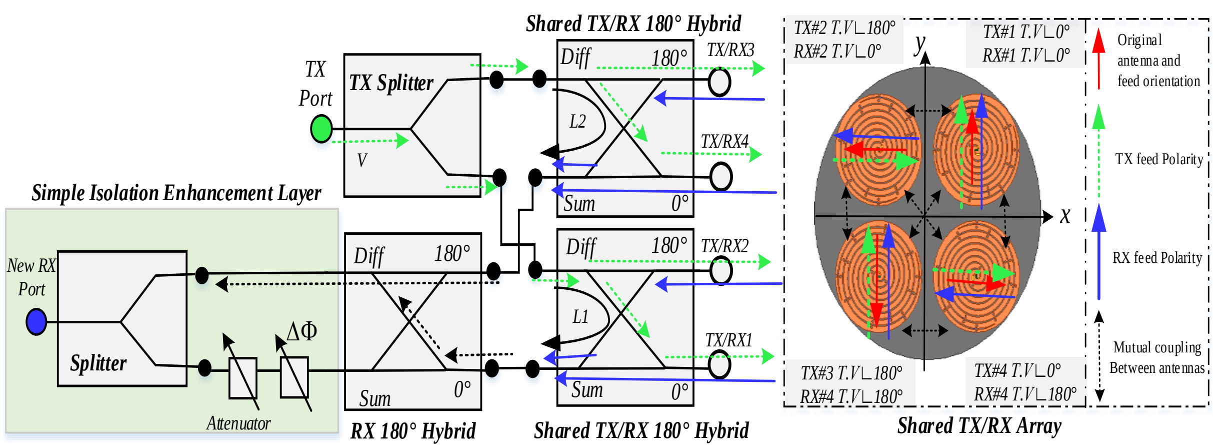

Figure 6.8: Signal flow diagram of the TX/RX excitation and TX signal cancelation of the broadside single CP monostatic circular C-STAR array configuration.

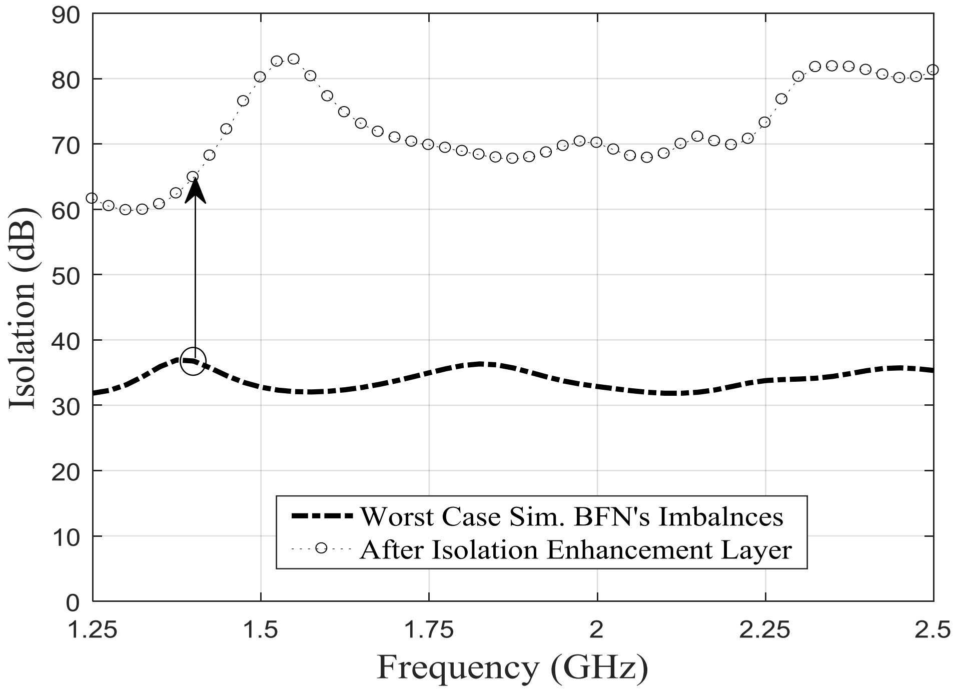

Figure 6.9: The isolation before and after the isolation enhancement layer.

6.4 Fabrication and Measurements

The spiral array is fabricated to experimentally verify the proposed C-STAR concept. The details of the simulated and fabricated C-STAR array geometries are shown in Fig. 6.10. The array consists of four two-arm slot Archimedean spirals as described in Section 6.3. The array is fabricated on a 0.76 mm-thick Rogers 4350 substrate with ε_r and tanδ of 3.66 and 0.004, respectively and is backed by a 22 cm diameter ground plane. Six resistors with resistance of: 900, 750, 412, 300, 200, and 150 ohms are used at each arm termination to improve the axial ratio at low frequencies. To achieve good impedance match over the operating bandwidth, four microstrip to parallel strip lines baluns with impedance transformers are used to feed the spirals. The simulated and measured VSWRs of the fabricated array with and without connecting the array to the realistic TX/RX BFNs are shown in Fig. 6.11. As seen, the simulated and measured VSWRs are <2 over the most of the bandwidth.

The measured isolation of the fabricated C-STAR array is shown in Fig. 6.12. The BFN is realized by commercial-off-the-shelf hybrids and a power divider. As seen, TX/RX isolation >38 dB is achieved. The resistive termination is a necessary complex efficiency compromise needed to improve far-field performance. Its impact on the C-STAR sub-system isolation is insignificant as seen in Fig. 6.12. To demonstrate the importance of the BFN imbalances and asymmetric leakages on overall isolation, the simulated S-parameters of the array are cascaded with the measured responses of BFN in the AWR circuit simulator. As seen, the obtained isolation (simulated antenna with measured BFN) agrees well with the measured isolation (measured antenna with measured BFN), this confirming the analysis in Section 6.3. Another way to show the importance of imbalances and asymmetric leakages is to connect the simulated array's S-parameters to the two identical measured (shared) TX/RX 180° hybrids in AWR, but use a different RX-180° hybrid. As seen in Fig. 6.12, the achieved isolation is >50 dB over the bandwidth.

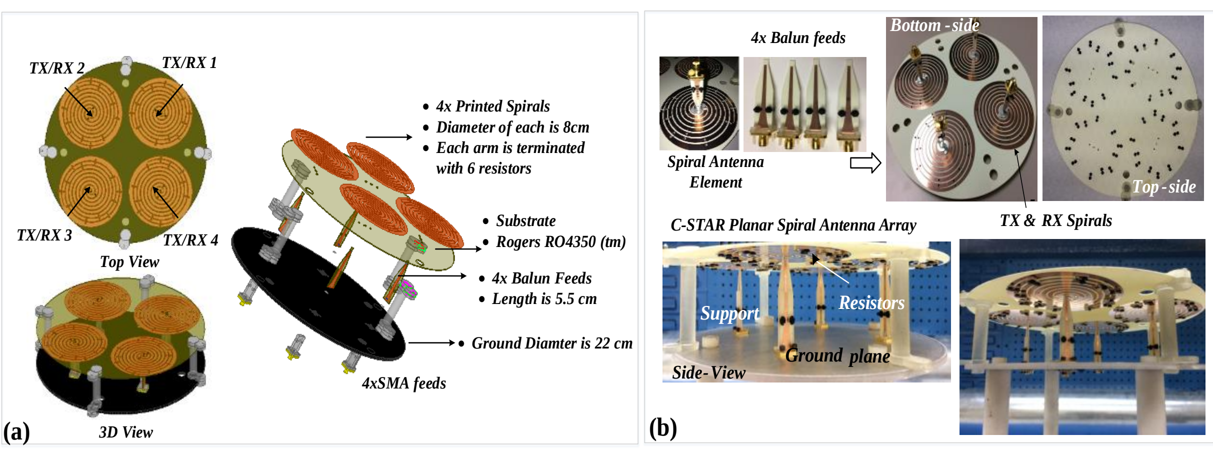

Figure 6.10: (a) Geometrical details of the proposed C-STAR Archimedean spiral array, and (b) the fabricated array

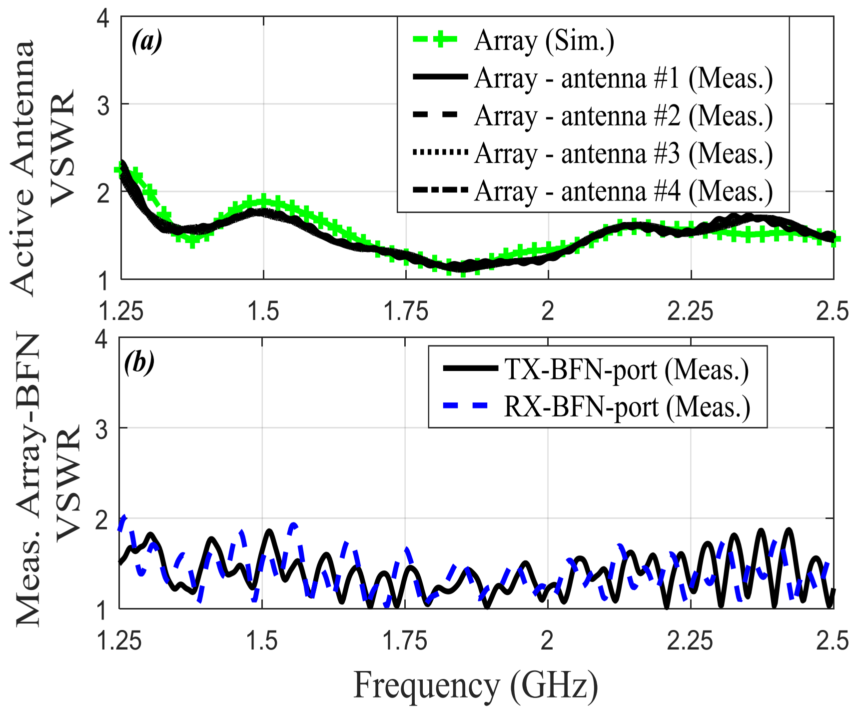

Figure 6.11: (a) Simulated and measured active VSWRs at the input of the TX/RX antenna array. (b) Measured VSWRs at the BFN's TX and RX ports once the array is connected to the TX/RX BFN.

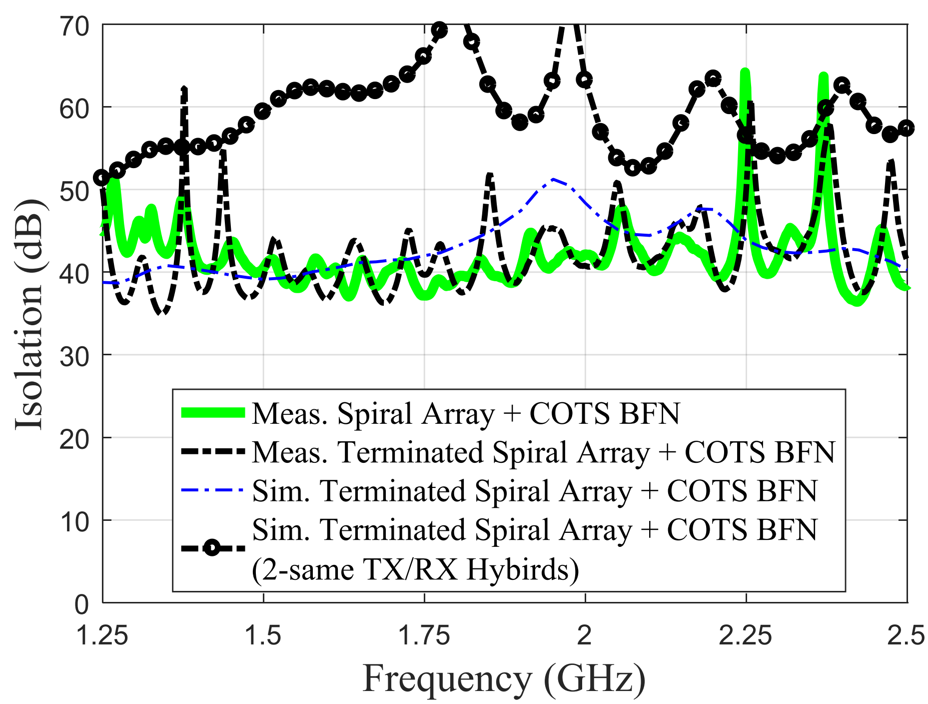

Figure 6.12: Simulated and measured isolation of the proposed C-STAR array.

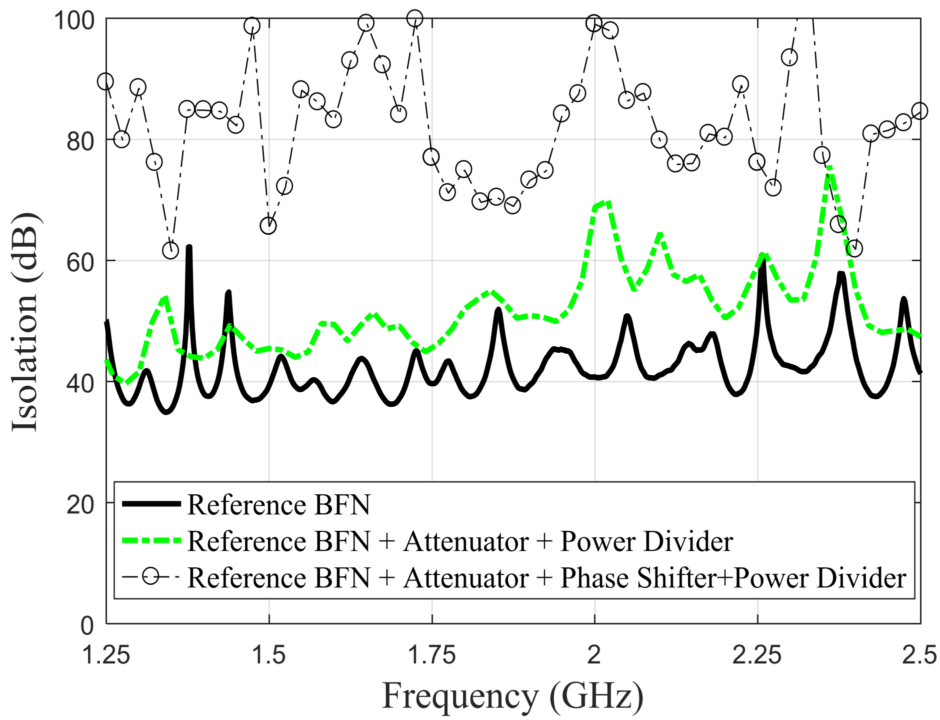

Figure 6.13: The improvement in measured isolation once the isolation enhancement layer is integrated with the reference BFN.

As discussed previously, the realistic BFN's amplitude and phase imbalances and mechanical assembly can contribute to realize imperfect symmetry and therefore degrade the isolation. To improve isolation, the unused sum port of the RX hybrid (Figs. 6.3 and 6.7) is connected first to a 25 dB attenuator and a power divider to combine the attenuated sum of the leakages and the reference RX signal plus the residual self-interference (i.e. the phase shifter has not been connected yet). The attenuation level is determined by the difference between the power levels of the residual leakages at the RX port and the tapped signal at the sum port. Measured isolation between 40-60 dB with improvement up to 18 dB is achieved compared to the original setup. To show the maximum possible isolation that can be achieved, an ideal tunable phase shifter and an attenuator are considered and both are cascaded with the measured antennas' and BFN's S-parameters in AWR. The phase shifter has a range of up to 180° in phase with 0.25° steps, and the attenuator has a range of 80 dB of attenuation with steps of 1.5 dB. As seen in Fig. 6.13, the isolation improvement with this cancellation layer can be higher than 50 dB.

The measured and simulated co-polarized realized gain of the TX and RX phase modes vary between 3 dBic and 9.7 dBic as shown in Fig. 6.14. Due to the considered excitations and antenna elements orientation, the aperture efficiency of the proposed C-STAR circular array configuration is ~50% for the TX and RX sides. Therefore, the realized gain of the array is 3 dB smaller than that obtained with the conventional sequential rotated arrays with CP antennas [136]. The simulated and measured axial ratios of TX and RX C-STAR arrays are also shown in Fig. 6.14.

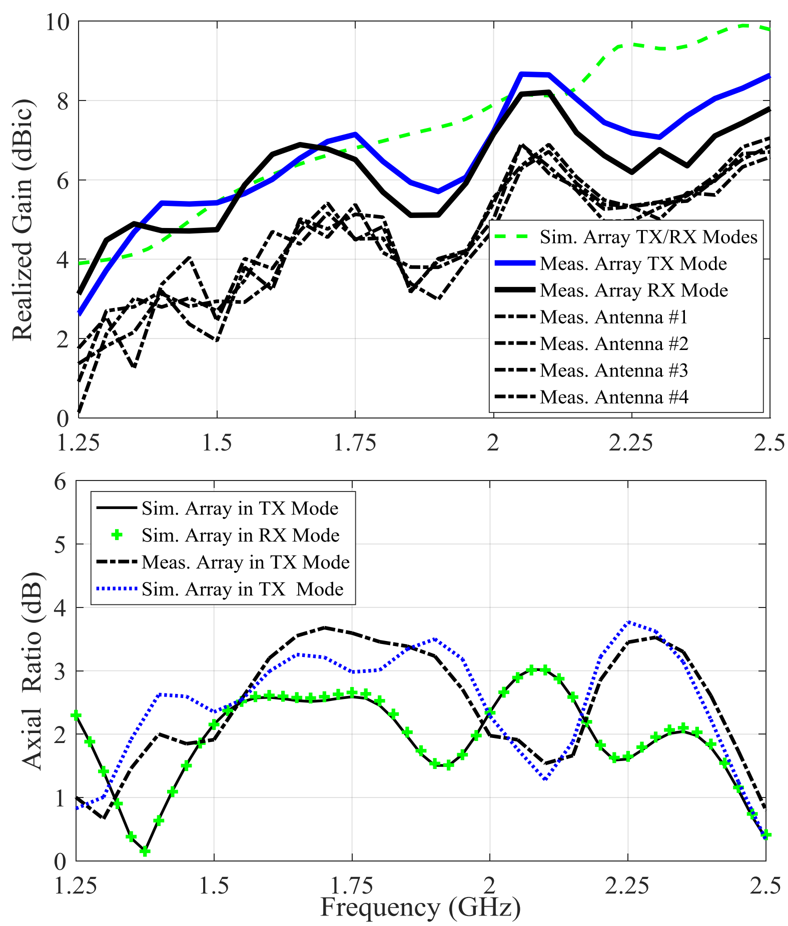

Figure 6.14: Simulated and measured (left) broadside axial ratio and (right) broadside realized gain of the C-STAR spiral array.

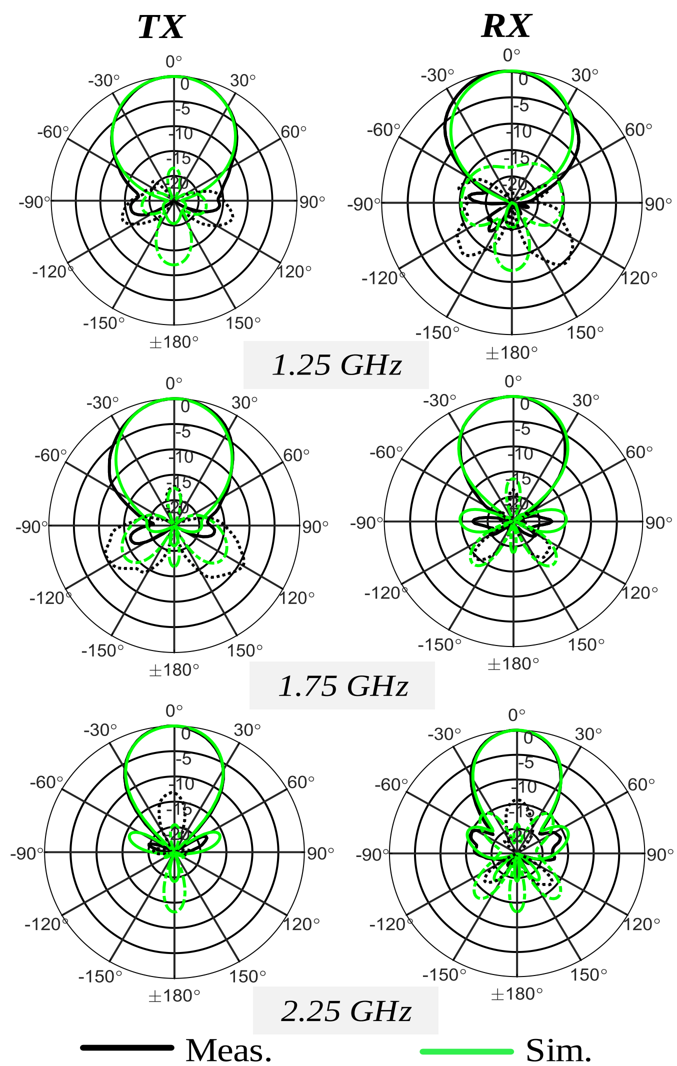

Figure 6.15: Simulated (dark-black) and measured (gray) TX (left) and RX (right) co-(solid) and cross-polarization (dashed) patterns of the C-STAR spiral array.

As seen, the TX and RX modes have simulated and measured boresight axial ratios <3 dB and <3.7 dB, respectively. The backed ground plane's height and finite size as well as the provided TX and RX excitations tend to degrade the axial ratio. To improve the polarization quality, the planar spiral antenna can be replaced with a conical structure. The simulated and measured radiation patterns are depicted in Fig. 6.15. As seen, good agreement between the measured and simulated results are obtained for both TX and RX sides. Measured radiation patterns of the TX mode in the azimuthal planes ($\phi = 0°$, and $90°$), and ($\phi = 45°$) are illustrated in Fig. 6.16. As seen, the beamwidth in the diagonal plane becomes narrower as the frequency increases compared to the principle planes. This is mainly due to the chosen array's excitation phases {0°, 180°, 180°, 0°}. Similar performance is observed for the RX mode.

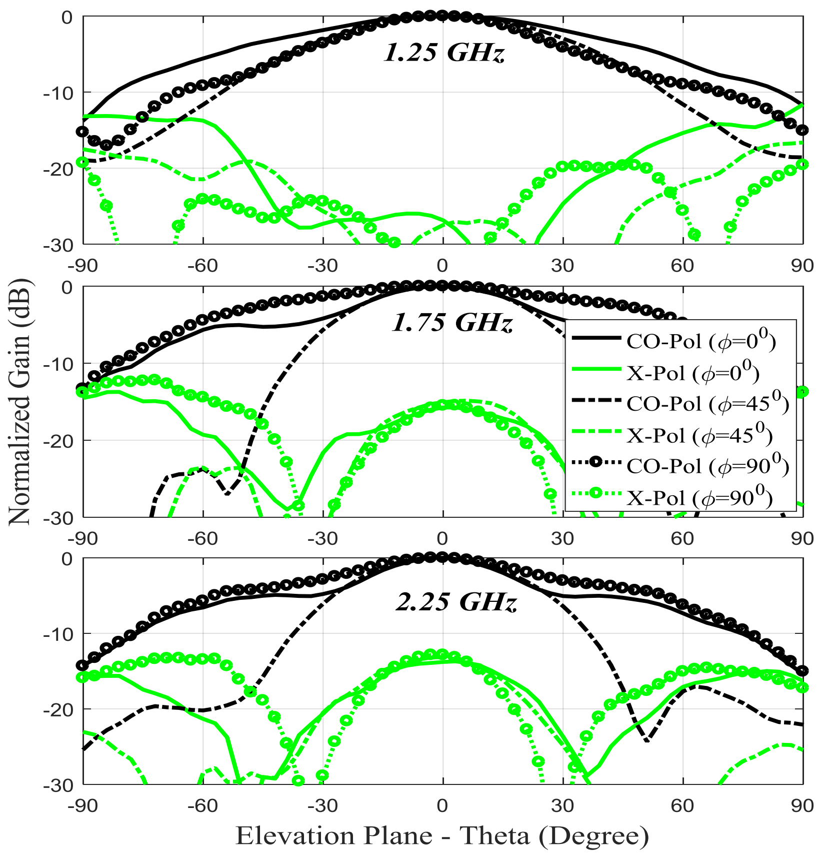

Figure 6.16: Measured principle at (ϕ =0°, 45°, and 90°) CP patters of the C-STAR spiral array in TX mode.

A true C-STAR monostatic array ideally has identical TX and RX radiation patterns. However, in the proposed configuration, the array is excited simultaneously with different sets of TX and RX phases, which impacts the pattern similarity. To quantify the similarity, the ECC parameter is considered. To calculate ECC, two sets of independent TX and RX far-field simulations or measurements are needed as described in the previous chapters. The simulated and measured results of the ECC are shown in Fig. 6.17. The ECC is taken over $\theta < \pm 30°$ and all azimuthal cuts. As seen, ECC >0.93 is obtained over an octave bandwidth indicating good pattern similarity between the TX and RX radiation patterns.

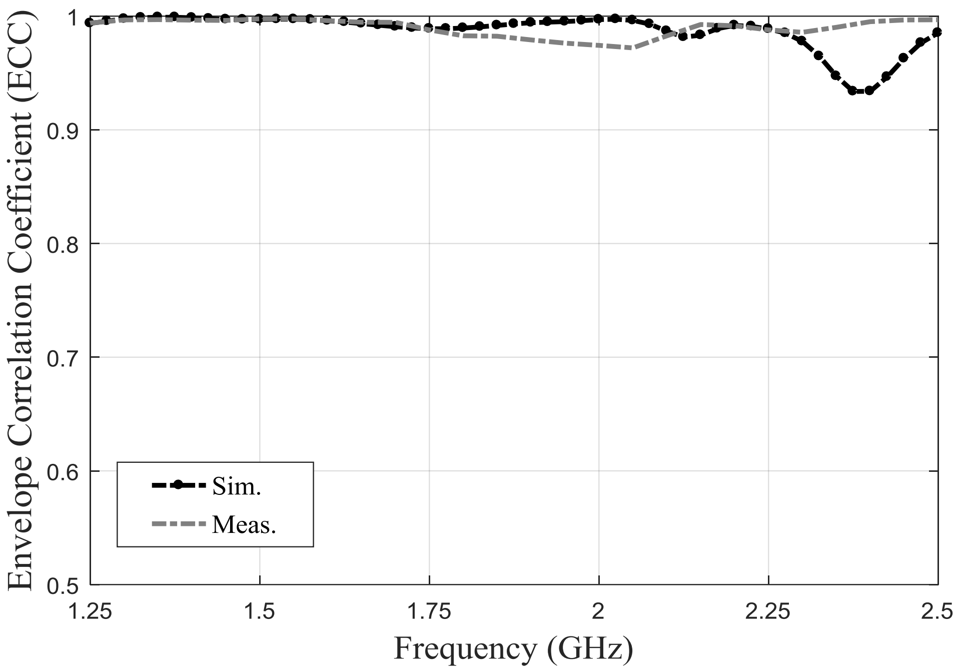

Figure 6.17: Measured and simulated ECC of a C-STAR spiral antenna array excited in TX and RX modes and at elevation angles between $\theta = \pm 30°$

6.5 Performance Comparison with Other C-STAR Broadside Arrays

The proposed C-STAR circular array configuration is compared to other state-of-the-art "measured broadside" C-STAR arrays in Table 6.1. Antenna multiplexing with quadrifilar spiral antennas [130] and a PIFA array [131] are used with BFN cancellations to achieve high measured TX/RX isolation over the narrow bandwidths of 860-960 MHz and 2.4-2.5 GHz, respectively. The level of coupling between the TX and RX antennas are high which leads to high power loss and a drop in total efficiency. These C-STAR systems also require two BFNs; one for TX and one for RX to achieve isolation 38-42 dB. In [132, 133], antenna's port multiplexing is used alongside BFN cancellation to achieve high measured TX/RX isolation 39-65 dB using sequentially rotated patch arrays. Each array's antenna element has its own TX/RX isolation over narrow bandwidths 5.4-5.6 GHz [132] and 2.4-2.5 GHz [133]. The coupling between TX and RX ports is improved since the feeding ports have orthogonal linear polarizations, but the C-STAR array has overall co-polarized CP polarization. However, with this configuration, two BFNs are required as well, one for TX and one for RX.

Table 6.1: Comparison between measured characteristics of Different C-STAR Broadside Arrays

	Isolation Improvement Technique	Isolation Min-Max	BW	TX/RX Max Gain/ AR	Dimensions In term of low Frequency	Complexity/ Cost /Number of Antennas/ Ports/ BFN	Monostatic/ Separation-Independent Bistatic	Efficiency/ ECC
[28]	Antenna Multiplexing and BFN Cancellation	38-43 dB	860-960 MHz	1 dBic/ 0.7 dBic/ <2 dB	~ $0.57\lambda \times 0.57\lambda$	High/ High/ 8 Antennas each has 1 Port/ 2×BFNs	Separation-Independent Bistatic	Moderate/ High
[29]	Antenna Multiplexing and BFN Cancellation	38-42 dB	2.4-2.5 GHz	6.25 dBic/ 6.25 dBic/ <4 dB	~ Radius $=0.4\lambda$	Moderate/ Low/ 8 Antennas each has 1 Port/ 2×BFNs	Separation-Independent Bistatic	Moderate / High
[30]	Antenna's Port Multiplexing and BFN Cancellation	39-54 dB	5.4-5.6 GHz	6 dBic/ 6 dBic/ <2 dB	~ $1.04\lambda \times 1.04\lambda$	Moderate/ Low/ 4 Antennas each has 2 Ports/ 2×BFNs	Monostatic	High/ High
[31]	Antenna's Port Multiplexing and BFN Cancellation	47-65 dB	2.4-2.5 GHz	7 dBic/ 7 dBic/ <1.6 dB	~ $2.4\lambda \times 2.4\lambda$	Moderate/ Low/ 4 Antennas each has 2 Ports/ 2×BFNs	Monostatic	High/ High
[32]	Antenna Multiplexing and BFN Cancellation	27-60 dB	0.5-2.75 GHz	13 dBic/ 13 dBic/ <4.7 dB	~ $0.62\lambda \times 0.71$	Low/ Low/ 7 Antennas each has 2 Ports/ Microstrip feed	Monostatic	Moderate / High
[38]	Antenna's Port Multiplexing, Polarization Diversity, and BFN Cancellation	53-65 dB	2.34-2.54 GHz	14.4 dBi / 14.4 dBi / Linear	-	Moderate/ Low/ 4 Antennas each has 2 Ports/ 2×BFNs	Monostatic	Moderate / Very Low
This Paper	No Antenna and Antenna's Port Multiplexing are Utilized. BFN Cancellation	38-62 dB	1.25-2.5 GHz	9.8 dBic/ 9.8 dBic/ <3.7 dB	~ Radius $=0.36\lambda$	Low/ Low/ 4 Antennas each has 1 port/ Partially Shared BFN	Monostatic	High/ Very High

In [134], a spiral C-STAR array is considered where each four-arm spiral antenna has two-arm assigned for TX and two-arm for RX. High measured isolation 27-60 dB can be achieved over ultra-wide bandwidth 0.5-2.75 GHz, yet, the existence of parasitic arms affects the far-field performance at low frequencies. In [137], antenna multiplexing, polarization diversity, and BFN cancellation are all utilized to achieve isolation 53-65 dB over a narrow bandwidth 2.34-2.54 GHz. In the proposed spiral C-STAR circular array configuration, the isolation level 38-62 dB is within the same range or higher level compared to the others over an octave of bandwidth 1.25-2.5 GHz. As seen in Table. 6.1, most approaches either use different antennas as TX and RX with two separate BFNs or antenna's port's multiplexing where each antenna has its own TX and RX ports and two separate BFNs. However, with the proposed configuration, each array's antenna operates as TX and RX simultaneously with a single feeding port and a partially shared BFN. This can lead to a decreased total number of TX/RX antenna elements, simpler BFN, reduced array size, and less complexity, and lower cost.

6.6 Summary

In this chapter, a wideband monostatic co-circularly-polarized broadside circular array C-STAR configuration is proposed. With this C-STAR configuration, the BFN complexity, overall array size, number of antenna elements, and cost are significantly reduced. The presented approach is developed based on antennas' orientation and partially shared BFN cancellation. In the absence of BFN's imbalances, asymmetric leakages, and array geometric asymmetries, the proposed concept can achieve theoretically infinite TX/RX isolation. For demonstration, two C-STAR arrays of four single circularly-polarized spiral and dual circularly-polarized conical sinuous antennas are utilized. To experimentally validate the proposed concept, the metal backed four two-arm spiral antenna array with four-element balun-feed is fabricated and measured over an octave of bandwidth 1.25-2.5 GHz. The results show average measured TX/RX isolation of >38 dB and >50 dB with an ideal isolation enhancement layer. Overall, good quality and similar TX/RX radiation patterns with average ECC >0.93 are obtained. Although the discussion presented in this chapter focused on the spiral and sinuous antennas, the proposed C-STAR concept can be applied with different types of single/dual CP antenna elements.

CHAPTER 7

CONCLUSIONS AND FUTURE WORK

7.1 Wideband Monostatic Co-Polarized Four-Arm C-STAR Spiral Antenna

Chapter 2 introduced a novel ultra-wideband, co-circularly-polarized, cost effective, circulator-less, monostatic C-STAR antenna sub-system based on a four-arm spiral antenna and feed cancellation technique. It has been theoretically proven that in the absence of asymmetric assembly and BFN's imperfections, infinite isolation is obtained between the TX and RX ports. Full-wave FEKO simulation and measurement are used to demonstrate that high isolation can be achieved with the proposed configuration over multi-octave bandwidths. A study on the influences of feed imbalances is also conducted to address some practical issues regarding the achievable isolation levels. The envelope correlation coefficient is proposed for first time in C-STAR configurations to quantify the degree of similarity between the TX and RX radiation patterns. To enhance the far-field performance and mitigate the radiation contamination effects of the parasitic arms, the spiral-helix is considered and its fabrication is used to experimentally demonstrate the proposed concept. Good match, isolation, patterns, gain, and ECC with moderate axial ratio are obtained with this proposed C-STAR antenna sub-system. Finally, a novel multi-layer coaxial exponential feed taper is proposed to feed the four-arm C-STAR spiral and avoid using the TX and RX 180° hybrids. Simulated isolation > 50 dB over 5:1 bandwidth is achieved using ANSYS HFSS tool.

7.2 Wideband Multimode Monostatic Co-polarized Four-Arm C-STAR Spiral Antenna Sub-system

Chapter 3 presented a wideband, multimode, monostatic, and dual-polarized C-STAR spiral antenna sub-system. The proposed C-STAR shared antenna sub-system utilizes multiple self-interference cancellation layers and the orthogonality of spiral modes to theoretically achieve infinite isolation between the TX and RX ports without any time, frequency, polarization, or spatial multiplexing. The C-STAR antenna sub-system configuration consists of a single four-arm spiral with four circulators, and two Butler matrix BFNs. The flexibility of achieving diverse circularly-polarized mode combinations (broadside and split-beam modes or RHCP and LHCP) using a single antenna while maintaining sufficient TX/RX isolation over a wide bandwidth is demonstrated. High-simulated isolation is achieved for all mode arrangements (1, 2, 3, and -1). The proposed theoretical baseline that is used to explain the isolation phenomenology is fully confirmed with these results. The measurements on a prototype are carried out to experimentally verify the proposed concept. Results show isolation between 23 and 38 dB for different mode arrangements. The obtained data emphasize the significance of imbalances. Even though the theoretical isolation is compromised in the presence of imbalances, more than 12 dB improvement is still seen compared to the isolation of COTS circulators. All modes have been shown to operate with excellent quality radiation patterns. For many C-STAR applications, the performance in isolation improvement that is afforded by the proposed C-STAR sub-system configuration justifies the additional cost and complexity of the BFN with circulators.

7.3 Wideband Multimode Lens-Loaded Co-polarized Eight-Arm C-STAR Spiral Antenna Sub-system

Chapter 4 reported a novel lens-loaded eight-arm spiral antenna with diverse co-polarized mode patterns for C-STAR applications. The proposed C-STAR shared antenna has two interleaved sets of four-TX and four-RX arms that are connected to two 4×4 Butler matrix BFNs. In this C-STAR configuration, the additional set of four-arm is introduced to the conventional four-arm spiral just to avoid the use of circulators as presented in Chapter 3 and further simplify the entire C-STAR sub-system. In the absence of any BFN imbalances and antenna geometry asymmetries, the proposed concept can achieve theoretically full self-interference cancellation between various TX/RX modes at either antenna's or BFN's ports. Computational and experimental studies are conducted to address the coupling from TX to RX arms. It is seen that the coupling is not really suppressed, but rather re-radiated and re-routed to the BFN or cancelled. Therefore, reduction in efficiency and far-field deterioration are the cost of achieving a multimode C-STAR antenna sub-system. As has been shown, the average measured TX/RX isolation over the operating modes' bandwidths is >38 dB. With this configuration, more radiating modes (i.e. mode 2 in TX or RX) are allowed while having high TX/RX isolation compared to the C-STAR configuration in Chapter 3. Introducing TX and RX with modes 1, 2, and 3 allows the eight-arm C-STAR spiral to be used for different concurrent applications; for instance, the spiral can be used for phase/amplitude comparison direction finding over a specific bandwidth while the antenna is transmitting simultaneously. It is also found that the eight-arm C-STAR configuration outperforms the four-arm C-STAR spiral-circulator sub-system (Chapter 3) with respect to isolation; however, the far-field degrades due to the introduction of parasitic arms and the radiation of undesired higher order modes. It is shown that the use of lens loading can mitigate this issue especially at high-frequencies.

7.4 Wideband Multimode Co-polarized Monostatic Omnidirectional C-STAR Antenna Arrays

Chapter 5 presented a novel wideband dual-layer, separation- and antenna-independent, linearly-polarized, omnidirectional circular C-STAR array sub-system. The proposed dual-layer C-STAR array has four TX and four RX antenna elements that are connected into two separate BFNs. Several advantages can be obtained with this omnidirectional C-STAR array configuration including, high TX/RX isolation over wide bandwidth without relying on the physical separation between the TX and RX array layers as well as similar co-polarized TX and RX radiation patterns. It is proven theoretically that this dual-layer C-STAR array configuration can achieve infinite TX/RX isolation regardless of the utilized array's antenna elements and the separation between the TX and RX layers. Average isolation >40 dB is measured with the fabricated dual-layer discone antenna array by either operating in mode 1 at TX/mode 1 at RX, or mode 0 at TX /mode 1 at RX.

In addition to the separation-independent dual-layer bi-static array, wideband, single- and dual-layer, omnidirectional, monostatic C-STAR circular array configurations are proposed. These simple array configurations consist of four or eight antenna elements which are all used simultaneously for TX and RX operations. This C-STAR configuration utilizes mode orthogonality and BFN cancellation to overcome realistic BFN's leakages and array's reflections. Wideband monocone antennas are used to verify the two proposed C-STAR concepts. Average isolation >30 dB is measured with the fabricated C-STAR monostatic arrays. Clearly, the mode orthogonality of the monostatic circular array shows great potential for improving the isolation between TX and RX without relying on any separation-, time-, frequency-, polarization-, or antenna-multiplexing.

7.5 Wideband Multimode Co-polarized Monostatic Broadside C-STAR Antenna Arrays

In chapter 6, a novel wideband monostatic co-circularly-polarized broadside circular C-STAR array configuration was proposed. With this C-STAR configuration, the BFN complexity and overall array size can be significantly reduced. The presented approach is developed based on the antenna orientation, geometrical symmetry, and partially shared BFN to cancel concurrently impedance mismatches, leakages from the shared BFN's components, and antenna coupling. For demonstration, two C-STAR arrays of four circularly-polarized spiral and dual circularly-polarized conical sinuous antennas are presented. In the absence of BFN's imbalances and array's geometrical asymmetries, the proposed concepts can achieve theoretically infinite TX/RX isolation. To experimentally verify the SI full-cancellation approach, a metal-backed four-element balun-fed two-arm spiral antenna array is fabricated and measured over an octave bandwidth. The results show average TX/RX isolation >38 dB over the operating bandwidth. An isolation enhancement layer is integrated with the TX/RX BFN and up to 50 dB isolation improvement is demonstrated. Overall, good quality and similar TX/RX radiation patterns are obtained. Although the discussion presented in this chapter focused on the spiral and sinuous antenna, the proposed C-STAR concept can be applied with different types of single/dual CP antenna elements and over wider bandwidth.

7.6 Original Contributions

The original contributions of this thesis are as follows:

- A simple unidirectional, circulator-less, four-arm C-STAR spiral antenna with good far-field performance, theoretically infinite isolation, and measured isolation >50 dB over multi-octave bandwidths is demonstrated [92]-[98].
- A symmetric coaxially-fed four-arm multilayered C-STAR spiral antenna to avoid using BFNs while maintaining high TX/RX isolation is introduced. With this feeding approach, the need for the two 180° hybrids is eliminated.
- The proposed four-arm C-STAR antenna can be utilized in different symmetrically structured arrays [134].
- Developed a novel ultrawideband, multimode, monostatic, C-STAR antenna with a circulator-BFN sub-system to cancel the undesired strong SI and achieve ideally infinite isolation irrespective of circulators' isolations. The presented configuration utilizes a single frequency-independent spiral antenna

to enable the multi-octave operation with significant size reduction and cost-effective implementation compared to the other state-of-the-art C-STAR systems [113]-[114].

- Developed a novel broadband multimode, circulator-less, lens-loaded eight-arm spiral antenna sub-system to suppress significant self-interference and provide instantaneously diverse directional and omnidirectional radiation patterns [117]-[118].
- Demonstrated different attractive multimode radiation characteristics (broadside or conical) with modes: 1, -1, 2, and 3 with C-STAR operation using either C-STAR antenna with circulator-BFN or lens-loaded eight-arm spiral antenna sub-systems [117]-[118].
- Mode orthogonality is utilized to achieve high isolation while radiating simultaneously different radiation pattern shapes (broadside or conical) with different modes [113]-[114], [117]-[118].
- Flush-mountable eight-arm spiral antenna is fabricated and used to enable broadband operation with significant size reduction [117]-[118].
- Flexibility of the four-arm spiral antenna with four-circulator and eight-arm spiral antenna BFN sub-systems concept to be extended to different four- or eight-port antenna and array configurations with dual-polarized capability is explained [131],[133].
- The benefit of the dielectric lens loading technique to improve the TX/RX isolation performance is demonstrated [118].
- Demonstrated and developed a novel wideband separation-independent, linearly-polarized, omnidirectional circular C-STAR dual-layer bi-static array sub-system. Theoretically infinite TX/RX isolation over wide bandwidth can be achieved with this C-STAR configuration without relying on the physical separation between the TX and RX array layers [127]-[128].

- Demonstrated a novel wideband co-polarized omnidirectional monostatic circulator-less circular C-STAR array. This C-STAR configuration utilizes the mode 1 and mixed-mode excitations to overcome the shared realistic BFN's leakage and reflections due to finite return loss [96], [129], [140].
- Demonstrated a novel dual-layer C-STAR monostatic array configuration sub-system. The upper array is flipped to cancel the leakages of the bottom layer while maintaining good omnidirectional radiation patterns [129].
- Mode orthogonality, antenna orientation, and BFN cancellation are all used in different omnidirectional circular arrays to show the great potential of improving the isolation between TX and RX ports without relying on any separation-, time-, frequency-, polarization-, or antenna-multiplexing [127]-[129].
- Developed a novel wideband monostatic single and dual co-circularly-polarized broadside circular C-STAR array configuration. The approach is implemented based on the antennas orientation and partially shared BFN cancellation. In absence of BFN' imbalances, symmetric leakages, and array geometrical asymmetries, the proposed concept can achieve theoretically infinite TX/RX isolation [135], [138].
- It is demonstrated that with the broadside C-STAR array configuration the BFN complexity, overall array size, and number of antenna elements can be all significantly reduced [135], [138].
- An ideal isolation enhancement layer is integrated to the original shared TX/RX BFN of the broadside C-STAR array, and up to 50 dB isolation improvement can possibly be achieved [135], [138].
- The proposed broadside C-STAR array concepts can be applied with different types of single/dual CP antenna elements [135], [138].

7.7 Future Work

The work performed in this thesis may be expanded in many directions including:

7.7.1 Coaxial-Feed C-STAR Spiral Array

In [134], a C-STAR antenna array with wideband simultaneous transmit and receive capability is proposed. The C-STAR array configuration utilizes a four-arm C-STAR spiral antenna as a unit cell to achieve high isolation between TX and RX ports and acceptable far-field performance. The proposed array is composed of N×N four-arm spirals arranged in a symmetrically shaped array. Each spiral has two arms for TX, and two arms for RX and is fed with planar microstrip feeds to eliminate the need for 180° hybrids. As an extension of that work and to further improve the total TX/RX isolation, the proposed coaxial-feed C-STAR spiral antenna in Chapter 2 can be utilized instead of the microstrip feeds.

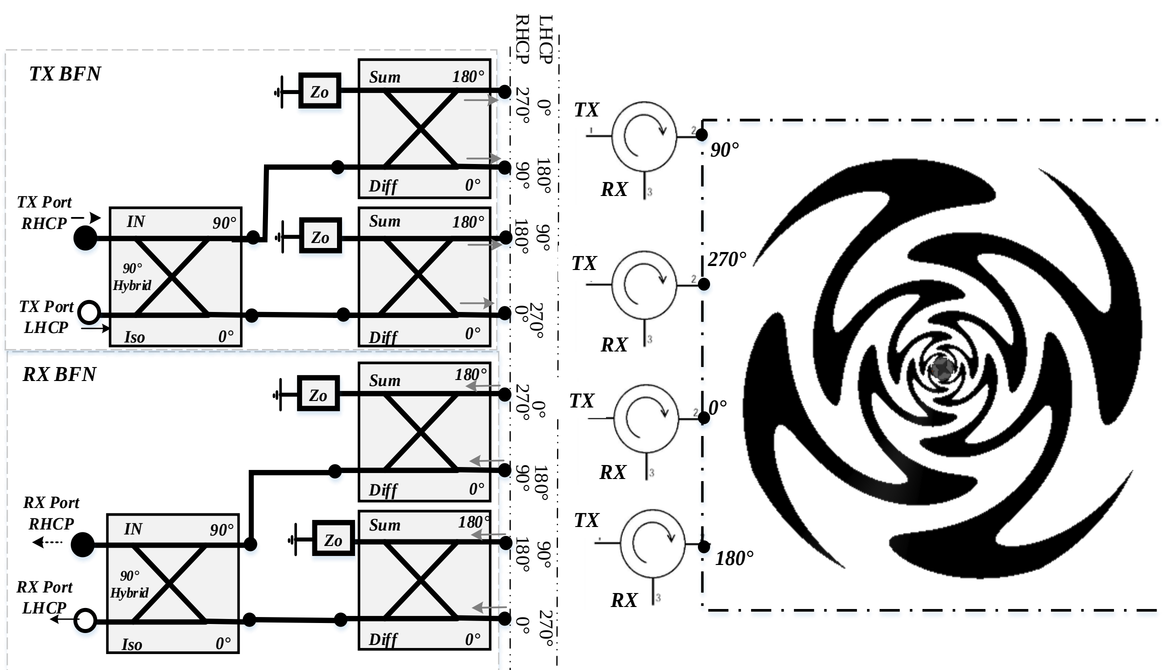

Figure 7.1: Schematic of the four-port sinuous C-STAR antenna sub-system.

7.7.2 Dual-Polarized Four- or Eight-port C-STAR Antenna Sub-system

The proposed C-STAR configurations in Chapter 3 and 4 can be extended to operate with dual-polarization capability. This can be accomplished by replacing the four- or eight-port spiral antenna with a dual-polarized antenna element. For example, a four- or eight-port sinuous C-STAR antenna sub-systems can be used as shown in Figs. 7.1 and 7.2 where each configuration TX and RX can produce either RHCP or LHCP. Note that RHCP and LHCP cannot be excited simultaneously while achieving high TX/RX isolation.

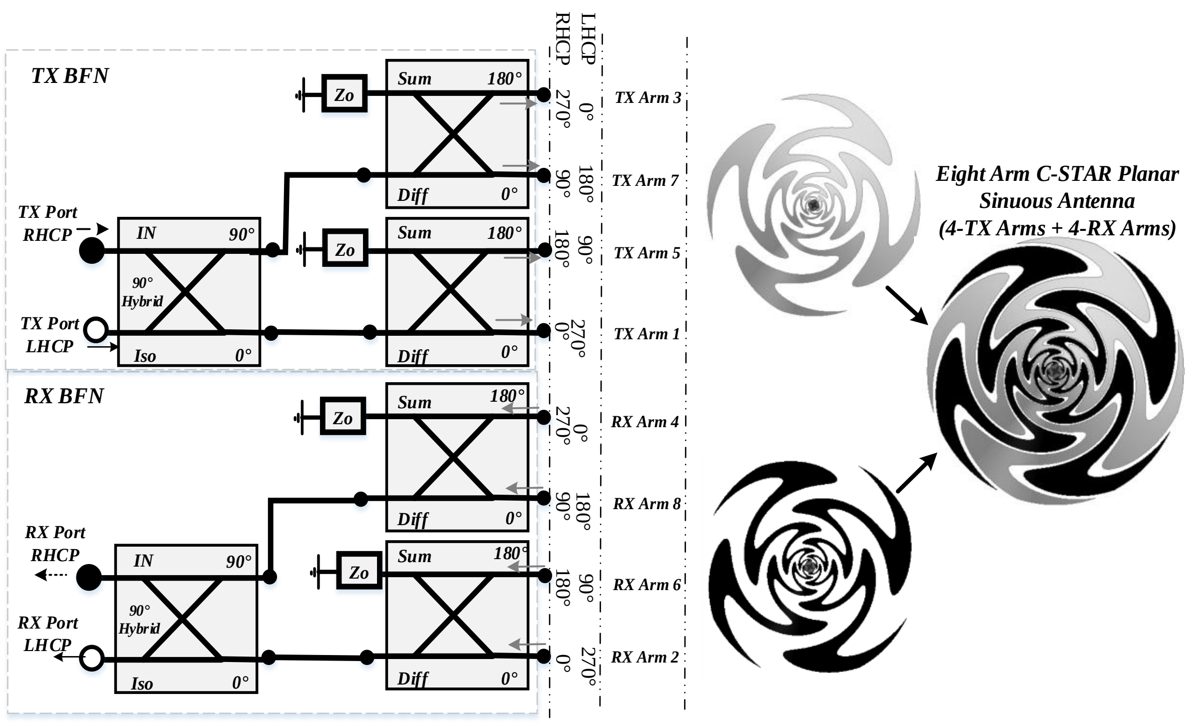

Figure 7.2: Schematic of the eight-port sinuous C-STAR antenna sub-system.

7.7.3 Isolation Improvement in C-STAR Configurations

To compensate for the BFN's imbalances and antenna's fabrication/assembly imperfection, tunable variable attenuators and phase shifters can be added before the RX COTS BFN and after TX COTS BFN. As shown in Fig. 7.3, the measured S-parameters of the TX/RX BFN are connected in AWR to the measured eight-arm lens-loaded C-STAR spiral antenna. In-between there are eight variable attenuators and phase shifters. Hence, only mode 1 at TX and mode 1 at RX case is considered. The improvement in TX/RX isolation after partially recovering from these amplitude and phase imbalances is plotted in Fig. 7.4. Note that the same principle can be applied for all of the proposed C-STAR antennas and arrays to further improve the isolation.

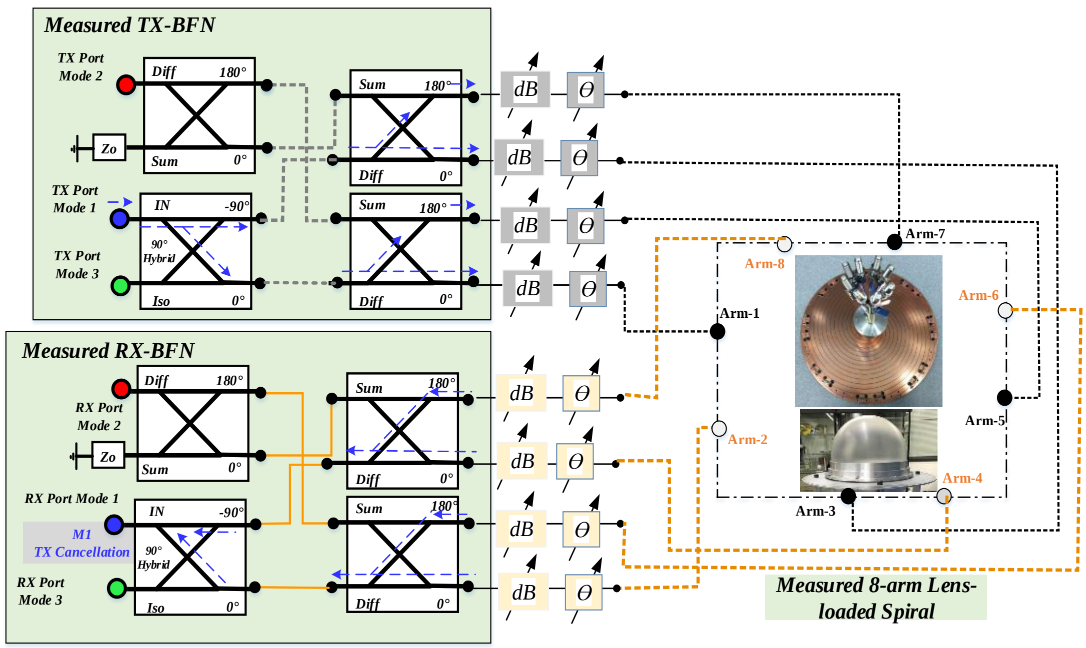

Figure 7.3: The measured TX/RX BFN are connected in AWR to the measured the 8-arm lens-loaded spiral antenna. Mode 1 TX/Mode 1 RX case is considered.

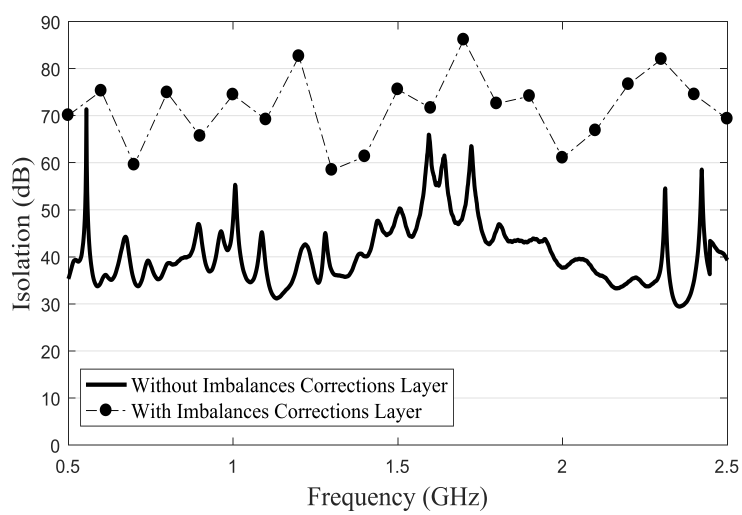

Figure 7.4: Isolation (mode 1 at TX /mode 1 at RX) before and after compensating for the amplitude and phase imbalances of the BFN.

7.7.4 Other Future Applications of the Proposed C-STAR Circular Arrays

7.7.4.1 Null Steering and C-STAR Systems

Null steering application can possibly operate concurrently with the proposed C-STAR antenna and array systems (Chapters 4 and 5). Yet, several challenges will emerge and detailed research is required to overcome them. As an example, it is known that the four-element circular array can be used to realize a null steering system as explained in [120]. Thus, the proposed dual-layer configuration in Chapter 5 can be used to achieve concurrent C-STAR and null steering operation as shown in Fig. 7.5. As seen, one layer can be assigned for C-STAR purposes (mode 0 at TX) and (mode 1 or mixed mode at RX), while the other layer is utilized for null steering applications. Some null steering measured results from [120] are included to demonstrate the possibility of using four-element circular array for null steering. From this initial analysis, the C-STAR and null steering layers should operate at different frequencies. If the two layers have to operate on the same frequency, another isolation cancellation layer should be added to the RX side to cancel any SI from the TX null steering layer.

7.7.4.2 Phase only Direction Finding and C-STAR Systems

A similar principle to (7.7.4.1) can be applied to achieve concurrent C-STAR and direction funding operations using the dual-layer circular array configuration in Chapter 5, where one layer is used for C-STAR whereas the other layer is used for phase-only direction finding by comparing the phase difference of mode 0 and mode 1 to estimate the direction of arrival in the azimuthal plane (i.e. at certain “Phi” angle), as shown in Fig. 7.6. A look up table can be generated based on the phase difference between mode 0 and mode 1. Also, to avoid any ambiguity, a linear phase relation should be maintained, which is not taken into account in this current design. Moreover, with this configuration, the isolation is still high between the C-STAR TX side and the direction finding RX side without the need of adding any extra cancellation layers. We believe this realization is feasible; future work will include improving the C-STAR performance and validating the proposed concept.

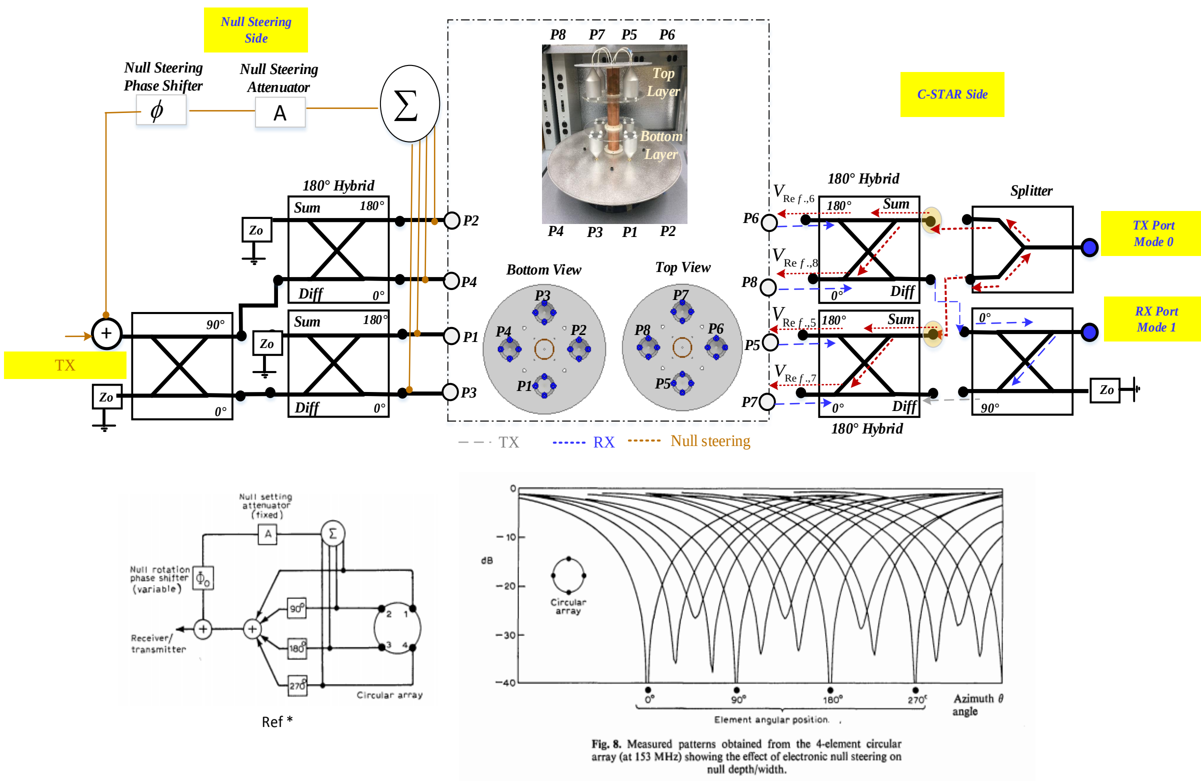

Figure 7.5: Dual-layer circular array for C-STAR and null steering sub-system.

7.7.4.3 Simultaneous Electronic Attack and Support

Due to the radiation characteristics of the utilized modes and the explained cancellation mechanism, the proposed single- or dual-layer circular arrays can be used for simultaneous electronic attack (jamming) and electronic support (spectrum sensing) operations. As an example, the mode 0 at TX / mode 1 at RX configuration is considered in Fig. 7.7. Once the TX port is excited, mode 0 radiation is formed by the array for jamming purposes. Some of the TX signals are reflected back due to array impedance mismatch and cancelled at the RX port as explained mathematically in the Chapter 5. The leakage in BFN will be cancelled as well. Ideally, only the sensed

RX signal is received at the RX port. Operation is similar for the other proposed configurations, where (1) the single layer that is excited with mode 1 at the TX side for jamming while the mixed mode at RX side (2) the dual-layer with mode 1 at the TX side (Jammer) and mode 0 at the RX side. Furthermore, one layer can be used for jamming and the other layer for phase-only direction finding (Electronic support measures) as explained in Section (7.7.4.1). Although the excited modes are orthogonal, their radiation characteristics are still suitable for the intended applications. Different scenarios are possible, but the practical realization, system integration, power handling, and electronic support requirements need to be fully studied in the future.

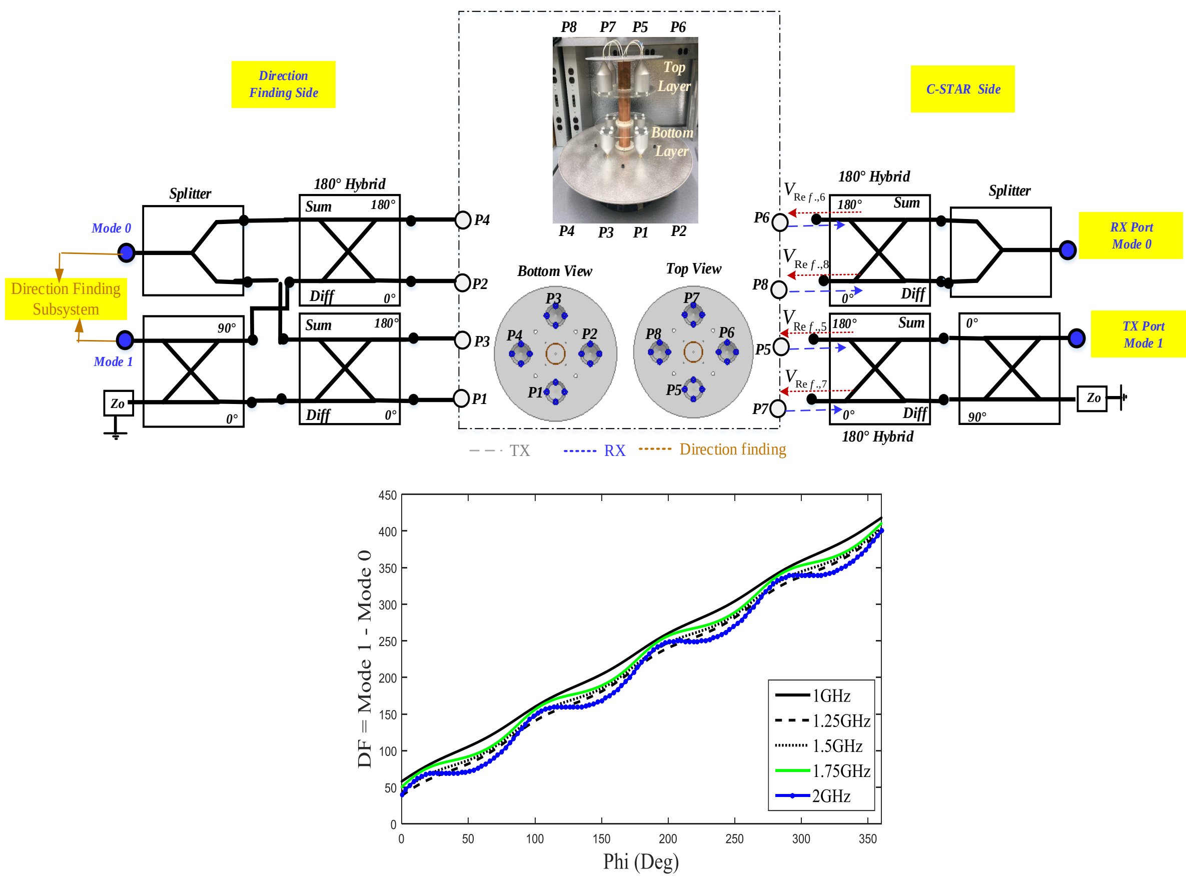

Figure 7.6: Dual-layer circular array for C-STAR and direction finding sub-system.

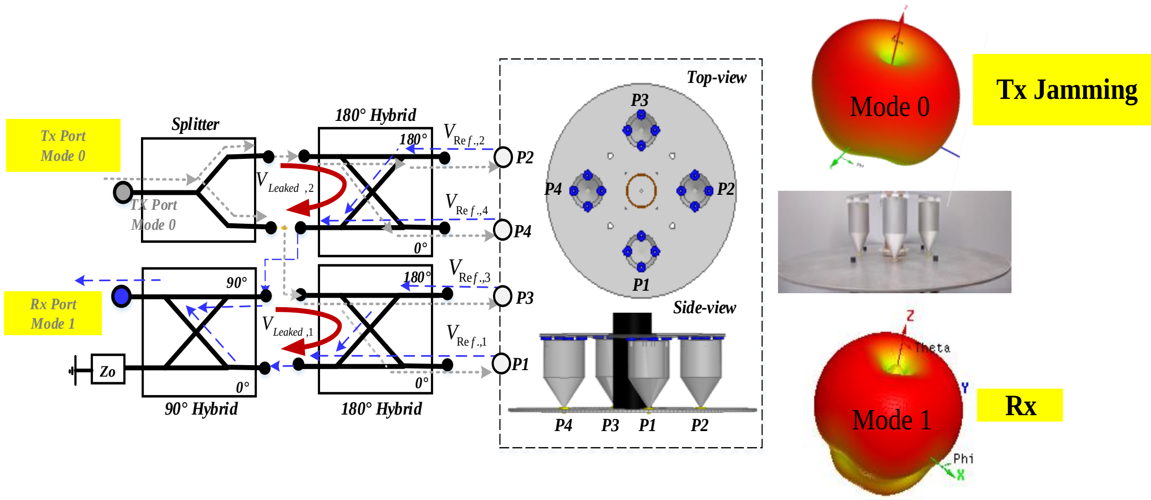

Figure 7.7: Single layer circular array for C-STAR jamming and sensing applications.

7.7.5 Multipath Effects on C-STAR Systems

As in conventional communication systems in the receiving mode, multipath signals are received by the array, routed through the BFN, and superimposed constructively or destructively at the RX port, which will impact the received signal level, but not the systems isolation and C-STAR operation. However, if either the C-STAR antenna or array is placed in multipath environment, the reflected TX signals could couple back to the RX side. Since the symmetry is most likely broken in the assumed random environment, the coupled signal will not be cancelled at the RX port and the isolation will be eventually degraded. To further show the impact of these reflections, different examples are considered in Fig. 7.8. Notice that objects are placed very close to the single layer circular array in Chapter 5. In Fig. 7.8, cases 1, 2, and 4 show the array is surrounded by nearby objects asymmetrically which leads to reduced isolation level. Nevertheless, case 3 shows that the isolation remains high since the nearby objects are placed symmetrically at the two sides. Objects have less impact on the isolation the further they are from the antenna. To recover from these multipath effects, an isolation enhancement layer can be utilized. Note that, a more detailed isolation study is needed for every antenna array placement scenario.

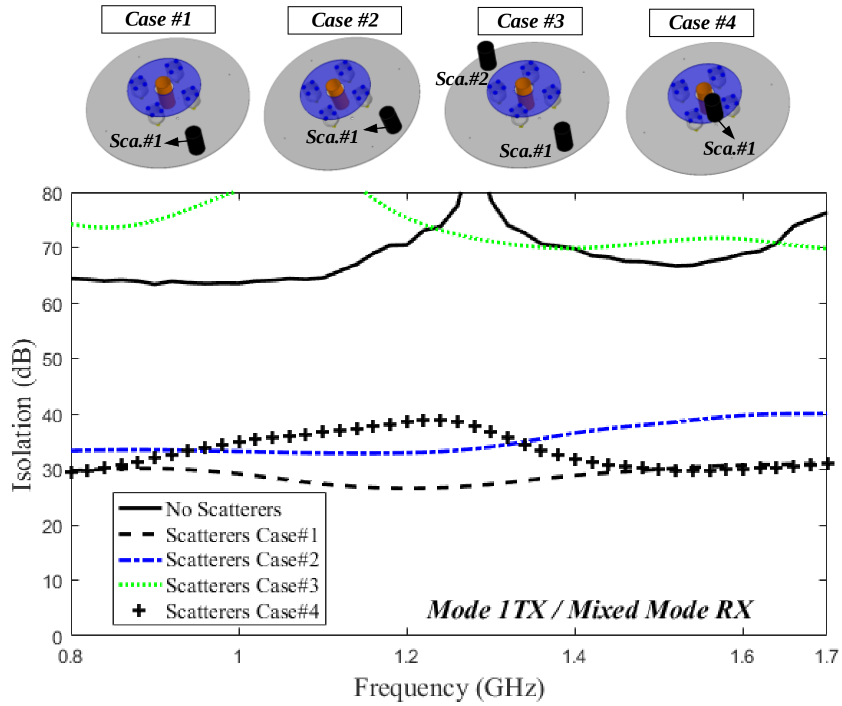

Figure 7.8: The effect of the nearby objects on the TX/RX isolation level of the single layer circular C-STAR array excited with mode 1 at TX and mixed mode at RX.

7.7.6 C-STAR Spiral Antenna and Array Sub-system Power Handling

The proposed C-STAR four- and eight-arm antenna presented in Chapters 2 and 4 of this thesis were designed with high power-handling capacity in mind, but due to existence of the parasitic arms, the radiation efficiency is reduced at lower frequencies. Therefore, the fabricated antennas were only subjected to low-power testing. The omnidirectional and broadside C-STAR array configurations in Chapters 5 and 6, on the other hand, can handle higher power due to low coupling mechanism between the TX and RX ports. However, a redesign using more suitable materials and subjected to high RF power-handling measurements would be part of future work.

Bibliography

[1] H. Ju, X. Shang, H. V. Poor and D. Hong, "Bi-directional use of spatial resources and effects of spatial correlation," in *IEEE Transactions on Wireless Communications*, vol. 10, no. 10, pp. 3368-3379, October 2011.

[2] H. Ju, D. Kim, H. V. Poor and D. Hong, "Bi-directional beamforming and its capacity scaling in Pairwise Two-Way Communications," in *IEEE Transactions on Wireless Communications*, vol. 11, no. 1, pp. 346-357, January 2012.

[3] D. Kim, S. Park, H. Ju and D. Hong, "Transmission capacity of full-duplex-based two-way Ad Hoc networks with ARQ protocol," in *IEEE Transactions on Vehicular Technology*, vol. 63, no. 7, pp. 3167-3183, September 2014.

[4] I. Randrianantenaina, H. Elsawy, and M. Alouini, “Limits on the capacity of in-band full duplex communication in uplink cellular networks,” *IEEE Globecom Workshops*, February 2015, pp. 1-6.

[5] N. V. Shende, Ö. Gürbüz and E. Erkip, "Half-duplex or full-duplex communications: Degrees of freedom analysis under self-interference," in *IEEE Transactions on Wireless Communications*, vol. 17, no. 2, pp. 1081-1093, February 2018.

[6] T. Riihonen, S. Werner, and R. Wichman, “Hybrid full-duplex/halfduplex relaying with transmit power adaptation,” *IEEE Transactions Wireless Communication*, vol. 10, no. 9, September 2011, pp. 3074-3085.

[7] T. Riihonen, S. Werner and R. Wichman, "Transmit power optimization for multiantenna decode-and-forward relays with loopback self-interference from full-duplex operation," *2011 Conference Record of the Forty Fifth Asilomar Conference on Signals, Systems and Computers (ASILOMAR)*, Pacific Grove, CA, November 2011, pp. 1408-1412.

[8] X. Rui, J. Hou and L. Zhou, "On the performance of full-duplex relaying with relay selection," in *Electronics Letters*, vol. 46, no. 25, pp. 1674-1676, December 2010.

[9] I. Krikidis, H. A. Suraweera, P. J. Smith and C. Yuen, "Full-duplex relay selection for amplify-and-forward cooperative networks," in *IEEE Transactions on Wireless Communications*, vol. 11, no. 12, pp. 4381-4393, December 2012.

[10] D. Kim, S. Park, H. Ju and D. Hong, "Transmission capacity of full-duplex-based two-way ad-hoc networks with ARQ protocol," in *IEEE Transactions on Vehicular Technology*, vol. 63, no. 7, pp. 3167-3183, September 2014.

[11] G. Zheng, I. Krikidis, J. Li, A. P. Petropulu and B. Ottersten, "Improving physical layer secrecy using full-duplex jamming receivers," in *IEEE Transactions on Signal Processing*, vol. 61, no. 20, pp. 4962-4974, October 2013.

[12] S. Vishwakarma and A. Chockalingam, Sum secrecy rate in full-duplex wiretap channel with imperfect CSI, arXiv preprint, 2013. [Online]. Available: http://arxiv.org/abs/1311.3918.

[13] O. Cepheli, S. Tedik and G. Karabulut Kurt, "A high data rate wireless communication system with improved secrecy: full duplex beamforming," in *IEEE Communications Letters*, vol. 18, no. 6, pp. 1075-1078, June 2014.

[14] M. Duarte *et al.*, "design and characterization of a full-duplex multiantenna system for WiFi networks," in *IEEE Transactions on Vehicular Technology*, vol. 63, no. 3, pp. 1160-1177, March 2014.

[15] W. Zhou, K. Srinivasan, and P. Sinha, "RCTC: rapid concurrent transmission coordination in full duplex wireless networks," *2013 21st IEEE International Conference on Network Protocols (ICNP)*, Goettingen, October 2013, pp. 1-10.

[16] Y. S. Choi and H. Shirani-Mehr, "Simultaneous transmission and reception: algorithm, design and system level performance," in *IEEE Transactions on Wireless Communications*, vol. 12, no. 12, pp. 5992-6010, December 2013.

[17] E. F. W. Alexanderson, "Simultaneous sending and receiving," in *Proceedings of the Institute of Radio Engineers*, vol. 7, no. 4, pp. 363-378, August 1919.

[18] D. Bharadia, E. McMilin, and S. Katti, “Full duplex radios,” in Proc. ACM SIGCOMM, October 2013.

[19] A. Sabharwal et al., “In-band full-duplex wireless: challenges and opportunities,” arXiv:1311.0456, 2014.

[20] T. Tchoffo, B. Uguen, and L-M. Aubert, “Antennas link synthesis using near field chamber measurements,” *in Proc. 1st European Antennas and Propagation Conference*, pp. 1-5, November 2006.

[21] D. Shrekenhamer et al., “Cascaded metasurfaces for broadband antenna isolation,” Proc. SPIE, vol. 9544, p. 954424, September 2015, doi: 10.1117/12.2188413.

[22] P. V. Prasannakumar, M. A. Elmansouri and D. S. Filipović, "Wideband decoupling techniques for dual-polarized bi-Static simultaneous transmit and receive antenna sub-system," in *IEEE Transactions on Antennas and Propagation*, vol. 65, no. 10, pp. 4991-5001, October 2017.

[23] J. A. M. Lyon, C. J. Digenis, W. W. Parker, and M. A. H. Ibrahim. (Jun. 1968). “Electromagnetic coupling reduction techniques,” Dept. Electr. Eng., Univ. Michigan, Ann Arbor, MI, USA, Tech. Rep. AFAL-TR-68-132. [Online]. Available: https://deepblue.lib.umich.edu/handle/ 2027.42/6402

[24] E. Tsakalaki, E. Foroozanfard, E. de Carvalho and G. F. Pedersen, "A 2-order MIMO full-duplex antenna system," *The 8th European Conference on Antennas and Propagation (EuCAP 2014)*, The Hague, 2014, pp. 2546-2550.

[25] E. Foroozanfard, O. Franek, A. Tatomirescu, E. Tsakalaki, E. D. Carvalho and G. F. Pedersen, "Full-duplex MIMO system based on antenna cancellation technique," in *Electronics Letters*, vol. 50, no. 16, pp. 1116-1117, July 31 2014.

[26] E. Aryafar, M.A. Khojastepour, K. Sundaresan, S. Rangarajan, and M. Chiang, “MIDU: enabling MIMO full-duplex,” *In Proc. ACM MobiCom*, August 2012.

[27] H. Nawaz and I. Tekin, "Double-differential-fed, dual-polarized patch antenna with 90 dB interport RF isolation for a 2.4 GHz in-band full-duplex transceiver," in *IEEE Antennas and Wireless Propagation Letters*, vol. 17, no. 2, pp. 287-290, February 2018.

[28] C. Y. D. Sim, C. C. Chang and J. S. Row, "Dual-feed dual-polarized patch antenna with low cross polarization and high isolation," in *IEEE Transactions on Antennas and Propagation*, vol. 57, no. 10, pp. 3405-3409, October 2009.

[29] H. Nawaz and I. Tekin, "Compact dual-polarised microstrip patch antenna with high interport isolation for 2.5 GHz in-band full-duplex wireless applications," in *IET Microwaves, Antennas & Propagation*, vol. 11, no. 7, pp. 976-981, June 2017.

[30] H. Nawaz and I. Tekin, "Dual-polarized, differential fed microstrip patch antennas with very high interport isolation for full-duplex communication," in *IEEE Transactions on Antennas and Propagation,* vol. 65, no. 12, pp. 7355-7360, December 2017.

[31] B. Q. Wu and K. M. Luk, "A broadband dual-polarized magneto-electric dipole antenna with simple feeds," in *IEEE Antennas and Wireless Propagation Letters*, vol. 8, pp. 60-63, December 2009.

[32] P. Teo, Ki, Lee, and C. Lee, "Maltese-cross coaxial balun-fed antenna for GPS and DCS1800 mobile communication," in *IEEE Transactions on Vehicular Technology*, vol. 52, no. 4, pp. 779-783, July 2003.

[33] X. Yang, Y. Liu, Y. X. Xu and S. x. Gong, "Isolation enhancement in patch antenna array with fractal UC-EBG structure and cross slot," in *IEEE Antennas and Wireless Propagation Letters*, vol. 16, pp. 2175-2178, May 2017.

[34] H. Qi, X. Yin, L. Liu, Y. Rong and H. Qian, "Improving isolation between closely spaced patch antennas using interdigital lines," in *IEEE Antennas and Wireless Propagation Letters*, vol. 15, pp. 286-289, June 2016.

[35] H. Qi, L. Liu, X. Yin, H. Zhao and W. J. Kulesza, "Mutual coupling suppression between two closely spaced microstrip antennas with an asymmetrical coplanar strip wall," in *IEEE Antennas and Wireless Propagation Letters*, vol. 15, pp. 191-194, June 2016.

[36] M. Duarte *et al.*, "Design and Characterization of a full-duplex multiantenna system for WiFi networks," in *IEEE Transactions on Vehicular Technology*, vol. 63, no. 3, pp. 1160-1177, March 2014.

[37] M. Duarte and A. Sabharwal, "Full-duplex wireless communications using off-the-shelf radios: Feasibility and first results," *2010 Conference Record of the Forty Fourth Asilomar Conference on Signals, Systems and Computers*, Pacific Grove, CA, 2010, pp. 1558-1562.

[38] K. Haneda, E. Kahra, S. Wyne, C. Icheln and P. Vainikainen, "Measurement of loop-back interference channels for outdoor-to-indoor full-duplex radio relays," *Proceedings of the Fourth European Conference on Antennas and Propagation*, Barcelona, Spain, July 2010, pp. 1-5.

[39] M. A. Khojastepour, K. Sundaresan, S. Rangarajan, X. Zhang, and S. Barghi, “The case for antenna cancellation for scalable full-duplex wireless communications,” *In Proc. 10th ACM Workshop Hot Topics Network*, 2011, pp. 1-6.

[40] E. Everett, A. Sahai and A. Sabharwal, "Passive self-interference suppression for full-duplex infrastructure nodes," in *IEEE Transactions on Wireless Communications*, vol. 13, no. 2, pp. 680-694, February 2014.

[41] J. Choi, M. Jain, K. Srinivasan, P. Levis, and S. Katti, “Achieving single channel, full duplex wireless communication”. [Online]. Available: https://web.stanford.edu/~skatti/pubs/mobicom10-fd.pdf.

[42] A. Khojastepour, K. Sundaresan, S. Rangarajan, X. Zhang, and S. Barghi, “The case for antenna cancellation for scalable full-duplex wireless communications,” In Proc. ACM Hotnet, 2011.

[43] A. K. Khandani, “Methods for spatial multiplexing of wireless two-way channels,” U.S. Patent US7817641 B1, 2010.

[44] M. Pozar, Microwave Engineering, 3rd ed. New York: Wiley, 2005.

[45] S. M. Wentworth, Applied Electromagnetics: Early Transmission Lines Approach, John Wiley and Sons Inc., 2007.

[46] DITOM Microwave Inc., CA, USA. [Online]. Available: https://www.ditom.com/single_junction_ circulators.php.

[47] RF-Lambda. CA, USA. [Online]. Available: http://rflambda.com/index.jsp.

[48] C. H. Cox and E. I. Ackerman, "Photonics for simultaneous transmit and receive," *2011 IEEE MTT-S International Microwave Symposium*, Baltimore, MD, June 2011, pp. 1-1.

[49] V. Dmitriev, G. Portela and L. Martins, "Magneto-optical photonic crystal-based three-port circulators with low symmetry," *2015 SBMO/IEEE MTT-S International Microwave and Optoelectronics Conference (IMOC)*, Porto de Galinhas, November 2015, pp. 1-5.

[50] Z. Wang and S. Fan, "Broadband optical circulators in two dimensional magneto-optical photonic crystals," *2005 Quantum Electronics and Laser Science Conference*, December 2005, pp. 461-463 Vol. 1.

[51] S. K. Cheung, T. P. Halloran, W. H. Weedon and C. P. Caldwell, "MMIC-based quadrature hybrid quasi-circulators for simultaneous transmit and receive," in *IEEE Transactions on Microwave Theory and Techniques*, vol. 58, no. 3, pp. 489-497, March 2010.

[52] Y. E. Wang, “Time-Varying Transmission Lines (TVTL) - A new pathway to non-reciprocal and intelligent RF front-ends,” *IEEE Radio and Wireless Symposium*, January 2014, pp. 148-150.

[53] G. Lathikre, N. Jolivet, S. Nobilet, R. Gillard, and J. E Hilard, “A novel balanced circulator for FDD MC-CDMA communications,” *IEEE Microwave Conference*, October 2004, pp. 605-608.

[54] M. E. Knox, "Single antenna full duplex communications using a common carrier," *WAMICON 2012 IEEE Wireless & Microwave Technology Conference*, Cocoa Beach, FL, April 2012, pp. 1-6.

[55] W. Lim and J. Yu, “Balanced circulator structure with enhanced isolation characteristics,” *Microwave and Optical Technology Letters*, vol. 50, no. 9, September 2008, pp. 2389-2391.

[56] H. L. Lee, D. H. Park, J. W. Yu and M. Q. Lee, "Compact antenna module with optimized Tx-to-Rx isolation for monostatic RFID," in *IEEE Microwave and Wireless Components Letters*, vol. 27, no. 12, pp. 1161-1163, December 2017.

[57] G. Lasser, R. Langwieser and A. L. Scholtz, "Broadband suppression properties of active leaking carrier cancellers," *2009 IEEE International Conference on RFID*, Orlando, FL, May 2009, pp. 208-212.

[58] S. L. Karode and V. F. Fusco, "Feedforward embedding circulator enhancement in transmit/receive applications," in *IEEE Microwave and Guided Wave Letters*, vol. 8, no. 1, pp. 33-34, January 1998.

[59] J. R. Yang, D. W. Kim and S. Hong, "Quasi-circulator for effective cancellation of transmitter leakage signals in monostatic six-port radar," in *Electronics Letters*, vol. 45, no. 21, pp. 1093-1095, October 8 2009.

[60] J. Jung, J. Kim, S. Kim, and K. Lee, “New circulator structure with high isolation for time division duplexing radio systems,” *IEEE VTC-2005-Fall. 2005 IEEE 62nd Vehicular Technology Conference*, January 2005, pp. 2766-2769.

[61] B. Chiang and M. Holdip, "Progressively phased circular arrays used in antenna isolation," *1974 Antennas and Propagation Society International Symposium*, Atlanta, GA, USA, June 1974, pp. 289-292.

[62] T. Snow, C. Fulton and W. J. Chappell, "Multi-antenna near field cancellation duplexing for concurrent transmit and receive," *2011 IEEE MTT-S International Microwave Symposium*, Baltimore, MD, August 2011, pp. 1-1.

[63] K. E. Kolodziej, P. T. Hurst, A. J. Fenn and L. I. Parad, "Ring array antenna with optimized beamformer for Simultaneous Transmit And Receive," *Proceedings of the 2012 IEEE International Symposium on Antennas and Propagation*, Chicago, IL, July 2012, pp. 1-2.

[64] W. F. Moulder, B. T. Perry and J. S. Herd, "Wideband antenna array for simultaneous transmit and receive (STAR) applications," *2014 IEEE Antennas*

and Propagation Society International Symposium (APSURSI), Memphis, TN, July 2014, pp. 243-244.

[65] E. Yetisir, C. C. Chen and J. L. Volakis, "Wideband low profile multiport antenna with omnidirectional pattern and high isolation," in *IEEE Transactions on Antennas and Propagation*, vol. 64, no. 9, pp. 3777-3786, September 2016.

[66] A. Batgerel and S. Eom, "High-isolation microstrip patch array antenna for single channel full duplex communications," *IET Microwave Antenna and Propagation*, vol. 9, no. 11, August 2015, pp. 1113-1119.

[67] R. Saleem, M. Bilal, K. B. Bajwa, and M. F. Shafique, "Eight-element UWB-MIMO array with three distinct isolation mechanisms," *IEEE Electronics Letters*, vol. 51, no. 4, February 2015, pp. 311-313.

[68] M. Jain et al., "Practical, real-time, full duplex wireless," *In Proc. 17th Annual International Conference Mobile Computer Network*, 2011, pp. 301-312.

[69] D. Bharadia and S. Katti, "Full duplex MIMO radios," *In Proc. 11th USENIX Symposium*, 2014, pp. 359-372.

[70] N. Phungamngern, P. Uthansakul, and M. Uthansakul, "Digital and RF interference cancellation for single-channel full-duplex transceiver using a single antenna," *in Proc. 10th Intentional Conference ECTI-CON*, 2013, pp. 1-5.

[71] M. Duarte *et al.*, "Design and characterization of a full-duplex multiantenna system for WiFi Nnetworks," in *IEEE Transactions on Vehicular Technology*, vol. 63, no. 3, pp. 1160-1177, March 2014.

[72] M. Duarte, C. Dick and A. Sabharwal, "Experiment-driven characterization of full-duplex wireless systems," in *IEEE Transactions on Wireless Communications*, vol. 11, no. 12, pp. 4296-4307, December 2012.

[73] M. Duarte and A. Sabharwal, "Full-duplex wireless communications using off-the-shelf radios: Feasibility and first results," *2010 Conference Record of the Forty Fourth Asilomar Conference on Signals, Systems and Computers*, Pacific Grove, CA, April 2010, pp. 1558-1562.

[74] E. Ahmed, A. M. Eltawil and A. Sabharwal, "Self-interference cancellation with phase noise induced ICI suppression for full-duplex systems," *2013 IEEE Global Communications Conference (GLOBECOM)*, Atlanta, GA, December 2013, pp. 3384-3388.

[75] The Evolution of Mobile Technologies: 1G 2G 3G 4G LTE – Qualcomm. [Online]. Available: https://www.qualcomm.com.

[76] UMTS Forum. Mobile traffic forecasts 2010-2020 report, London, U.K. [Online].Available:http://www.umts-forum.org/component/option,com_docman/task,cat_view/gid,485/Itemid,213.

[77] B. Allen, M. Dohler, E. Okon, W. Malik, A. Brown, D. Edwards, *Ultra Wideband Antennas and Propagation for Communications, Radar and Imaging*. West Sussex, UK: Wiley, 2006.

[78] H. Schantz, *The Art and Science of Ultra-Wideband Antennas*. Reading, MA: Artech House, 2005.

[79] N. Fortino, J-Y Dauvignac, G. Kossiavas, and X. Begaud, "Overview of UWB Antennas" *in Ultra Wide Band Antennas*. NJ: John Wiley, 2011, chapter 5.

[80] R. H. Duhamel and J. P. Scherer, "Frequency Independent Antennas," *in Antenna Engineering Handbook*, 3rd Ed. New York: Mc-Graw Hill, 1993, chapter 14.

[81] D. S. Filipović and T. P. Cencich Sr., "Frequency Independent Antennas," *in Antenna Engineering Handbook*, 4th Ed. New York: Mc-Graw Hill, 2007, chapter 13.

[82] R. G. Corzine and J. A. Mosko, *Four-Arm Spiral Antennas*. Artech House, Norwood, MA, 1990.

[83] T. W. Hertel and G. S. Smith, "Analysis and design of two-arm conical spiral antennas," *IEEE Transactions on Electromagnetic Compatibility*, vol. 44, August 2002, pp. 1-14.

[84] R. H. DuHamel, "Dual polarized sinuous antennas," U.S. Patent 4658262, April 14,
1987.

[85] R. H. DuHamel and D. Isbell, "Broadband logarithmically periodic antenna structures," *IRE International Convention,* vol. 5, pp. 119-129, March 1957.

[86] A. Lestari, A. G. Yarovoy and L. P. Ligthart, "RC-loaded bow-tie antenna for improved pulse radiation," in *IEEE Transactions on Antennas and Propagation*, vol. 52, no. 10, pp. 2555-2563, October 2004.

[87] T. Holzheimer, "The low dispersion coaxial cavity as an ultra wideband antenna," *2002 IEEE Conference on Ultra Wideband Systems and Technologies (IEEE Cat. No.02EX580)*, Baltimore, MD, USA, August 2002, pp. 333-336.

[88] N. P. Agrawall, G. Kumar and K. P. Ray, "Wide-band planar monopole antennas," in *IEEE Transactions on Antennas and Propagation*, vol. 46, no. 2, pp. 294-295, Feb 1998.

[89] E. Baum and E. G. Farr, "Impulse radiating antennas," *in Ultra-Wideband, Short-Pulse Electromagnetics*, H. L. Bertoni, L. Carin, and L. B. Felsen, Eds. New York: Plenum, 1993.

[90] R. T. Lee and G. S. Smith, "A design study for the basic TEM horn antenna," in *IEEE Antennas and Propagation Magazine*, vol. 46, no. 1, pp. 86-92, Feb 2004.

[91] J. Fisher, "Design and performance analysis of a 1-40GHz ultra-wideband antipodal Vivaldi antenna," *in Proc. German Radar Symposium GRS 2000*, October 2000, pp. 237-241.

[92] M. A. Elmansouri, E. A. Etellisi, and D. Filipović, "Ultra-wideband Circularly-Polarized Simultaneous Transmit and Receive (STAR) Antenna System," *IEEE International Symposium Antennas Propagation & USNC/URSI Nat. Radio Scilicet Meeting*, Jul. 2015, pp. 508-509.

[93] D. S. Filipović, M. Elmansouri, and E. A. Etellisi, "On the Wideband Simultaneous Transmit and Receive (STAR) Capabilities with Single Antenna Apertures," *Antenna Application Symposium*, September 2015.

[94] E. A. Etellisi, M. Elmansouri, and D. S. Filipović, "Wideband Monostatic Simultaneous Transmit and Receive (STAR) Antenna," *IEEE Transaction Antennas and Propagation*, vol. 64, no.1, January 2016, pp. 6-15.

[95] M. Elmansouri, P. Valaleprasannakumar, E. Tianang, E. Etellisi, and Dejan Filipović and D. S. Filipović, "Realization of multi-decade simultaneous transmit and receive (STAR) antenna sub-system," *to be submitted to IEEE Transaction Antennas and Propagation.*

[96] E. A. Etellisi, M. Elmansouri, and D.S. Filipović, "Antenna Systems for Simultaneous Transmit and Receive (STAR) Applications," *International Microelectronics Assembly and Packaging Conference*, October 2017, vol. 2017, no. 1, pp. 590-594.

[97] M. Elmansouri, P. Valaleprasannakumar, E. Tianang, E. A. Etellisi, and Dejan Filipović, "A demonstration of a simultaneous transmit and receive (STAR)

antenna sub-system operating Over 90:1 BW," 42st Annual GOMACTech Conference, March 2017.

[98] D. S. Filipović, M. A. Elmansouri, E. A. Etellisi, "Ultrawideband Co-polarized Simultaneous Transmit and Receive Aperture (STAR)," U.S. Patent App15/626,004.

[99] FEKO: Computational Electromagnetics EM Software and Systems (SA) Pty Ltd. [Online]. Available: http:/www.feko.info.

[100] M. J. Radway and D. S. Filipović, "Four-armed spiral-helix antenna," in *IEEE Antennas and Wireless Propagation Letters*, vol. 11, pp. 338-341, March 2012.

[101] M. P. Karaboikis, V. C. Papamichael, G. F. Tsachtsiris, C. F. Soras and V. T. Makios, "Integrating compact printed antennas onto small diversity/ MIMO terminals," *IEEE Transaction Antennas Propagation*, 2008, vol. 56, no. 7, pp. 2067-2078.

[102] S. Blanch, J. Romeu and I. Corbella, "Exact representation of antenna system diversity performance from input parameter description," *IEEE Electronic Letters*, vol. 39, no.9, 2003, pp. 705-707.

[103] H.T. Hui, W.T.O. Yong, K.B. Toh, "Signal correlation between two normal-mode helical antennas for diversity reception in a multipath environment," *IEEE Transaction Antennas Propagation*, vol. 52, no. 2, 2004, pp. 572-576.

[104] J. L. Volakis, M. W. Nurnberger, and D. S. Filipović, "A broadband cavity-backed slot spiral antenna," in *IEEE Antennas Propagation Magazine,* vol. 43, no. 6, pp. 15-26, 2001.

[105] H. Nakano, S. Sasaki, H. Oyanagi, and J. Yamauchi, "Cavity-backed Archimedean spiral antenna with strip absorber," *IET Microwave*, Antennas Propag., vol. 2, no. 7, pp. 725-730, 2008.

[106] M. Elmansouri, "Joint Time/Frequency Analysis and Design of Spiral Antennas and Arrays for Ultra-Wideband Applications," P.hD thesis, University of Colorado, Boulder, Colorado, 2013.

[107] S. Tang, C. Lin, and S. Hung, "Ultra-wideband quasi-circulator implemented by cascading distributed balun with phase cancellation technique," *IEEE Transaction on Microwave Theory and Techniques*, vol. 64, no. 7, July. 2016, pp. 2014-2112.

[108] J. L. Young, R. S. Adams, B. O'Neil, and C. M. Johnson, “Bandwidth optimization of an integrated microstrip circulator and antenna assembly: Part 1,” *IEEE Antennas Propagation Magazine*, 2007, vol. 49, no.1, pp. 82-91.

[109] R. S. Adams, B. O’Neil, and J. L. Young, “The circulator and antenna as a single integrated system,” *IEEE Antennas and Wireless Propagation Letters*, April 2009, vol. 8, pp. 165-168.

[110] W. Kim, M. Le, J. Kim, H. Lim, J. Yu, B. Jang, J. Park, “A passive circulator with high isolation using a directional coupler for RFID,” *IEEE MTT-S International Microwave Symposium*, June 2006, pp. 1177 - 1180.

[111] M. Elmansouri, J.B Bargeron, D. S. Filipović, “Simply-fed four-arm spiral-helix antenna,” *IEEE Transaction Antennas Propagation*, 2014, vol. 64, no. 9, pp. 4864-4868.

[112] AWR Microwave Office: RF/microwave design software. [Online]. Available: www.awrcorp.com/products/niawr-design-environment/microwave-office.

[113] D. S. Filipović, M. Elmansouri, and E. A. Etellisi, “On wideband simultaneous transmit and receive (STAR) with a single aperture,” *IEEE International Symposium on Antennas and Propagation*, June 2016.

[114] E. A. Etellisi, M. A. Elmansouri, and D. S. Filipović, “Wideband multimode monostatic spiral antenna STAR sub-system,” *IEEE Transaction Antennas Propagation*, vol. 65, no. 4, April 2017, pp. 1845-1854.

[115] HFSS: High Frequency Structure Simulator Ansoft Corporation [Online]. Available: http://www.hfss.com.

[116] R. Sammeta and D. S. Filipović, "Improved efficiency lens-loaded cavity-backed transmit sinuous antenna", *IEEE Transaction Antennas Propagation*, vol. 62, no. 12, December 2014, pp. 2000 - 2009.

[117] E. A. Etellisi, M. A. Elmansouri and D. S. Filipović, "Wideband dual-mode monostatic simultaneous transmit and receive antenna system," *2016 IEEE International Symposium on Antennas and Propagation (APSURSI)*, Fajardo, 2016, pp. 1821-1822.

[118] E. A. Etellisi, M. A. Elmansouri, and D. S. Filipović, “In-band full-duplex multimode lens-loaded 8-Arm spiral antenna” *IEEE Transaction Antennas Propagation Communication*, February 2018, vol. 66 no. 04.

[119] A. W. Rudge, K. Milne, and D. E. Davies, “Circular arrays,” in The Handbook of Antenna Design, *vol. 2. IET*, 1983, ch. 12.

[120] D. E. N. Davies and M. S. A. S. Rizk, "A broadband experimental null-steering antenna system for mobile communications," in *Radio and Electronic Engineer*, vol. 48, no. 10, pp. 509-517, October 1978.

[121] J. Guy and D. E. Davies, “Novel method of multiplexing radio-communication antennas using circular-array configuration,” *IEEE Microwaves, Optics and Antennas,* vol. 130, no.6, 1983, pp. 410 - 414.

[122] J. Davis and A. Gibson, “Phase mode excitation in beamforming arrays,” *In Proc. European Microwave Conference*, September 2006, pp. 1786-1789.

[123] N. Shende, O. Gurbuz, E. Erkip, “Half-duplex or full-duplex relaying: a capacity analysis under self-Interference,” Mar. 2013, [Online]. Available: https://arxiv.org/abs/1303.0088.

[124] Z. Wei, X. Zhu, S. Sun, Y. Huang, L. Dong and Y. Jiang, "Full-Duplex Versus Half-Duplex Amplify-and-Forward Relaying: Which is More Energy Efficient in 60-GHz Dual-Hop Indoor Wireless Systems?," in *IEEE Journal on Selected Areas in Communications*, vol. 33, no. 12, pp. 2936-2947, Dec. 2015.

[125] E. Everett and A. Sabharwal, “Spatial self-interference isolation for in-band full-duplex wireless: a degrees-of-freedom analysis,” Jun. 2015, [Online]. Available: arXiv:1506.03394.

[126] J. Choi, M. Jain, K. Srinivasan, P. Levis, and S. Katti, “Achieving single channel, full duplex wireless communication,” *The 16th Annual Int. Conference on Mobile Computer Network,* Chicago, IL, July 2010, pp. 1-12.

[127] E. A. Etellisi, M. A. Elmansouri and D. S. Filipović, "Wideband simultaneous transmit and receive (STAR) circular array system," *2016 IEEE International Symposium on Phased Array Systems and Technology (PAST)*, Waltham, MA, October 2016, pp. 1-5.

[128] E. A. Etellisi, M. Elmansouri, and D.S. Filipović, “Wideband simultaneous transmit and receive (STAR) bi-layer circular array,” *IEEE International Symposium Antennas Propagation & USNC/URSI Nat. Radio Scilicet Meeting*, July 2015, pp. 227-228.

[129] E. A. Etellisi, M. A. Elmansouri, and D. S. Filipović, “Broadband full-duplex monostatic circular antenna arrays,” *IEEE Antennas and Propagation Magazine*, February 2018, accepted.

[130] W. G. Lim, W. I. Son, K. S. Oh, W. K. Kim and J. W. Yu, "Compact integrated antenna with circulator for UHF RFID system," in *IEEE Antennas and Wireless Propagation Letters*, vol. 7, pp. 673-675, 2008.

[131] A. Kee, M. Elmansouri and D. S. Filipovic, "Circularly polarized PIFA array for simultaneous transmit and receive applications," *2017 IEEE Int. Symp. on Antennas and Propag. & USNC/URSI National Radio Science Meeting*, San Diego, CA, 2017, pp. 2303-2304.

[132] H.-S. Jang, W.-G. Lim, W.-I. Son, S.-Y. Cha, and J.-W. Yu, “Microstrip patch array antenna with high isolation characteristics,” *Microwave Opt. Technical Lett*ers, vol. 54, no. 4, pp. 973-976, April 2012.

[133] J. Ha, M. A. Elmansouri, P. Prasannakumar and D. S. Filipovic, "Monostatic co-polarized full-duplex antenna with left- or right-hand circular polarization," in *IEEE Transaction on Antennas and Propagation*, vol. 65, no. 10, pp. 5103-5111, October 2017.

[134] M. A. Elmansouri, A. J. Kee and D. S. Filipovic, "Wideband antenna array for simultaneous transmit and receive (STAR) applications," *IEEE Antennas and Wireless Propagation Letters*, vol. 16, pp. 1277-1280, 2017.

[135] E. A. Etellisi, M. A. Elmansouri, and D. S. Filipovic, “Wideband monostatic spiral array for full-duplex applications”, *IEEE Int. Symposium on Antennas and Propag*ation *& USNC/URSI National Radio Science Meeting*, San Diego, California, July 2017.

[136] T. Zhang, W. Hong and K. Wu, "Analysis and optimum design of sequential-rotation array for gain bandwidth enhancement," in *IEEE Transaction on Antennas and Propagation*, vol. 63, no. 1, pp. 142-150, January 2015.

[137] A. Batgerel and S. Y. Eom, "High-isolation microstrip patch array antenna for single channel full duplex communications," *IET Microwave, Antennas & Propag*ation, vol. 9, no. 11, pp. 1113-1119, August 2015.

[138] E. A. Etellisi, M. A. Elmansouri, and D. S. Filipović, “Wideband Monostatic Co-Polarized Co-channel Simultaneous Transmit and Receive (C-STAR) Broadside Array Configuration”, IEEE Transaction Antennas Propagation, (to be submitted).

[139] M. Elmansouri, P. Valaleprasannakumar, E. Tianang, E. Etellisi, and Dejan Filipovic, “0.5-45GHz simultaneous transmit and receive (STAR) antenna system for electronic attack,” 41st Annual GOMACTech Conf., Orlando, FL, March 2016.

[140] E. A. Etellisi, M. Elmansouri, and D.S. Filipović, “Wideband Monostatic Co-Polarized Co-Channel Simultaneous Transmit and Receive Omnidirectional and Broadside Antenna Arrays,” IEEE URSI, CO Boulder, 2018.